Aeroacoustic Simulation of Modern Propellers

Giulia Chirico

Thesis submitted in fulfilment of the requirements for the
Degree of Doctor of Philosophy

School of Engineering
College of Science and Enginnering
University of Glasgow

Declaration

I hereby declare that this dissertation is a record of work carried out in the School of Engineering at the University of Liverpool during the period from May 2015 to August 2015 and in the University of Glasgow from September 2015 to July 2018. The dissertation is original in content except where otherwise indicated.

July 2018, ...

(Giulia Chirico)

Abstract

Turboprop aircraft are the best choice for short and middle-haul flights, because of their considerably higher fuel efficiency compared to turbofans. However, their acoustic emissions need to be reduced to comply with future noise certification standards, and to improve the comfort of passengers and crew.
The CFD solver of the University of Glasgow HMB3 was employed for comparing different propeller innovative designs and installation options on a twin-engined high-wing aircraft, with the objective to identify the quietest solution. Tonal noise was directly computed from (U)RANS results. Cabin sound was estimated via experimental transfer functions.
The propeller design is the key to decrease the emitted sound at source level. A blade geometry that unloads the tip and operates at lower RPM yielded relevant noise reductions (up to 6 dB in OSPL), without strong performance penalties. Hub arrangements aiming to redistribute the acoustic energy over more frequencies did not clearly appear more pleasant for passengers.
The presence of the airframe modifies the propeller inflow, and causes additional noise sources as well as sound waves reflections. The need of simulating the whole airplane in real operating conditions to accurately evaluate in-flight noise was highlighted. At cruise conditions, and with propellers in phase, the counter-rotating top-in layout was found the quietest, with a benefit in interior OSPL of more than 4 dB compared to co-rotating propellers. The inboard-up propeller rotation developed louder noise because of the higher blade loading on the fuselage side, and of constructive sound waves interferences. Acoustic interferences can instead be used favourably by propeller synchrophasing, naturally promoting noise cancellation. This strategy led to more than 3 dB of OSPL noise reduction inside the cabin for co-rotating propellers, whereas was not beneficial for the counter-rotating top-in layout.

Acknowledgements

My deepest gratitude is devoted to my supervisor Prof. George Barakos for his guidance, encouragement, and constant support. His technical knowledge, advice, and contagious enthusiasm made this thesis a reality and kept me motivated.

Special thanks to Dr. Mark Woodgate and Dr. Massimo Biava for sharing their expertise in numerical methods, and for all those times they answered my questions and helped me solve my computational problems.

Many thanks have to be granted to Dr. Nicholas Bown from Dowty Propellers and Principal Engineer Trevor Wood from GE Global Research, whose contributions and experience significantly improved this work.

The financial support by Dowty Propellers is gratefully acknowledged, as well as the access to the EPCC's Cirrus HPC Service, the EPSRC funded ARCHIE-WeSt HPC, and the computing systems of the Universities of Liverpool and Glasgow. The use of the geometries and experimental data of the IMPACTA project from ARA and NLR is also acknowledged.

I would also like to thank all the CFD Lab members, past and present, for making me feel at home and creating a stimulating work environment, and Mamta Kanabar, whose precious teachings of yoga gave me the physical and mental strength to keep going.

Most importantly, I would like to express my great appreciation to my family and friends, for their unconditional support, trust, understanding, and source of motivation.

Last but not least, thanks to *C.* for all the patience and love during my study.

Publications

Journal Papers

G. Chirico, G. N. Barakos, N. Bown, "Numerical aeroacoustic analysis of propeller designs", *The Aeronautical Journal*, Vol. 122, No. 1248 (2018), pp. 283–315, doi:10.1017/aer.2017.123.

G. Chirico, G. N. Barakos, N. Bown, "Propeller installation effects on turboprop aircraft acoustics", *Journal of Sound and Vibration*, Vol. 424 (2018), pp. 238–262, doi:10.1016/j.jsv.2018.03.003.

Papers in Conference Proceedings

G. Chirico, G. N. Barakos, "Computational Aeroacoustic Analysis of Propeller Configurations", *Proceedings of the Applied Aerodynamics Research Conference, 19-21 July 2016, Bristol, UK.*

G. Chirico, G. N. Barakos, N. Bown, "Computational Aeroacoustic Analysis of Propeller Installation Effects", *Proceedings of the European Rotorcraft Forum, 12-15 September 2017, Milan, Italy.*

G. Chirico, G. N. Barakos, N. Bown, "Acoustic Assessment of Twin-Engined Turboprop Layouts", *Proceedings of the 7^{th} European Conference on Computational Fluid Dynamics, 11-15 June 2018, Glasgow, UK.*

Presentations without Proceedings

G. Chirico, G. N. Barakos, "Propeller Computational Aeroacoustic Analysis", *UK Vertical Lift Network Annual Technical Workshop, 9-10 May 2016.*

G. Chirico, G. N. Barakos, N. Bown, "Aeroacoustic Analysis of Modern Propeller Designs", *UK Vertical Lift Network Annual Technical Workshop, 22-23 May 2017.*

Contents

List of Figures

List of Tables

Nomenclature

Acronyms

AD Actuator Disk

AF$= N_b \frac{100000}{16} \int_{0.2}^{1.0} \frac{c(r)}{D} r^3 \, \mathrm{d}r$ Activity Factor (of the propeller) [-]

AL Actuator Line

ALE Arbitrary Lagrangian Eulerian

ARA Aircraft Research Association

ASPL A-weighted Sound Pressure Level

BEM Blade Element - Momentum theory

BILU Block Incomplete Lower-Upper

BPF Blade Passing Frequency

BSL Baseline

CAA Computational AeroAcoustics

CFD Computational Fluid Dynamics

CNTI Counter-rotating top-in propellers

CNTIψ_s Counter-rotating top-in propellers with -ψ_s degrees of synchrophasing

CNTO Counter-rotating top-out propellers

CO Co-rotating propellers

COψ_s Co-rotating propellers with ψ_s degrees of synchrophasing

CPU Central Processing Unit

DES Detached Eddy Simulation

EARSM Explicit Algebraic Reynolds Stress Model

EC European Commission

FFA Aeronautical research institute of Sweden

FFT Fast Fourier Transform

FW-H Ffowcs Williams - Hawkings

GE General Electrics

HMB3 Helicopter Multi Block

HPC High Performance Computer

IMPACTA IMproving the Propulsion Aerodynamics and aCoustics of Turboprop Aircraft

JORP Joint Open Rotor Program

K-H Kirchhoff - Helmholtz

LES Large Eddy Simulation

MIT Massachusetts Institute of Technology

MPI Message Passing Interface

MUSCL Monotone Upwind Schemes for Scalar Conservation Laws

MUSCL4 4^{th} order accurate in space MUSCL scheme

NASA National Aeronautics and Space Administration

NLR Netherlands aerospace centre

OASPL Overall A-weighted Sound Pressure Level

ODE Ordinary Differential Equation

ONERA French national aerospace research center

OSPL Overall Sound Pressure Level

PSD Power Spectral Density

RANS Reynolds-Averaged Navier-Stokes

RPM Revolutions Per Minute

SAS Scale Adaptive Simulation

SPL Sound Pressure Level

SST Shear Stress Transport

TF Transfer Function

TL Transmission Loss

URANS Unsteady Reynolds-Averaged Navier-Stokes

WT Wind Tunnel

Greek Symbols

α Incidence angle [deg]

α_T Thrust line incidence [deg]

γ Gas specific heat capacity ratio [-]

δ_i Dimension of the local grid cell (i component) [grid units]

δ_{ij} Kronecker delta

Δs Grid spacing [grid units]

$\nu_t = \frac{\mu_T}{\rho}$ Turbulent kinematic viscosity [m^2/s]

ε Rate of dissipation of the turbulent kinetic energy [m^2/s^3]

$\eta = J\frac{C_T}{C_P}$ Propeller efficiency [-]

Θ Fuselage azimuthal coordinate [deg]

$\theta_{\Delta t}$ Propeller azimuth degrees per time step [deg]

κ von Kármán constant [-]

μ Molecular dynamic viscosity [Pa·s]

μ_T Turbulent Eddy viscosity [Pa·s]

τ_{ij} Viscous stress tensor [Pa], Reynolds stress tensor [kg/(m·s^3)]

τ Computational pseudo time [-]

ρ_∞ Free-stream density [kg/m^3]

ρ Fluid density [kg/m^3]

ψ Azimuthal blade coordinate, increasing with in the rotation direction [deg]

ψ_b Azimuthal position of the reference blade [deg]

ψ_s Starboard propeller synchrophasing angle [deg]

ω Specific dissipation rate of the turbulent kinetic energy [1/s]

$\boldsymbol{\omega}$ Rotor rotation vector [rad/s], Vorticity [1/s]

ω_x Vorticity component in x direction [1/s]

Latin Symbols

a_∞ Free-stream speed of sound [m/s]

c Blade root chord [m]

$c(r)$ Blade chord at radial position r [m]

C_D Drag coefficient [-]

C_F Force coefficient [-]

C_L Lift coefficient [-]

C_m Moment coefficient [-]

C_n Normal force coefficient [-]

$C_p = \frac{p-p_\infty}{\frac{1}{2}\rho_\infty V_\infty^2}$ Pressure coefficient [-]

$C_P = \frac{P}{\rho_\infty n^3 D^5}$ Power coefficient (propeller convention) [-]

C_t Tangential force coefficient [-]

$C_T = \frac{T}{\rho_\infty n^2 D^4}$ Thrust coefficient (propeller convention) [-]

D Propeller diameter [m], Aircraft drag [N]

$\mathscr{D}$ Turbulent destruction [Kg/(m·s^3)]

e Specific internal energy [(m/s)^2]

E Total energy of the fluid per unit mass [(m/s)^2]

f Frequency [Hz]

f_i Acting body force on the fluid (i component) [N/Kg]

f_{Nyq} Nyquist frequency [Hz]

f_{samp} Sampling frequency [Hz]

Fy Aircraft resultant side force [N]

$\mathbf{F}_i$ Inviscid flux vector [-]

$\mathbf{F}^i$ Inviscid flux vector in x direction [-]

$\mathbf{G}^i$ Inviscid flux vector in y direction [-]

$\mathbf{H}^i$ Inviscid flux vector in z direction [-]

$\mathbf{F}_v$ Viscous flux vector [-]

$\mathbf{F}^v$ Viscous flux vector in x direction [-]

$\mathbf{G}^v$ Viscous flux vector in y direction [-]

$\mathbf{H}^v$ Viscous flux vector in z direction [-]

i, j, k Spatial indices of curvilinear co-ordinate system

IX, IY TF points indices

$J = \frac{V_\infty}{n \cdot D}$ Propeller advance ratio [-]

k Turbulent kinetic energy per unit mass [(m/s)^2]

L Aircraft lift [N], Defining length scale of the problem [m]

ℓ Turbulent length scale [m]

Mx Aircraft resultant roll moment [N·m]

$M_{h,\mathbf{T}IP} = \sqrt{M_{\mathbf{T}IP}^2 + M_\infty^2}$ Tip helical Mach number [-]

$M_{\mathbf{T}IP} = \frac{V_{\mathbf{T}IP}}{a_\infty}$ Tip geometric Mach number [-]

$M_\infty = \frac{V_\infty}{a_\infty}$ Free-stream Mach number [-]

$n = \frac{\mathbf{RPM}}{60}$ Propeller angular velocity [rounds/s]

$\mathbf{n}$ Normal unity vector [-]

n, m Time and pseudo-time steps indices

N Propeller geometric periodicity index

N_b Propeller number of blades [-]

N_p Number of points per wave length [-]

$p(\mathbf{x})$ Pressure field [Pa]

$p(\mathbf{x}, t)$ Pressure time signal [Pa]

$p'(\mathbf{x},t)$ Unsteady pressure time signal [Pa]

$p_{\mathbf{r}ef}$ Acoustic pressure reference for the SPL [Pa]

P Propeller power [W]

$\mathbf{P}$ Vector of conservative variables [-]

$\mathscr{P}$ Turbulent production [Kg/(m·s^3)]

Q Second invariant of the velocity gradient tensor [1/s^2], Torque [N·m]

Q_p Torque of the port propeller [N·m]

$Q_{\mathbf{SAS}}$ Additional source term for ω in the SAS turbulence model [Kg/(m^{3}s^2)]

$\mathbf{q}$ Heat flux vector [W/m^2]

r Blade radial coordinate [-]

R Propeller radius [m]

$\mathbf{R}$ Residual vector [-]

$\mathbf{R}^*$ Unsteady residual vector [-]

R_{sp} Specific gas constant [J/(Kg·K)]

$Re_{\mathbf{T}IP} = \frac{V_{\mathbf{T}IP} \cdot c \cdot \rho_\infty}{\mu}$ Tip Reynolds number [-]

$Re_\infty = \frac{V_\infty \cdot c \cdot \rho_\infty}{\mu}$ Free-stream Reynolds number [-]

$Ret = \frac{\mu_T}{\mu}$ Turbulent Reynolds number [-]

$\mathbf{S}$ Source term vector [-]

S_{ij} Strain rate tensor [1/s]

t Time [s]

T Propeller thrust [N], Temperature [K]

T_p Thrust of the port propeller [N]

Tu Turbululence level [-]

$\mathbf{u} = (u,v,w)^T$ Fluid velocity vector [m/s]

$V(t)$ Time dependent control volume with boundary $\partial V(t)$ [m^3]

$\mathbb{V}$ Cell volume [grid units^3]

$V_{\mathbf{T}IP}$ Propeller tip speed velocity [m/s]

V_∞ Free-stream velocity [m/s]

$\mathbf{W}$ Vector of conserved variables [-]

X Aircraft longitudinal coordinate [m]

$\mathbf{x}$ Position vector [m]

x,y,z Spacial coordinates in Cartesian system [m]

x_w, y_w, z_w Wing spacial coordinates [grid units]

z_f Idealized fuselage longitudinal coordinate [grid units]

Mathematical Operators

$\frac{d(\cdot)}{dx}$ Derivative of $(\cdot)$ with respect to the variable x

∇ Nabla (Del) - vector of partial derivative operators (gradient, divergence, and curl)

$\frac{\partial(\cdot)}{\partial x}$ Partial derivative of $(\cdot)$ with respect to the variable x

$(\cdot)^T$ Transpose of matrix $(\cdot)$

$\Delta(\cdot)$ Variation of $(\cdot)$

Subscript and Superscript

$(\cdot)_{amb}$ Ambient value of the variable $(\cdot)$

$(\cdot)_{max}$ Maximum value of the variable $(\cdot)$

$(\cdot)_{min}$ Minimum value of the variable $(\cdot)$

$(\cdot)_{ref}$ Reference value of the variable $(\cdot)$

$(\cdot)_{rms}$ Root Mean Square of the variable $(\cdot)$

$\widehat{(\cdot)}$ Fourier transform of the variable $(\cdot)$

$\tilde{(\cdot)}$ Nondimensional variable of the variable $(\cdot)$

$\overline{(\cdot)}$ Time average value of the variable $(\cdot)$

Notes: In the present dissertation variables indicated in bold are vector variables. Also, when an equation is reported in indicative notation, the Einstein's notation is used, which implies summation for repeated indices.

Chapter 1

Introduction

1.1. Motivation

Short to medium range flights make up to 95% of the total air traffic on European routes [1]. At the same time, propeller-driven aircraft are the best option to decrease the fuel burnt during these flights, as they have a considerably higher propulsive efficiency in comparison to a similar capacity jet aircraft [2, 3]. The aircraft weight relative to turbofan aircraft is lower, and, generating thrust from a larger mass flow, propellers allow up to 30% savings in fuel burn with respect to an equivalent turbofan engine. Turboprops also need shorter take-off/landing lengths and climb time, making them preferable for operations from smaller regional airports and inner city airports with a short runway. In addition, current propeller designs (see Figure 1.1 for an example) allow to achieve a similar speed, with a very long available flight range.

However, future environmental certifications will require a reduction in the aircraft acoustic emissions. Compared to the capabilities of typical new aircraft in 2000, European targets aim to reduce the perceived acoustic footprint of flying aircraft by 50% for 2020 [5] and to achieve a total noise abatement of 65% for 2050 [6]. Current turboprops still emit substantial noise: on average, the interior noise of advanced turboprops is approximately 25 dB higher than turbofans [7]. Moreover, they are perceived by passengers as more annoying than turbofans because of the several tone components forming the propeller sound spectra. The challenge is therefore to improve propeller acoustics without a significant performance penalty.

Starting from the IMPACTA project [8, 9] of Dowty Propellers* , which aimed to reduce and/or modify the noise spectra of the whole turboprop propulsion system, this work studies innovative blade and hub designs, as well as different propeller

* Project in collaboration with the Aircraft Research Association (ARA) [10], the Netherlands Aerospace Center (NLR) [11], and the CFD Laboratory of the University of Glasgow [12].

(a) Dowty Propellers R391 propeller system for Lockheed Martin's C-130J Super Hercules. The same design is used on the Alenia Aeronautica C-27J.

(b) Dowty Propellers R381 propeller system for the Saab 2000.

(c) Dowty Propellers R408 propeller system of the Bombardier Q400 Dash 8. The same design is used on the Antonov AN-132D and the AVIC's MA700.

Figure 1.1: Example of current propeller designs [4].

installation options, to identify the quietest solution. Computational Fluid Dynamics (CFD) is used to perform this analysis, assessing various numerical methods to find the most suitable for capturing propeller sound generation process, thus enabling an adequate evaluation of their actual acoustics in flight.

1.2. Propeller Acoustics

The acoustic signature of a propeller includes *thickness noise* due to the blades volume displacement, *steady-loading noise* due to the blades steady forces, *unsteady-loading noise* due to azimuthally not uniform loading, *quadrupole noise* due to non-linear effects, and *broadband noise* due to turbulence [13]. The relative importance of each source depends on both propeller design and operating conditions.

Propellers always operate in a distorted flow-field because of incidence thrust angle, presence of the airframe and inflow turbulence. Flow distortion results in additional noise, mainly unsteady loading noise, which is usually significant. Under non-uniform and/or unsteady inflow conditions the sound directivity pattern also differs from an ideal inflow case. Tonal noise was shown to vary by up to 8 dB as a consequence of unsteady loading, with effects in the up-stream direction stronger than for the down-stream [14]. The presence of the airframe also affects, notably, the noise propagation. The sound propagating through the fuselage boundary layer undergoes refraction because of velocity and temperature gradients, the impact of the sound waves with the fuselage is subject to scattering, and the wing can provide noise shielding. It is therefore important to analyse propellers as installed system, because disregarding installation effects can lead to a substantial under-prediction of the actual sound levels and to wrong directivities [13].

1.2.1 Noise Spectral Characteristics

Propeller noise is composed of harmonic noise, narrow-band random noise and broadband noise. The different spectral characteristics of these three elements are shown in Figure 1.2.

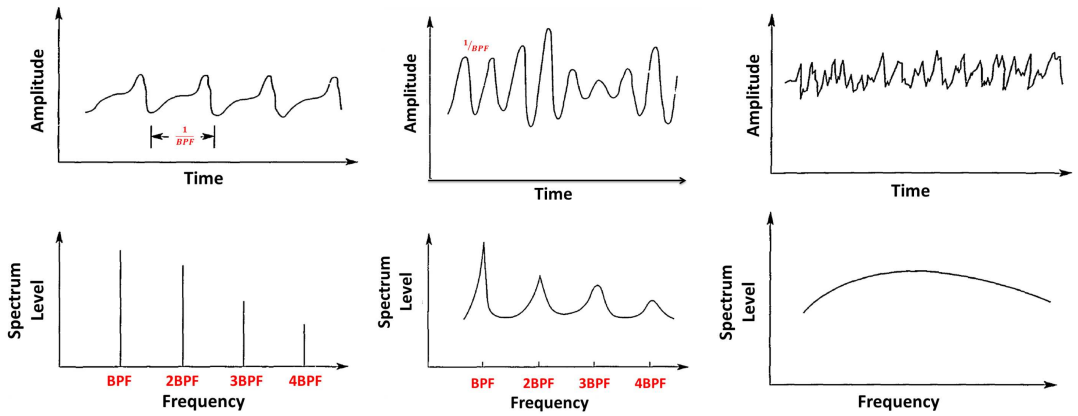

(a) Harmonic noise. (b) Narrow-band random noise. (c) Broadband noise.

Figure 1.2: Spectral characteristics of propeller noise components [13].

Harmonic noise is periodic, i.e. its time signature can be represented by a constant rate pulse. Given a propeller with N_b blades running at constant angular velocity n, the noise discrete peaks appear at the Blade Passing Frequency $BPF = N_b \cdot n$ and its integer multiples. The highest sound pressure level occurs at the fundamental frequency, followed by an almost linear decrease as the harmonic order increases [15]. Extra sub-harmonics arise in the noise spectra if there are asymmetries in the blade geometry

and/or in the azimuthal blade spacing. Besides, if a piston engine is used, its periodic non-uniform rotational motion also produces tonal noise, modulating the noise spectra if there is coincidence between BPF tones and the engine crank frequency or adding further harmonics otherwise [16].
Narrow-band random noise is almost periodic and its spectrum shows distinct tones. Yet, the acoustic energy is not concentrated at isolated frequencies but spreads out, especially at the higher frequencies.
Broadband noise is random in nature and contains components at all frequencies, resulting in a continuous spectrum. Its contribution to the total noise of an aircraft in flight was found to be not significant with respect to the other noise sources [17].

1.2.2 Sound-Generating Mechanisms

The sources of propeller noise can be categorised depending on their time nature in the rotating-blade system of reference, i.e. from the point of view of an observer seated on a propeller blade. In this system we distinguish between steady, unsteady and random sound sources.
Steady sources are caused by the propeller rotation and contribute tonal noise. The helical blade-tip Mach number $M_{h,\mathrm{TIP}}$ is the main propeller operating parameter for tonal noise and its increase results in a rapid increase of higher harmonic noise levels. At subsonic tip speeds, steady noise sources are *(i)* the periodic flow displacement caused by the finite thickness of the blades - *thickness noise*, and *(ii)* the periodic pressure disturbance caused by the blade motion producing thrust and torque - *loading noise*. Thickness noise, whose amplitude is proportional to the blade volume, can be described by a monopole source and it is prevailing at high speeds, i.e. for a typical general aviation propeller $M_{h,\mathrm{TIP}} \geq 0.6-0.7$. Loading noise is instead dominant at low to moderate speeds and can be represented by an acoustic dipole with its radiation lobes directed forward and backward of the blade disk plane. For transonic blade section speeds, non linear effects become important and they can be modelled with quadrupole sources distributed in the volume surrounding the blades - *(non-linear quadrupole noise)*. Linear thickness and loading sources are enhanced by the quadrupole source and the noise increases, especially for unswept blades.
Unsteady sources include both periodic and random variations of the blade loading. Every inflow distortion constant in time, e.g. a shaft tilt relative to the inflow, results in blade loading cyclic changes for each propeller revolution and thus generate noise at the propeller tones. This can raise or lower the steady loading noise depending on the azimuthal position of the disturbance. In addition, the sound directivity is no

longer axisymmetric but exhibits a number of lobes determined by the distortion order. Unsteady loading noise is significant for contra-rotating propellers, especially for low-speed operations, because of the aerodynamic interference between the two rotors. Particular conditions can also cause nearly-periodic blade loading, as for example a vortex ingestion.
Random sources are related to flow turbulence and contribute broadband noise. Two sources can be important for propeller noise: *(i)* the interaction between the blade leading edge and the inflow turbulence, and *(ii)* loading fluctuations at the trailing edge due to the turbulent boundary layer and the connected interaction between tip vortex and trailing edge. An acoustic dipole with the axis perpendicular to the blade chord can be used to model this noise component.

1.2.3 Noise Predictions Methods

Since the 1920s experimental and theoretical investigations have been carried out to understand and predict propeller noise, the development of computers contributing widely. By the end of the century a large number of methods were developed of both empirical and theoretical character, of various complexity and accuracy, included those currently used.
It is noted that nearly all propeller acoustic prediction techniques, still today, deal only with the tonal noise component, because this is normally the most significant. For broadband noise, a general and comprehensive model is not even yet reported, despite the need for it was first recognised in the 1930s [18, 19, 20]. Scaling noise laws [21] and semi-empirical approaches based on specific source mechanisms (e.g. Proudman's formula [22, 23] or flat-plate scattering derived methods [24, 25, 26, 27, 28, 29]) are therefore nowadays usually adopted.

Empirical Methods

Empirical methods deliver estimates of noise levels, at engineering accuracy, from gross parameters such as flight and rotation speeds, number of blades, power, *etc* via simple procedures involving charts and hand held calculators. They are therefore mainly used for preliminary design analysis.
As an example of these methods, we recall here those proposed by Magliozzi in 1971 [30], by Smith in 1981 [31], and by Dobrzynski in 1994 [32]. The first is reported to give overall sound level estimates within 3 dB in the near-field and within 6 dB in the far-field. The second deduces an equation from A-weighted sound level measurements of certification tests and, taking into account blade twist and thickness, gives far-field

flyover noise within 2.2 dB_A. The third starts from a theoretical method and includes an empirical piston engine noise prediction.

Theoretical Methods

Theoretical methods are more complex and more detailed than empirical methods, offering more accurate predictions especially in the near-field, and thus essential in the case of cabin noise evaluation. They usually require at least a workstation and are therefore used for advanced design and research. They are based on the description of the noise generation process, with various level of approximation and simplifying hypothesis. A chronological summary of the key works on propeller theoretical harmonic noise prediction methods is presented in Table 1.1. A comprehensive review of methods and efforts up to 1995, for both harmonic and broadband noise predictions, was done by Metzger [35].

The great majority of the methods still employed today, to compute propeller tonal noise, can be derived from the Ffowcs Williams-Hawkings (FW-H) equation [42] published in 1969 (see Table 1.1). Approaches in the time domain follow Farassat's formulations [48, 54], usually adopting his formulation 1A for sub-sonic source regions and formulation 3 for super-sonic ones. Time-domain methods can treat blade geometry with any desired level of accuracy and can be applied to unsteady loading without modifications. Frequency-domain techniques, on the other hand, follow Hanson's approach to represent the propeller blades as helicoidal surfaces [51, 52]. The Fourier transformation eliminates the numerical derivatives and the computation of retarded blade locations needed in the time-domain methods. This results in easily coded formulas (with some versions even solved by hand, if the effective radius formulation is employed [13]). Some precision in the blade geometry representation is generally lost and the version for unsteady loading is slightly more complex than the steady one. However, results have good accuracy for harmonics up to fairly high order and this method can be more convenient if one is interested in noise harmonics rather than pressure waveforms (the latter are determined by summing a Fourier series, whereas they are the direct output of time-domain techniques). In addition, frequency-domain approaches give direct insight to the effects of blade geometry and operating conditions on the tonal noise, enabling valuable analysis of the sound spectrum per frequency.

An alternative to the FW-H equation is the Kirchhoff-Helmholtz (K-H) theorem, which expresses the acoustic field produced by a definite volume containing sound sources in terms of the flow variables at its bounding surface [55]. This approach is usually less

1919-1920	**Lynam and Webb** [33],**Bryan** [34] Earliest attempts to develop a noise prediction method based on the Lancester's intuition that propeller noise "is due to the movement of pressure centers of constant or nearly constant magnitude in a circular orbit" [35]. No estimate of sound levels was given.
1936	**Gutin** [36] First analytical expression of radiated sound energy and directional properties for the lower propeller harmonics under static conditions (blade aerodynamic forces represented by a ring of dipoles). First theory addressing correctly the noise generation process.
1937-1940	**Deming** [37, 38] Extensions of Gutin's work to account for blade thickness (symmetric airfoil at zero angle of attack assumed), higher harmonic noise (via empirical relations), and thrust and torque contributions (using an algebraic equation for their span-wise distribution). First assessment of blades number impact on sound pressure at BPFs tones: at given tip Mach, the more the blades the lower the harmonic sound pressure level.
1952-54	**Lighthill** [39, 40] Equation for the acoustic radiation of small turbulent flow regions embedded in an infinite homogeneous fluid with constant density and sound speed ("Acoustic Analogy"). Basis of most modern aeroacoustic theories.
1954	**Garrick and Watkins** [41] General expression of both near and far sound pressure field for any given harmonic under subsonic forward flight conditions (symmetric pressure load assumed) - based on Gutin's theory. First acknowledgement of the importance of inflow distortion.
1969	**Ffowcs Williams and Hawkings** [42] Expression for the density field radiated by turbulence in the presence of arbitrarily moving surfaces (Ffowcs Williams-Hawkings equation), showing that propeller noise is due to blade thickness as a monopole, loading variation as a dipole and non linear effects, important for unswept blades at transonic tip speed, as a quadrupole - founded on Curle's expansion of Lighthill's theory including solid boundaries effects [43]. Nowadays still employed for rotor and propeller far-field noise predictions.
1975-1992	**Farassat** [44, 45, 46, 47, 48, 49, 50] Time-domain formulations of the FW-H equation for both subsonic and supersonic rotating blades, considering the actual blade surface and including non-uniform inflow conditions. Theoretical basis of many state-of-the-art prediction methods..
1976-1993	**Hanson** [51, 52, 53] Frequency-domain method to solve the FW-H equation, theoretical basis of modern frequency-domain noise estimation approaches. Refraction and scattering by the fuselage and the boundary layer included via matching analytical expressions of incident and scattered waves.

Table 1.1: Propeller tonal noise analytical prediction methods: a time-line of key publications.

exercised because of its more restricted applicability, but can be more efficient since it requires only velocity and pressure, and not their derivatives, it does not involve volume integrals, and it avoids the complex quadrupole term computation.

The Use of Computational Fluid Dynamics

The most recent approach to propeller noise predictions makes direct use of CFD codes. It is the highest-fidelity technique and the most appropriate for near-field installed noise, especially for high cruise or tip speeds, since it naturally includes actual distorted propeller inflow conditions, accurate blade loads and interactions with the airframe.

The first Computational AeroAcoustic (CAA) simulations were carried out between the late 1980s and the early 1990s, using Euler's equations. Despite the improved capabilities of modern computers, the direct computation of the whole propeller sound field with Navier-Stokes equations is still excessively expensive and time-consuming, because of the high Reynolds number of such flows. CAA computational challenges arise from the specific character of aeroacoustic problems. These are, by nature, time-dependent, usually covering a wide frequency range, and multiple-scales, i.e. the length scale of the sound source is significantly different from the acoustic wavelengths. Moreover, sound waves have amplitudes remarkably small compared to the mean flow perturbations (often 5 to 6 orders smaller) and decay very slowly, actually reaching the boundaries of a finite computational domain. Demanding requirements and computational issues of CAA simulations are described in detail in references [56, 57, 58], together with the developed numerical schemes and some applications. A review of the recent progress in this field, up until 2014, is done by Lele *et al.* in [59]. Since direct CAA is nowadays prohibitive for far-field noise computations [59, 60], the current strategy is therefore to couple CFD in the near-field with an acoustics analogy method in the far-field (see literature survey for examples of this approach regarding propeller noise). As for CFD methods in particular, steady or unsteady Reynolds-Averaged Navier-Stokes equations (RANS/URANS) are normally used for tonal noise, whereas Large Eddy Simulation (LES) or hybrid techniques (see Section 2.3) are employed if broadband noise is of interest as well.

1.2.4 Control of Propeller Noise

From the understanding of the generating mechanisms and the analysis of the governing equations, it is possible to obtain guidance to limit propeller noise. Targets and constraints are various:

1. near-field noise requirements, mainly concerning cruise conditions, include cabin noise comfort and airplane structural acoustic fatigue;

2. far-field noise requirements, generally related to low-speed operating conditions, comprise noise certifications and additional community noise restrictions.

Reducing Noise at Source

Noise control approaches can act on propeller operating conditions and/or design parameters, to reduce the sound at source maintaining the required thrust.
Since all sound sources have radiation efficiencies determined by the relative velocity, lowering the tip speed reduces the noise almost always: the actual benefit depends on the specific design and operating conditions, but an overall noise reduction was observed to vary as 40 times the tip Mach number for conventional propellers of the 1970s [13].
Another strategy based on propeller operating conditions is to lessen the disk loading by increasing the propeller diameter D, as the loading noise decreases as approximately $1/D^2$ [13]. Moreover, the propeller efficiency at low-speed tends to be higher with a larger diameter, and thus the increase in the diameter can be combined with a lower tip speed to achieve further noise reductions.
Loading noise can also be significantly reduced, especially at higher harmonics, by increasing the blade count. Although adding blades raises the frequencies generated, and hence perceived noise levels can increase (particularly during high-speed cruise), a noise reduction can still generally be obtained. Quadrupole noise benefits as well from a larger blade count.
Thickness noise, which is relevant at high-speed cruise, is not considerably affected by this choice, provided that the blade volume is decreased by reducing the blade chord because more blades means more thickness noise. The effect on the spectrum of a decrease in blade thickness and chord depends on the airfoil shape. A thickness reduction at constant chord yields lower noise levels at all harmonics, with a noise decrease that goes approximately as the square of the blade volume [13].
During high-speed cruise, a larger blade sweep is also very effective in reducing the propeller noise, particularly as sweep increases. Blade twist and plan-form distributions are instead shown to have only a small effect on propeller noise, whereas they strongly affect the aerodynamics.
Airfoil sections do not contribute significantly to lower harmonic sound levels, although some airfoil sections appear better than other for noise reduction [13].
Flow control via vortex generator blowing jets (see e.g. [61]), or plasma actuators (see

e.g. [62]), has been recently studied to improve propeller efficiency by suppressing the boundary layer separation. Producing a more attached flow on the propeller blades, it can be imagined that these techniques could be also advantageous for reducing noise emissions, however their acoustic benefit has not yet been thoroughly investigated.[†]

Reducing Noise once Installed

The strategies described above aim to reduce propeller noise at its source. Although this should always be considered, sometimes it is not enough to satisfy the cabin sound levels requirements, and additional control measures must be adopted.

In multi-propeller aircraft, lower noise levels can be achieved by promoting noise cancellation between the different sound sources. This is done by propeller synchrophasing, i.e. setting a relatively fixed shift in the blades position so that destructive acoustic interferences naturally occur. Since constant-speed variable-pitch propellers are typically employed, the desired propeller relative blade angle is simply attained by accelerating or decelerating the slave propeller(s) via small adjustments in the blade pitch. Synchrophasing is thus a very interesting passive noise, and vibration, control strategy, because its implementation doesn't result in additional weight and it acts across the sound spectrum. On the contrary, classic passive methods, such as the frequently used tuned fuselage dampers, increase the structure weight and reduce noise only at specific tones.

Active control strategies, usually employed in conjunction with passive methods, allow for further reductions in cabin noise levels acting on the lower harmonics, generally on the first two or three. These use an optimised combination of microphones and loudspeakers, or active tunable vibration absorbers (see as an example the systems adopted in the SAAB 2000 [65], in the ATR42 [66] or in the A400M [67]). Active controls have the advantage of operating over the whole flight envelope, including unsteady variations in excitation due to turbulence and gusts.

Hybrid active-passive control solutions, using microphones and accelerometers as sensors, and loudspeakers and vibration generators as actuators, are also being currently studied [68].

[†] It is instead noted that, for pusher configurations, pylon blowing flow control was successfully demonstrated to provide significant noise reductions, specially for higher harmonics, by reducing the wake velocity deficit and making its profile uniform. As an example, the works of Rego *et al.* [63] and Bury *et al.* [64], respectively on a single propeller and a counter-rotating open rotor, are cited here.

1.3. Literature Survey

Major research efforts were carried out in the 1980s and 1990s, after the high oil prices caused by the world energy crisis of 1973-1974 made turboprops an attractive alternative to the widely employed, and less efficient, turbojets and turbofans. Aerodynamics and acoustics of advanced propeller designs were investigated, being both linked to the aircraft sale and usage costs, via experimental, analytical and numerical approaches. The first few computational aeroacoustic studies were also conducted at that time. With the fall of fuel prices in the late 1980s, these research programmes ended before having achieved enough maturity to convince the aviation industry. Because of new environmental regulations, nowadays, interest in propeller-driven aircraft resurfaced. New research is developing, focusing on propeller acoustics, since turboprop's fuel efficiency is already high. Work on isolated propellers is mainly performed to establish accurate noise prediction methods with reasonable computational cost, and to find quieter propeller designs. Investigations on installed propellers seek to improve our understanding of the complex propeller-airframe interaction physics, and to find aerodynamically and acoustically better installation solutions. Exploiting the capabilities of modern computers, CFD techniques are often employed to study the near-field propeller noise, whereas aeroacoustics methods are used to propagate the sound in the far-field.
The literature survey presented in the following, is divided into works performed on isolated propellers, and studies on propeller installation effects, since this thesis is organised the same way. The literature search reported here is focused only on aerodynamics and acoustics of aircraft single-rotation propellers, in isolation or mounted in tractor configuration, as this is the subject of the present research. A review of the studies carried out on propellers in pusher configuration, or in other applications, e.g. contra-rotating open-rotors, ducted propellers, or marine propellers, is not discussed. However, it is noted that the same methods can be used to investigate even these configurations.

1.3.1 Isolated Propeller Studies

Most relevant and comprehensive works of the 1980s and 1990s regarding acoustics of isolated propellers are presented in Table 1.2. Experimental activities, as well as analytical and/or numerical/theoretical predictions, are included.
Overall, it can be concluded that, regarding experiments, numerous wind tunnel tests have been performed, but more extensive and reliable experimental datasets were needed to assess the accuracy of predictive methods in detail [35]. Regarding nume-

Author	**Propeller**	**Experiments**	**Theoretical Approach** (Aerodynamics + Acoustics)
Succi *et al.* [69] (MIT)	1/4 replicas of 2-bladed 1C160 propeller and two modified versions (one heavily loaded, and one with the peak radial loading moved inboard)	angular, fixed-velocity and fixed-J wake and acoustic surveys for each propeller with minimum/symmetric/asymmetric fairings (MIT anechoic WT)	lifting line + array of point sources forward spiralling, each with motion and force of corresponding blade section (≡ Farassat's formulation of FW-H eq.)
Various authors [70, 71, 72, 73, 74] (NASA)	NASA SR-*series* propellers: 8-bladed models with 0, 30 and 45 deg tip sweep angle (SR2, SR1M and SR7A, SR3, respectively), 10-bladed models with 40 and 60 deg tip sweep angle (SR6, SR5, respectively)	• axial force and torque measures with installed rotating balance, acoustic data from pressures transducers on WT walls/near-wall and lateral translating probe microphones, at cruise and take-off/landing conditions (NASA Lewis 8x6 ft/anechoic 9x15 ft WTs) • flight noise tests using propeller models mounted above the fuselage of the Jetstar aircraft	• lifting line, 2D airfoil + linear time-domain propagation (Farassat) • 3D non-linear steady aerodynamics + linear time-domain propagation (Farassat) • 3D steady exact linear lifting surface + linear frequency-domain propagation (Hanson) • 3D unsteady exact linear lifting surface + linear frequency-domain propagation (Hanson) • 3D steady Euler + linear frequency-domain propagation (Hanson) • actuator disk, unloaded linear lift response + linear frequency-domain propagation (Hanson) • 3D steady Euler + direct estimate in the near-field, linear integral propagation in the far-field
Gounet *et al.* [75] (ONERA)	• Aerospatiale general aviation propellers † • 8-bladed SR1 and SR3 NASA propellers⋆ • 12-bladed ONERA propfan scaled model	performance and blade distortion measurements, plus far-field microphones recordings without acoustic lining on the walls, for M_∞=0.25-0.75 and no incidence (ONERA S1-MA transonic WT)	• not specified simple method + frequency domain FW-H approach in aircraft reference system: flat blades and chord- compactness source approximation for moderate speeds and far-field predictions, blade shape accounted in the thickness term for high advancing speeds and fuselage estimates • direct evaluation from 3D Euler eq. computations†

Table 1.2: Isolated propeller acoustics most relevant and comprehensive studies in the 1980s and 1990s (Legend: ⋆ = predictions compared against not proprietary experimental data; † = evaluation against experiments not shown; ◇ = full numerical calculations used as main method of predictions evaluation). *(Part 1/3)*

Author	**Propeller**	**Experiments**	**Theoretical Approach** (Aerodynamics + Acoustics)
Tam *et al.* [76] (USA universities)	8-bladed NASA SR3 propeller*	N/A	aerodynamic loading assumed as known + linearised boundary-value problems of inviscid compressible fluid for thickness and loading noise, with weakly non-linear propagation effects included via Whitham's non-linearisation procedure using the equal area rule of his shock-fitting method
Schulten [77, 78, 79] (NLR)	• model scale 6-bladed conventional propeller • NASA SR7a propfan with 8 and 2 blades* • 6-bladed Fokker 50 propeller (scale 1:5)* • 6-bladed model scale SNAAP propellers *	microphones measures in the wake of the propeller mounted on a slender central body over various aerodynamic conditions (low-speed anechoic DNW WT)	lifting surface with leading edge suction force correction + frequency wave number formulation of generalised K-H theorem in separated cylindrical coordinates.
Parry *et al.* [80, 81, 82, 83] (UK universities)	• generic 7- and 12-bladed propellers$^{\diamond}$ • 6-bladed Fokker 50 propeller (scale 1:5)*	N/A	aerodynamics considered given by established steady codes + near- and far-field asymptotic expressions of Hanson's frequency-domain formulas in the limit of "many-bladed propellers" for all harmonics at both sub-sonic and super-sonic propeller operating speeds
Whitfield *et al.* [84, 85] (GE)	NASA 8-bladed SR2 and SR3, 10-bladed SR6 propeller models*	N/A	3D non-linear Euler code or simplified loading distributions + frequency-domain non-compact source linear acoustic for the far-field, adjusted via Šulc's semi-empirical method for the near-field (the direct use of flow solutions for near-field noise is assessed and dropped because of the excessive computational cost)

Table 1.2: Isolated propeller acoustics most relevant and comprehensive studies in the 1980s and 1990s (Legend: * = predictions compared against not proprietary experimental data; † = evaluation against experiments not shown; $^{\diamond}$ = full numerical calculations used as main method of predictions evaluation). *(Part 2/3)*

Author	**Propeller**	**Experiments**	**Theoretical Approach** (Aerodynamics + Acoustics)
Zandbergen *et al.* [86] (NLR)	6-bladed Fokker 50 propeller (scale 1:5)	near- and far-field acoustic measurements with axially transversing microphones varying incidence and side-slip angles for M_∞=0.12-0.23 and $M_{h,TIP}$=0.5-0.77 (low-speed DNW WT in acoustic configuration with open jet test section)	strip analysis + developed Succi's subsonic compact time-domain solution of FW-H eq. with loading noise accounting for blade cyclic loading and velocity variations due to non axisymmetric inflows and thickness noise accounting for blade velocity variations only
Brouwer [87] (NLR)	6-bladed Fokker 50 propeller (scale 1:5)*	N/A	both aerodynamics and acoustics computed from an integral equation for the circulation derived from the application of Van Dyke's method of matching asymptotic expansions in the reciprocal blade aspect ratio for high aspect ratio blades in an axial compressible flow at subsonic speeds
Scrase *et al.* [88] (ARA)	JORP propellers: 6-bladed scaled high speed design with ARA-D/A airfoils and relatively large tip chord, versions with unswept and moderately swept plan-form	simultaneous measures of running blade shapes, blade and spinner pressures, thrust, torque and acoustic field of the propellers mounted on a minimum interference spinner from static to M_∞= 0.75 conditions (acoustically lined transonic ARA WT)	experimental data + Dowty's prediction method based on FW-H eq. in the time domain accounting for shock waves in the thickness term as quadrupole contribution (aerodynamic methods used in Dowty: strip wake based on modified Lock-Goldstein ideal wake, steady 3D Euler code)

Table 1.2: Isolated propeller acoustics most relevant and comprehensive studies in the 1980s and 1990s (Legend: * = predictions compared against not proprietary experimental data; † = evaluation against experiments not shown; $^\diamond$ = full numerical calculations used as main method of predictions evaluation). *(Part 3/3)*

rical predictions, given shape and motion of the propeller, state-of-the-art methods of that time already delivered noise estimates with reasonable accuracy. They were able to capture differences due to changes of blade design, operating conditions, as well as observer position, and allowed the analysis of the parameters affecting the sound levels among which blade loading, tip Mach number, sweep and asymmetric inflow (see e.g. [69, 89, 70, 77, 78, 86]). As Metzger states at the end of in his review [35] "it appears that deficiencies in the accuracy of propeller noise predictions, in many cases, may be related not to the noise methods being used but the accuracy and detail of the aerodynamic inputs to the calculations". The importance of precise aerodynamic data including leading-edge suction force, tip vortex, root and tip load distributions and stall behavior, was explicity recognised for example in [77, 72, 88, 79], and predictions obtained using a 3D non-linear Euler code showed good agreement with measurements, with discrepancies of the same order as the differences between experimental datasets [84].
Notable results of these studies are the following:

(a) The blade sweep was recognised as a key parameter to reduce propeller noise by promoting acoustic phase cancellation, and advanced designs leading up to 6-9 dB noise reductions were succesfully planned and tested [70]. Blade sweep was also observed from experiments to have a significant impact on the propeller aeroelastic properties [70], which were found important to determine sound levels, especially for higher harmonics (during NASA's PTA project it was demostrated that propeller blades deformation, due to centrifugal and aerodynamic loading, can give differences up to 5 dB, and therefore necessary in noise predictions [90]).

(b) The FW-H equation, in time or frequency domain, was the method most commonly adopted for acoustic predictions, usually neglecting the quadrupole term because of its complexity and its irrelevance for propeller conditions below transonic regimes [91]. Linear acoustic theories were shown to adequately predict noise for subsonic tip speeds, but overestimated sound levels for supersonic tip speeds [70]. On the other hand, a generalised K-H approach yielding velocity field, hydrodynamic wake and acoustic pressure, was proven effective in computing economically the sound field at a large number of points accounting for volume sources, thus representing an efficient alternative to determine the incident acoustic field on a fuselage [77, 79]. A weakly non-linear acoustic and shock-wave theory was also proposed to account for non-linear propagation effects [76], showing their importance in the case of high-subsonic cruise speeds

to accurately predict the waveforms of the aircraft incident sound field.

(c) Simple and explicit formulae derived from asymptotic theory in the limit of large blade number were shown to retain the accuracy of full integral expressions, for both near- and far-field at all propeller operating conditions [80, 81, 82, 83], requiring at most 5% of the CPU time needed for the original integrals [80]. Asymptotic expressions also provided important insight into sound generation (e.g. dependence on forward and tip Mach numbers, effects of sweep and noncompacteness, identification of the blade tip and the Mach radius as dominant in the far-field at subsonic and supersonic regimes respectively, etc.), making them useful in preliminary design. Conclusions derived from asymptotic theories have been later confirmed by exact numerical evaluation of the acoustic radiation integrals by Carley [92, 93]. Extending Chapman's work [94], Carley proposed a fast method to compute the 3D acoustic field of a rotating source in forward motion with arbitrary strength distribution. The method enables the analysis of the whole noise field, by constrast to the "single-point" techniques originated from the FW-H equation, and the execution of parametric studies in reasonable time. He reported a total of 16h of real time on a personal computer to calculate 484812 field points in the case of constant source strength along the blade radius [92].

(d) The method of matched asymptotic expansions of Van Dyke [95, 96] was tested and found not applicable to realistic propellers with high aspect ratio (AR), yieldig unphysical results. This was because the problem expansion parameter AR^{-1} was not small enough. The method showed that 3D effects were more important for propeller blades than for fixed wings [87]. However, the integral equation resulting from the circulation approximation gave accurate aerodynamic loadings and reasonable estimates of sound levels and phase angle, at least for the BPF, with minimum computational cost.

The first computational aeroacoustics efforts developed from the late 1980s, e.g. [97, 98] (see Metzger [35] for a short summary), employed Euler's equations to determine the complete near-field of transonic propellers. Euler's equations take into account the non-linear effects usually neglected with the exclusion of the quadrupole term. The accuracy of sound level estimates was remarkably improved compared to linear predictions. Korkan *et al.* [97] showed discrepancies of maximum 2 dB for the SPL(BPF) at helical tip Mach numbers up to 1.07, and an averaged difference of 5 dB at $M_{h,\mathrm{T}IP}$ of 1.14 and 1.21. Meijer *et al.* [99] presented estimates for the first three harmonic tones within 2 dB for $M_{h,\mathrm{T}IP} \leq 1$ and within 3 to 5 dB for $M_{h,\mathrm{T}IP} = 1.08$.

Grid density and feasibility of the approach, as well as effects of numerical damping and the use of non-reflective boundaries for the CFD domain, were discussed.

Recent relevant works are listeded in Table 1.3. As can be seen, the majority of these couples a CFD simulation of the flow around the propeller blades with an integral approach, based on the acoustic analogy, to determine the acoustic far-field. The accuracy of lower-fidelity models for both aerodynamics and acoustics is also tested against experimental data and/or higher-fidelity methods. From these investigations it is clear that:

(a) The two-steps method *'CFD in the near-field + acoustic solver in the far-field'* was demostrated to be successful for propeller noise predictions, enabling sound level estimates with acceptable accuracy, at least at the blade passing frequency and in the vicinity of the propeller plane [100, 101, 102, 104, 106]. Marinus *et al.* [100] reported an average agreement of about 5 dB with large discrepancies only far upstream of the propeller plane for the first two harmonics. SPL(BPF) estimates of De Gennaro *et al.* [101, 102] showed a difference from experimental data of maximum 2 dB for locations approximately 20 degrees behind the propeller plane and of maximum 5 dB further back. Results of Hambrey *et al.* [106] underpredict sound levels by 4 to 11 dB at BPF and by 9 to 32 dB at 2BPF, with the larger discrepancies at larger distances. Despite a validation of noise predictions against experimental data, a thorough analysis of the numerical errors that can be made in this two-steps approach is not carried out in the above cited studies. However, Giauque *et al.* [111] showed that meshes of moderate density (i.e. $\sim$ 8 M cells per blade) were adequate for lower harmonics noise, the maximum SPL converging well provided the integration FW-H surface contains all relevant sound sources. FW-H results were also found strongly dependent on the wave operator Mach number [111], thus potentially affecting OSPL directivities because of the heterogeneous baseflow generated by the propeller.

(b) Full-domain unsteady CFD computations [104, 106] did not result in significant impovements in the far-field tonal noise level estimates, compared to single-blade steady RANS simulations. This proved the latter to be effective (and preferable because of the lower computational cost) in capturing trends for design analysis. The use of a two-step method with limited costs, as for example that proposed by Marinus *et al.* [100], was shown to be viable and reliable for multidisciplinary optimisation studies during propeller design phases [112, 113].

Author	Propeller	Aerodynamics	Acoustics
Marinus *et al.* [100]	• NASA SR1: 8-bladed model • NASA SR3: 8-bladed model	single-blade RANS, $k-\varepsilon$ with no-slip wall conditions (ANSYS FLUENT)	Farassat 1A formulation of FW-H eq. without quadrupole term [54] in a medium-fixed reference system accounting for the sonic singularity via a truncated first order Taylor expansion [100]
De Gennaro *et al.* [101, 102]	NASA SR2: 8-bladed model	single-blade RANS, $k-\omega$ SST (ANSYS FLUENT) [grid size: $\sim 1.7M$ and $\sim 10.5M$ cells]	FW-H formulation for moving surfaces [103] without quadrupole term
Tan *et al.* [104]	NASA SR2: 8-bladed model	DES, $k-\omega$ SST (CD-Adapco STAR-CCM+) [grid size: $\sim 78M$ cells]	• FW-H formulation for moving surfaces [103] corrected for quadrupole sources [91] • direct evaluation from pressure solution
Hambrey *et al.* [105, 106]	NASA SR2: 4- and 8-bladed models	(A) BEM including variable lift coef. and swirl (B) panel and free vortex methods (SmartRotor) (C) URANS, $k-\omega$ SST (CD-Adapco STAR-CCM+) [grid size: $\sim 3.7M/\sim 7.5M$ cells]	(A) Hanson's helicoidal surface [107] (B),(C) Farassat 1A formulation of FW-H eq. without quadrupole term [54]
Kotwicz Herniczek *et al.* [108]	• NASA SR2: 4- and 8-bladed models • NASA SR3: 2-, 4- and 8-bladed models • NASA SR7: 8-bladed model • others 2- and 6-bladed models	improved BEM	• Deming's analytical method [37, 38] without effective-radius approximation • modified Barry and Magliozzi method [109] • Hanson's helicoidal surface theory [107, 110]

Table 1.3: Isolated propeller acoustics recent (last decade) studies. Predictions validated against not proprietary experimental data: refer to original papers for references.

(c) Predictions of Hanson's helicoidal surface theory [107], with BEM aerodynamic loading data in input, are confirmed consistent and reasonable also for modern propellers, making this low-order technique a valuable fast alternative for first noise evaluation [108, 105]. An average error of 7.2 dB for the maximumum tonal noise, over 14 experimental test cases, is reported by Kotwicz Herniczek *et al.* [108].

1.3.2 Installed Propeller Studies

Tables 1.4 and 1.5 present a summary of major efforts concerning wing mounted tractor propellers carried out in the eighties and nineties by research centers and industries, respectively. Extensive experimental and numerical investigations were performed both in the USA and Europe. On the experimental side, a substantial amount of data was collected from model and full-scale tests (see e.g. [117, 118, 141, 142]). A good agreement between them was found, validating the scaled wind tunnel measurements approach [147]. Experiments were performed at cruise and low-speed take-off/landing operating conditions. On the prediction side, methods developed at that time were proven to give estimates of free-field noise that were excellent in trends, and generally good in absolute levels [90]. Moreover, they allowed to evaluate, with a reasonable accuracy, both intensity and directivity of maximum sound levels on the exterior fuselage, capturing the differences between port and starboard aircraft sides in the case of co-rotating propellers due to the different inflow [142, 116].
Key findings of these works are now discussed.

(a) The aerodynamic interaction between propeller and airframe is significant for both components, and unsteady. So, steady actuator disk computations can only give an estimate of the average flow field, whereas time marching 3D simulations are needed to accurately capture the interaction physics, especially for propellers operating at incidence [128, 129, 130, 132, 133]. The presence of the wing behind the propeller mainly causes nearly uniform upwash, the other installation effects being second order [127]. Non-zero propeller inflow angle relative to the flight-path, and propeller inflow distortion due to wing-generated upwash, were found both very important for propeller actual noise levels in flight [138]. The wing downstream the propeller was generally[‡] seen to increase the tone noise levels

[‡] Studying a propeller in front of an infinite wing analytically, using a 3D free wake-BEM model coupled with a full-surface moving medium form of the FW-H eq., Marretta *et al.* found that the radiated noise of the installed propeller is lower than that of the isolated case [148]. In a few of the data points analysed by Zandbergen *et al.* [142] it also appear that the addition of the wing slightly reduces the sound levels of the isolated propeller at incidence. Wind tunnel tests of the SR7A propeller at take-off conditions with a straight wing in the propeller wake at minimum distance showed no tonal noise increase at zero angle of attack [73].

Project (Sponsor)	**Experimental Activities**	**Numerical Activities**
PTA (NASA)	Full-scale in-flight campaign using the SR-7L advance propeller [114, 115, 116]: acoustic measurements near and far from the propeller to map the noise source directivity, fuselage surface pressures and cabin noise data, under a wide set of operating conditions (altitude, propeller tip speed and prop-fan inflow angle varying) [full reports by Little *et al.* [117, 118]]	• Noise predictions with Farassat's linear formulations of the FW-H eq. [119, 49], fuselage scattering and refraction included - aerodynamics and aeroelasticity in input [120] • Near-field noise estimates at an angle of attack [121] via frequency domain methods [51, 122] vs direct computation, both using as input 3D unsteady Euler pressures [123, 124]
ATP (NASA)	Wind tunnel tests of model scale SR propellers with downstream mounted wing: (a) 4- and 8-bladed SR2, lightly-loaded high M_{TIP} vs heavily-loaded low M_{TIP} conditions - microphone carriage measurements with a mapping area of ± 60 deg axially and laterally [125, 126], (b) SR7A at take-off conditions varying propeller angle of attack and wing droop angle - measures form blade kulites, wall fixed microphones arrays and translating microphone probe [127, 73]	N/A
GEMINI II* (EC)	Wind tunnel experiments of a 1:8 full-span scale model of typical commercial 50-seater co-rotating 6-bladed biturboprop [128] to investigate the aerodynamic interactions between propeller slipstream and airframe at transonic conditions	Euler/Navier-Stokes computations (time accurate vs steady state adopting an actuator disk method to represent the propeller) [129, 130]
APIAN (EC)	Wind tunnel tests campaign for the enhanced GEMINI II model [131, 132]: aerodynamic and acoustic measures to study aircraft aerodynamic coefficients, propellers performance, slipstream effects, pressure distributions on wing, nacelle and fuselage, near- and far-field noise	Steady and unsteady Euler simulations combined with the ONERA radiation acoustic code, solving the FW-H eq. in the frequency domain, and the NLR acoustic code for scattering and refraction [133]
Swedish research activities* (FFA)	Low-speed wind tunnel survey on a propeller-nacelle-wing scaled model varying incidence, yaw, free-stream speed, propeller thrust coefficient and nacelle geometry: surface pressure and slipstream flow-field data acquired [134, 135]	Time-averaged panel code predictions, coupled with a propeller slipstream model employing BEM theory [136, 137]

Table 1.4: Main research efforts performed in the 1980s and 1990s to study aerodynamics and acoustics of installed tractor propellers (Legend: * = only aerodynamics studied).

by a few dB and their variation rate with angle of attack, as well as broadband noise [138, 127, 147].

(b) The highest sound levels were found in the vicinity of the propeller plane [145, 142]. Here the propeller rotational noise was seen to be the dominant sound

Company	Experimental Activities	Numerical Activities
Lockheed-Georgia	Wind-tunnel tests of 1:10 scale model of 4-bladed propeller and engine of the C-130, un-installed and installed on the left outer wing panel, at full-power take-off conditions, varying incidence and flap angles [138]: detailed slip-stream velocity survey, microphone arcs recordings underneath and 30 degrees on the side	• Propeller wake predictions with analytical models based on vortex theory [139] • Noise estimates with Hamilton Standard computer program [140] vs Farassat's method [45]
Saab (FAA)	• In-flight acoustic measurements of interior and exterior noise of the twin-engined, co-rotating, turboprop Saab 2000 aircraft [141] • Thorough study of both tonal and broadband noise sources on the aircraft, together with passive and active tailored control measures adopted [65]	Calculations with a time-domain linearized version of the FW-H eq. [45] including non-uniform propeller inflow and time-varying blade loads [141]
Fokker and Dowty (NLR)	Wind tunnel measurements of sound pressures (amplitude and phase) on the fuselage wall of a twin-engined turboprop full model with 4-bladed co-rotating propellers (metallic and composite blades tested): tunnel and rotational speeds, as well as angle of attack varying [142]	Acoustic predictions based on Succi's subsonic compact time solution of FW-H eq. [143, 144] with aerodynamic inputs from strip analysis - quadrupole and broadband noise neglected, non-uniform inflow, fuselage reflections and boundary layer effects considered
LET (Czechoslovak research institutes)	In-flight measurements of propeller noise and turbulent pressure fluctuations on the fuselage, separately, of a light turboprop aircraft with two co-rotating 3-bladed propellers: straight level flight at 3000 m and different air speeds, keeping constant the propeller RPM [145]	Near-field estimates using (a) Gutin's original relation without simplifying hypothesis of large distance [146], (b) a proposed modified formula according to [36] with empirical basis [145]

Table 1.5: Main industrial activities performed in the 1980s and 1990s to study aerodynamics and acoustics of installed tractor propellers. In brackets the academic partner(s) of the research.

source [145] and, in particular, the first three tones were recognised as the main contributors to the interior cabin noise [65]. For co-rotating propellers, both external and internal acoustic fields are louder on the aircraft side that is closer to the propeller approaching the fuselage with more loaded blades [145, 142, 141, 121], i.e. for a propeller positive inflow the noise is highest on the side near the down-going blade tips. In-flight measurements on a light commercial twin-engined aircraft with 3-bladed propellers co-rotating at 1900 RPM showed differences of as much as 5 dB between port and starboard fuselage sidewalls [145].

(c) Fuselage scattering, wing and nacelle reflections, as well as boundary layer

refraction, must be included for accurate sound levels predictions [121, 90], in addition to the complex non-uniform flowfield in which the propeller operates when installed, and the actual running blade shape. Pressure fluctuations on the fuselage wall, due to locally separeted flow, were also found to contribute significantly to the total noise in flight [145]. Therefore, it could be concluded that direct noise computations are "viable and reliable" in the near-field, provided an appropriate mesh density, since they resolve the whole pressure field and they naturally account for non-linear propagation effects [121]. The first Euler CFD noise predictions on the fuselage of an high-speed aircraft under actual non-axial inflow conditions conducted by Hall in 1994 [149] showed good agreement with wind tunnel data for attached flow. Nonetheless, much work remained to be done, especially regarding grid numerical dissipation and viscous solver validation, before Navier-Stokes codes could be used [147].

In recent years, whereas the research on propellers in isolation mainly focused on their acoustics, the majority of the investigations regarding installed propellers examined aerodynamics. This was needed to gain more insight into the propeller-wing complex interactions (e.g. [150, 151, 152, 153]), to develop fast performace prediction methods (e.g. [154, 155, 156, 157]), or to analyse specific configurations (e.g. [158, 159, 160, 161, 162, 163]). As for isolated propellers, CFD is frequently employed. RANS plus actuator disk (AD), as well as URANS with actuator line (AL) or fully resolved propeller blades, proved capable of modeling the interactional flowfield with good accuracy, if numerical diffusion of the wake is prevented by a sufficient mesh density. URANS+AL were shown to be equivalent to the full-blade model, if the radial loading distributions at every azimuthal position is given. The cheapest RANS+AD gave time-averaged data with only a slightly reduced accuracy [164].
Valuable aeroacoustic studies have been performed at DLR within the BNF project that investigates a 9-bladed propeller mounted ahead of a wing with a Coanda flap at take-off conditions. This work aims at the integration of small regional airports in the European aviation network. A 1:9 scale model was analysed numerically [165] using a point source ring model for thickness and loading propeller noise, and linearised Euler equations to propagate the sound over a mean flow computed by RANS. A FW-H solver was coupled to it, if far-field predictions were required. Wind tunnel tests were also conducted [166] to measure the acoustic field via far-field microphones and microphone array. Predictions agreed well with esperimental data, for both levels (up to the 4^{th} tone) and directivities (up to the 2^{nd} tone), especially in the case of high propeller rotational speed, indicating a better accuracy in the thickness noise

component estimate. Significant deviations from the isolated acoustic field were observed due to the presence of the high-lift wing. The SPLs increased by 5 to 10 dB in most directions, mostly because of the loading noise component, probably due to the interaction tip vortices-wing. Constructive and desctructive acoustic interferences between direct and wing reflected or emitted sound waves were seen, and broadband noise was generated by the interaction of the propeller slipstream with the flap.

Another notable work on the noise generated by a propeller in tractor configuration was carried out by Boots *et al.* [167], focusing on the effects of the wing down-stream and vertical positions. The studied test case consisted in a 4-bladed scaled SR2 propeller at cruise conditions and a wing with a constant chord of 1.6R behind. The problem was simulated using a in-house code, SmartRotor, which combined a potential panel method for the lifting surfaces and a vortex particle method solving Navier-Stokes equations for the wake, with an acoustic solver based on the FW-H equation. No experiments were performed and numerical predictions were validated for the SR2 propeller in pusher layout against the experiments of Soderman *et al.* [168]. The authors highlighted that no other published literature on propeller-wing acoustics included sufficient validation data or employed an open geometry. SmartRotor SPL predictions underestimated experimental data by 2-3 dB at all harmonics for the propeller in isolation, whereas for the installed pusher propeller the first tone was underpredicted by almost 10 dB while the higher tones, up to the 7^{th}, matched well. The fairly good agreement indicated that, despite inviscid and incompressible, the method ability of wake predictions at a relatively low computational cost makes it suitable for wing-vortex interaction noise predictions. The presence of the wing was found not to alter the harmonic noise significantly, since the fluctuations of the wing loading due to the unsteady propeller slipstream were much weaker than the blade loads, but to increase by 25 dB the broadband noise. Its downstream position was shown to have little effect on sound levels, whereas the SPL at the fundamental frequency was minimum when the propeller axis was aligned with the wing, and increased when moved vertically away.

The effect of passive porosity at the leading edge of the wing was instead extensively investigated at TU Delft, with the objective of assessing its effectiveness in reducing structure-borne noise. The studied setup consisted in a scaled 4-bladed propeller, mounted up-stream of a straight symmetric pylon. Planar and strereoscopic particle-image velocimetry was used to fully characterize the flow, analysing the wake and measuring the surface pressure and the corresponding aerodynamic loading [169]. Numerical computations were performed with the commercial software PowerFLOW [170],

solving the explicit transient compressible Lattice-Boltzmann equation for a finite number of directions [171]. The good agreement against experiments, regarding thrust, propeller wake and surface pressure fluctuations, validated the numerical approach. Sound pressure in the near-field was extracted directly from the CFD solution, whereas the noise in the far-field was estimated using the formulation 1A of the FW-H equation extended for a convective wave equation [172]. The comparison between solid and flow-permeable leading edge showed that the latter generates a thicker boundary layer on the retreating blade side of the pylon, mitigating here the amplitude of the surface pressure fluctuations but locally increasing the drag. Overall, at a distance of 4R, the pourous leading edge increased the OASPL up to 1 dB on the advancing blade side, while decreased it up to 2 dB on the retreating side, only for up-stream receiver angles, by reducing third and fourth harmonics. Broadband noise was found to increase in all directions.

Finally, important acoustic efforts were also conducted for the design of the A400M military transport aircraft [67, 173], mostly to develop passive and active control systems to manage the high internal noise levels in the loadmaster area. The noise originated from the specific configuration chosen to maximize aircraft efficiency [67], with four engines of 8-bladed propellers, of which adjacent pairs are counter-rotating.

Propeller Synchrophasing

Concerns about possible high sound levels developed by propellers operating at transonic or supersonic tip speeds designed in the 1980s drove, already at that time, studies on propeller synchrophasing as a means of noise reduction. Analytical and experimental attempts to study the problem used monopole/dipole sources and a cylindrical shell to represent the fuselage. They showed that the propeller phase angles did not alter the external pressure field significantly, but affected considerably the internal noise [174, 175]. The latter appeared to be directly coupled with the cylinder's vibration modes which govern the sound transmission and its propagation in the cabin interior. These investigations also indicated that the acoustic energy comes in and out of the fuselage in specific regions whose position strongly depends on the propeller phase shift, the majority of the energy entering in any case over a length of one shell diameter.

An analytical technique to optimize the propeller phase angles, based on a systematic search among combinations of propellers signatures in the frequency domain, was presented in [176] and employed with the flight-test data of a NATC Navy/Lockheed P-3C. Results showed that synchrophasing could change the total sound energy, and

not only redistribute it. Reductions up to 8 dB of the average cabin noise in a four-engined aircraft, but only 1.5 dB in a twin-engined, were reported [176, 177].
All cited works underlined that the optimum synchrophase angle varies with cabin location, sound frequency and fuselage layout, thus the angle selection is a compromise and configuration-dependent. Flight and environmental conditions were recently proved to also influence the synchrophase optimum angle [178], showing that the synchrophaser should ideally be adaptive, and that this could be achieved with a small number of microphones placed in the right locations. Investigations on adaptive synchrophasing controllers have been carried out by different organizations, resulting in tested prototypes and various patents such as [179, 180, 181, 182, 183, 184] (refer to [185] for a brief but comprehensive description). Nevertheless, the synchrophase angles are usually set a priori into the electronic synchrophasing system of the aircraft and thus a preliminary optimization study becomes important to obtain noise reduction for the primary aircraft operating conditions. The analytical propeller signature analysis technique is still currently used for these studies [186, 7], using experimental data as input. It is, however, noted that this theory implies that the contributions of each propeller combine in a linear way, which seems a reasonable assumption from the comparison with experimental data but it is not well proven.

1.4. Research Gaps and Thesis Novelties

1.4.1 Isolated Propeller Acoustics

Based on the literature survey, it can be concluded that the sound of a propeller in isolation is nowadays widely known and that can be adequately predicted by existing numerical methods. Consequently, to meet the future demanding targets on aircraft acoustic emissions, research needs to move towards the analysis of propeller designs, thus to seek a quieter one. Previously conducted acoustic optimisation studies concentrate on blade geometric parameters, whereas variations in the hub configuaration is not yet examined. In this work two innovative hub designs are assessed against a baseline conventional configuration, and compared against a blade with inboard-moved loading which has been shown to be (yet) the best strategy to lower noise levels. RANS computations are used, since they are an efficient and accurate high-fidelity approach to evaluate propeller harmonic noise.
Unsteady RANS and DES simulations are shown to not remarkably improve estimates of far-field sound levels. However, their accuracy has not been assessed for near-field noise predictions where the wake unsteadiness can be important for the broadband

component. Different CFD methods of both advanced URANS and hybrid URANS-LES families, namely SAS and DES, are therefore evaluated in this work to find the most suitable technique to study this problem.

1.4.2 Installed Propeller Acoustics

The actual complex acoustic field of a turboprop aircraft has not been fully addressed yet. Very few recent studies on installation effects are available in the literature and analyse only a propeller-nacelle-wing combination, focusing on the interaction between the propeller slipstream and the wing. To the best of the author's knowledge, the presence of the complete airframe, as well as the interference than can generate with the sound field of the other propeller(s), are not yet considered. It is clear that these two elements may significantly alter noise levels and noise directivity, making the research on an isolated propeller, or on a propeller with an infinite wing downstream, not representative of the real in-flight situation. To lower turboprop cabin noise levels, there is a clear need for investigations of the sound field developed by complete aircraft. Time-accurate CFD calculations are chosen to study this problem given their ability, as shown by previous work, of accounting for all important sound generating mechanisms and propagation effects.
Synchrophasing has been shown effective in reducing noise levels and its basic principle is well understood. The effect of flight conditions has also been studied. However, its behaviour in the presence of the airframe is not completely known and linearity of the flow-field is still assumed. The knowledge of the whole aircraft acoustic near-field from CFD enables to gain more insight in the physics of synchrophasing, assessing its noise benefits without symplifing hypothesis and investigating the most beneficial blade shift.
The literature also showed the lack of open experimental data regarding installed propellers against which numerical methods can be validated. For this reason, Dowty Propellers started in 2012 a wind tunnel test campaign investigating aerodynamics and acoustics of a scaled tractor propeller propulsion unit installed on a wing. The model employed is referred to as IMPACTA [8, 187]. This dataset is used in the present work to validate CFD predictions for installed propeller flows (see Section 4.2).

1.4.3 Thesis Objectives

The motivation behind this PhD thesis is therefore to improve our understanding of propeller near-field noise in flight, and analyse different options, at design and installation levels, to decrease turboprop acoustic emissions. Accordingly, the present

research was focused on:

- analysis of the noise spectrum of innovative propeller designs;
- study of CFD methods suitable to estimate propeller acoustics;
- comprehensive investigation of the acoustic field of a turboprop aircraft, assessing the impact of propeller rotational direction and synchrophasing.

Thesis Outline

The present thesis begins with the description, and the validation, of the employed numerical methods. The results then follows, divided in two parts. The first is dedicated to the studies on propellers in isolation. The second presents the analysis of propellers installed on a twin-engined turboprop aircraft.
In particular, the thesis is organised as follows:

Chapter 2 describes the CFD solver, HMB3, including its formulation and its computational details;

Chapter 3 presents the adopted approach to estimate noise levels, outide and inside the aircraft;

Chapter 4 reports on solver validation for propeller flows;

Chapter 5 focuses on the evaluation of innovative propeller designs;

Chapter 6 is dedicated to the analysis of the CFD method suitable for propeller acoustics;

Chapter 7 investigates propeller installation effects and compares co-rotating *vs* counter-rotating turboprop configurations;

Chapter 8 assesses propellers synchrophasing;

Chapter 9 provides the main conclusions of this research and suggests future work.

Chapter 2

The CFD Flow Solver HMB3

In this thesis, all numerical simulations were performed using the in-house parallel CFD solver Helicopter Multi Block (HMB3) [188, 189] of the University of Glasgow. This solver, based on the control volume method, was initially developed for rotorcraft flows using multi-block structured grids. HMB3 has been revised and updated over a number of years and can now handle moving, sliding, overlapping and unstructured computational domains. It has been successfully applied to several problems including ship-helicopter operations, tilt-rotors, fixed wing aircraft, transonic cavity flows, wind turbines and hybrid air vehicles.

2.1. Flow Solver Formulation

HMB3 is a 3D flow solver for the compressible Navier-Stokes equations. The complete system of the Navier-Stokes equations comprises the conservation laws of the fluid, combined with its two thermodynamic equations of state for the pressure p and the temperature T:

$$\begin{cases} \text{mass conservation (i.e. continuity equation),} \\ \text{momentum conservation (i.e. Newton's 2nd Law),} \\ \text{energy conservation (i.e. 1st law of thermodynamics),} \\ p = p(e,\rho), \qquad T = T(e,\rho). \end{cases}$$

Because pressure and temperature are defined by the equations of state, the system is formed by two scalar and one vector equations for the unknowns: fluid density ρ, velocity $\mathbf{u}$ and specific internal energy e. The two equations of state are necessary to close the system of Navier-Stokes equations, making it determined. It is a non linear

system of incomplete parabolic nature* .

The continuity equation simply asserts that mass must be conserved, or rather that it remains constant over time. In Cartesian coordinates x_i this can be written as:

$$\frac{\partial \rho}{\partial t} + \frac{\partial (\rho u_i)}{\partial x_i} = 0. \tag{2.1}$$

Newton's 2nd Law expresses the balance of the linear momentum and is written, in Cartesian coordinates, as:

$$\frac{\partial (\rho u_i)}{\partial t} + \frac{\partial \left(\rho u_i u_j\right)}{\partial x_j} = \rho f_i - \frac{\partial p}{\partial x_i} + \frac{\partial \tau_{ij}}{\partial x_j} \tag{2.2}$$

where f_i represents any acting body force, and τ_{ij} is the viscous stress tensor. Assuming a Newtonian fluid and applying Stoke's hypothesis (i.e. the bulk viscosity is zero), the viscous stress tensor is defined as:

$$\tau_{ij} = \mu \left[\left(\frac{\partial u_i}{\partial x_j} + \frac{\partial u_j}{\partial x_i} \right) - \frac{2}{3} \delta_{ij} \frac{\partial u_k}{\partial x_k} \right], \tag{2.3}$$

where μ is the molecular viscosity and δ_{ij} the Kronecker delta.

The 1st law of thermodynamics states that the total energy of an isolated system is constant. This can be written, again in Cartesian coordinates, as:

$$\frac{\partial \rho E}{\partial t} + \frac{\partial}{\partial x_j} \left[u_i (\rho E + p) \right] - \frac{\partial}{\partial x_j} \left(u_i \tau_{ij} - q_j \right) = 0, \tag{2.4}$$

where E is the total energy of the fluid per unit mass, and $\mathbf{q}$ is the heat flux vector. The total energy per unit mass is defined as:

$$E = \left(e + \frac{1}{2} u_i u_i \right), \tag{2.5}$$

where $\frac{1}{2} u_i u_i$ represents the kinetic energy per unit mass. The heat flux vector is determined using Fourier's law:

$$q_i = -k_h \frac{\partial T}{\partial x_i}, \tag{2.6}$$

where k_h is the heat transfer coefficient.

An ideal gas approximation is assumed in the solver, i.e. the ideal gas law $p = \rho R_{sp} T$ is used to relate pressure and density. By default dry air is considered, and hence the specific gas constant R_{sp} is set to $R_{sp} = 287.058 \frac{J}{KgK}$.

Finally, Sutherland's law is used to determine the molecular viscosity of air:

$$\mu = \mu_0 \left(\frac{T}{T_0} \right)^{\frac{3}{2}} \left(\frac{T_0 + 110}{T + 110} \right), \tag{2.7}$$

where, as usual, $T_0 = 273.15$ K and, for air, $\mu_0 = 18.510^{-6} \frac{\text{kg}}{\text{m·s}}$.

* The mass conservation law is a hyperbolic equation, not having a laplacian term, while momentum and energy conservation are parabolic.

2.1.1 Governing Equations in Conservative Vector Form

The Navier-Stokes equations are written in the solver in a conservative and dimensionless form for programming convenience, so that continuity, energy and momentum equations (Eq. 2.1, 2.2 and 2.4 respectively) are expressed by the same generic equation. Using for brevity a vector notation, the Navier-Stokes equations can be written in conservative form as:

$$\frac{\partial \mathbf{W}}{\partial t} + \frac{\partial \left(\mathbf{F}^i + \mathbf{F}^v\right)}{\partial x} + \frac{\partial \left(\mathbf{G}^i + \mathbf{G}^v\right)}{\partial y} + \frac{\partial \left(\mathbf{H}^i + \mathbf{H}^v\right)}{\partial z} = \mathbf{S}. \tag{2.8}$$

Here, $\mathbf{W}$ is the vector of conserved variables

$$\mathbf{W} = (\rho, \rho u, \rho v, \rho w, \rho E)^T, \tag{2.9}$$

where u, v and w are the three components of the velocity vector, while $\mathbf{F}$, $\mathbf{G}$ and $\mathbf{H}$ are the flux vectors in the x-, y- and z-direction respectively. The superscripts i and v in Equation 2.8 denote the inviscid and viscid components of the flux vectors. The inviscid flux vectors are given by:

$$\begin{aligned} \mathbf{F}^i &= \left(\rho u, \rho u^2 + p, \rho uv, \rho uw, u(\rho E + p)\right)^T, \\ \mathbf{G}^i &= \left(\rho v, \rho uv, \rho v^2 + p, \rho vw, v(\rho E + p)\right)^T, \\ \mathbf{H}^i &= \left(\rho w, \rho uw, \rho vw, \rho w^2 + p, w(\rho E + p)\right)^T. \end{aligned} \tag{2.10}$$

The viscous flux vectors, containing terms for the heat flux and viscous forces exerted on the body, are:

$$\begin{aligned} \mathbf{F}^v &= (0, \tau_{xx}, \tau_{xy}, \tau_{xz}, u\tau_{xx} + v\tau_{xy} + w\tau_{xz} + q_x)^T, \\ \mathbf{G}^v &= (0, \tau_{xy}, \tau_{yy}, \tau_{yz}, u\tau_{xy} + v\tau_{yy} + w\tau_{yz} + q_y)^T, \\ \mathbf{H}^v &= (0, \tau_{xz}, \tau_{yz}, \tau_{zz}, u\tau_{xz} + v\tau_{yz} + w\tau_{zz} + q_z)^T. \end{aligned} \tag{2.11}$$

$\mathbf{S}$ represents source terms, usually set to zero except for axial rotors solved in a fixed reference frame (refer to Section 2.2.3 for the description of this formulation).

2.1.2 Non Dimensionalisation

The fundamental units of measure which appear in the Navier-Stokes equations and the thermodynamic relations used to close the system are length, mass, time and temperature. Therefore, to obtain the non-dimensional form of the equations, only four reference independent variables are needed. HMB3 uses a length L_{ref}, a density ρ_{ref}, a velocity U_{ref} and a temperature T_{ref}. The values of the reference variables are arbitrary, and are usually chosen depending on the nature of the problem. In Table 2.1 the typical choices employed are reported. Through the reference variables, the non-

dimensional length $\tilde{x_i}$, density $\tilde{\rho}$, velocity $\tilde{u_i}$ and temperature $\tilde{T}$ can be defined directly as:

$$\tilde{x_i} = \frac{x_i}{L_{ref}}, \quad \tilde{\rho} = \frac{\rho}{\rho_{ref}}, \quad \tilde{u_i} = \frac{u_i}{U_{ref}}, \quad \tilde{T} = \frac{T}{T_{ref}}. \tag{2.12}$$

The other variables of the problem, such as time t, pressure p, molecular viscosity μ, internal energy e and kinetic energy k, can be easily a-dimensionalised using a combination of the reference variables as follows:

$$\tilde{t} = \frac{U_{ref}}{L_{ref}}t, \quad \tilde{p} = \frac{\gamma\, {M_{ref}}^2}{\rho_{ref}\, {U_{ref}}^2}p, \quad \tilde{\mu} = \frac{\mu}{\mu(T_{ref})}, \quad \tilde{e} = \frac{e}{{U_{ref}}^2}, \quad \tilde{k} = \frac{\mu(T_{ref})}{\rho_{ref}\, L_{ref}\, {U_{ref}}^3}k, \tag{2.13}$$

where the gas heat capacity ratio γ is equal to 1.4 for dry air.

2.2. Numerical Methods

HMB3 uses a cell-centered finite volume approach combined with an implicit dual time-stepping method.

In a cell-centered finite volume approach the computational domain is divided in a finite number of non-overlapping control volumes and the governing equations are applied in integral conservation form to each of them. The Navier-Stokes equations in integral form using the Arbitrary Lagrangian Eulerian (ALE) formulation for time-dependent domains with moving boundaries are of the form:

$$\frac{d}{dt}\left(\int_{V(t)} \mathbf{W} dV\right) + \int_{\partial V(t)} (\mathbf{F}_i(\mathbf{W}) - \mathbf{F}_v(\mathbf{W})) \cdot \mathbf{n} dS = \mathbf{S}, \tag{2.14}$$

where $V(t)$ is the time dependent control volume and $\partial V(t)$ its boundary.

The spatial discretization of these equations leads to a set of Ordinary Differential Equations (ODE) in time, for each computational cell. The semi-discrete equation is of the form:

$$\frac{d}{dt}\left(\mathbf{W}_{i,j,k}\mathbb{V}_{i,j,k}\right) + \mathbf{R}_{i,j,k} = 0, \tag{2.15}$$

	not-rotary wing system or rotary wing system in forward-flight	rotary wing system in axial flight
L_{ref}	Characteristic length of the problem L	Rotor aerodynamic chord c
ρ_{ref}	Free-stream density ρ_∞	Free-stream density ρ_∞
U_{ref}	Free-stream velocity U_∞	Rotor tip velocity V_{TIP}
T_{ref}	Free-stream temperature T_∞	Free-stream temperature T_∞

Table 2.1: Typical reference variables used in HMB3 non-dimensionalisation. Rotary wing systems include rotors, propellers and wind turbines.

where i, j, k represent the spatial components, $\mathbb{V}_{i,j,k}$ denotes the cell volume and $\mathbf{R}_{i,j,k}$ represents the flux residual. A curvilinear co-ordinate system i, j, k is adopted to simplify the formulation of the discretised terms, since body-conforming grids are employed. Note that the governing equations are solved in the i, j, k spatial domain, so no transformation into the Cartesian domain is used.

Osher's upwind scheme [190] is usually adopted to resolve the convective fluxes for its robustness, accuracy and stability properties. The flux-splitting scheme of Roe [191] is also available in the solver. The Monotone Upstream-centered Schemes for Conservation Laws (MUSCL) variable extrapolation method [192] is employed to formally provide second-order accuracy. The van Albada limiter [193] is used to remove any spurious oscillations across large changes of gradients such as shock waves. An extension of Van Leer's MUSCL scheme is also implemented in HMB3 to achieve higher accuracy in space, up to 4^{th} order on Cartesian grids. The formulation of this scheme, hereby called MUSCL4, is presented in Section 2.2.4. The central differencing spatial discretization method is used for the viscous terms. Boundary conditions are set by using ghost cells on the exterior of the computational domain. In particular, for solid boundaries, ghost cell values are extrapolated from the interior (ensuring the normal component of the velocity on the solid wall is zero) for Euler flow, and the no-slip condition is set for viscous flows. In the far-field, ghost cells are set at the free-stream conditions.

The time discretization of the finite volume ODEs (Eq. 2.15), using a fully implicit method and approximating the time derivative by second order backward difference, gives the unsteady residual $\mathbf{R}^*_{i,j,k}$ as:

$$\mathbf{R}^*_{i,j,k} = \frac{3\mathbf{W}^{n+1}_{i,j,k}\mathbb{V}^{n+1}_{i,j,k} - 4\mathbf{W}^{n}_{i,j,k}\mathbb{V}^{n}_{i,j,k} + \mathbf{W}^{n-1}_{i,j,k}\mathbb{V}^{n-1}_{i,j,k}}{2\Delta t} + \mathbf{R}_{i,j,k}(\mathbf{W}^{n+1}) = 0. \tag{2.16}$$

This equation is non-linear in $\mathbf{W}^{n+1}_{i,j,k}$ and doesn't allow an explicit closed-form solution. Equation 2.16 is therefore solved by an iterative method in pseudo-time τ, i.e. the solution is marched in pseudo-time, for each real time step Δt. In particular, Jameson's original implicit dual-time approach [194] is adopted. During the time integration process, the system of equations to be solved is therefore:

$$\frac{\mathbf{W}^{m+1}_{i,j,k} - \mathbf{W}^{m}_{i,j,k}}{\Delta\tau} + \frac{1}{\mathbb{V}_{i,j,k}}\mathbf{R}^*_{i,j,k}(\mathbf{W}^{m+1}) = 0, \tag{2.17}$$

where $\Delta\tau$ is the pseudo time step increment. Here, the flux residual $\mathbf{R}^*_{i,j,k}$ is evaluated at the new pseudo time step $m+1$ and, being unknown, is approximated via a linear

expansion in time truncated to first order:

$$\mathbf{R}^*_{i,j,k}(\mathbf{W}^{m+1}) \approx \mathbf{R}^*_{i,j,k}(\mathbf{W}^m) + \frac{\partial \mathbf{R}^*_{i,j,k}}{\partial \mathbf{W}_{i,j,k}} \left(\mathbf{W}^{m+1}_{i,j,k} - \mathbf{W}^m_{i,j,k} \right), \tag{2.18}$$

where $\frac{\partial \mathbf{R}^*_{i,j,k}}{\partial \mathbf{W}_{i,j,k}} = \frac{\partial \mathbf{R}_{i,j,k}}{\partial \mathbf{W}_{i,j,k}} + \frac{3\mathbb{V}_{i,j,k}}{2\Delta t}\mathbf{I}$ from the definition of the unsteady residual (Eq. 2.16). By substituting Equation 2.18 into Equation 2.17, and changing it from conservative variables $\mathbf{W}$ to primitive variables $\mathbf{P} = (\rho, u, v, w, p)^T$, the linear implicit system to be solved finally becomes:

$$\left[\left(\frac{\mathbb{V}_{i,j,k}}{\Delta \tau} + \frac{3\mathbb{V}_{i,j,k}}{2\Delta t} \right) \frac{\partial \mathbf{W}_{i,j,k}}{\partial \mathbf{P}_{i,j,k}} + \frac{\partial \mathbf{R}_{i,j,k}}{\partial \mathbf{P}_{i,j,k}} \right] \Delta \mathbf{P}_{i,j,k} = -\mathbf{R}^*_{i,j,k}(\mathbf{W}^m), \tag{2.19}$$

where $\Delta \mathbf{P}_{i,j,k}$ is here used for $\left(\mathbf{P}^{m+1}_{i,j,k} - \mathbf{P}^m_{i,j,k} \right)$. The formulation of the system in primitive variables guarantees simplicity and stability of the solver.

The full linear system of equations is solved in a coupled manner. For a block-structured mesh, Eq. 2.19 represents a large sparse matrix, and is thus solved via a Krylov subspace algorithm, the generalised conjugate gradient method [195]. The Block Incomplete Lower-Upper BILU [195] factorisation is used as pre-conditioner, in a decoupled manner between grid blocks to reduce the communication between processors when the flow solver is used in parallel mode.

The Jacobian matrix is first-order approximate. This is done by removing the dependence in the MUSCL interpolation for the inviscid fluxes, and adopting a thin shear layer type approximation in the computation of the viscous fluxes. In this way, the ill-conditioning of the problem is avoided, and the overall size of the linear system is reduced, with consequent advantages in the parallelisation. As regards the turbulent equations, only the destruction terms are accounted for in the approximate Jacobian, and so no clipping to zero is required.

2.2.1 Solver Parallelisation and Scalability Performance

The solver adopts a domain decomposition method to run in parallel mode. The Message Passing Interface MPI tool [196, 197] is used for the communication between the processors. The strategies applied to the flow solver in order to improve the efficiency of the parallelisation, among which the allocation on each processor of a vector containing the halo cells for all the blocks in the grid, are described in [198].

Computations undertaken in this work have been performed on the local Beowulf Cluster “Jupiter” of the CFD Laboratory and, for larger grids, the EPSRC funded “ARCHIE-WeSt” HPC [199] and the EPCC’s “Cirrus” Tier-2 HPC Service [200]. The characteristics of the three computers are reported in Table 2.2. A comparison of their

performance against the UK National Supercomputing Tier-1 Service ARCHER [201] is presented in [202].

	Jupiter	ARCHIE-WeSt [199]	Cirrus [200]
Servers	Pentium 4 CH2	Dell C6100	SGI/HPE ICE XA
File System	Network File System (NFS)	Lustre parallel distributed	DDN Lustre parallel distributed
Nodes Connection	Gigabit Ethernet	4xQDR Infiniband Interconnect	single Infiniband fabric, FDR interface (54.5 Gb/s BW)
Nodes CPUs	8-core Dual Intel Xeon E5-2650	6-core Dual Intel Xeon X5650	two 18-core Intel Xeon E5-2695 (Broadwell)
Frequency Processors	2.0 GHz	2.66 GHz	2.1 GHz
Nodes Total Memory	64 GB	48 GB	256 GB

Table 2.2: Technology specifications of computing systems used in this work.

Very good scalability performance were shown on all these High Performance Computer (HPC) facilities, on 3D fully turbulent problems for meshes up to 1 billion cells and 16384 cores [202]. HMB scaling within a node was seen to be effective up to about 12 cores, on both Xeon and KNL nodes. Only a very little reduction in wall clock time per iteration was observed when more cores were used. Between nodes, the scaling is also very good: 90% efficiency was achieved on ARCHER and Cirrus.

2.2.2 Spatial and Temporal Discretization

Besides their effects on the accuracy of the aerodynamic predictions and on the simulation convergence, both spatial and temporal discretizations are related to the frequencies that are directly resolved by the computation:

- Given a grid spacing Δs and a minimum number of points per wave length N_p needed to describe an acoustic wave, the maximum frequency that can be solved in the simulation is $f_{max} = \frac{a}{\Delta s \cdot N_p}$, where a is the speed of sound. Note that the required number of points N_p is chosen not only to avoid aliasing, but also based on the spectral properties of the employed computational scheme.

- Considering a propeller operating with angular velocity n, if a time resolution corresponding to $\theta_{\Delta t}$ propeller azimuth degrees per time step is employed, the sampling frequency of the CFD simulation is $f_{samp} = \frac{360n}{\theta_{\Delta t}}$ and, using Nyquist's theorem [203], the maximum frequency resolved by the simulation is $f_{max} = \frac{180n}{\theta_{\Delta t}}$.

Therefore, for acoustic simulations, mesh density and time-step sizes must be suitable to achieve the desired frequency resolution. The discretizations in space and time adopted for each simulation are given and justified in the corresponding sections. In

general, the grid spacing Δs was dictated by the target frequency, while the time-step Δt was selected to achieve fast convergence of the computation.

2.2.3 Axial Flight Formulation

The study of a propeller in axial flight, with a constant rotation rate $\|\boldsymbol{\omega}\|$, can be formulated as a steady flow problem, assuming that the wake from the blades is steady in the frame of reference of the blade. The computational cost can be then further reduced by using the periodicity of the flow in the azimuthal direction, e.g. if the propeller has N_b blades, a $1/N_b$ segment of the domain with periodic boundary conditions is enough.
In practice, adopting a non-inertial reference frame, the grid remains fixed and the centripetal and Coriolis acceleration terms are accounted for by introducing in the ALE formulation of the Navier-Stokes equations (Eq. 2.14) a mesh velocity $\mathbf{u}_{mesh}$ and a source term $\mathbf{S}_{axial}$ in the momentum conservation law:

$$\begin{cases} \mathbf{u}_{mesh} = \boldsymbol{\omega} \times \mathbf{x} \\ \mathbf{S}_{axial} = [0, -\rho\,\boldsymbol{\omega} \times \mathbf{u}_{ax}, 0]^T \end{cases} \tag{2.20}$$

where $\boldsymbol{\omega}$ is the rotation vector, $\mathbf{x}$ the position vector of each cell and $\mathbf{u}_{ax}$ the local velocity field in the rotor-fixed frame of reference. The mesh velocity $\mathbf{u}_{mesh}$ corresponds to a solid-body rotation $\boldsymbol{\omega}$ of the grid in the direction of the propeller.
The use of the non-inertial reference frame also helps imposing boundary conditions because the "undisturbed" velocity field is vanishing and is not position-dependent, as opposed to what happens in a rotating reference system. Unperturbed free-stream conditions are usually applied on the far-field surfaces of the computational domain, using a linear extrapolation in the axial direction on the inflow and outflow surfaces. This boundary condition is shown to be suitable only if the far-field boundaries are far enough from the propeller that no flow re-circulation occurs within the computational domain [204]. For small computational domains Froude's "potential sink/source" approach [205] is instead employed. Further details on the implementation and validation of the axial flow formulation in the HMB solver are given in [189].

2.2.4 MUSCL4 Scheme

The underlying idea of this scheme is to add high-order correction terms, via successive differentiation, to the MUSCL-reconstructed state of the cell interfaces. This means that the high-order derivatives are applied only to the inviscid fluxes, whereas the viscous fluxes are maintained 2^{nd} order. The formulation was first proposed by

Burg [206] for unstructured finite volume codes up to 3^{rd} order in spatial accuracy and then extended by Yang *et al.* [207, 208] to achieve 4^{th} order accuracy. This is a compact finite volume scheme, thus no major modification to the original HMB code was required for its implementation. A small dissipation δ (a value of 10^{-4} has been chosen after some calibration cases) is introduced in the scheme thus to reduce spurious oscillation while maintaining the same level of accuracy.
The Fourier analysis of the scheme showed that: *(i)* the spectral resolution of MUSCL4 is considerably higher than that of MUSCL scheme, potentially enabling the resolution of higher frequencies associated with flow structures such as vortices and small length-scale waves; *(ii)* the dissipation error is also reduced with respect to the MUSCL scheme. The scheme was exercised on various test cases including two- and three-dimensional flows, steady and unsteady. MUSCL4 results showed that wakes are preserved for longer and with higher resolution compared to MUSCL predictions, even on coarse grids, yielding higher accuracy.
CPU and memory overheads associated with the additional terms were found to be reasonably small for medium grid sizes, up to 10 million cells. The CPU penalty of the scheme is mainly due to the additional data exchanged in parallel computations, whereas the extra effort to determine the gradients with the Green-Gauss method[†] is rather small (less than 1% to compute the first derivative and less than 2% for the second derivative). The additional terms in the MUSCL4 scheme yield to 23% memory overhead when a two-equation turbulence model is used for a 3D problem.
More details on the scheme formulation in HMB3, and all validation test cases, are presented in [210, 211].

2.3. Turbulence Modelling

The Navier-Stokes equations completely describe turbulent flows. However, at high Reynolds numbers, it is difficult to solve for all temporal and spatial turbulent scales because of their large number. The most common approach is to reduce the number of unknown turbulent scales by time-averaging the Navier-Stokes equations, getting to the Reynolds-Averaged Navier-Stokes equations (RANS). The RANS equations model statistically all turbulent scales, enabling mean flow quantities predictions at a moderate computational cost with adequate engineering accuracy for flows without internal instabilities. However, by construction, RANS can not provide the unsteady data that are necessary in some applications as, for example, the identification of

[†] The Green-Gauss method is applied to compute the successive differentiation since the least-squares approach is not accurate and stable for highly-stretched meshes [209].

aerodynamic noise sources. In addition, RANS methods are too diffusive when employed on coarse grids and, even when spacial and temporal resolution are sufficient, the formation of the turbulent energy cascade is prevented by their too high dissipation.

Another strategy, named Large Eddy Simulation (LES), is based on resolving scales larger than the grid cells while modelling the smaller ones with a sub-grid model, so that basically most of the turbulent kinetic energy k is resolved and most of the dissipation ε is modelled. This approach bears less modelling uncertainties and gives unsteady data by its constitutive nature, yielding to more accurate results than RANS in the case of complex phenomena like flow separation, re-attachment or vortex shedding. However, LES is computationally expensive[‡] because it requires a very fine grid and time-step (as a rule of thumb, LES provides reliable predictions only if k is modelled to at least 80% [213]) and cannot benefit from domain symmetries. Coupling of LES with time-dependent RANS (URANS) models become therefore the main strategy to make LES affordable for a wide range of industrial applications.

Several turbulence models, of both URANS and hybrid LES/URANS families, are available in the HMB3 solver. The idea and the equations behind the models used in this work, i.e. $k-\omega$ SST, SAS[§] and DES, are presented below. The $k-\omega$ SST model was chosen as reference model, because of its reliability for attached boundary-layer flows with adverse pressure gradient, and because it appeared in the literature the most successfully used for propeller acoustic CFD simulations.

2.3.1 URANS Linear Eddy Viscosity Models

The time averaging process of RANS results in additional unknowns, named Reynolds stresses, which must be modelled. Linear eddy viscosity models assume the Boussinesq hypothesis [214] for the Reynolds stress tensor τ_{ij}, expressing it as:

$$\tau_{ij} = 2\mu_t \left(S_{ij} - \frac{1}{3}\frac{\partial u_k}{\partial x_k}\delta_{ij} \right) - \frac{2}{3}\rho k \delta_{ij}, \tag{2.21}$$

where μ_t is the turbulent eddy viscosity, and the strain rate tensor S_{ij} is defined as:

$$S_{ij} = \frac{1}{2}\left(\frac{\partial u_i}{\partial x_j} + \frac{\partial u_j}{\partial x_i} \right). \tag{2.22}$$

The Reynolds stress tensor represents momentum diffusion due to turbulence in the mean flow. Thus, making an analogy between molecular diffusion and fluctuation

[‡] To give an idea of LES computational cost, we just mention that: *(i)* for a typical bluff-body flow at $Re = 40{,}000$ it is found that LES is from 10 to 100 times more expensive than RANS $k-\varepsilon$ models [212]; *(ii)* close to walls, at high Reynolds numbers, the computational effort of LES is of the same order of magnitude as DNS [213].

[§] The SAS turbulence model was implemented in the HMB3 solver for this work.

transport, Boussinesq simply assumes that the Reynolds stress tensor is aligned with, and proportional to, the mean rate-of-strain tensor. This way, the six unknown elements of τ_{ij} are written as a function of only one new unknown μ_t.

Menter's $k-\omega$ Shear Stress Transport Model (SST)

This model [215] originates from the combination, via a blending function, of the Wilcox $k-\omega$ model [216] and the high-Reynolds-number version of the $k-\varepsilon$ model [217]. The first is used in the sub-layer and logarithmic regions of the boundary layer for its robustness, accuracy and boundary conditions simplicity, the second in the boundary layer outer wake region and in free shear layers because of its independence from the free-stream values. The eddy viscosity definition is also modified to account for the transport of the principal turbulent shear stress described by Bradshaw's assumption [218].
The transport equations for the turbulent variables k and ω of the SST model are, in the conservative form, given by:

$$\begin{cases} \frac{\partial(\rho k)}{\partial t} + \frac{\partial(\rho u_j k)}{\partial x_j} = \mathscr{P} - \beta^* \rho \omega k + \frac{\partial}{\partial x_j}\left[(\mu + \sigma_k \mu_t)\frac{\partial k}{\partial x_j}\right], \\ \frac{\partial(\rho \omega)}{\partial t} + \frac{\partial(\rho u_j \omega)}{\partial x_j} = \frac{\gamma}{\nu_t}\mathscr{P} - \beta \rho \omega^2 + \frac{\partial}{\partial x_j}\left[(\mu + \sigma_\omega \mu_t)\frac{\partial \omega}{\partial x_j}\right] + 2(1-F_1)\frac{\rho \sigma_{\omega 2}}{\omega}\frac{\partial k}{\partial x_j}\frac{\partial \omega}{\partial x_j}, \end{cases} \tag{2.23}$$

where the turbulent production $\mathscr{P}$ is computed from:

$$\mathscr{P} = \tau_{ij}\frac{\partial u_i}{\partial x_j}. \tag{2.24}$$

As recommended in [219], a production limiter is employed in the k equation as follows:

$$\min(\mathscr{P}, 20\beta^* \rho \omega k). \tag{2.25}$$

The coefficient β^* is set to 0.09.
The turbulent eddy viscosity μ_t is determined as:

$$\mu_t = \frac{\rho a_1 k}{\max(a_1 \omega, \Omega F_2)}, \tag{2.26}$$

where $F_2 = \tanh\left(\arg_2^2\right)$ and $\arg_2 = \max\left(2\frac{\sqrt{k}}{\beta^* \omega d}, \frac{500\nu}{d^2 \omega}\right)$,

being $\Omega = \sqrt{2W_{ij}W_{ij}}$ and $W_{ij} = \frac{1}{2}\left(\frac{\partial u_i}{\partial x_j} - \frac{\partial u_j}{\partial x_i}\right)$.

The constant a_1 is set to 0.31.
Each constant in the model ϕ is defined by a blend between an inner ϕ_1 and an outer ϕ_2 values as follows:

$$\phi = F_1\phi_1 + (1-F_1)\phi_2. \tag{2.27}$$

Here, the blending function is $F_1 = \tanh\left(\arg_1^4\right)$, where

$\arg_1 = \min\left[\max\left(\frac{\sqrt{k}}{\beta^*\omega d}, \frac{500\nu}{d^2\omega}\right), \frac{4\rho\sigma_{\omega 2}k}{d^2\max\left(2\rho\sigma_{\omega 2}\frac{1}{\omega}\frac{\partial k}{\partial x_j}\frac{\partial \omega}{\partial x_j}, 10^{-20}\right)}\right]$, and d is the distance from the field point to the nearest wall.
The values of the constant coefficients are reported in Table 2.3.

$\sigma_{k1} = 0.85$	$\beta_1 = 0.075$	$\gamma_1 = \frac{\beta_1}{\beta^*} - \frac{\sigma_{\omega 1}\kappa^2}{\sqrt{\beta^*}}$	$\sigma_{\omega 1} = 0.5$
$\sigma_{k2} = 1.0$	$\beta_2 = 0.0828$	$\gamma_2 = \frac{\beta_2}{\beta^*} - \frac{\sigma_{\omega 2}\kappa^2}{\sqrt{\beta^*}}$	$\sigma_{\omega 2} = 0.856$

Table 2.3: Coefficients of the SST turbulence model. κ is the von Kármán constant, taken as 0.41.

In the original reference [215] boundary conditions for the turbulent variables are recommended as follows:

$$\begin{cases} \frac{10^{-5}U_\infty^2}{Re_L} < k_{\text{farfield}} < \frac{0.1U_\infty^2}{Re_L}, \quad \frac{U_\infty}{L} < \omega_{\text{farfield}} < 10\frac{U_\infty}{L} \\ k_{wall} = 0, \quad \omega_{wall} = \frac{60\nu}{\beta_1(\Delta d_1)^2} \end{cases} \tag{2.28}$$

where L should be "the approximate length of the computational domain" and the free-stream turbulent eddy viscosity is obtained from chosen k_{farfield} and ω_{farfield} values that should be between 10^{-5} and 10^{-2} times the free-stream laminar viscosity.
Note that the SST model differs from Menter's baseline model (BSL) [215] only for the computation of the turbulent eddy viscosity and the value of the constant σ_{k1} (originally set to 0.5).

SST Turbulence Model with Controlled Decay

To avoid the turbulent variables decay that occurs in the free-stream and is not physical, a new version of the SST model has been proposed by Spalart [220]. This formulation differs from the original SST model only for the addition of a sustainability term in each turbulent transport equation that has the effect of nullifying the destruction term in the free-stream if the turbulence levels are equal to the ambient levels:

$$\begin{cases} \frac{\partial(\rho k)}{\partial t} + \frac{\partial(\rho u_j k)}{\partial x_j} = \mathscr{P} - \beta^*\rho\omega k + \frac{\partial}{\partial x_j}\left[(\mu + \sigma_k\mu_t)\frac{\partial k}{\partial x_j}\right] + \beta^*\rho\omega_{\text{amb}}k_{\text{amb}}, \\ \frac{\partial(\rho\omega)}{\partial t} + \frac{\partial(\rho u_j \omega)}{\partial x_j} = \frac{\gamma}{\nu_t}\mathscr{P} - \beta\rho\omega^2 + \frac{\partial}{\partial x_j}\left[(\mu + \sigma_\omega\mu_t)\frac{\partial \omega}{\partial x_j}\right] + 2(1-F_1)\frac{\rho\sigma_{\omega 2}}{\omega}\frac{\partial k}{\partial x_j}\frac{\partial \omega}{\partial x_j} + \beta\rho\omega_{\text{amb}}^2. \end{cases} \tag{2.29}$$

The extra-terms do not affect the model's behavior inside the boundary layer, provided reasonable turbulence levels are imposed in the free-stream (i.e. Tu $\leq 1\%$), because they are orders of magnitude smaller than the corresponding destruction terms.
The free-stream boundary conditions proposed for this version of the model are:

$$k_{\text{farfield}} = k_{\text{amb}} = 10^{-6} U_{\infty}^2, \quad \omega_{\text{farfield}} = \omega_{\text{amb}} = \frac{5U_{\infty}}{L}, \tag{2.30}$$

where L is the defining length scale of the problem. It is noted that the chosen value of k_{farfield} corresponds to a free-stream Tu level of 0.08165%.

For more details or variations of the cited and others models used in the literature, the reader can refer to the *Turbulence Modelling Resource* of NASA Langley Research Center [221] and the associated references.

A Note on Linear Eddy Viscosity Models

The linear dependency between the turbulent stress and the mean strain-rate tensor that is assumed in the Boussinesq model can be too restrictive in some complex aerodynamic problems. In particular, the solution might show poor accuracy near the edges on turbulent regions or in mild-separated flows predictions. On the other hand, solving a transport equation for each stress component, as it is done in the Reynolds-stress transport modelling, can be suitable for a wider range of problems but it is too computationally expensive and time consuming for industrial purposes. Therefore, to improve the solution behavior of the two-equations turbulence models, an interesting and feasible approach is to adopt a non-linear constitutive model for the turbulent stress tensor. Amongst these models the Explicit Algebraic Reynolds Stress $k-\omega$ Model (EARSM) of Hellsten [222] is regularly used in the literature and available in HMB3. This model derives from Menter's BSL [215] but adopts the explicit algebraic Reynolds-stress model of Wallin and Johansson [223] as constitutive model for the turbulent stress tensor (the constant coefficients are also re-calibrated): the non-linear contribution is thus introduced in the definitions of turbulent production and eddy viscosity. It is shown that the solution accuracy improves especially near the edges of turbulent regions and in mild-separated flows. Hence, this model could represent a valuable and interesting alternative for the problem studied in the present work and it will be considered in future studies, after an *ad-hoc* calibration.

2.3.2 Hybrid LES/URANS Methods

LES and RANS computational costs and predictions accuracy, plus the structural similarities of their governing and turbulence equations, make natural to combine them

in a single united approach so to use LES only where is needed and RANS where is reliable and efficient. In this way, the model employs the same transport equation in the whole computational domain, transitioning from LES to RANS behavior depending on a given criterion. Hybrid methods have developed following different URANS/LES coupling strategies:

(a) a pure LES model can be used in some regions of the domain and a pure RANS in the remaining areas - *segregated* and *interfacing* models;

(b) the two models can be added together in a weighed manner via local mixing coefficients - *blending* models;

(c) the selected model can be altered to include the behavior of the other, usually a RANS model is adapted to LES capability - *second generation URANS* models.

An extensive review and assessment of numerous hybrids methods is presented by J. Fröhlich and D. von Terzi in [213]. The state of the art, at 2017, of hybrid RANS/LES modelling for turbulent flows is reported by Chaouat in [224].

SST - Scale Adaptive Simulation (SAS)

The Scale Adaptive Simulation is an improved URANS approach able to generate spectral content in unsteady flows thanks to its ability to operate as a scale-resolving mode [225]. Under specific conditions, the model naturally balances the contribution of modelled and resolved part of the turbulent stress tensor by adjusting the turbulent length scale to local flow inhomogeneities. SAS models comply with the following characteristics [226]:

1. a second mechanical scale, dependent on the second (or higher) velocity derivatives, is introduced in the selected RANS model;

2. the model must provide a RANS solution in stationary flows while allowing the break-up of the large unsteady structures like LES in flow regions with transient instabilities - this without explicit dependency of the model on grid size or time step;

3. damping of resolved turbulence must be introduced at high wave numbers depending on the grid resolution limit.

Menter and Egorov derived the first “scale-adaptive” model, named as KSKL [225], by introducing the second derivative of the velocity field, and consequently the von Kármán length scale κ, in Rotta’s KL model [227, 228]. The motivation of this

modelling choice originates from the analysis of the third derivative term of the exact transport equation of the quantity kL, L being a turbulent integral length scale, derived by Rotta. In this way, the model reduces the eddy viscosity according to the locally resolved vortex size represented by κ in unsteady flow regions, by resolving the turbulent spectrum up to the grid limit and avoiding single-mode vortex structure typical of RANS. The KSKL model was then transformed by the authors to other variables, thus to include its scale-adaptive capability in existing two-equations turbulence models.

The turbulent transport equations of the SST-SAS model [229, 226] differ from those of the SST model (Equations 2.23) only by the introduction of an additional source term Q_{SAS} for the specific dissipation rate ω of the form:

$$Q_{SAS} = \max\left[\rho\xi_2\kappa\mathbb{S}^2\left(\frac{\ell}{\ell_{\nu\mathrm{K}}}\right)^2 - C_{SAS}\frac{2\rho k}{\sigma_\Phi}\max\left(\frac{1}{k^2}\frac{\partial k}{\partial x_j}\frac{\partial k}{\partial x_j}, \frac{1}{\omega^2}\frac{\partial \omega}{\partial x_j}\frac{\partial \omega}{\partial x_j}\right), 0\right], \tag{2.31}$$

where ℓ is the length scale of the modelled turbulence:

$$\ell = \frac{\sqrt{k}}{\sqrt[4]{\beta^*}\omega}, \tag{2.32}$$

and $\ell_{\nu\mathrm{K}}$ is the von Kármán length scale derived from a 3D generalisation of the classic boundary layer definition, lowerly bounded to provide adequate damping for high wave numbers:

$$\ell_{\nu\mathrm{K}} = \max\left(\frac{\kappa\mathbb{S}}{|\nabla^2\mathbf{u}|}, C_s\sqrt{\frac{\kappa\xi_2}{\beta/\beta^* - \gamma}}\sqrt[3]{\Omega_{CV}}\right). \tag{2.33}$$

Here, $|\nabla^2\mathbf{u}| = \sqrt{(\nabla^2 u)^2 + (\nabla^2 v)^2 + (\nabla^2 w)^2}$ is the magnitude of the velocity Laplacian, C_s is the Smagorinsky coefficient properly tuned on the adopted discretization scheme, and Ω_{CV} is the control volume size.

$\mathbb{S}$ is a scalar invariant of the strain rate tensor S_{ij}:

$$\mathbb{S} = \sqrt{2S_{ij}S_{ij}}, \tag{2.34}$$

which in this model is also used to compute the turbulent production term as

$$\mathscr{P} = \mu_t\mathbb{S}^2. \tag{2.35}$$

Finally, the constant coefficients of the model are $\xi_2 = 3.51$, $C_{SAS} = 2$ and $\sigma_\Phi = 2/3$.

Detached Eddy Simulation

DES can be defined as a "3D unsteady numerical solution using a single turbulence model which functions as sub-grid-scale model in regions where the grid density is fine

enough (i.e. the grid spacing is significantly smaller than the flow turbulence length scale) for a LES and as RANS model in regions where is not" [230]. In practice, this means that the boundary layer is treated by RANS while the massive separated regions are treated by LES, so that the *attached eddies* internal to the boundary layer are modelled whereas the *detached* ones are resolved. The zone amid the RANS and the LES regions, called *gray area*, represents one of the weaknesses of the model and may cause problems if the flow separation is not abrupt. In particular, the original formulation of the DES model (DES97) [60] suffers from a significant delay in the development of the Kelvin-Helmholtz instability [231, 232], and thus in the transition from modelled to resolved turbulence in free and separated shear layers [233]. This problem mainly derives from the adopted definition of the sub-grid length scale Δ, and hence in the literature various alternative enhanced definitions have been proposed [233], among which the DDES [234], the IDDES [235] and the recent "shear layer adapted" DES [236, 237] formulations.

In this work, the original DES97 formulation based on the SST model was used. The DES method [60] was first derived from the Spalart-Allmaras one-equation turbulence model [238]. However, a DES model can be originated from any RANS model by modifying appropriately the length scale ℓ_{RANS} which is explicitly or implicitly involved in it, i.e. $\ell_{DES} \doteq \min(\ell_{RANS}, C_{DES}\Delta)$, where Δ is the sub-grid length scale of the DES model and C_{DES} the only new constant coefficient. In the DES97 formulation, the sub-grid length scale is taken as the largest dimension of the local grid cell δ_i:

$$\Delta = \max(\delta_x, \delta_y, \delta_z). \tag{2.36}$$

Menter's SST model has been easily adapted to DES mode [239] by simply changing the destruction term in the k transport equation as follows:

$$\mathscr{D}_{k-\omega SST} = \beta^* \rho \omega k = \frac{\rho k^{3/2}}{\ell_{k-\omega SST}} \implies \mathscr{D}_{DES} = \frac{\rho k^{3/2}}{\ell_{DES}}, \tag{2.37}$$

where the DES length scale ℓ_{DES} is in this case:

$$\ell_{DES} = \min(\ell_{k-\omega SST}, C_{DES}\Delta), \tag{2.38}$$

being the RANS length scale $\ell_{k-\omega SST} = \sqrt{k}/(\beta^*\omega)$. The model coefficient C_{DES} is computed using Menter's blending function F_1 with coefficients calibrated for the $k-\varepsilon$ and for the $k-\omega$ components of the model:

$$C_{DES} = F_1 {C_{DES}}^{k-\omega} + (1-F_1){C_{DES}}^{k-\varepsilon}, \tag{2.39}$$

with ${C_{DES}}^{k-\omega} = 0.78$ and ${C_{DES}}^{k-\varepsilon} = 0.61$.

2.4. Mesh Generation Techniques

Despite the geometric complexity of the test cases with the propeller in installed configuration, block-structured hexagonal meshes were chosen to ensure an orthogonal and flow-aligned mesh, thus to keep the numerical errors to a minimum. This choice allows as well to benefit from the higher efficiency and lower memory requirements of a structured code. Depending on the needs of each simulation (e.g. relative motion, grid regularity, grid topology simplification, difference of mesh density in different areas), fully matched, sliding planes or chimera grids were employed. Brief descriptions of the latter methods are provided below. All grids were generated using the ICEM-Hexa™ meshing software of ANSYS [240].

2.4.1 Sliding Planes Approach

The sliding plane algorithm [241] enables the computation of multi-component non-matching grids in relative motion, as is the case for a turboprop aircraft (see Figure 2.1). The grids of the different components exchange information across sliding surfaces, i.e. for the turboprop aircraft of Figure 2.1, the moving propeller meshes are inserted into the fixed aircraft mesh that has complementary empty drums built to host them. Thus, the various grids do not overlap but they have co-located boundary surfaces.
Since the various meshes are generated independently, the cell faces of adjacent grids may not match, and therefore the halo cells of each block on a sliding surface have to be populated with interpolated values. For each pair of adjacent sliding surfaces the method requires the identification of the neighboring cells for each halo cell, and the interpolation of the solution at the centroids of the latter. The interpolation is performed using the cell-face overlap method illustrated in Figure 2.1(c), where the weight of each neighbor of the halo cell is directly proportional to the fraction of the overlapping cell face area. It is noted that this approach, despite is the preferred one in finite volume methods, does not naturally enforce the conservation of flow variables, and differences in grid sizes may act as spatial filter. The evaluation of the overlapping area is carried out in the curvilinear reference system used by the solver so that the sliding-mesh interfaces can be of arbitrary shape, including non-planar as the lateral surface of the propeller drums. Because only one layer of cells is used for the interpolation, this technique is first order in the normal direction to the sliding plane and the only requirement that the two adjacent blocks have to satisfy for an accurate interpolation is a similar dimension of the cells in this direction. The search of the neighboring cells and the determination of the interpolation weights, for each relative position of the component grids, is carried out in the simulation pre-processing phase and stored thus

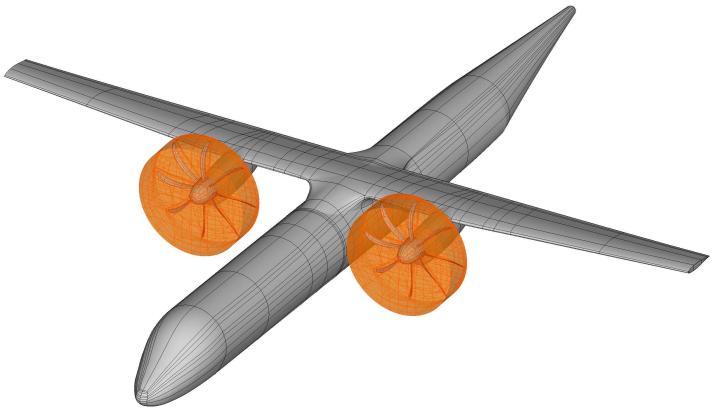

(a) Sliding planes surfaces, in orange, for a turboprop aircraft grid.

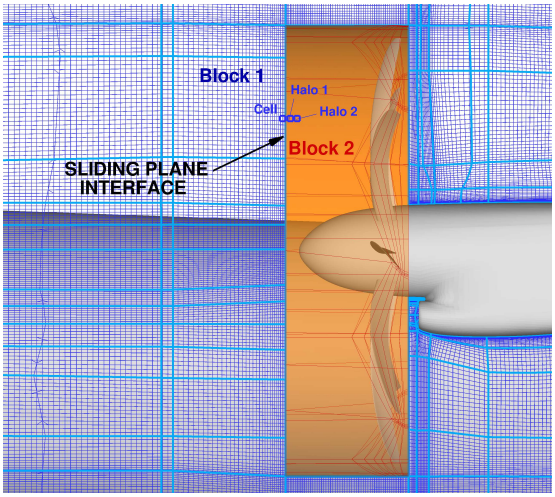

(b) Lateral view: propeller grids, in orange, inserted in the aircraft grid, in blue, with sketch of halo cells along the sliding plane interface.

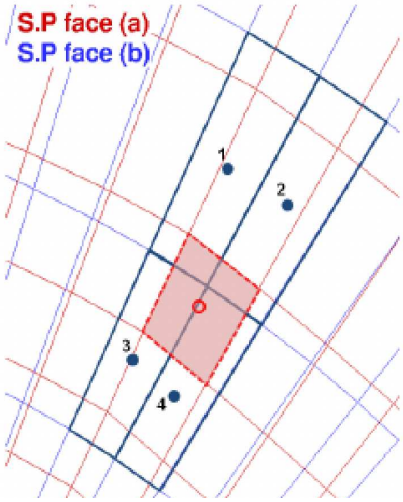

(c) Area weighted interpolation between the non-matching cell faces of the two adjacent sliding blocks (Cartesian coordinate view).

Figure 2.1: Example of sliding planes three-component grid.

to not introduce a high computational penalty. Please refer to Steijl and Barakos [241] for more details about implementation and validation of the sliding planes technique in HMB3.

2.4.2 Chimera Over-set Method

The chimera technique [242] allows for computation on grid systems formed by independently generated, overlapping, non-matching sub-domains. The different sub-domains are sorted hierarchically, with higher *Levels* having higher priority. The exchange of information between the sub-domains is done by interpolation following the level priority. As an example, Figure 2.2 shows the two-level chimera grid for the Baseline IMPACTA blade studied in isolation: *Level 0* covers the background domain and includes the spinner; *Level 1* contains the blade grid. For each relative

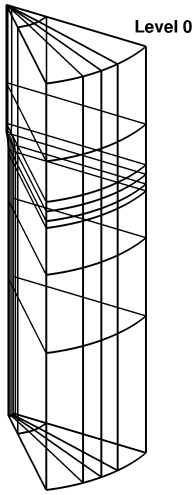

(a) Background grid (level 0).

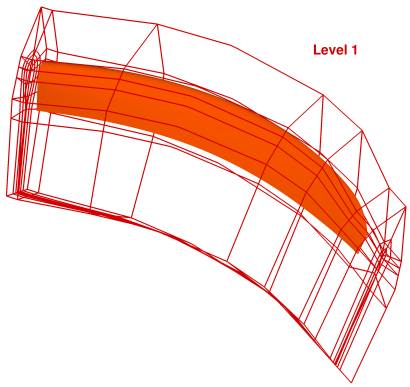

(b) Blade grid (level 1).

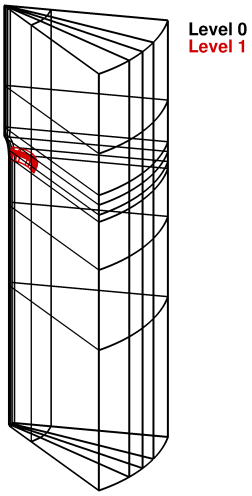

(c) View of the assembled grid.

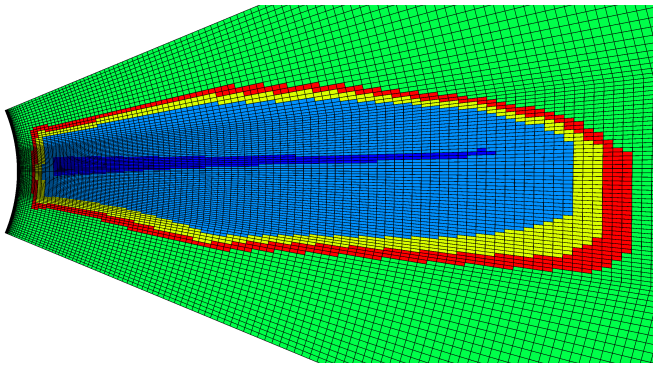

(d) Cells localisation for the background level: computational cells in green, fringe cells (last layer of computational cells) in red, interpolation cells in yellow, cells overlapping with level 1 in light-blue, cells overlapping with solids part (the blade) in dark blue.

Figure 2.2: Example of chimera overset two-component grid.

position of the sub-domains, an overset mesh search is carried out to identify *(i)* which cells do not need interpolation because they overlap with higher level cells or with a solid, *(ii)* which cells require interpolated flow information from the grid they overlap with ("interpolation cells"), *(iii)* which cells do not need any special treatment ("computational cells") - see Figure 2.2(d). The cell localisation process is performed by a range-tree algorithm starting from the identification of the points situated inside the minimum volume bounding boxes of each solid. This algorithm guarantees high efficiency and good performance in parallel computations. The interpolation weights are also determined during the overset search. Zero-order, least squares and inverse distance methods are available in the solver to perform the interpolation. No specific additional treatment is implemented to assure conservation during the interpolation. All information about the method and its implementation in HMB3 can be found in Jarwowsky *et al.* [242].

Chapter 3

Noise Estimation Approach

3.1. Propeller Acoustic Field

The propeller near-field noise is directly evaluated from the unsteady CFD results: the time history of the pressure field $p(\mathbf{x},t)$ is extracted from the flow-field solutions at different time steps, or captured by numerical probes at points of interest. The first approach allows to investigate the whole sound field that is developed by the propeller and to produce visualisations that, especially in the case of installed configurations, can be very useful to locate noise sources and to identify possible acoustic interferences. However, due to the large mesh size, it is only possible to store the full flow-field solutions for a short time range, i.e. equivalent to one or two blade passages. For some specific locations, longer pressure signals can be instead saved, and stored without memory issues, using numerical probes. Imitating experimental probes, this tool enables recording the time history of all simulation variables at the cell center nearest to any desired point. It is noted that the localisation of the probes is performed in the grid pre-processing phase only, and that during the computation the probe is always associated to the cell identified as the closest in the initial grid position. This means that if the probe is inside a moving block, e.g. near the propeller blade, the probe will move accordingly.

For steady simulations, as for the isolated propeller in axial flight, an equivalent unsteady pressure signal $p(\mathbf{x},t)$ can be easily generated from the steady solution *a posteriori*: the flow-field is rotated at the propeller angular velocity and the pressure field is interpolated and extracted at the selected positions with the chosen time sampling. If the computational domain contains only a segment of the propeller because of geometric periodicity, first the flow-field of the full propeller is reconstructed by copying and rotating the sub-domain.

Having the unsteady pressure field $p'(\mathbf{x},t) = p(\mathbf{x},t) - \overline{p(\mathbf{x},t)}$ directly from the

computations, the Overall Sound Pressure Level (OSPL) and the Sound Pressure Level (SPL) as function of the sound frequency f are estimated as follows:

$$OSPL = 10\log_{10}\left(\frac{{p'_{rms}}^2}{{p_{ref}}^2}\right) \text{ dB}, \tag{3.1}$$

$$SPL(f) = 10\log_{10}\left(\frac{PSD(p')}{{p_{ref}}^2}\right) \text{ dB}, \tag{3.2}$$

where p_{ref} is the acoustic reference pressure which is equal to $2 \cdot 10^{-5}$ Pa (this corresponds to the typical threshold of hearing for a sinusoidal signal at roughly 2 kHz).

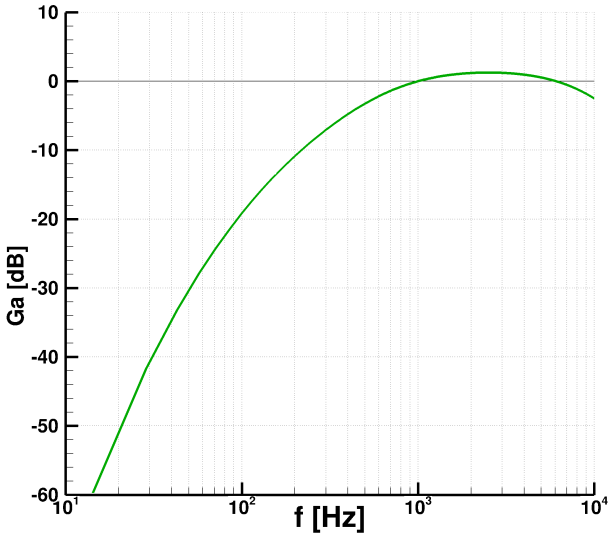

Figure 3.1: Gain of the A-weighting noise filter [243].

To take into account the hearing sensitivity of the human ear, the A-weighting filter can be applied to the sound pressure estimates. It is noted that, to certify large transport aircraft, the loudness-corrected weighting Effective Perceived Noise Level (EPNL) is required [244]. However, the A-weighting filter is here used because is the standard for environmental noise, among which roadway, railway and aircraft noise (even if it was originally designed for sound pressure levels lower than 55 dB, it is the one usually employed to assess hearing damage caused by loud noise). According to acoustic standards [243] and [245], the A-weighted SPL (ASPL) is determined as:

$$ASPL(f) = SPL(f) + 20\log_{10}(G_A(f)) + 2 \text{ dB}_A, \tag{3.3}$$

where $G_A(f)$ is the frequency-dependent filter gain defined as:

$$G_A(f) = \frac{12200^2 \cdot f^4}{(f^2+20.6^2)(f^2+12200^2)\sqrt{f^2+107.7^2}\sqrt{f^2+737.9^2}} \text{ dB}. \tag{3.4}$$

The effect of the A-weighting is shown in Figure 3.1 via the visualisation of the filter gain $G_A(f)$.

3.2. Aircraft Interior Cabin Noise

Within the activities of the IMPACTA project, NLR performed a series of tests on a Fokker 50 aircraft to experimentally determine the cabin noise response of a typical commercial airplane [246]. Tests were conducted inside a hangar, employing a

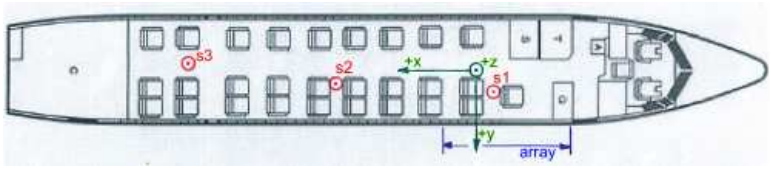

(a) Cabin layout and source and array positions for the reciprocal measurements. The propeller plane is at $x = 0$. The example passenger considered for the analysis in this thesis is located in position S1.

(b) Microphone array mounted on transversing mechanism for the reciprocal transmission loss measurements method.

(c) Transfer function measurements using a direct technique.

Figure 3.2: NLR experimental setup to determine the cabin noise response of a typical commercial airplane using the RNLAF Fokker 50 U-05 [246].

reciprocal technique [247, 248], i.e. the aircraft fuselage was excited from the inside with a known noise source and microphones were used outside to determine the normal particle velocity via near-field acoustic holography [249]. The fuselage starboard region, where the propeller field normally impinges, was covered for a total length of $L = 3.10$ m extended $3L/4$ upstream and $L/4$ downstream of the propeller rotation plane. A linear microphone array, mounted on a moving traversing mechanism, allowed to scan 32 x 32 points following the fuselage surface from the bottom middle line to the top, excluding the row exactly at the middle of the fuselage (see Figures 3.2(b) and 5.6).

The strength of the sound source inside the cabin was measured simultaneously to the microphones data acquisition, thus the Transfer Function (TF) contains information about both magnitude and phase. For comparing the designs, however, only the real part of the pressure signal is used. Due to the monopole limitation of the uniform acoustic dodecahedron source employed, measurements were possible for frequencies between 100 Hz and 1250 Hz. Therefore, a second experiment was set up to extend the TF data to a frequency range between 57 Hz, i.e. $f = {}^{BPF}/_{2}$, which appears in the spectra of modified hubs, to 10 kHz. At that time, a direct technique was adopted performing measurements with pure tone excitation using CFD computed signals as input for the speakers (see Figure 3.2(c)), and transfer functions were determined by extrapolation. It is noted that the extrapolation method may give results of inferior accuracy than the reciprocal measurements (also because the measurements with the direct technique contain the fuselage reflected field as well as the incident field) and thus introduce uncertainties. It is also highlighted that this test setup does not account for the boundary layer noise and for the vibrations caused by running engines and transmitted by the wings to the fuselage (structure-borne noise). However, these noise sources have a small effect on the interior noise in comparison to the sound levels caused by the propeller blades (air-borne noise) [67]. Moreover, the TF are used here for a relative evaluation of different designs or installation layouts. Therefore, it is expected that the limitations reported above do not significantly alter the conclusions of the study.

Different positions inside the cabin were considered in the experiments, while the aircraft 28 seats layout in a 2-1 configuration of Figure 3.2(a) was kept fixed. The analysis performed in this thesis are representative of a passenger seated on the starboard side of the plane slightly ahead of the propeller plane, on the second seat away from the window (position S1 in Figure 3.2(a)). Data relative to other passenger positions were not made available to the author.

To visualize the aircraft response to the incoming pressure field, the Transmission Loss (TL) and the phase modification maps are presented, for some frequencies, in Figures 3.3 and 3.4, respectively. The TL was defined as follows:

$$TL = 20\log_{10}\left(\frac{|TF|}{dS}\right)\text{dB}, \tag{3.5}$$

dS being the surface covered by each microphone. As can be seen, the aircraft response is shown to be non uniform in space, and highly dependent on the frequency of the incoming pressure field. In the transmission through the structure of the fuselage the noise levels are reduced by more than 20 dB. Below 500 Hz, specific areas with low TL levels, i.e. high transmission, can be identified, probably in correspondence of specific

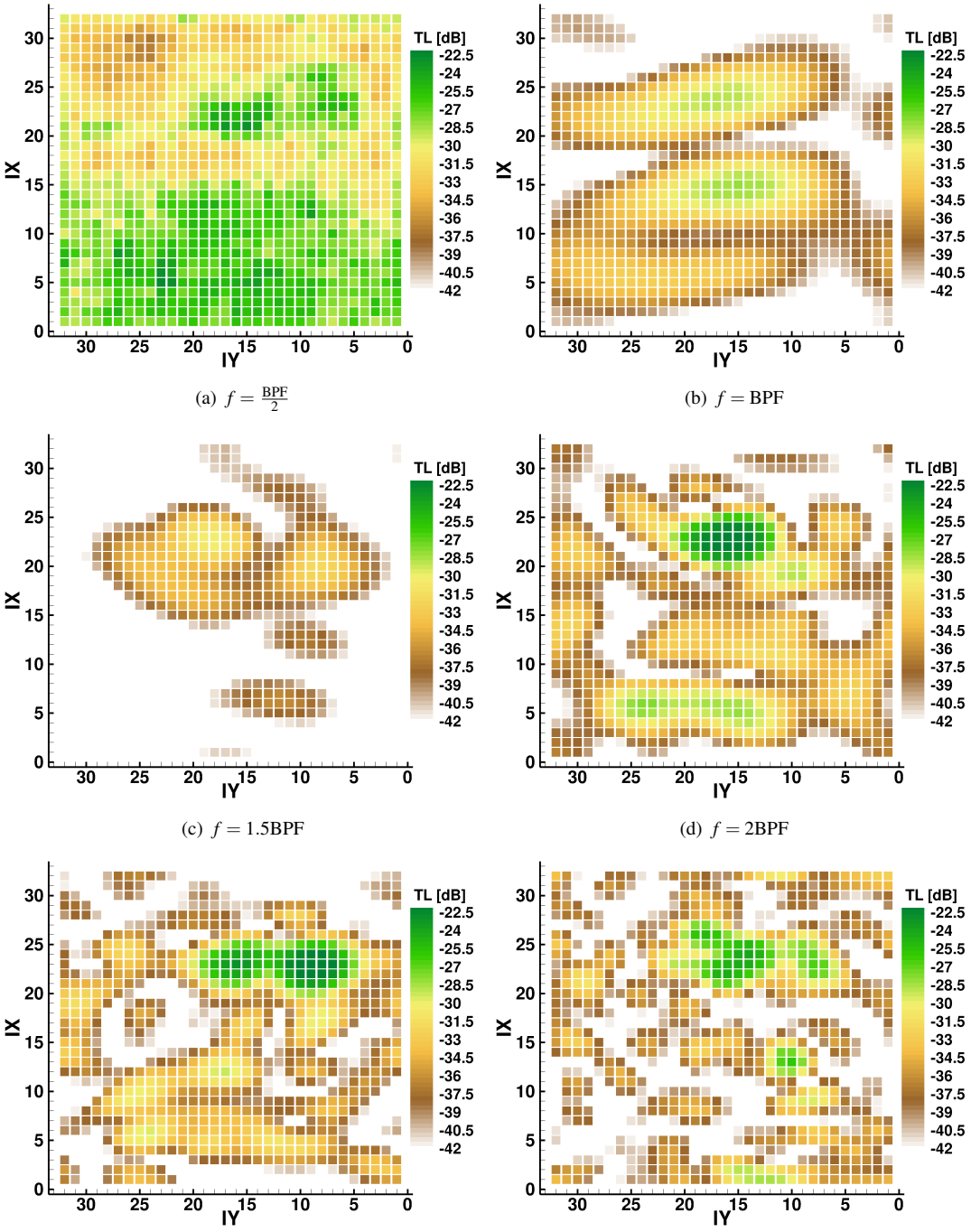

(a) $f = \frac{\text{BPF}}{2}$ (b) $f = \text{BPF}$

(c) $f = 1.5\text{BPF}$ (d) $f = 2\text{BPF}$

(e) $f = 2.5\text{BPF}$ (f) $f = 3\text{BPF}$

Figure 3.3: Transmission Loss maps as a function of the sound incident frequency: experimental measurements by NLR on a Fokker 50 aircraft [246]. Results shown at the harmonics of the Baseline IMPACTA propeller design (BPF= 114.152 Hz). Please refer to Figures 5.6 and 7.5 for the definition of the the azimuthal and the longitudinal TF points indices, IX and IY respectively.

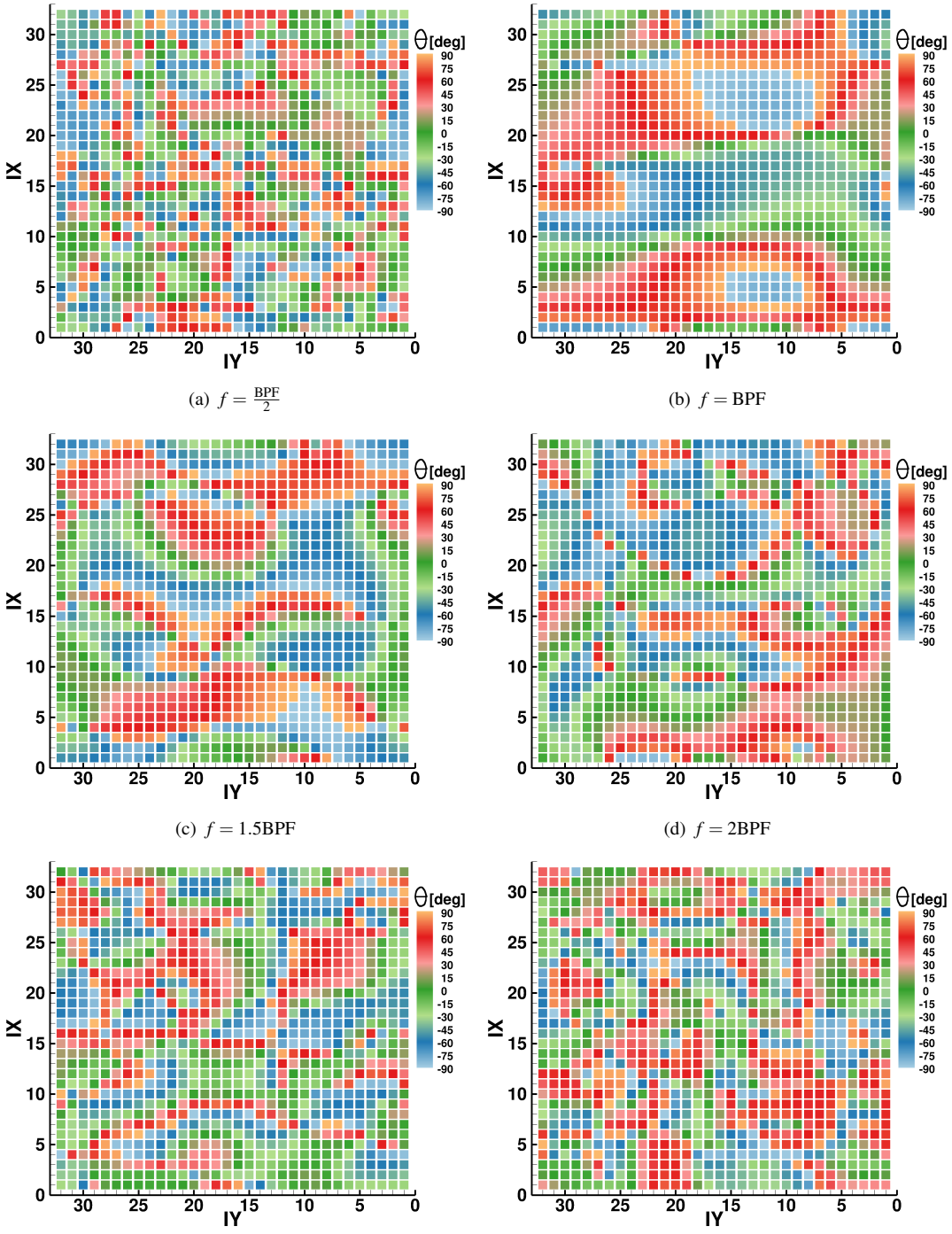

(a) $f = \frac{\text{BPF}}{2}$

(b) $f = \text{BPF}$

(c) $f = 1.5\text{BPF}$

(d) $f = 2\text{BPF}$

(e) $f = 2.5\text{BPF}$

(f) $f = 3\text{BPF}$

Figure 3.4: Phase modification, i.e. TF arguments, maps as a function of the sound incident frequency: experimental measurements by NLR on a Fokker 50 aircraft [246]. Results shown at the harmonics of the Baseline IMPACTA propeller design (BPF= 114.152 Hz). Please refer to Figures 5.6 and 7.5 for the definition of the the azimuthal and the longitudinal TF points indices, IX and IY respectively.

structural component of the fuselage or windows. At higher frequencies, a more scattered response can be seen with, in general, the top part of the fuselage providing a high attenuation and the bottom a reduction between 30 and 40 dB. The TF imaginary part appears often large in magnitude near the locations of higher transmission, thus introducing a substantial shift in phase when the pressure waves enter the fuselage shell. This means that, potentially, the scenario inside the cabin may differ significantly from that outside, since the result of the acoustic interferences amongst the various sound waves will be different.
With the transfer functions known, given the pressure signals at the fuselage exterior, the acoustic pressure amplitude inside the cabin can be easily estimated, and thus the pressure time history for the passenger considered. The procedure, which consists in a convolution between the pressure signals and the TF, is performed in the frequency domain for simplicity. The steps are the following:

1. computation of the Discrete Fourier Transform of the unsteady pressure signals predicted on the fuselage external surface;
2. multiplication of the complex Fourier coefficients from each signal by the complex TF value at the same frequency;
3. summation of the contribution of all 32 x 32 positions;
4. computation of the Inverse Discrete Fourier Transform to get the acoustic pressure signal as function of time at the specified location inside the cabin.

In this way, the aircraft structural response is accounted for without the need of a computationally expensive structural model. A stronger coupling between aeroacoustics and structural vibrations is beyond the scope of the analysis at this stage, since there is no intention of estimating absolute noise levels but only a relative comparison between the different propeller designs or installation layouts is of interest.

The main codes implemented to estimate both exterior and interior noise are reported in Appendix A.

Chapter 4

HMB3 Validation for Propeller Aerodynamics and Acoustics

HMB3 has been validated for propeller flows against experimental data from the JORP [88] and the IMPACTA [250, 187] wind tunnel tests. The first allowed the comparison of the blade pressure predictions for a propeller in isolation. The second enabled the assessment of HMB3 aerodynamic and acoustic numerical results for an installed propeller.

	Un-swept JORP	**Baseline IMPACTA wind tunnel model**	
	cruise conditions	cruise conditions	climb conditions
Number of blades N_b	6	8	8
Radius R	0.456 m	0.457 m	0.457 m
Root chord c	0.114 m	0.044 m	0.044 m
BPF	376 Hz	540.2 Hz	588.4 Hz
Thrust line incidence α_T	0 deg	-2 deg	0 deg
Free-stream Mach number M_∞	0.692	0.5	0.45
Tip Mach number M_{TIP}	0.529	0.578	0.627
Tip Reynolds number Re_{TIP}	1.163e6	0.56e6	0.51e6

Table 4.1: HMB3 validation: propeller parameters and test conditions.

4.1. The JORP Propeller

4.1.1 Test Case Description

The JORP model was a single row, six bladed propeller, mounted on a minimum interference spinner, representative of a high-speed design of the late eighties. Simple un-swept and moderately-swept blade planforms were tested, with a relatively large tip chord. A view of the un-swept version of the JORP model in the ARA wind tunnel is

reported in Figure 4.1(a).

Using the axial flight assumptions, RANS simulations of the unswept JORP, at fixed pitch, were performed by Barakos and Johnson [251]. Blade parameters and test conditions are reported in Table 4.1. The single-blade computational domain was extended up to the far-field and the hub was modelled as a cylinder, to speed up convergence of the steady-state simulation. The k-ω turbulence model [252] was employed. A visualisation of the propeller vortical structures predicted b the solver is presented in Figure 4.1(b) via Q criterion* [253, 254].

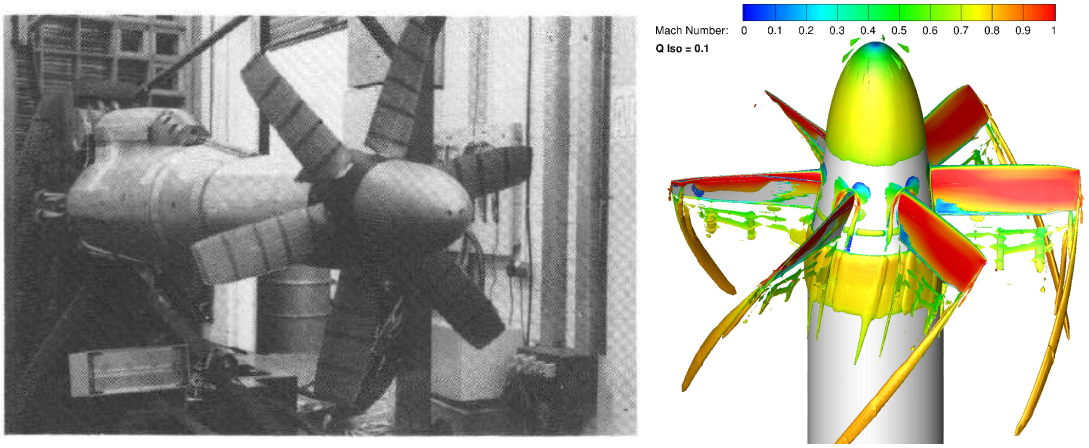

(a) Un-swept JORP model mounted in the ARA wind tunnel [88].

(b) HMB numerical prediction of the wake: iso-surfaces of Q, colored by Mach number [251].

Figure 4.1: Un-swept version of the JORP wind tunnel model.

4.1.2 Comparison with Experimental Data

Figure 4.2 shows the pressure coefficient distribution at different radial positions along the blade. A visualisation of the flow-field around the different profiles, with streamlines and Mach color iso-levels, is also reported in the same figure. Some discrepancies are visible in Figure 4.2, specially regarding the suction peak. This is believed to be due, on one hand, to the uncertainty in the knowledge of the experimental pitch angle and, on the other hand, to possible installation effects. It is also noted that the CFD adopted a fully turbulent model, whereas small laminar regions were observed on the blades during the tests. However, the trend of the normal force coefficient along the blade is well captured.

* The Q criterion identifies as vortices the flow regions where the second invariant of the velocity gradient tensor $\nabla\mathbf{u}$, $Q = \frac{[tr(\nabla\mathbf{u})]^2 - tr(\nabla\mathbf{u}^2)}{2}$, is positive, i.e. $Q > 0$. For incompressible flows Q is a local measure of the excess rotation rate compared to the strain rate since, being $\nabla\cdot\mathbf{u} = 0$, $Q = \frac{1}{2}(||\Omega||^2 - ||S||^2)$ where S and Ω are the symmetric and anti-symmetric components of $\nabla\mathbf{u}$, respectively. In addition, the criterion also require that the pressure in the eddy region is lower than the ambient pressure.

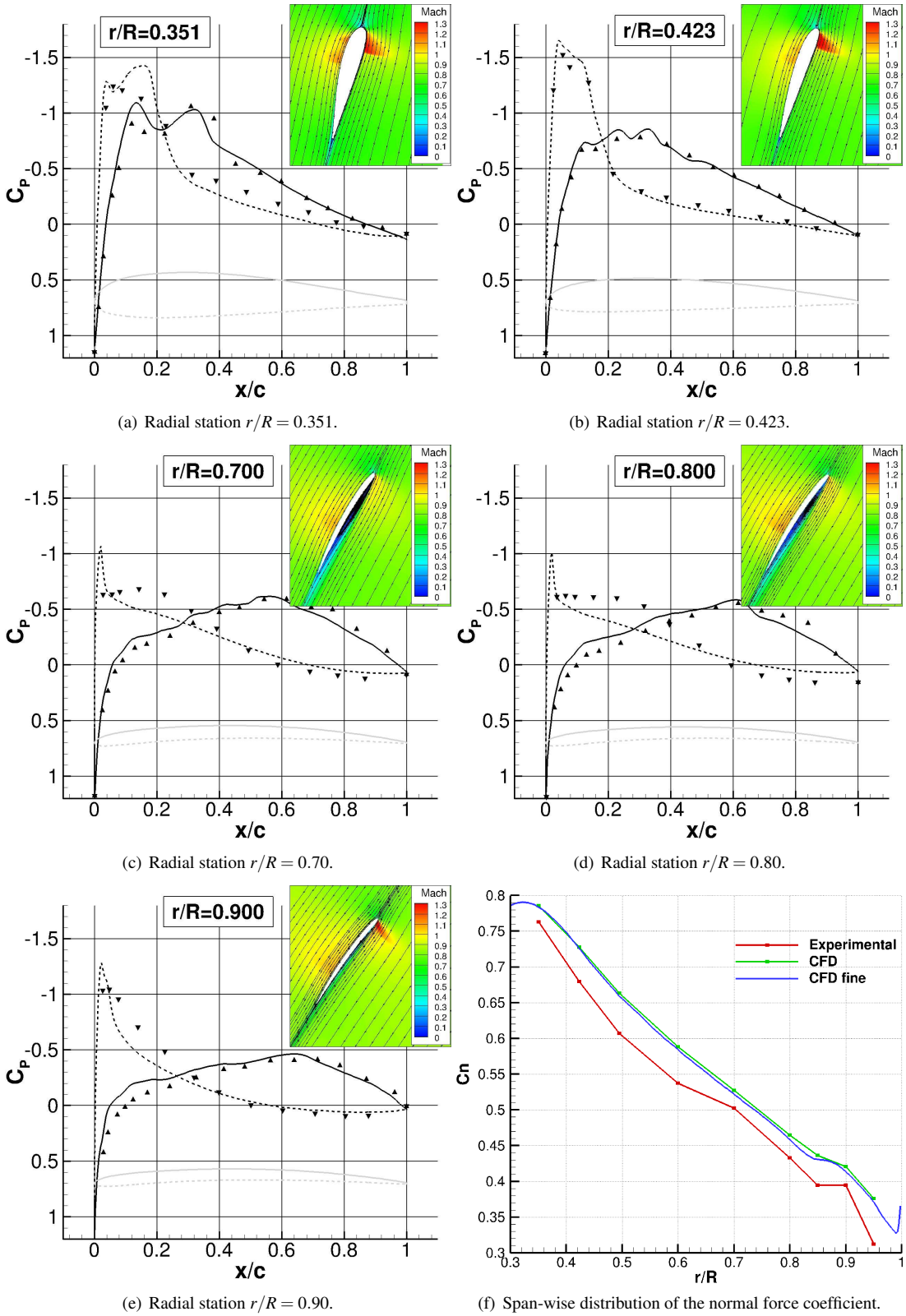

(a) Radial station $r/R = 0.351$.

(b) Radial station $r/R = 0.423$.

(c) Radial station $r/R = 0.70$.

(d) Radial station $r/R = 0.80$.

(e) Radial station $r/R = 0.90$.

(f) Span-wise distribution of the normal force coefficient.

Figure 4.2: Pressure coefficient distribution along different stations of the unswept version of the JORP propeller: comparison between numerical results of HMB [251] and experimental data [88] (triangular points). Some discrepancies are visible but the span-wise trend of the normal force coefficient is well captured.

4.2. The IMPACTA Turboprop Power-plant

4.2.1 Test Cases Description

The IMPACTA wind tunnel model is a 1:4.83 scale model of an installed turboprop power-plant and includes propeller, nacelle, intake, and part of the wing. The model was tested in the Transonic Wind Tunnel of ARA [255], mounted in the test section aligned with the free-stream and inverted, i.e. the model was upside down. Figure 4.3(a) shows the geometry and dimensions of the model. The propeller angular rotation

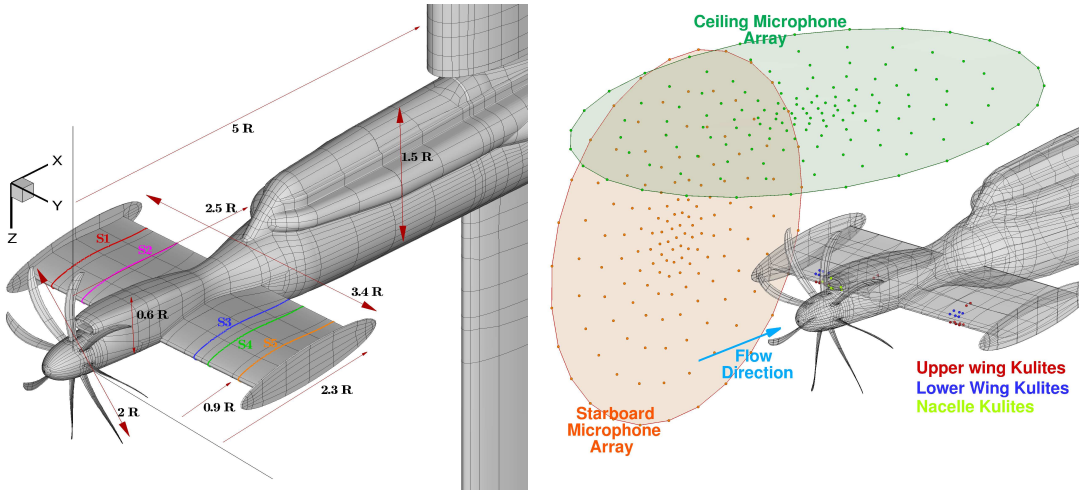

(a) Geometry of the model with dimensions ($R = 0.4572$ m) and wing stations instrumented with pressure taps.

(b) Unsteady pressure sensors location: Kulites™ on the model and microphone arrays on the acoustic liner.

Figure 4.3: IMPACTA wind tunnel scaled model with the Baseline propeller design.

was clockwise as viewed from the rear, thus the model port wing ($y < 0$) is affected by the propeller up-wash and the starboard wing ($y > 0$) by the propeller down-wash. The propeller rotation axis, coincident with the grid x axis, was inclined by -2 degrees with respect to the fuselage axis and the wing pitch angle was 5.3 degrees with respect to the propeller thrust axis. The propeller parameters, and the cruise and climb operating conditions of the tests, are summarised in Table 4.1. The structured multi-block CFD grid for HMB3 was built by assembling five separate components: the propeller drum, the inflow, the front part of the model, the back part of the model, and the outflow. The sliding plane technique was employed to exchange flow information between the different grids. This allowed for: *(i)* the relative motion between the propeller and the rest of the model, and *(ii)* a grid topology simplification, as well as a reduction of the number of cells in different parts of the computational domain. A visualisation of the grid is presented in Figure 4.4. To have a perfectly symmetric computational domain, the propeller drum was generated by copying and rotating a single-blade mesh. All other grid components were mirrored about the $y = 0$ plane. An "O" grid topology

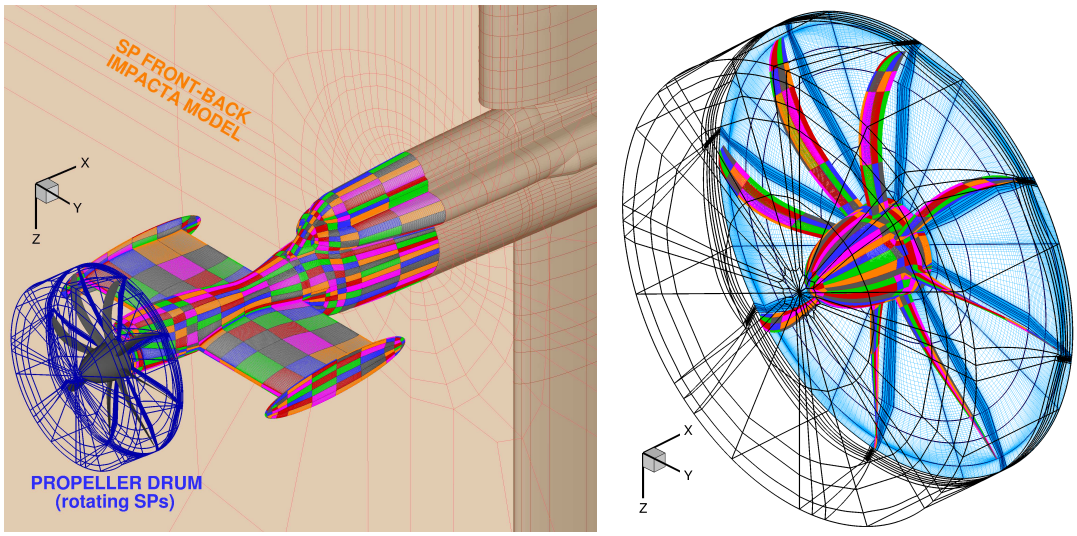

(a) Grid layout and surface mesh of the model front part.

(b) Detail of the propeller mesh.

Figure 4.4: Computational grid for the Baseline IMPACTA wind tunnel scaled model.

surrounds the whole model to form a regular boundary layer and the computational mesh spacing ensures that $y^+ \leq 1$ by using a hyperbolic mesh point distribution and a wall grid stretching ratio ranging from 1.1 to 1.15. All geometric details of the wind tunnel model were represented in the mesh. The wind tunnel walls were not modelled in the CFD simulations. The far-field boundaries have been extended beyond the wind tunnel test section and were treated using far-field boundary conditions. This was the case because the experimental data was corrected to take into account the channel effect produced by the acoustic liner fitted in the wind tunnel. The description of the adopted correction procedure, and its effectiveness, is reported in Appendix B. Preliminary validation tests to verify the numerical setup are presented in Appendix C. URANS computations were performed using the $k-\omega$ SST [215] turbulence model. A temporal resolution of 360 steps per propeller revolution was adopted, i.e. one unsteady step corresponds to 1 degree of propeller azimuth. The simulations were started from an undisturbed free-stream flow conditions and more than 4 propeller revolutions, i.e. a flow particle travel distance of approximately 10 propeller diameters, were needed to obtain statistically time-invariant flow predictions. Numerical probes were introduced in the simulations at the cell centers nearest to the position of the unsteady pressure sensors (see Figure 4.3(b)), to record the pressure evolution in time and to allow a comparison of the noise spectra. A coarse grid of 20.1 million cells and a finer grid, with a spatial resolution doubled in all directions giving a total of about 161.3 million cells, were used for the simulations at cruise conditions. Simulations at climb conditions were performed only with the fine grid.

Figure 4.5 shows, using the Q criterion, the wake structures of the IMPACTA power-plant, at cruise conditions. Two blade tip vortices are observed to impact on the stub wing, the first one at approximately 1/3 of the wing chord.

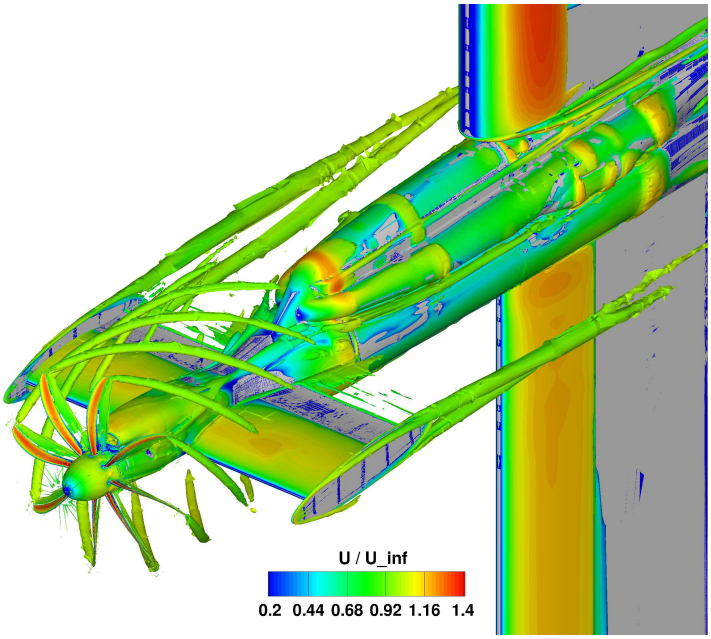

(a) Coarse mesh solution.

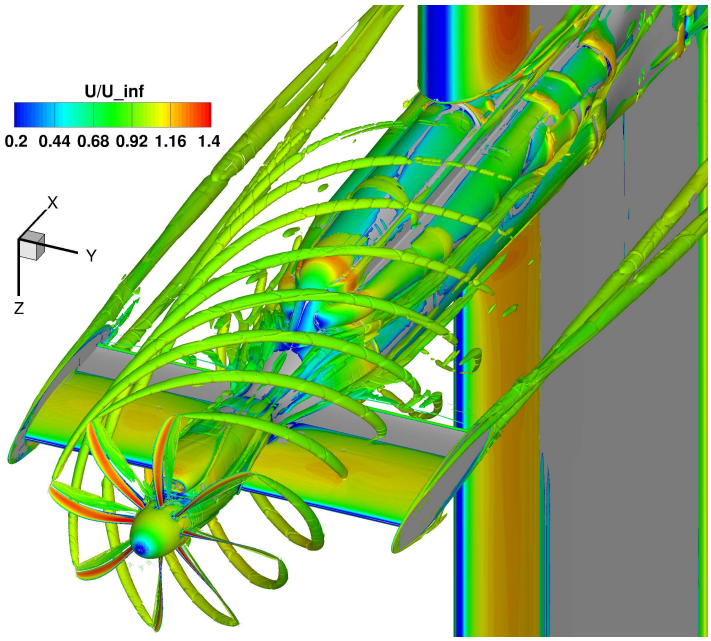

(b) Fine mesh solution.

Figure 4.5: IMPACTA wind tunnel scaled model at cruise conditions - flow-field instantaneous visualisation via iso-surfaces of Q (non-dimensional value of 0.005), colored by non dimensional axial velocity: comparison between numerical results of the coarse and fine grids. Differences in the resolution between the two grids are evident, the coarse one anyway preserving the propeller wake up to the wing.

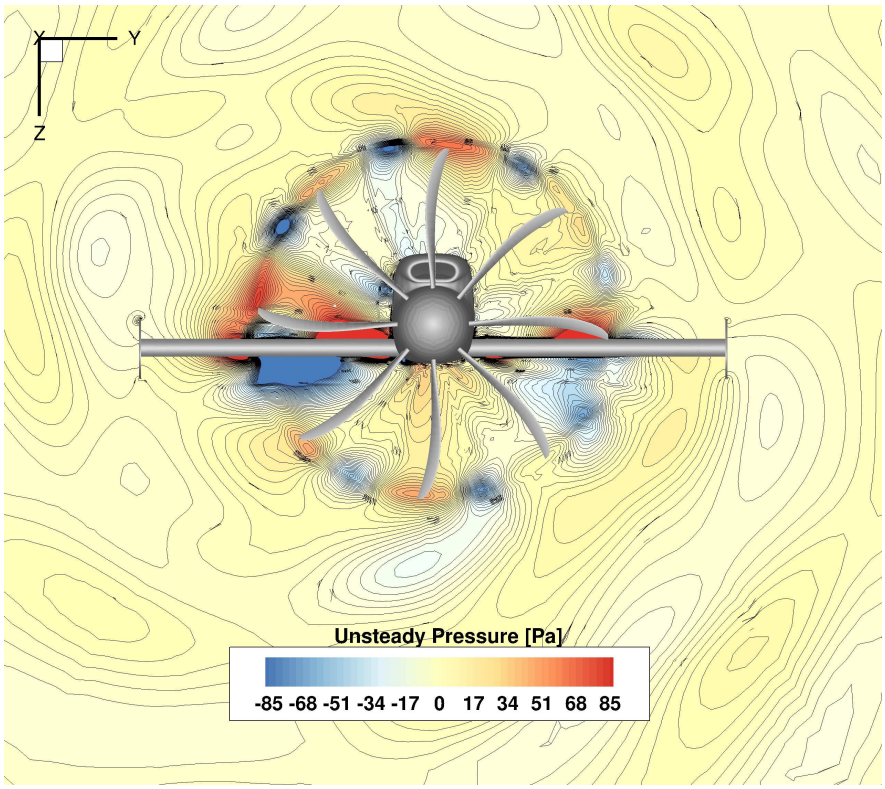

(a) Coarse mesh solution.

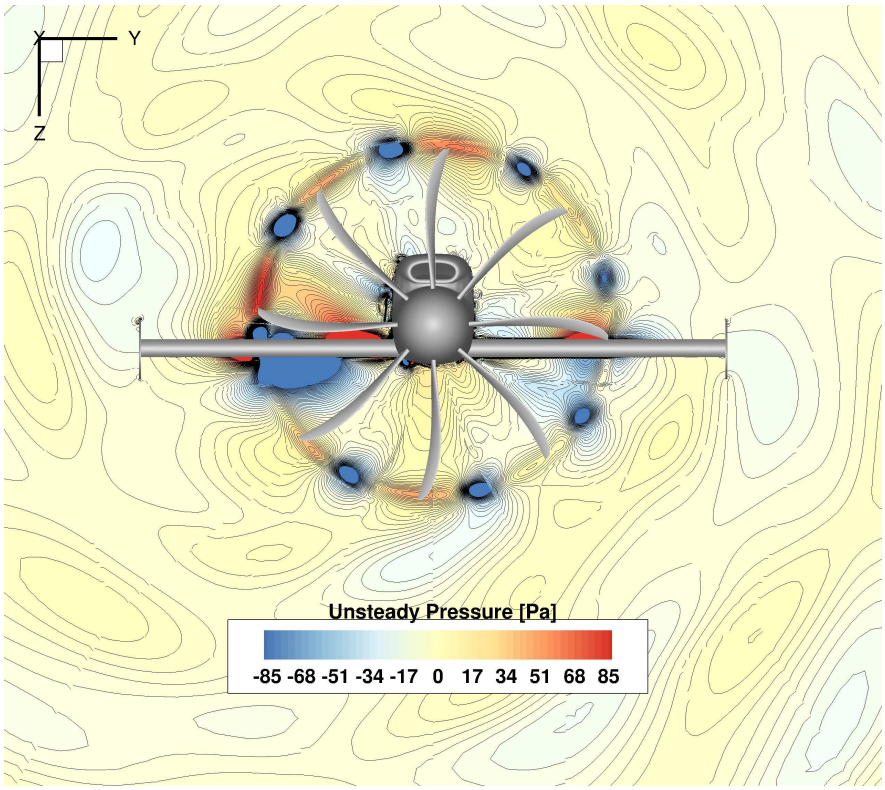

(b) Fine mesh solution.

Figure 4.6: IMPACTA wind tunnel scaled model at cruise conditions - acoustic field instantaneous visualisation via unsteady pressure: comparison between numerical results of the coarse and fine grids. *Part 1/2: plane parallel to the propeller rotational plane, at a down-stream distance of 1R.* The distortion of the typical spiral radiation pattern of a rotating source in subsonic forward motion, due to the presence of the airframe, is captured by the solver. The starboard side experiences weaker and less extended pressure fluctuations than the port side because of the lower loading - both meshes allow to capture this difference. Smaller dispersion is seen in the fine mesh solution.

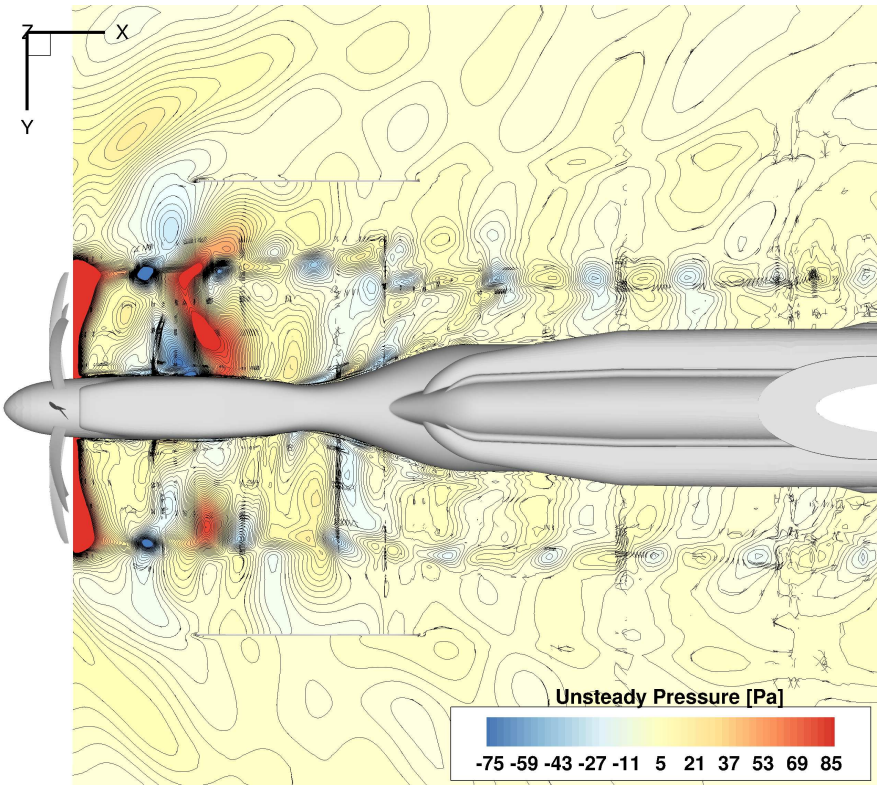

(c) Coarse mesh solution.

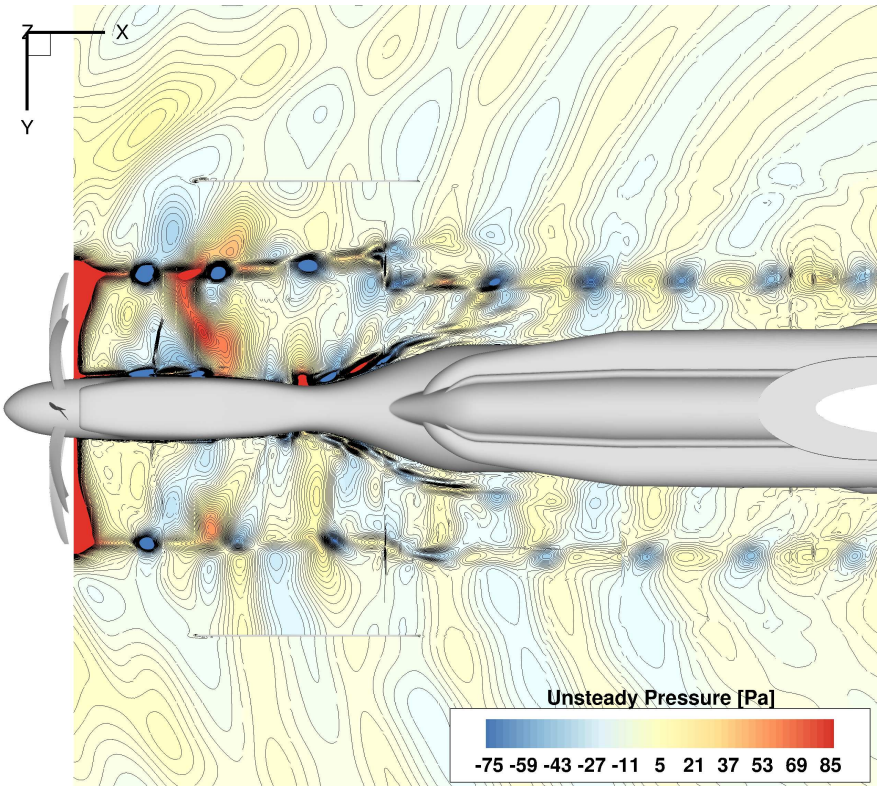

(d) Fine mesh solution.

Figure 4.6: IMPACTA wind tunnel scaled model at cruise conditions - acoustic field instantaneous visualisation via unsteady pressure: comparison between numerical results of the coarse and fine grids. *Part 2/2: longitudinal plane at spinner height ($z = 0$).* The down-stream propagation of the propeller sound waves and their interaction with the wing is well-resolved by the CFD. Significantly lower dissipation is observed in the fine mesh solution.

Figure 4.6 presents the instantaneous unsteady pressure field for a transversal plane at 1R down-stream the propeller plane, and for the longitudinal plane at spinner height. The typical spiral radiation pattern of the sound field of a rotating source in a subsonic forward motion, although modified by the presence of the nacelle and stub wing, are visible (see, as example, the analytical works of Carley [92, 93] for a sketch of the noise field of a forward-flying propeller). The larger pressure fluctuations, sources of the highest noise levels, appear at the propeller slip-stream boundary, where the blade tip vortices propagate. The interaction of the propeller wake with the stub wing is also seen to cause strong pressure perturbations, generating further noise. The scenario on port ($y < 0$) and starboard ($y > 0$) wings differ, the latter displaying weaker and less extended pressure oscillations. This is attributable to both the less loaded propeller blades, consequence of the thrust line incidence, and to the lower wing loading, due to the propeller down-wash, on that side of the model. Pressure fluctuations also appear on the nacelle surface because of the blade root vortices impact, generating additional noise, and again these are larger on the port side. Finally, a distortion in the acoustic field propagation can be observed at the wing trailing edge, where the flows on upper and lower wing surfaces encounter and mix.

Results of the two grids are compared. Differences in the resolution of both propeller wake and unsteady pressure field are important. The coarse mesh still allows to preserve the propeller wake down-stream up to the wing (see Figure 4.5(a)), however the fine mesh conserves it for approximately double the distance (see Figure 4.5(b)). Moreover, the higher spatial resolution yields tighter vortex cores and enables to resolve also smaller vortical structures. The fine grid shows significant improvements in the solution of the acoustic field as well (Figures 4.6(b) and 4.6(d)), because of the lower dissipation acting on the sound waves in their propagation. The coarse mesh captures nevertheless the differences between the starboard and port sides of the model, as shown in Figures 4.6(a) and 4.6(c).

4.2.2 Comparison with Experimental Data

Propeller Performance

The propeller performance were measured during the wind tunnel tests by means of a rotary shaft balance mounted aligned with the thrust axis. The thrust coefficient was determined from the shaft thrust data, corrected for RPM[†] and hub gap force[‡] , and the hub drag coefficient estimated from runs with no blades installed. This way,

[†] During blades-off, wind-off spinner runs, it was found that measurements from the shaft balance varied with RPM in a repeatable way. Corrections to axial force and torque were therefore derived from these measurements.

[‡] The force in the hub gap was calculated from a weighted average of the pressure measurements from 36 pressure taps arranged in 6 rings in the hub gap. Weights were calibrated to account for faulty pressure taps.

an apparent thrust coefficient is obtained, quantifying the blades thrust. The power coefficient was computed directly from the steady state torque measure of the rotary shaft balance, since the correction due to the RPM was negligible.
HMB3 estimates obtained on the fine mesh are compared against ARA averaged measurements in Table 4.2. The numerical estimate of the thrust coefficient C_T was determined via the integration of the pressure and viscous loads on the blades surface only, thus to eliminate the contribution of the spinner. For the cruise case, a second

Validation Case	C_T	C_T^*	C_P
Cruise ($RPM \sim 4050$, $M_\infty = 0.5$, $\alpha_T = -2$ deg)	+25.78%	+26.61%	+25.44%
Climb ($RPM \sim 4400$, $M_\infty = 0.45$, $\alpha_T = 0$ deg)	+6.27%	N/A	+10.16%
Cruise$''$ ($RPM \sim 4400$, $M_\infty = 0.5$, $\alpha_T = -2$ deg)	+6.19%	+6.83%	+14.70%

Table 4.2: IMPACTA Baseline scaled model propeller performance evaluation: comparison against experimental data. HMB3 predictions computed by averaging results over one propeller revolution vs balance mean value over runs of 4.8 s.

estimate, C_T^*, was also computed following the same approach used in the experiments: the loads integration was performed on both blades and spinner, and the results of a steady only-spinner simulation (see Section C.2) were subtracted from this. The prediction of the power coefficient C_P was performed by integrating the moment on both blades and spinner surfaces. HMB3 estimates have a positive offset in both thrust and power. This can be due to *(i)* a CFD over-prediction, *(ii)* effects of the wind tunnel, and/or *(iii)* measurement or calibration errors. It is noted that the uncertainty of the balance measurements is not known by the author. Thrust predictions show a closer agreement with experiments than power, as can be expected from the usually higher accuracy in both measurements and predictions of forces with respect to moments. The C_T estimate result slightly better compared to C_T^*, probably because the evaluation of the spinner drag in the steady computation can't properly account for the effect of the rotation.
Since the discrepancy with the experiments at cruise conditions is not small, an additional case was performed just as further check for propeller performance predictions. Test conditions were similar to the cruise case, but with higher RPM (see Table 4.2). This last computation was run only with the coarse grid to minimise the run time, since no significant differences are observed in the propeller loads prediction between coarse and fine meshes. The deviation of the numerical estimates from the measures for this test is similar to that of the climb case, suggesting a lower accuracy of the experimental data in the cruise case. This belief is also corroborated from the good agreement of the wing pressure that is shown in the following section. An actual large difference in

the propeller thrust would in fact cause a significant discrepancy in the wing loading, since the slip-stream effect would be wrongly predicted.

Overall therefore an over-estimation of propeller loading is seen compared to ARA experimental data. The trend of the performance indices with RPM and Mach number is however captured by the CFD, as shown in Figure 4.7.

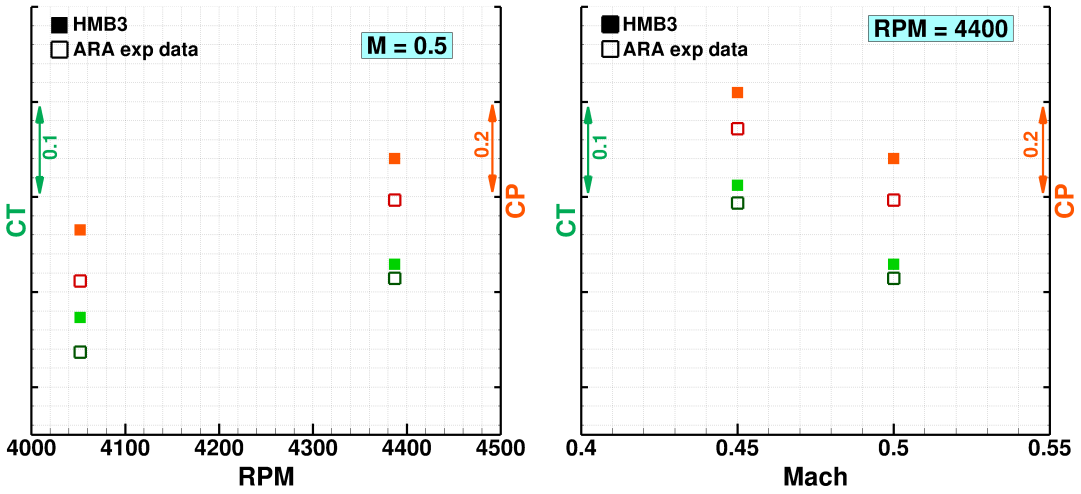

(a) Variation with RPM: validation cases Cruise and Cruise″.

(b) Variation with free-stream Mach number: validation cases Climb and Cruise″.

Figure 4.7: IMPACTA Baseline scaled model thrust and power coefficients comparison against experimental data. HMB3 predictions computed by averaging results over one propeller revolution vs balance mean value over runs of 4.8 s. Propeller loading is over-estimated by the CFD, however the trend with RPM and Mach number is captured.

Wing Pressure

The predicted wing pressure coefficient is compared against experimental data provided by ARA. Measurements of the steady pressure sensors were taken on runs of 15 seconds, i.e. approximately 1000 propeller revolutions. Numerical data were instead averaged over one revolution.

In Figure 4.8 results relative to the cruise conditions are presented. Very good agreement between the HMB3 URANS averaged solution and measurements can be observed at all instrumented span-wise wing stations. The effect of the propeller slip-stream on the wing loading is captured by the CFD, as can be seen from the differences in the chord-wise C_p distribution between corresponding wing sections on port and starboard side. No remarkable difference is observed between coarse and fine grid predictions, thus it is concluded that the resolution of the coarse grid is adequate for the wing loads.

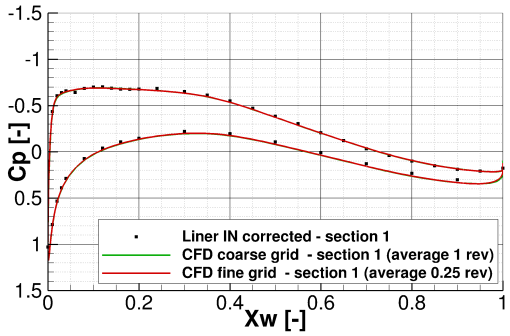

(a) Span-wise station S1: $y = -0.9R$.

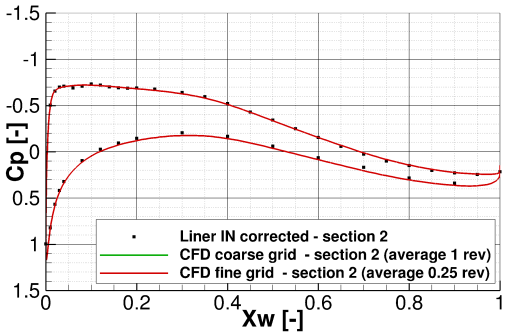

(b) Span-wise station S2: $y = -0.7R$.

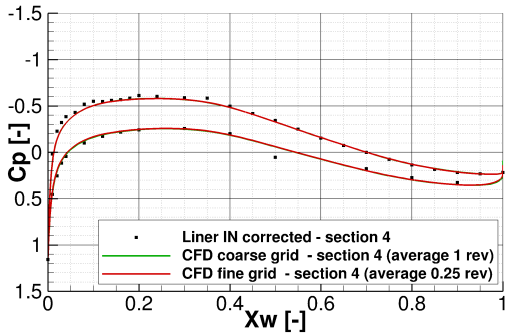

(c) Span-wise station S4: $y = 0.7R$.

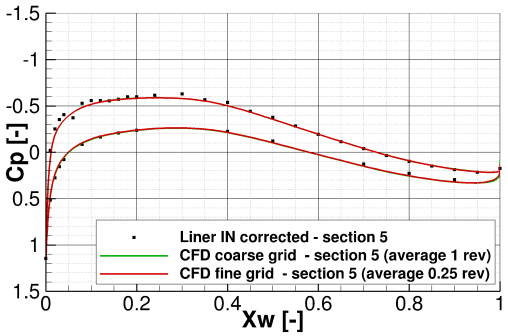

(d) Span-wise station S5: $y = 0.9R$.

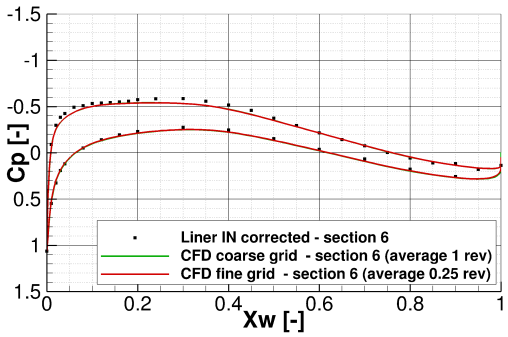

(e) Span-wise station S6: $y \sim 1.3R$.

Figure 4.8: Pressure coefficient distribution along different stations of the wing of the IMPACTA Baseline scaled model at **cruise** conditions: comparison between numerical results of HMB3 and experimental data [250] (rectangular points). Sections S1 and S2 on the port wing (up-stroking blade side), S4, S5 and S6 on the starboard wing (down-stroking blade side): refer to Figure 4.3(a) for the exact location of the sections. Very good agreement is observed. The coarse grid is shown adequate for wing loading estimates.

Figure 4.9 shows the C_p comparison for the climb case. HMB3 predictions match quite well the experimental data. Only a small under-prediction of the suction peak and slightly larger loads from about $0.3x_w$ to the trailing edge are visible, both probably due to the experimental data correction not perfectly calibrated for this case (see Appendix B). On the starboard wing inside the propeller slip-stream (sections S4 and S5), instead,

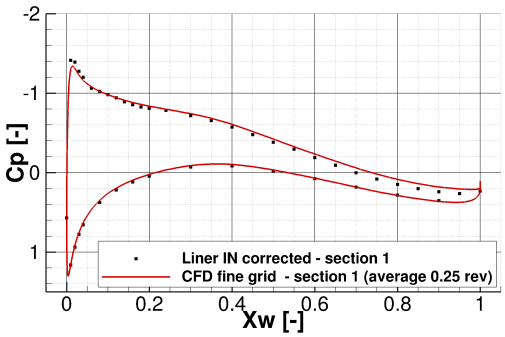

(a) Span-wise station S1: $y = -0.9R$.

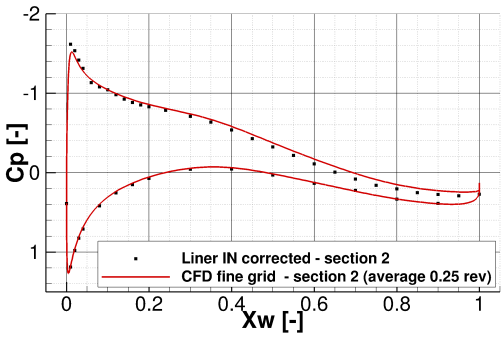

(b) Span-wise station S2: $y = -0.7R$.

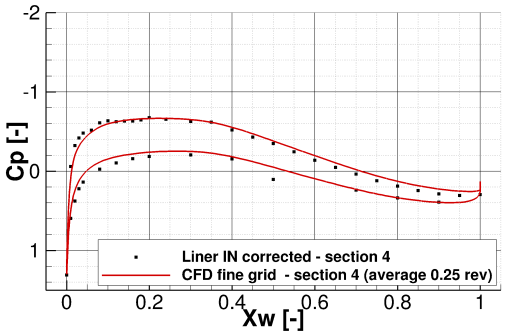

(c) Span-wise station S4: $y = 0.7R$.

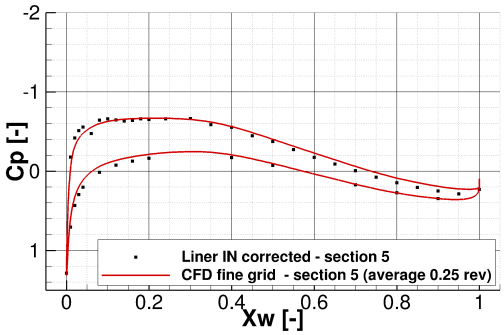

(d) Span-wise station S5: $y = 0.9R$.

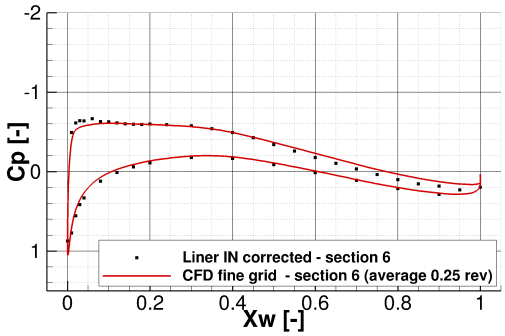

(e) Span-wise station S6: $y \sim 1.3R$.

Figure 4.9: Pressure coefficient distribution along different stations of the wing of the IMPACTA Baseline scaled model at **climb** conditions: comparison between numerical results of HMB3 and experimental data [250] (rectangular points). Sections S1 and S2 on the port wing (up-stroking blade side), S4, S5 and S6 on the starboard wing (down-stroking blade side): refer to Figure 4.3(a) for the exact location of the sections. Good agreement is seen, the small discrepancies probably due to the not perfectly calibrated wind tunnel data correction for this case.

the numerical results slightly deviate from measurements on the lower pressure curve between the leading edge and $0.3x_w$. Yet it is noted that, for this case, the experimental data differ between the tests with and without acoustic liner in the wind tunnel section (see Figures B.3(c) and B.3(d)), and that HMB3 predictions follow closely the C_p curve of the liner-OUT case. Any difference shown here is therefore thought to be due to the

presence of the liner inside the wind tunnel, and the consequent channel effect.

Power-plant Noise

To assess the acoustic results of HMB3 URANS simulations, the data of Kulite™ sensors installed on the model and of the microphone arrays on the ceiling and starboard wind tunnel walls are used. Locations of the unsteady pressure sensors in the IMPACTA experiments are shown in Figure 4.3(b). The numerical sound spectra is compared against Kulite™ recordings in Figures 4.10 and 4.11 for the cruise and the climb case, respectively.
The numerical pressure time signal is stored for one propeller revolution only. Therefore, since the signal length significantly influences the frequency study, the experimental signal is analysed considering only a segment corresponding to one propeller revolution. Moreover, the measurements, which are taken at 41 kHz, are filtered at the CFD Nyquist frequency ($\sim$12152 Hz and $\sim$13240 Hz for cruise and climb cases, respectively) using a 4^{th} order Butterworth filter [256]. Finally, it is noted that both tonal as well as broadband sources of pressure fluctuations are included in the measured spectra, whereas only tonal noise can be predicted by URANS simulations.
Differences between the coarse and the fine grid predictions are evident (Figure 4.10). The coarse grid solves up to the second harmonic on the stub wing, while the fine mesh up to the third. At higher frequencies the CFD does not have enough spacial resolution and the numerical spectra rapidly decay, while the experimental signals show broadband noise content. On the engine intake, distinct tones are instead visible, up to the eighth propeller harmonic, in both experiments and HMB3 predictions (the mesh density is here quite high because of the geometric complexity of the intake region and the distance from the noise sources is small so numerical dissipation is not significant). In general, the agreement between CFD and experiments is good for both propeller tested conditions. On average, using the fine grid, SPL estimates of URANS computations are within 3 dB for the first two tones and within 4 dB for the third harmonic, depending on the wing location. Smaller discrepancies are seen on the engine intake even at higher tones (here the coarse grid significantly over-estimates noise levels for lower harmonics). However, discrepancies between HMB3 predictions and measures are noted for some Kulite™ sensors, e.g. on the starboard upper wing side at cruise conditions and on the port lower wing at climb conditions. This could be due to errors in the signals or calibration of the sensor.

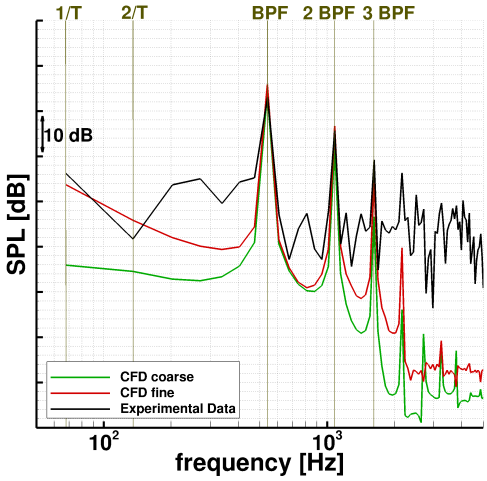

(a) Port upper wing: $x_w = 0.05c_w$, $y_w = -0.92R$.

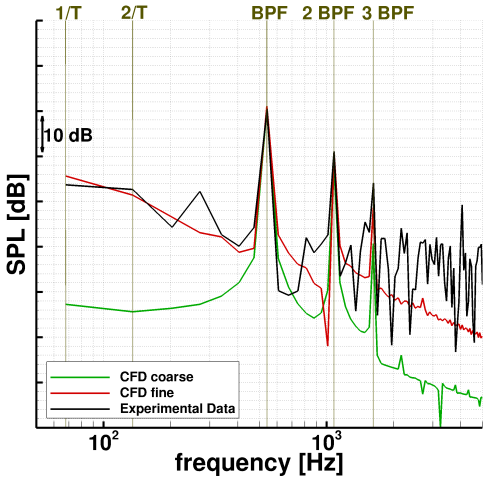

(b) Port lower wing: $x_w = 0.05c_w$, $y_w = -0.92R$.

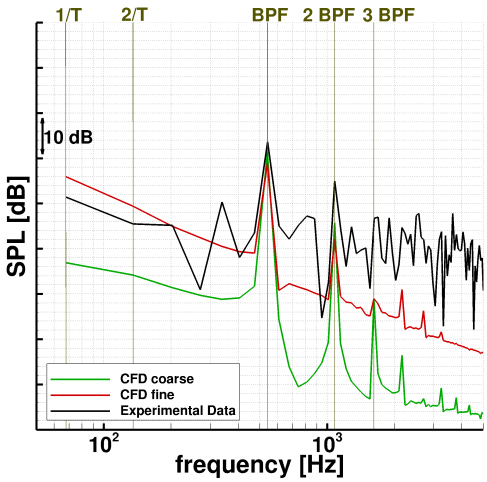

(c) Starboard upper wing: $x_w = 0.05c_w$, $y_w = 0.92R$.

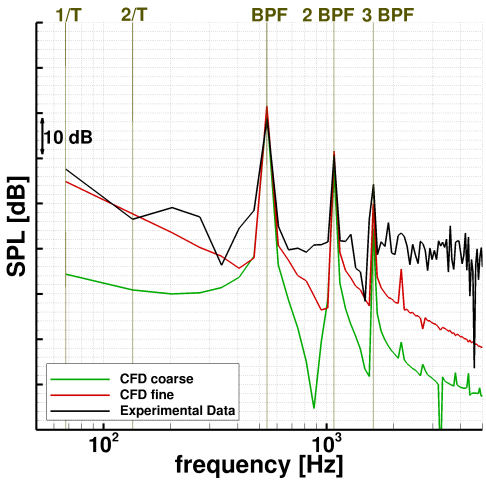

(d) Starboard lower wing: $x_w = 0.05c_w$, $y_w = 0.92R$.

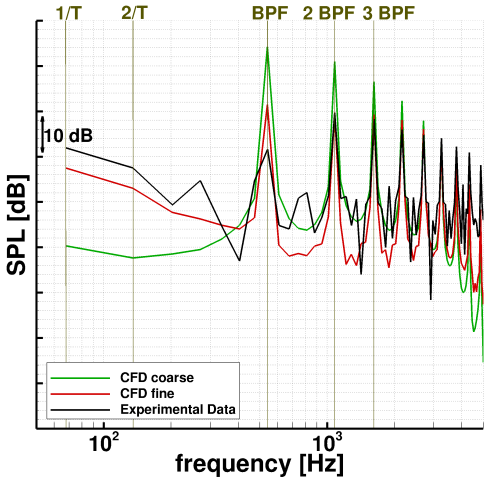

(e) Starboard engine intake rim.

Figure 4.10: Sound pressure level spectra on the IMPACTA wind tunnel model at **cruise** conditions: comparison between HMB3 URANS numerical results and Kulite™ measurements. The fine mesh yields adequate estimates for the first three propeller tones, whereas the coarse one solves up to the second.

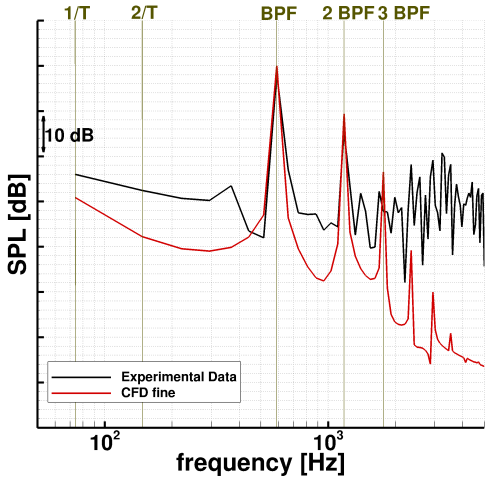

(a) Port upper wing: $x_w = 0.05c_w$, $y_w = -0.92R$.

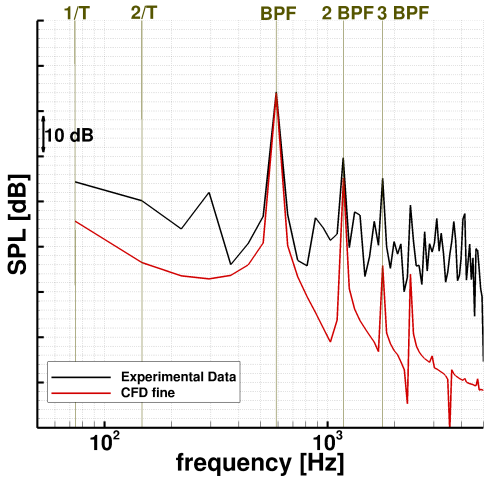

(b) Port lower wing: $x_w = 0.05c_w$, $y_w = -0.92R$.

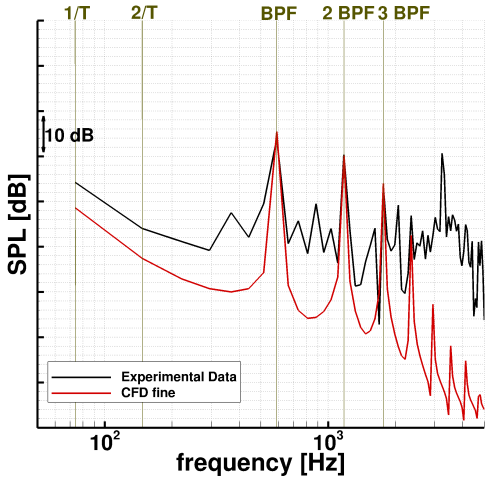

(c) Starboard upper wing: $x_w = 0.05c_w$, $y_w = 0.92R$.

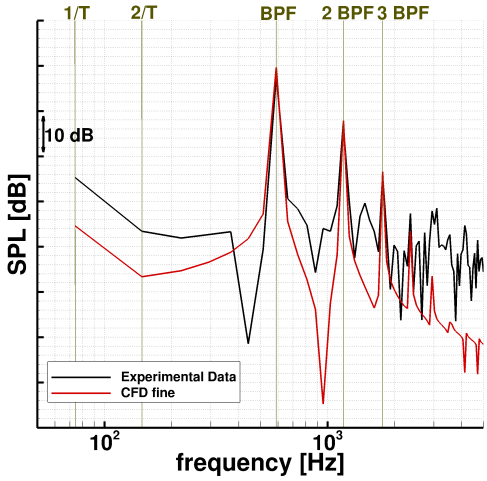

(d) Starboard lower wing: $x_w = 0.05c_w$, $y_w = 0.92R$.

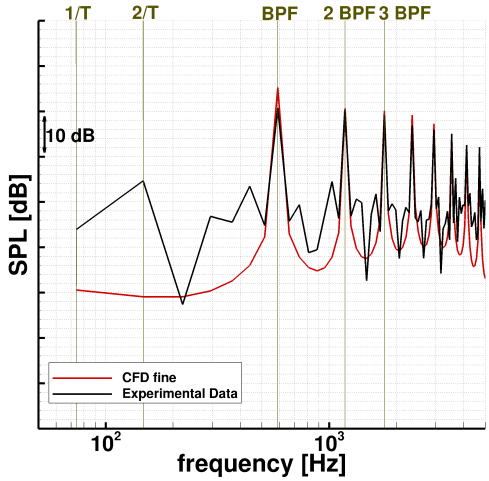

(e) Starboard engine intake rim.

Figure 4.11: Sound pressure level spectra on the IMPACTA wind tunnel model at **climb** conditions: comparison between HMB3 URANS numerical results and Kulite™ measurements. Fairly good agreement is noted up to the third propeller harmonic.

Audio recordings of microphones on the wind tunnel walls allow for an evaluation of noise predictions in the near-field, at some distance from the turboprop engine model. Experimental data of the individual microphones are affected by reverberation in the working section, installed noise sources and parasitic noise due to the propeller rig. Consequently, interference fringes are present in the microphone array measurements of the incident sound field. So, the comparison between CFD predictions and microphone recordings is made via an area-weighted average of the SPL using only the central microphones of the arrays (in particular, 71 over 144 sensors - see Figure 4.3(b)). In particular, the averaging grid is built so that each of the considered microphones is the central point of azimuthally equally spaced cells. This way, no interpolation of the data is needed before performing the area-weighted average.

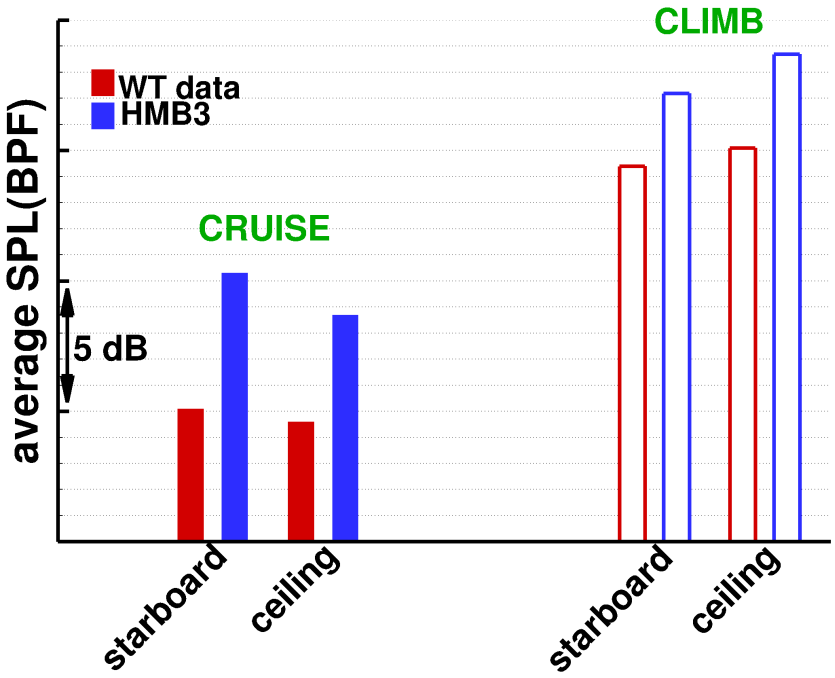

Figure 4.12: Near-field IMPACTA wind tunnel model sound levels: microphone arrays area-averaged SPL for the first tone. Comparison of HMB3 results against ARA experimental data. CFD results predict higher levels, however the different sound directivities of the different propeller operating conditions are correctly captured.

Figure 4.12 presents the average sound levels of the first harmonic for both arrays, at cruise and climb conditions. HMB3 over-predicts by a few dB the averaged acoustic liner measurements (discrepancies range from 2.8 dB to 5.2 dB), the climb case showing overall a closer agreement. It is noted that the CFD results display the same trends as the experiments when comparing the data from the starboard and the ceiling arrays at the same propeller operating conditions, indicating that HMB3 captures correctly the differences in the sound propagation of the different conditions.

This is a complex setup, and a demanding calculation, so the overall obtained agreement is seen as satisfactory.

4.3. Conclusive Remarks

On the whole, a good agreement between numerical results and experimental data is observable, regarding both aerodynamics and acoustics. HMB3 can thus be considered reliable to solve the flow on and around the propeller blades, the noise levels of the dominant tones in the near-field, and the physics of the interaction with the airframe when the propeller is installed. Within the inherent limitations of the URANS solutions, its predictions showed an adequate accuracy, comparable with state-of-the-art estimates computed by other researchers with various CFD solvers (please refer to the literature survey in Section 1.3 for specific data). In particular, provided a sufficient mesh resolution, absolute sound levels of the first three propeller harmonics could be determined by HMB3 within 2 to 3 dB. Moreover, trends and directivities were correctly captured at all different propeller operating conditions tested, therefore enabling confidence in the use of HMB3 numerical results for comparison purposes, with uncertainties of less than 1 dB.

Chapter 5

Blade and Hub Designs Study*

This Chapter focuses on the numerical study of the near-field tonal noise of an isolated propeller. The acoustic properties of various designs are analysed. The designs include the IMPACTA Baseline propeller, an innovative blade geometry and two different hub configurations.
RANS simulations are employed to directly estimate the noise reaching a fictitious fuselage, and acoustic TFs are used to evaluate the noise perceived inside it. This method aims, in a comparative way, to assess the overall acoustics of a turboprop aircraft, at low computational cost.
Contrary to the Heidmann technique [257] nowadays used during aircraft design (see [258] for a review of current noise design prediction tools), RANS equations capture the distinct characteristic acoustic features of different propeller geometries. Hence, they enable the assessment of emitted sound spectrum and overall noise levels of various propeller designs, early in the design stage.

5.1. IMPACTA Propellers Design

The IMPACTA propeller is a new-generation design, aiming for high efficiency at high speeds. It has 8 blades with a radius R of 2.209 m and a chord c of 0.213 m. The sections of the blades are thin, highly twisted and swept back ($\sim 51^\circ$ at $0.7R$). The propeller operates at high loading conditions. Besides the Baseline propeller, three different designs were considered: an Offloaded Tip blade, a Staggered hub and an Unequally-Spaced hub.† The modified geometries are shown in Figure 5.1, against the Baseline design. The operating cruise conditions for the IMPACTA propellers are reported in Table 5.1. The three propellers are designed to deliver the same thrust.

* The work presented in this Chapter is published in G. Chirico *et al.* , "Numerical aeroacoustic analysis of propeller designs", *The Aeronautical Journal*, Vol. 122, No. 1248, pp. 283-315, doi:10.1017/aer.2017.123, 2018.

† All propeller geometries were designed from, and belong to, Dowty Propellers [4].

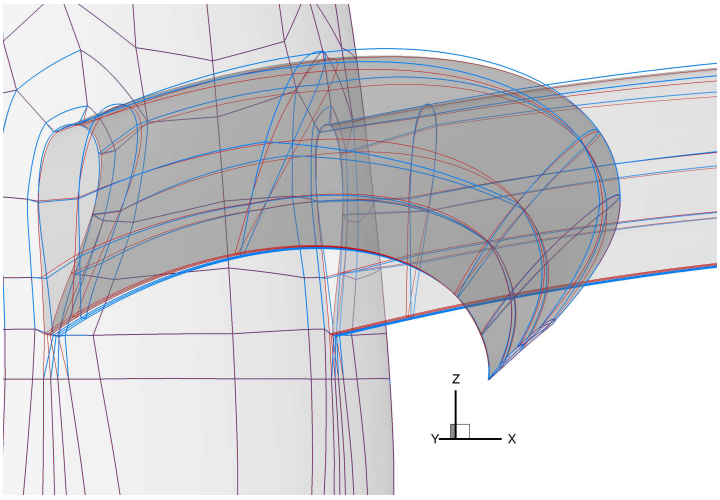

(a) Offloaded Tip blade (light blue).

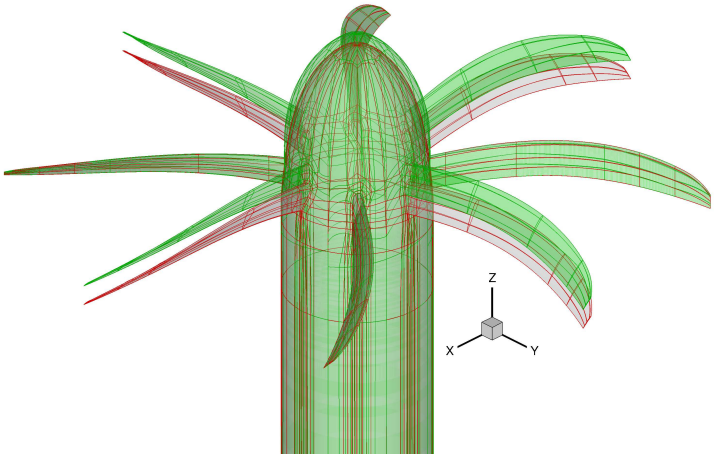

(b) Staggered hub (green).

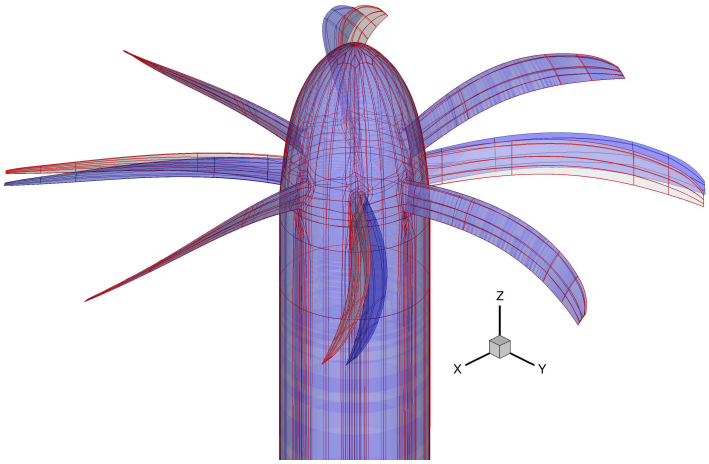

(c) Unequally-spaced hub (blue).

Figure 5.1: IMPACTA modified propeller geometries vs Baseline design (grey and red).

	Baseline blade	Offloaded Tip blade
Altitude [m]	7620	7620
Temperature [$^{\circ}C$]	248.62	248.62
Free-stream Mach number M_{∞}	0.5	0.5
Required thrust [N]	7851.11	7851.11
Blade incidence angle at 70%r	50.1	53.6
RPM	856.14	790.29
Tip Mach number M_{TIP}	0.627	0.578
Tip Reynolds number Re_{TIP}	1.24e06	1.15e06
Helical Mach number at 95%r	0.789	0.754

Table 5.1: Cruise operating conditions for the IMPACTA blades.

The Offloaded Tip blade is characterised by less tip twist than the Baseline design, and runs at a slightly higher pitch angle. This moves inboards the peak of the blade loading, and, as can be predicted from a simple semi-empirical analysis [15], should decrease the sound levels. Moreover, to achieve the same thrust, the Offloaded Tip blade operates at lower RPM, i.e. at a higher advance ratio, further increasing the blade pitch. Therefore, an additional noise reduction is expected from lowering the tip Mach number, in agreement with wind tunnel and in-flight experimental data [142, 114] showing significant reductions in the sound levels of the first tones with decreasing tip speed. Note that, because of the lower operating RPM, the Offloaded Tip design will have harmonics at lower frequencies.

The main idea behind the different hub designs is to modulate the noise spectrum by changing the geometric periodicity of the propeller, redistributing the acoustic energy on more frequencies. This should result in a more pleasant sound to the human ear. In particular, the Staggered hub has four blades offset towards the spinner tip by 2/3 of the root chord, while the Unequally-Spaced hub has the space between the blades modified by ± 4 degrees. The Staggered hub is expected to be more efficient, and noisier, than the Baseline due to the different inflow conditions seen from the second row of propeller blades. The higher efficiency also provides an opportunity to make the propeller hub and the spinner diameters smaller for a lower installation drag. Asymmetric blade spacing was instead shown to decrease the noise in some radiation directions [259] because of interference among the sound-waves of the individual blades.

5.2. Test Cases Description

All the IMPACTA designs were numerically studied in isolated configuration at cruise conditions. Steady RANS simulations were therefore performed, employing the axial

flight formulation described above. The $k-\omega$ SST turbulence model [215] was used to close the system of equations. The computed cases are summarised in Table 5.2.
It is noted that, from a steady computation, it is not possible to capture the broadband noise content, therefore the acoustic analysis will be focused only on tonal noise.

Propeller Design	Simulation	Conditions	$N^{\circ}_{\text{blades}}$	Grid	CPUs
Baseline	RANS, $k-\omega$ SST	Cruise	1	G1	32
Offloaded Tip Blade	RANS, $k-\omega$ SST	Cruise	1	G2	32
Staggered Hub	RANS, $k-\omega$ SST	Cruise	2	G3	64
Unequally-spaced Hub	RANS, $k-\omega$ SST	Cruise	2	G4	64

Table 5.2: IMPACTA design study: computational test cases.

5.2.1 Computational Grids

Multi-block structured grids were generated employing a classic "C−H" block topology around the blades. Using the axial flight formulation, only $1/N$ of the domain was represented, where N is the geometric periodicity index of the propeller. Therefore, $N = 8$ for the baseline hub configuration (Baseline and Offloaded Tip blades - grids G1 and G2 respectively) and $N = 4$ for the modified hub configurations (Unequally-spaced and Staggered designs - grids G3 and G4 respectively). The computational domain and the spinner were extended downstream to apply free-stream boundary conditions on the far-field boundaries, accommodating two propeller revolutions with the wake resolved over more that 180 degrees. Figure 5.2 shows the computational domain, the grid topology, and the surface mesh details for the IMPACTA Baseline design. The different grids were built to be as similar as possible, for all propeller designs, and limit the influence of the computational grid on the numerical predictions. The spatial resolution of the grid was chosen on the basis of grid convergence studies carried out for the JORP propeller [88, 251]. The wall spacing was selected to ensure a $y^{+} \sim 0.5$ on average along the blade, and values slightly higher than 1 towards the spinner junction. An exponential law was used to generate the points distribution in the boundary layer. The grids are quite regular in the area of interest, with stretched cells only inside the boundary layers, to perform wall-resolved Navier-Stokes computations. Stretched cells are also in the far-field, since a fine spatial resolution is not needed. Grid dimensions, and mesh quality indices, are reported in Table 5.3.

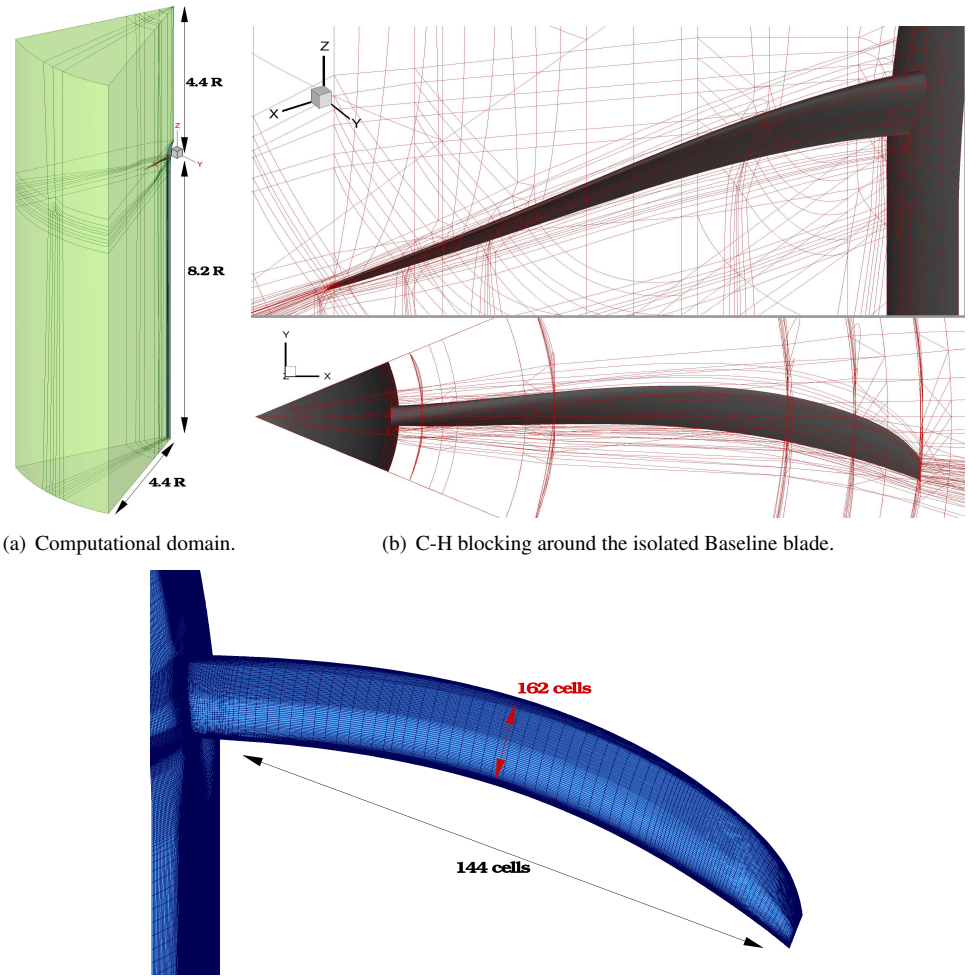

(a) Computational domain.

(b) C-H blocking around the isolated Baseline blade.

(c) Baseline design blade surface mesh details.

Figure 5.2: IMPACTA propellers: computational grids for the isolated computations.

Grid	Cells	Blocks	Max Aspect Ratio	Max Normal Skewness	Min Orthogonality
G1	11.25 M	482	850377	$2.3\ 10^{-5}$	$3.3\ 10^{-3}$
G2	11.25 M	482	850551	$2.8\ 10^{-5}$	$2.3\ 10^{-3}$
G3	24.6 M	964	596686	$1.3\ 10^{-5}$	$4.4\ 10^{-3}$
G4	28.3 M	964	799028	$1.4\ 10^{-5}$	$2.5\ 10^{-3}$

Table 5.3: Dimensions and properties [260] of the IMPACTA isolated blade(s) computational grids. Mesh quality indices reported are related to the whole grid, including boundary layer and far-field cells. The worst values of aspect ratio, normal skewness, and orthogonality over the whole grid are given.

5.3. Aerodynamic and Performance Discussion

Since the propeller aerodynamics is not the prime focus of this work, it is only noted here that the flow is mostly attached along the blade for all designs. As can be seen in Figure 5.3 for the Baseline blade, the flow separates only in a very small area (zone A) on the blade root suction side.

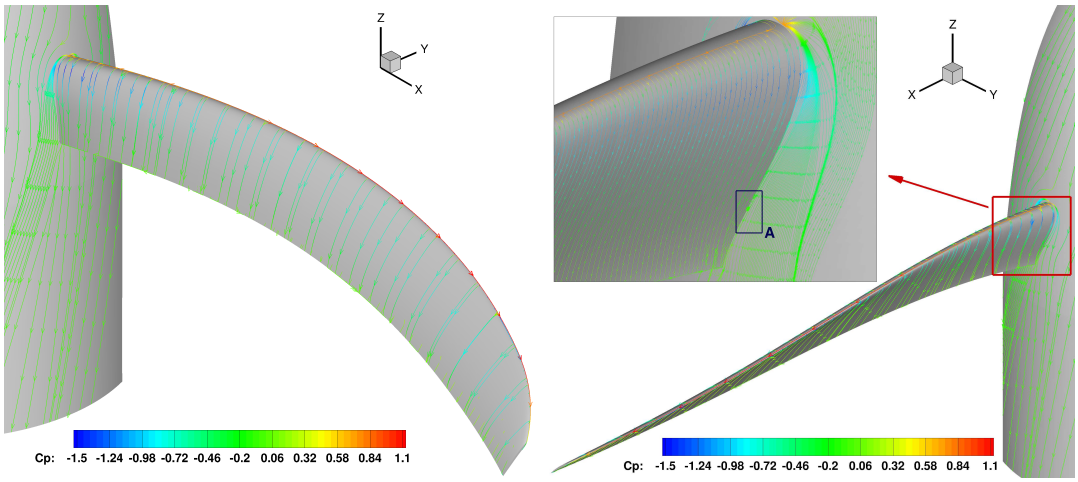

(a) Blade pressure side.

(b) Blade suction side.

Figure 5.3: Baseline IMPACTA propeller at cruise conditions: flow visualisation of the propeller through friction, colored by pressure coefficient. The flow on the blade is attached everywhere apart from a very small area on the root suction side (zone A).

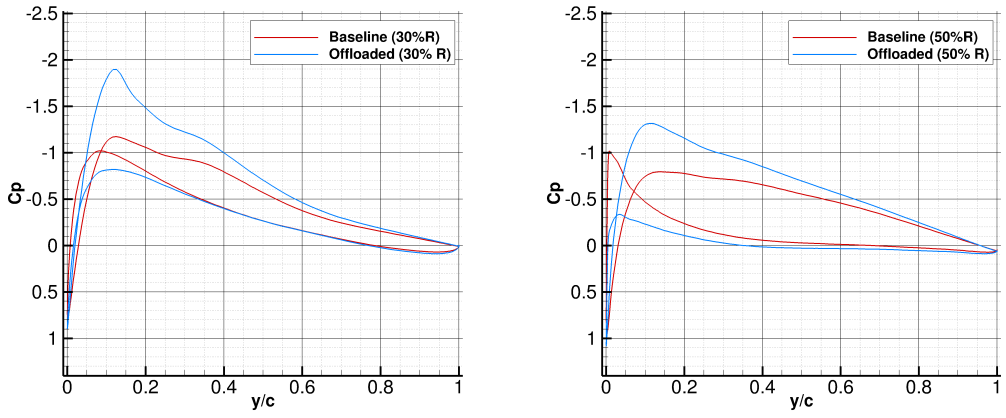

(a) Radial station $r/R = 0.3$.

(b) Radial station $r/R = 0.5$.

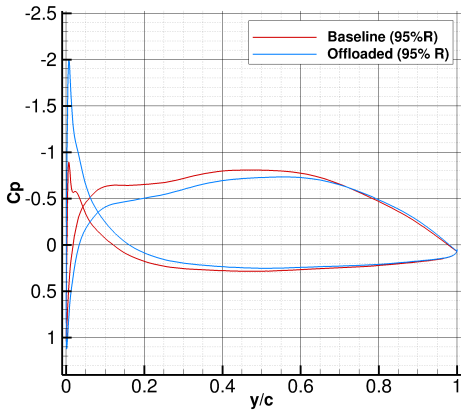

(c) Radial station $r/R = 0.95$.

Figure 5.4: Chord-wise pressure coefficient distribution at different blade stations for the Offloaded Tip blade compared to the Baseline blade. The different twist and pitch distribution of the Offloaded Tip design moved the loading span-wise towards the blade root.

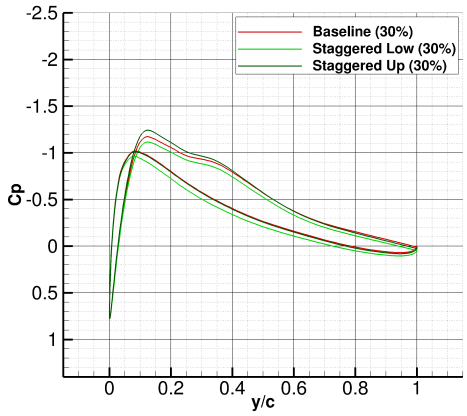

(a) Staggered hub: radial station $r/R = 0.3$.

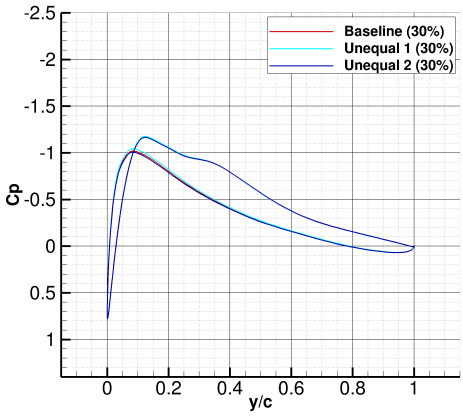

(b) Unequally-spaced: radial station $r/R = 0.3$.

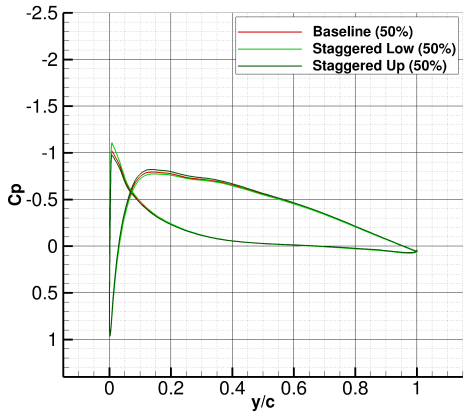

(c) Staggered hub: radial station $r/R = 0.5$.

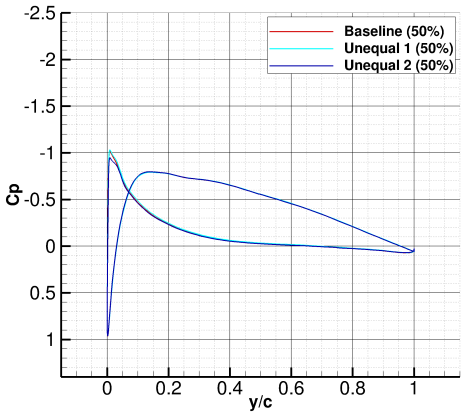

(d) Unequally-spaced: radial station $r/R = 0.5$.

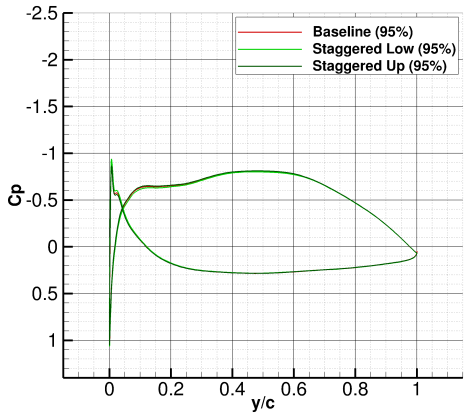

(e) Staggered hub: radial station $r/R = 0.95$.

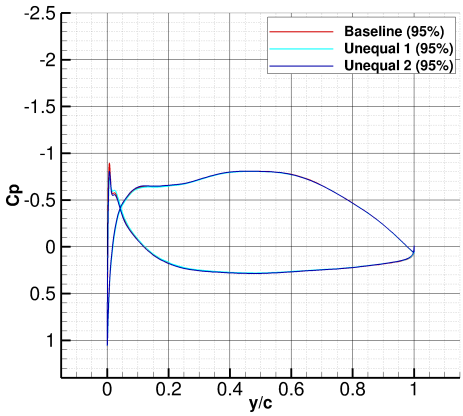

(f) Unequally-spaced: radial station $r/R = 0.95$.

Figure 5.5: Chord-wise pressure coefficient distribution at different blade stations for the modified IMPACTA hub designs compared to the Baseline: Staggered hub on the left, Unequally-spaced on the right. The blade loading slightly differs only near the root.

Because of the propeller noise source mechanism, it is important to look at the span-wise loading distribution. Figures 5.4 and 5.5 show the pressure coefficient distributions at three different blade stations for the modified propeller designs compared to the Baseline.
Significant differences are predicted only for the Offloaded Tip blade. As expected based on the geometric characteristics of this design, the peak loading is moved inboards (Figure 5.4). The modifications of the hub configuration (Figure 5.5) did not lead to any notable effects on the span-wise loading distribution. Small differences are seen only towards the blade root.

	Offloaded Tip	Unequally-spaced	Staggered
ΔThrust	+1.52%	-0.39%	+1.3%
ΔSPL(BPF)	-0.118 dB	+0.031 dB	-0.102 dB
ΔSPL(2·BPF)	-0.050 dB	+0.016 dB	-0.053 dB
ΔSPL(3·BPF)	+0.001 dB	+0.005 dB	-0.016 dB
ΔOASPL$_{max}$	-0.094 dB$_A$	+0.023 dB$_A$	-0.077 dB$_A$

Table 5.4: IMPACTA propellers thrust with respect to the Baseline design and correspondent noise levels corrections.

Table 5.4 compares the thrust of the various designs. It is observed that, at the fixed-pitch simulated conditions, the modified designs provide a different thrust with respect to the Baseline. Therefore, to carry out an unbiased acoustic comparison, i.e. at equal thrust, the noise levels of the various designs are corrected to account for the different blade loading. Semi-empirical approaches were used to determine the magnitude of this correction. In particular, the procedure described in [15] based on [261] was employed for the A-weighted OSPL, while the ESDU method derived from Gutin's theory [262, 36] was applied to the SPL of the various harmonics. Appendix D reports a short description of the two methods. The resulting corrections, reported in Table 5.4, are in any case small because the thrust differences were small.

5.4. Acoustic Discussion

5.4.1 Sound Field Analysis

An idealised fuselage representative of a high-wing aircraft was modelled, via an array of virtual microphones, to investigate the noise characteristics of the different designs. As shown in Figure 5.6, the monitoring points were arranged in a 32 by 33 matrix of half cylinder located approximately 5 chord lengths away from the blade tip. The idealised fuselage extends 11.5 blade root chords in front of the propeller rotational plane, and 4 chords behind.

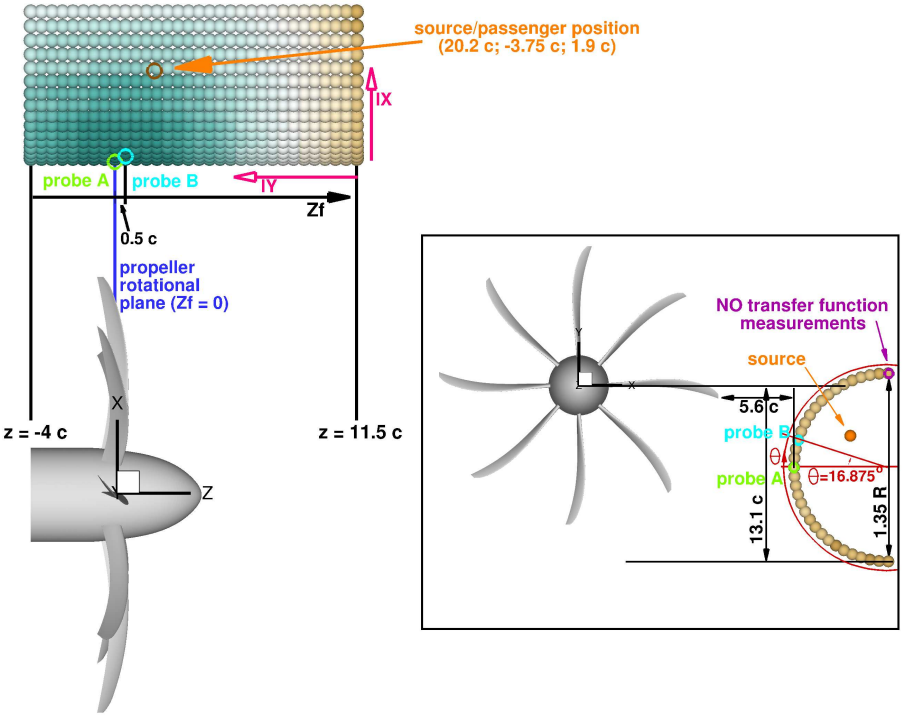

Figure 5.6: Acoustic analysis setup (top and frontal views): idealised fuselage representative of a high-wing narrow-body commercial aircraft.

Figure 5.7 shows, for the Baseline design, the incident pressure field $p(\mathbf{x})$ for two different azimuthal blade positions, i.e. at two different time instances of the equivalent unsteady simulation.

To estimate the noise at each selected point, an equivalent, one revolution long, unsteady pressure signal $p(\mathbf{x},t)$ was reconstructed from the steady CFD solution. Section 3.1 shows the details of the adopted procedure. A time sampling corresponding

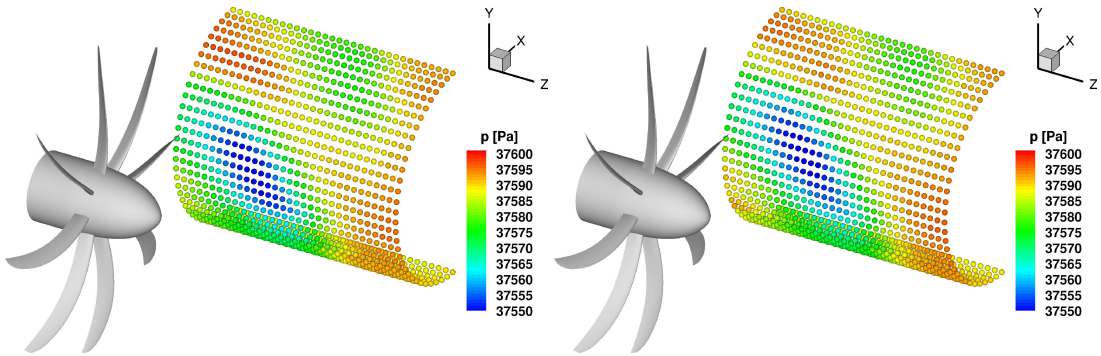

(a) $\psi_b = 0$ deg. (b) $\psi_b = 15$ deg.

Figure 5.7: Baseline IMPACTA propeller: instantaneous incident pressure distribution on the idealised fuselage. The time history of the impinging pressure is reconstructed a posteriori from the steady CFD solution.

to 0.25 degrees of propeller rotation was used. According to Nyquist's theorem [203], this means that the maximum captured frequency will be about 10 kHz. For the analysis it is assumed that, at the fuselage location, the incident unsteady pressure field can be approximated with only acoustic pressure fluctuations, whereas the hydrodynamic near-field is neglected due to the different source-observer distance scaling. This approach was deemed adequate for estimating the noise differences among different propellers as opposed to seeking absolute noise prediction levels. To compute the unsteady pressure statistical characteristics, the complete reconstructed signal of 1 revolution was used, and the Tecplot FFT algorithm [260] with a rectangular window function employed to estimate the PSD. To take into account the human hearing sensitivity, the A-weighting filter was also applied to the sound pressure estimates (again, see Section 3.1 for details). The OASPL was computed including the contribution of the first five harmonics.

The overall sound pressure levels (OSPLs) on the idealised fuselage at cruise operating conditions are presented in Figure 5.8, for all the designs. The corresponding OASPL values are also shown. No substantial differences are seen in the trend of the OSPL distribution. The higher noise levels are observed in the proximity of the propeller rotational plane, at approximately 17 degrees of azimuthal position, where the distance is minimal. As can be partly seen in Figure 5.7, the largest fluctuations of pressure occur at that angle. Moving away from this region, both in the longitudinal and in the azimuthal directions, the distance from the noise sources increases and the OSPL decreases. In particular, the OSPL peak for the Baseline design is predicted 0.5 chords in front of the propeller rotational plane (probe B in Figure 5.6). The Offloaded Tip blade and the Unequally-Spaced hub also show the OSPL maximum at the same position. The Staggered hub design instead exhibits the maximum noise level $0.5c$ further ahead because of the forward translation of the first blade-row.

The A-weighting filter yields lower noise levels for all cases. This is because the filter gains are negative for frequencies below 1 kHz (see Figure 3.1), so for the first eight harmonics of the IMPACTA propellers. The noise reduction due to the A-weight filter for the Offloaded Tip blade is higher in magnitude than for the other designs because its harmonics are at lower frequencies. With the exception of the Offload-Tip design, it is observed that the point of maximum OASPL is found at a fuselage station downstream with respect to the OSPL peak location.

Regarding the noise levels, the Offloaded Tip blade shows an acoustic footprint significantly quieter than the Baseline with a decrease of 6.2 dB_A for the maximum OASPL. Staggered and Unequally-Spaced hubs, instead, yield slightly higher noise

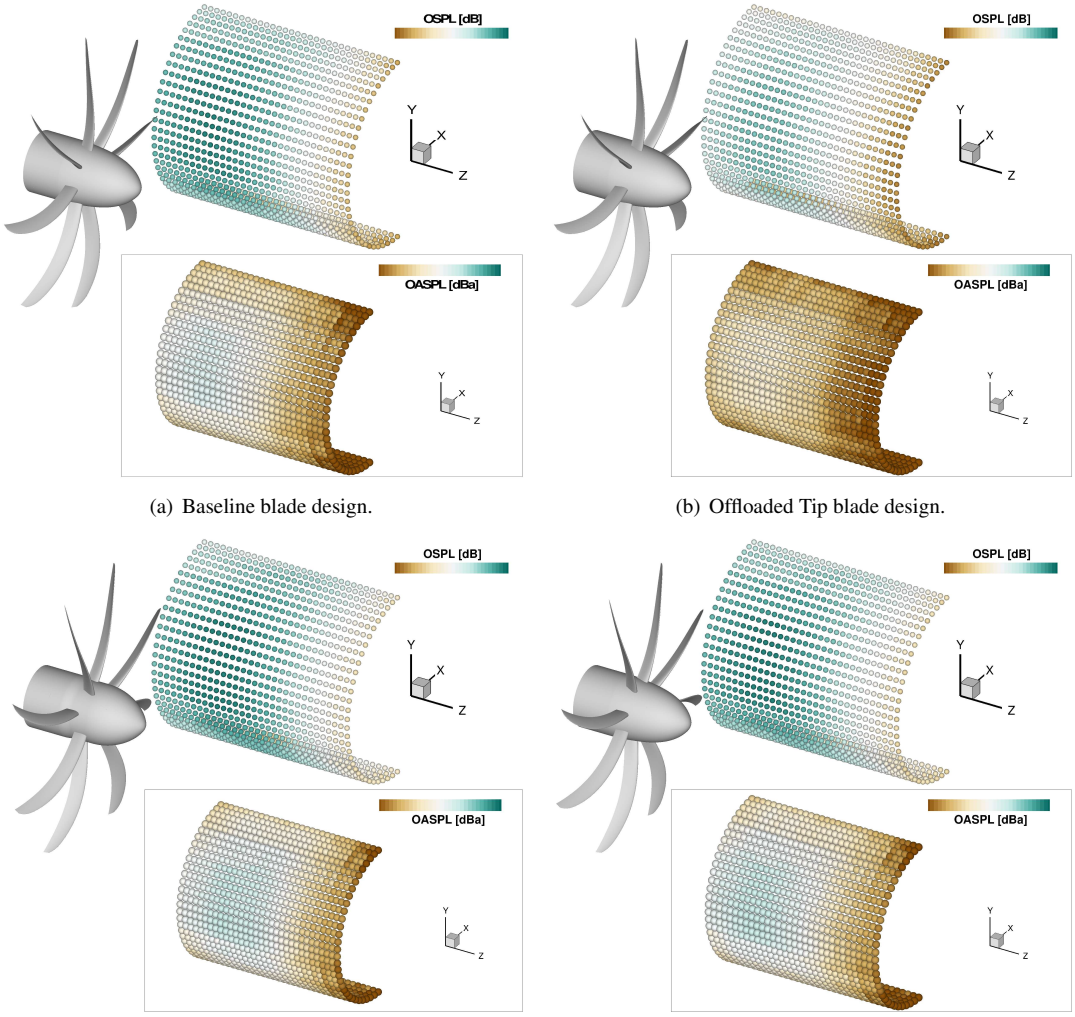

(a) Baseline blade design.

(b) Offloaded Tip blade design.

(c) Staggered hub design.

(d) Unequally-spaced hub design.

Figure 5.8: OSPL, and OASPL up to the fifth harmonic, on the idealised fuselage for the different IMPACTA propeller designs. The color scale range is equal to 30 dB. No important differences are noted regarding the trends, the highest noise levels being at the minimum distance from the blade tip. The Offloaded Tip blade appear significantly quieter than all other propeller designs.

levels with respect to the Baseline with +1.98 dB_A and +2.31 dB_A for the maximum OASPL, respectively. It can be noted that, unlike the OSPL, the OASPL of the Staggered hub is lower than the Unequally-Spaced for a large part of the fuselage. This is because of the different distribution of the acoustic energy over the frequencies. This can be better understood looking at the noise spectra.

Figure 5.9 shows, as an example, the constant bandwidth SPL spectrum for the Baseline propeller, at the closest monitoring point to the blade tip (probe B of Figure 5.6). Tones at the blade passing frequency ($BPF = 114.152$ Hz) and its multiples are clearly visible. The expected linear decay, typical of ideal inflow conditions, is also observed. The predicted SPL values are in good agreement with estimates provided

by the designer [9], with a maximum discrepancy of less then 1.5 dB for the first few tones.

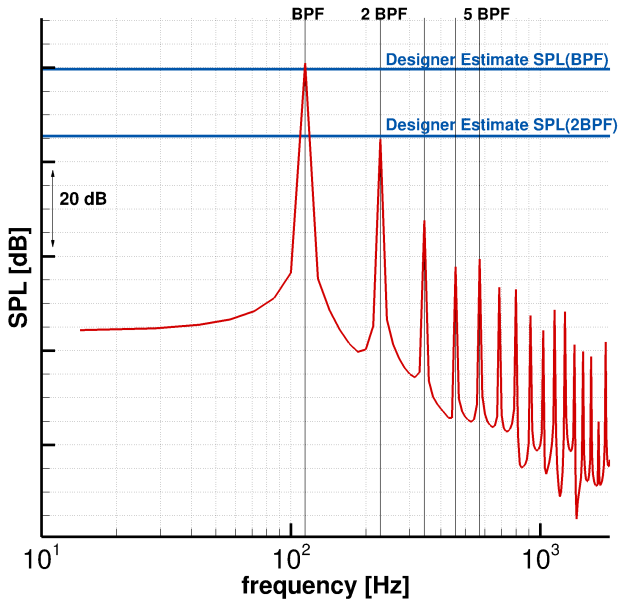

Figure 5.9: Baseline design at cruise conditions: SPL spectrum at the closest point of the idealised fuselage to the blade tip ($z_f = 0$c, $\Theta = 16.875$ deg). Tones at the BPF and its multiples appear clearly in the RANS solution, approximately following the linear ideal decay of an uniform axial inflow. Estimated levels of lower tones agree well with data of the designer.

A comparison between the spectra of the different designs at probe B is reported in Figure 5.10. Table 5.5 reports the sound pressure levels of the first three BPF harmonics for the modified designs, together with the OASPL level. Data are relative to the Baseline propeller values at the same location. The Offloaded Tip blade, as explained, shows tones at lower frequencies, and is significantly quieter than the Baseline design, with an appreciable noise level reduction up to at least the fourth tone. The Staggered and Unequally-Spaced hubs show additional tones at multiple of BPFs/2 due to the different geometric periodicity. Their acoustic energy is thus spread over more frequencies, and, in total, they are slightly louder than the Baseline design. Differences in the frequency distribution of the acoustic energy between the Staggered

	Offloaded Tip	Unequally-spaced	Staggered
ΔSPL(BPF) [dB]	-4.406	-0.178	+0.657
ΔSPL(2·BPF) [dB]	-7.532	-2.410	-1.883
ΔSPL(3·BPF) [dB]	-6.536	+2.506	+5.838
ΔOASPL [dB$_A$]	-6.169	+2.218	+2.180

Table 5.5: Differences in noise levels between the modified designs and Baseline propeller at point B ($z_f = 0.5$c, $\Theta = 16.875$ deg).

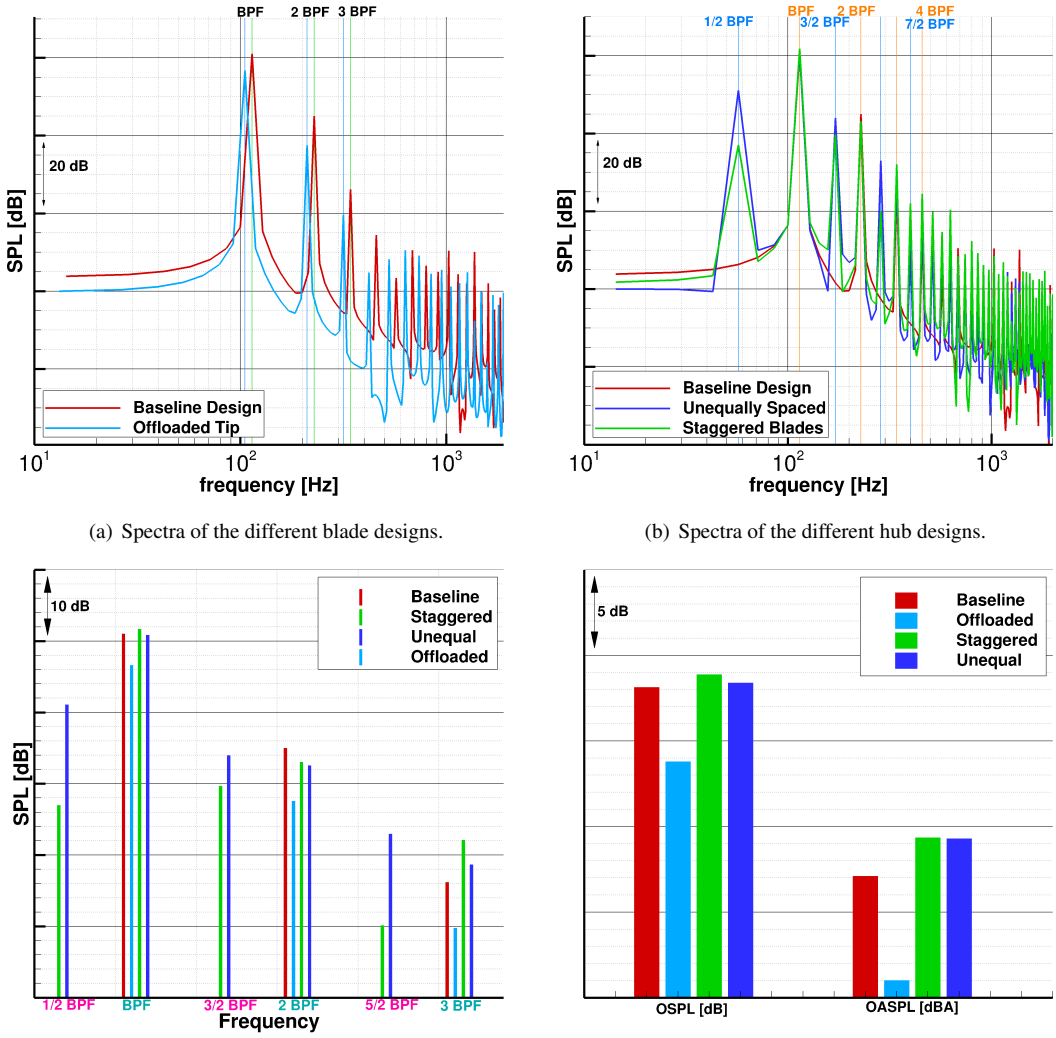

(a) Spectra of the different blade designs.

(b) Spectra of the different hub designs.

(c) SPL levels for the lower harmonics.

(d) OSPL and OASPL values.

Figure 5.10: SPL at the point B of the idealised fuselage ($z_f = 0.5$c, $\Theta = 16.875$ deg) for the different IMPACTA propeller designs. The Offloaded Tip exhibits harmonics at lower frequencies and an important sound levels reduction, at least up to the fourth harmonic. Spectra of Staggered and Unequally-spaced hubs have additional tones at BPFs/2, and result overall slightly noisier than the Baseline.

and the Unequally-Spaced hubs can be noted: the first has a SPL slightly higher than the second at BPFs tones, but significantly lower at BPFs/2 tones, thus resulting in almost the same values of OASPL.

Looking at the noise spectra at different locations on the fictitious fuselage, a sound directivity analysis was carried out. In particular, Figures 5.11 and 5.12 show the behavior of the first three BPF tones along the fuselage axis z_f and along the fuselage circumference (i.e. varying the fuselage azimuth Θ), respectively. In general, it is shown that, moving longitudinally, the BPF fundamental has an almost symmetric behavior with respect to the fuselage station where the maximum OSPL is registered.

Therefore, at the same distance from the propeller plane, the SPL of the BPF fundamental is slightly noisier ahead of the propeller than aft. Regarding the second tone, a symmetric behavior with respect to the propeller rotational plane is noted until about 7 chord lengths away. The third tone shows a less clear trend, with a relative peak around the propeller rotational plane. Finally, Figure 5.11 shows that the trends of the various tones are similar at different azimuthal positions. Moving along the fuselage azimuth (Figure 5.12), the maximum noise level at BPF and at 2 BPF is around 16-17 degrees, which is the point of minimum distance from the propeller tip, while at 3 BPF

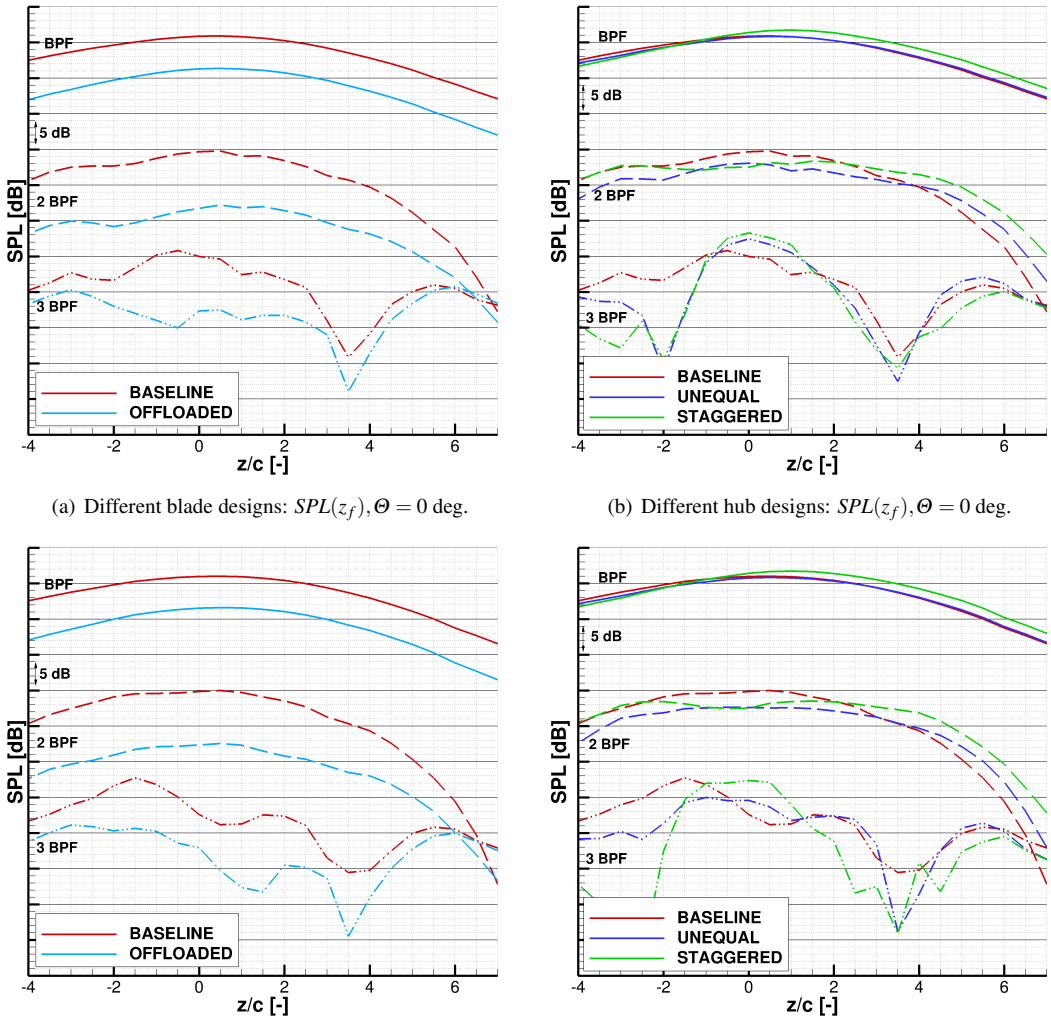

(a) Different blade designs: $SPL(z_f), \Theta = 0$ deg.

(b) Different hub designs: $SPL(z_f), \Theta = 0$ deg.

(c) Different blade designs: $SPL(z_f), \Theta = 16.875$ deg.

(d) Different hub designs: $SPL(z_f), \Theta = 16.875$ deg.

Figure 5.11: Trends of the SPL first three tones moving along the fuselage axis for the different IMPACTA propeller designs. See Figure 5.6 for the locations considered. Sound levels are maximum slightly ahead of the propeller rotational plane. The Offloaded Tip blade appears beneficial at all positions on the fuselage, for all three tones. The Staggered hub yields louder noise in front of the propeller, while small reductions are seen behind. The Unequally-spaced hub is almost identical to the Baseline at the BPF, and quieter at higher harmonics.

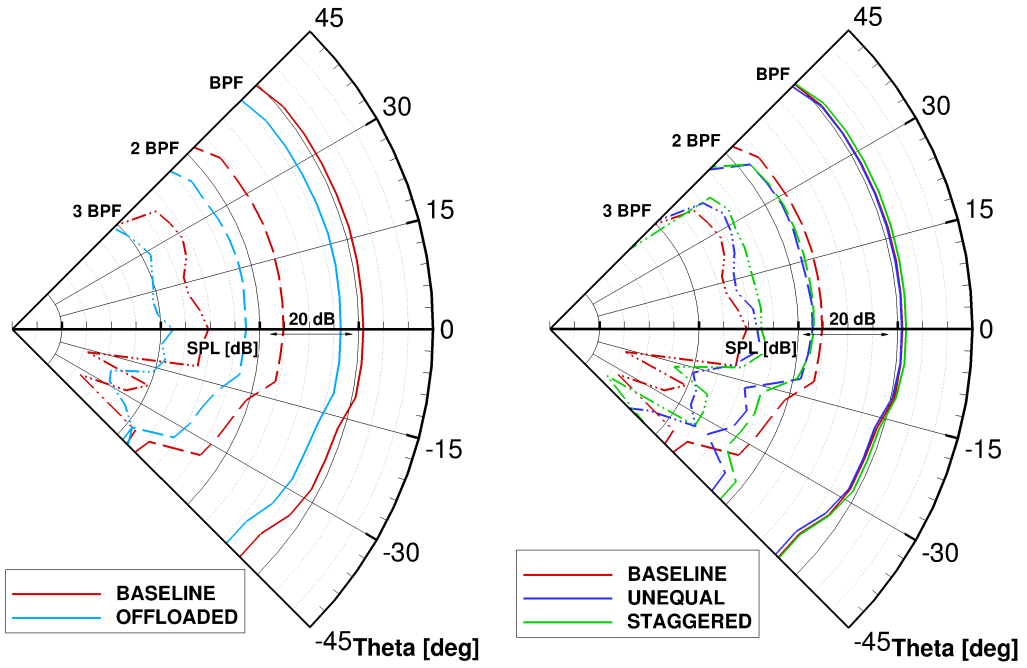

(a) Different blade designs: $SPL(\Theta), z_f = 0.5$c.

(b) Different hub designs: $SPL(\Theta), z_f = 0.5$c.

Figure 5.12: Trends of the SPL first three tones moving along the fuselage azimuth for the different IMPACTA propeller designs. See Figure 5.6 for the locations considered. Sound levels are maximum at approximately 16 deg, point of minimum distance from the tip. The Offloaded Tip is significantly quieter at all positions. The modified hub configurations show similar levels to the Baseline at the BPF, whereas they are quieter at 2BPF and louder at 3BPF.

the maximum is at higher Θ values. It is noted that, due to the hypothesis of steady and periodic flow, and the absence of the airframe in the simulation, points at the same radial distance from the propeller tip will show the same SPL. This is expected not to be the case in an installed configuration.

Regarding the modified propeller designs, it is observed from Figures 5.11 and 5.12 that:

(a) The Offloaded Tip blade shows lower noise levels at all positions on the fuselage. This blade produces the same trend as the Baseline, moving along the fuselage axis, at BPF, but has a flatter trend at 2 BPF.

(b) Compared to the Baseline, the BPF tone of the Staggered hub design has a slightly higher SPL in front of the propeller plane and lower SPL behind it. The 2 BPF tone is quieter in the vicinity of the propeller plane and louder after 3 chord lengths.

(c) The Unequally-Spaced hub BPF tone is almost identical to that of the Baseline, while for the 2 BPF tone small differences are seen and a similar trend to the Staggered hub is observed.

5.4.2 Cabin Noise Estimate

The noise inside the cabin for a passenger located slightly ahead of the propeller plane, on the second seat away from the window (see Figure 3.2(a)), is evaluated via experimentally-obtained transfer functions [246]. Section 3.2 shows the details of the TF that was contributed to the IMPACTA project by NLR.

Some of the pressure amplitude maps (i.e. $|\hat{p}'(\mathbf{x},f)|$) on the external fuselage surface, and the corresponding maps inside the cabin after the TF application, are presented in Figures from 5.13 to 5.15 for the Baseline, the Staggered and the Unequally-Spaced designs. Results are here non dimensionalised using the corresponding $\max|\hat{p}'(\mathbf{x},\text{BPF})|_{\text{Baseline}}$ values. The magnitude of the pressure amplitude inside the

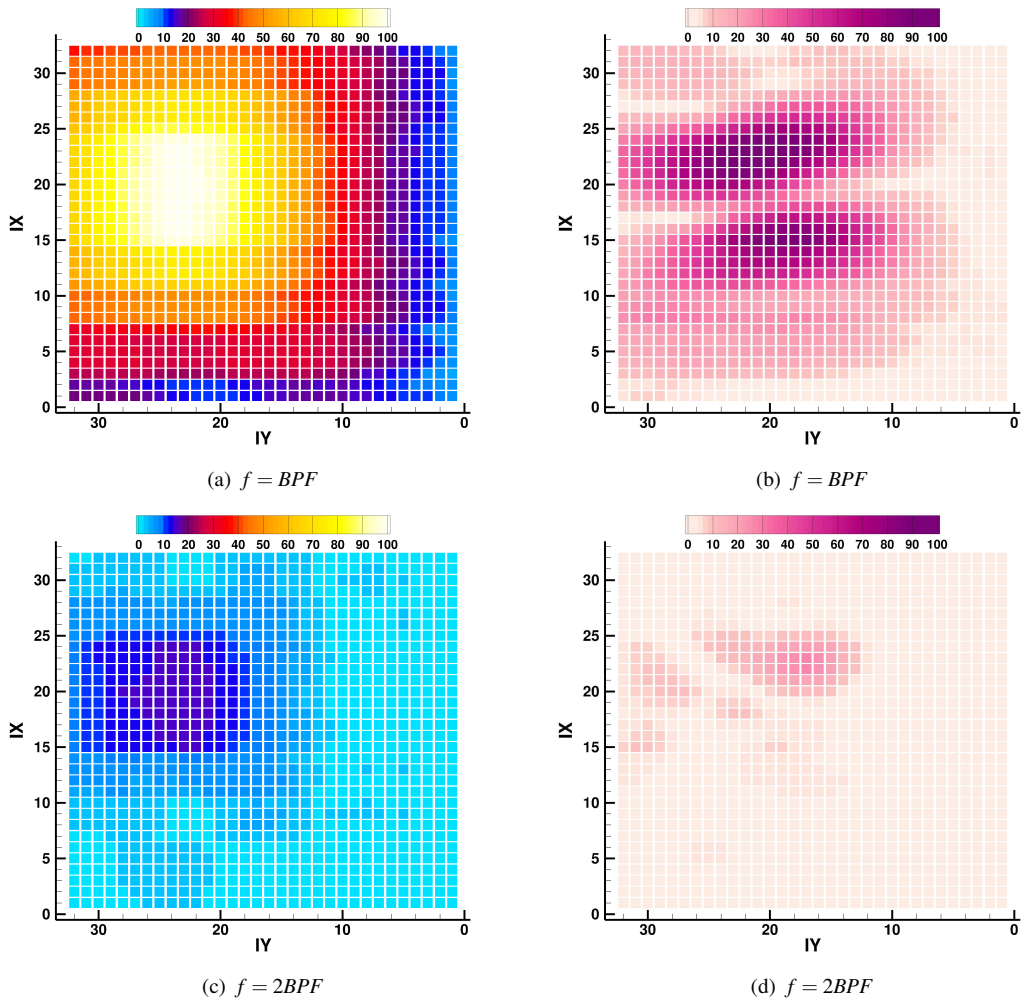

(a) $f = BPF$ (b) $f = BPF$

(c) $f = 2BPF$ (d) $f = 2BPF$

Figure 5.13: Non-dimensional pressure fluctuations amplitude maps before (left) and after (right) the TF application: **Baseline** IMPACTA propeller design. Please refer to Figure 5.6 for the definition of the azimuthal and the longitudinal TF points indices IX and IY. A different color-scale have been used for outside and inside scenarios because of the large difference in levels. The pressure surface distribution is considerably modified by the non-uniform characteristics of the fuselage filtering.

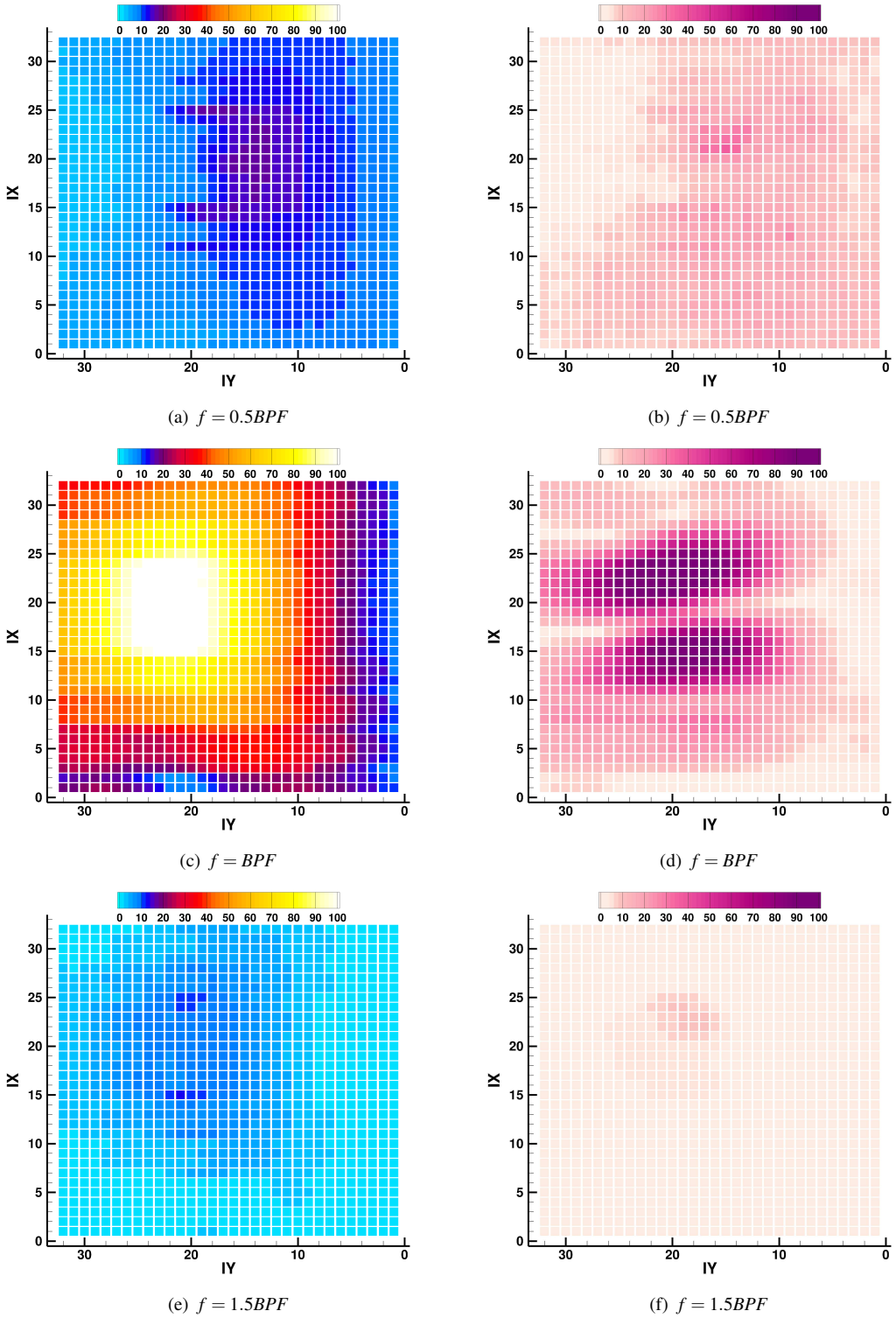

(a) $f = 0.5BPF$ (b) $f = 0.5BPF$

(c) $f = BPF$ (d) $f = BPF$

(e) $f = 1.5BPF$ (f) $f = 1.5BPF$

Figure 5.14: Non-dimensional pressure fluctuations amplitude maps before (left) and after (right) the TF application: **Staggered** hub IMPACTA design. Please refer to Figure 5.6 for the definition of the azimuthal and the longitudinal TF points indices IX and IY. A different color-scale have been used for outside and inside scenarios because of the large difference in levels. The great majority of the acoustic energy is at the BPF. The Staggered configuration remains slightly noisier inside the cabin.

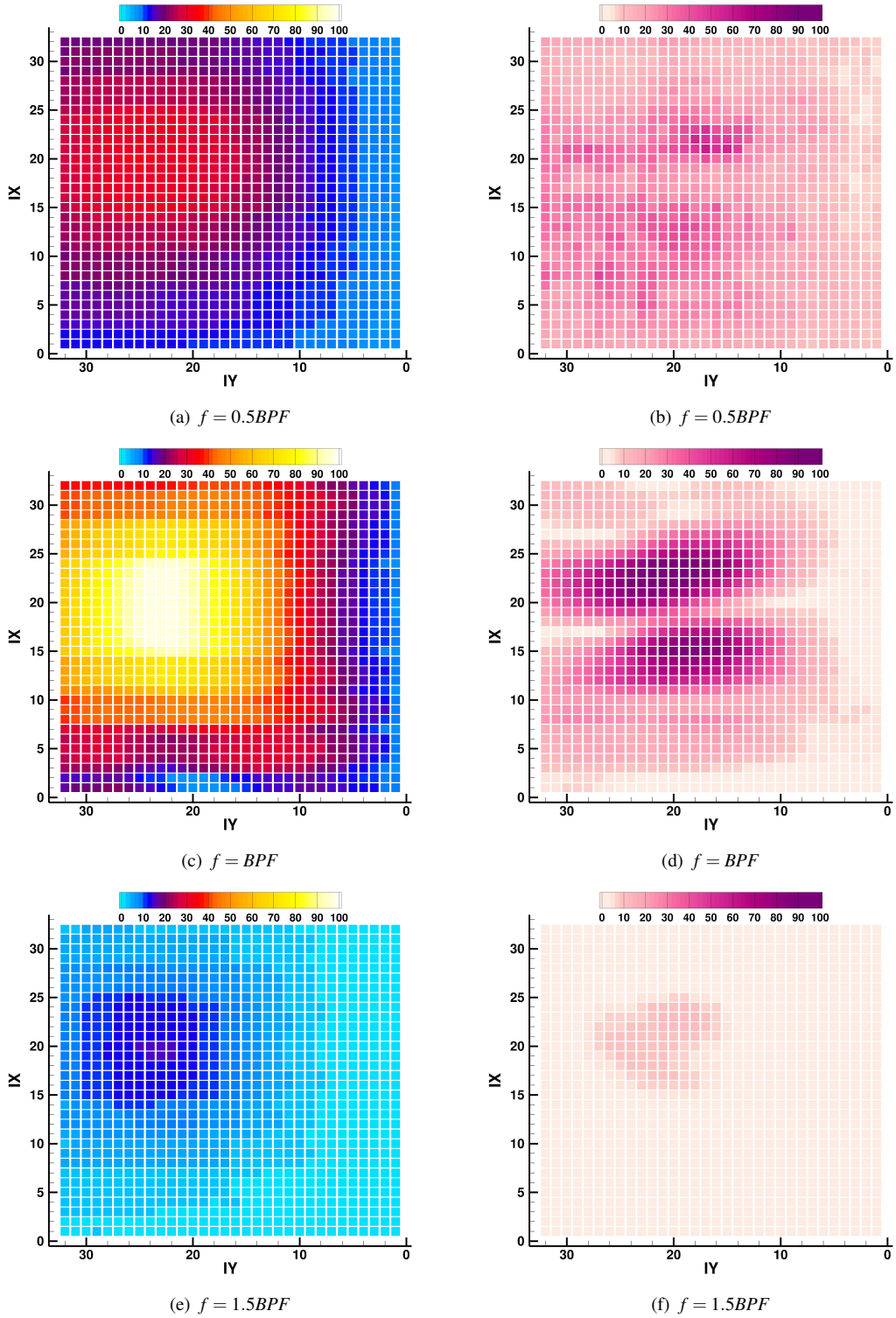

(a) $f = 0.5BPF$ (b) $f = 0.5BPF$

(c) $f = BPF$ (d) $f = BPF$

(e) $f = 1.5BPF$ (f) $f = 1.5BPF$

Figure 5.15: Non-dimensional pressure fluctuations amplitude maps before (left) and after (right) the TF application: **Unequally-Spaced** hub IMPACTA design. Please refer to Figure 5.6 for the definition of the azimuthal and the longitudinal TF points indices IX and IY. A different color-scale have been used for outside and inside scenarios because of the large difference in levels. The energy content at BPFs/2, in both levels and distribution, appears quite different between Staggered and Unequally-spaced hub designs.

cabin is considerably lower than outside, and the distribution differs significantly because of the non uniform transmission characteristics of the fuselage structure. The energy content of the BPF tone dominates, the 2 BPF tone having less than 30% of the energy of the BPF tone, and the 3 BPF tone having a maximum of 10%. Because of the initial energy content distribution and the high TL levels, the contribution of higher BPFs harmonics inside the cabin becomes negligible. Regarding the additional BPFs/2 harmonics of the modified designs, only the content at $f = 0.5$ BPF, and to a lesser extent the one at $f = 1.5$ BPF, seem to be significant in the transmission through the aircraft fuselage. It is interesting to observe the different pressure distributions predicted from the Staggered hub design with respect to the Baseline and the Unequally-Spaced. The acoustic footprint of the two distinct rows of blades is clearly visible on the fuselage in Figure 5.14.

The resulting pressure signal for the example passenger is compared, as an example, with that at point A on the exterior of the fuselage in Figure 5.16. Note that the shift in phase of the three signals is only due to the different azimuthal positions of the blades in the grid. In the same figure, the spectral content of the two signals is also reported.

Finally, Figure 5.17 shows the sound pressure level inside the cabin and the corresponding A-weighted value. As can be seen, the reduction of the unsteady pressure fluctuation amplitudes is significant inside the cabin, and the BPF tone dominates. The differences between the modified hubs and the Baseline are considerably reduced, but still visible.

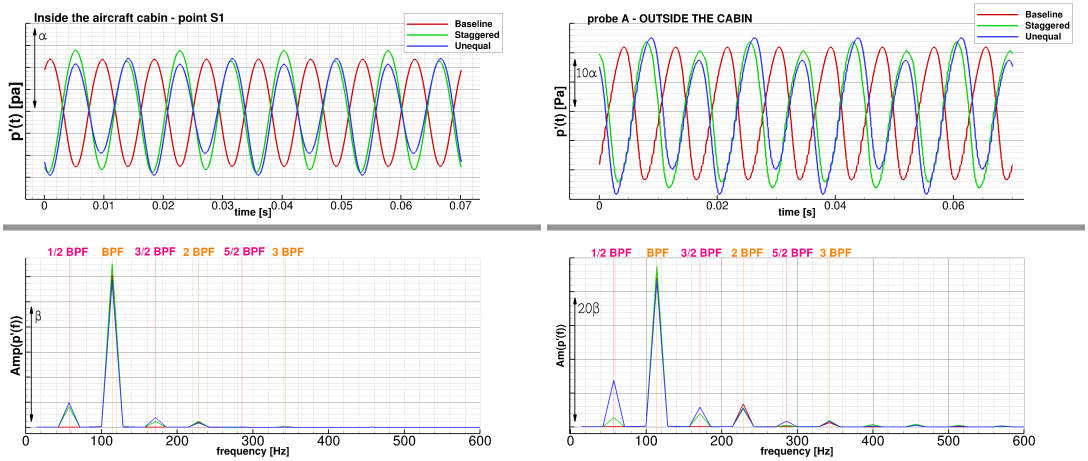

(a) Signal inside the cabin at the point S1.

(b) Signal at the point ($z_f = 0c$, $\Theta = 0$ deg) on the idealised fuselage (outside).

Figure 5.16: Unsteady pressure signal inside and outside the cabin: comparison between Baseline and modified hub designs of the IMPACTA propeller. The amplitude of the pressure fluctuations is importantly reduced during the transmission through the fuselage.

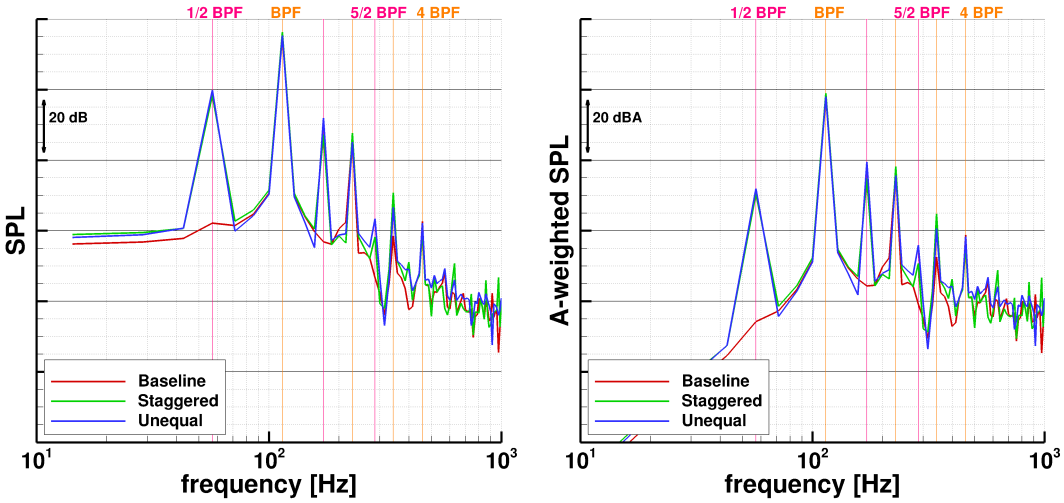

(a) SPL.

(b) A-weighted SPL.

Figure 5.17: Sound pressure level inside the aircraft cabin for the example passenger (point S1). Differences amongst the various propeller designs are considerably reduced inside the cabin, but still present.

5.5. Conclusive Remarks

Thanks to the combination of lower angular speed and inboard-moved loading, the Offloaded Tip blade is shown to be significantly quieter than the Baseline blade, appearing the best design solution among those analysed.

The modified hub configurations exhibit a greater number of spectral peaks, spreading the acoustic energy over more frequencies, and yield slightly higher noise levels, compared to the Baseline hub. Because of the fuselage transmission characteristics, their sound inside the cabin does not greatly differ from that produced by the Baseline. Therefore, experimental tests should be performed to evaluate if the perception advantages of a more continuous spectrum justify the extra manufacturing and structural complexities due to their specific blades arrangement. In a positive case, the Staggered design should probably be preferred over the Unequally Spaced, since it could benefit from an optimisation of the operating RPM considering its higher thrust.

Chapter 6

CFD Method Quantification

This Chapter investigates the numerical approach, analysing the impact on sound predictions of grid properties on one hand, and of the CFD method on the other. The effects of regularity and density of the computational mesh are first examined. The use of a 4^{th} order structured MUSCL scheme is then evaluated. Finally, two different turbulence models of the hybrid RANS-LES family, the SAS and the DES, are assessed. The objective is to seek the most suitable technique to study the propeller near-field acoustics.
The study is based on an isolated propeller in axial flight conditions, so that geometric and flow periodicity allow for the simulation of a single blade only. This is done to reduce the computational cost. The IMPACTA Baseline and the Offloaded-Tip blades are used in this analysis. The operating conditions of these two blades differ only in the angular velocity, the latter running at lower RPM (see Table 5.1 for geometries and flow conditions).

6.1. CFD Mesh Investigation

To study how mesh regularity and density affect the accuracy of the numerical acoustic estimates, the results obtained in Chapter 5 with a matched grid of approximately 11 M cells were compared against predictions of different chimera grids with a regular background grid of increasing spatial resolutions.

6.1.1 Description of Cases

Computational grids built and employed for this study are the following:

G0 Matched grid with non-regular cells due to the block topology for the blade. Section 5.2.1 shows the mesh details.

G1 Chimera grid with a uniform cells distribution in the axial direction, and a non-uniform in the azimuthal direction, in the background. The blade wake region is refined as shown in Figure 6.1(a).

G2 Chimera grid with the same size as G1, but uniform cell distribution in the background, in both axial and azimuthal directions.

G2a Refined version of grid G2 with intermediate mesh density, obtained by inserting a refined cylindrical grid in wake area, as an additional chimera level. The layout of G2a, and its dimensions, are presented in Figure 6.1(b).

G2b Refined version of grid G2 with fine mesh density, generated by increasing the spatial resolution of the refined cylindrical grid.

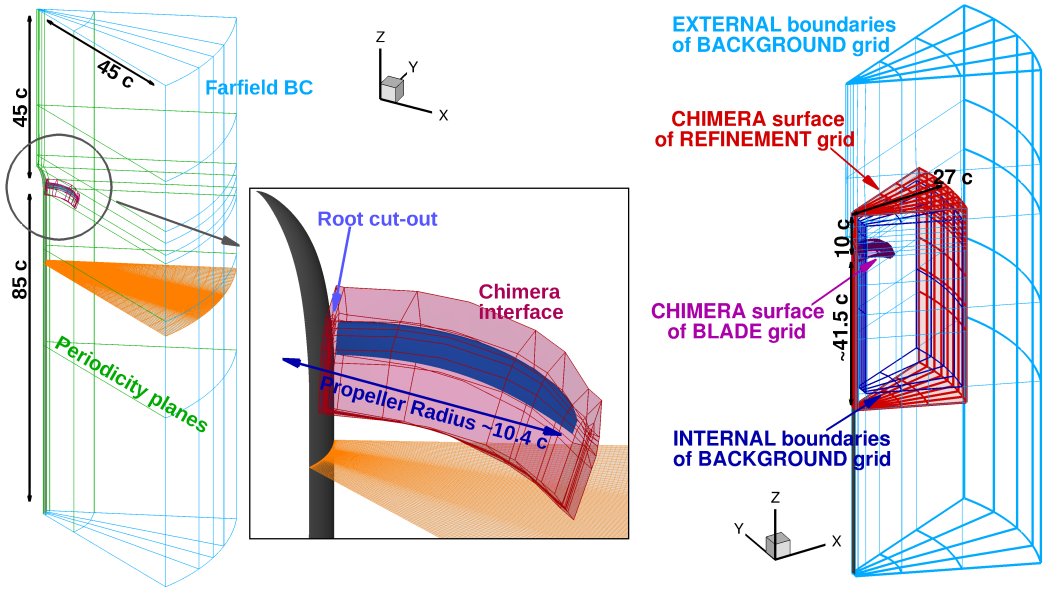

(a) Grid G1.

(b) Grid G2a.

Figure 6.1: Mesh properties analysis: computational domain layouts visualisation.

Grid	Mesh Size (N° of cells)	Min N° of points per wavelength for BPF	
		Baseline blade	Offloaded-Tip blade
G0	11.2 M	26	28
G1	10.3 M	26	28
G2	10.3 M	37	40
G2a	18.0 M	65	70
G2b	41.6 M	129	140

Table 6.1: Mesh Properties analysis: dimensions of the computational grids.

All chimera grids were assembled using the same foreground grid, so that there are no differences in the noise sources between the different cases. The foreground mesh was

generated using a "C-H" block topology around the blade, same way as the matched grid G0. The mesh density on, and around, the blade is also kept similar to that of grid G0. The only difference was in the point distribution in the boundary layer: as opposed to an exponential law, an hyperbolic law with an expansion ration varying from 1.11 to 1.15 was used. The chimera interface, as shown in Figure 6.1(a), is located at a distance equal to 1 root chord from the blade lateral and tip surfaces, and 2 root chords from the blade trailing edge. Note that, because of HMB3 limitations in localising the chimera boundary, the blade root was cut at 25% of the radius R (the spinner radius is 20% R) and the chimera surface lies in the gap between the blade and the spinner. The latter is always included in the background grid. The cylindrical refinement mesh of G2a and G2b grids extends, in fact, from the spinner-blade gap up to approximately 2.5 R in the radial direction (see Figure 6.1(b)), with the inboard chimera surface situated just before that of the blade grid. To reduce the allocated memory for these larger meshes, a hole in the background grid was created by removing the blocks overlapped by the refinement grid, since these cells would be non-computational. Sizes, and densities, of the different grids are reported in Table 6.1.
Table 6.2 summarises the cases computed. All simulations were carried out solving RANS equations, with the $k-\omega$ SST turbulence model.

Test ID	IMPACTA Blade	Grid
B0	Baseline	G0
B1	Baseline	G1
B2	Baseline	G2
B2a	Baseline	G2a
O0	Offloaded-Tip	G0
O1	Offloaded-Tip	G1
O2a	Offloaded-Tip	G2a
O2b	Offloaded-Tip	G2b

Table 6.2: Mesh Properties analysis: computational test cases.

6.1.2 Aerodynamic Results Presentation

Figure 6.2 shows the wake for the Baseline and Offloaded-Tip blades, comparing CFD results of the different grids. As can be seen, the presence of the blade root cut-out in the chimera grids generates a strong blade root vortex. This may affect the blade loads, and the propeller performance. To quantify its effect, Table 6.3 reports the comparison against the matched grid predictions. The bigger discrepancy for the Offloaded-Tip blade case may be due to the higher load at the inboard stations for this geometry with respect to the Baseline design. It is also noted that the iso-value of the Q

criterion used in the visualisations of the blade vortical structures is the same for both blades. For this reason, it appears that the wake of the Offloaded-Tip blade, which

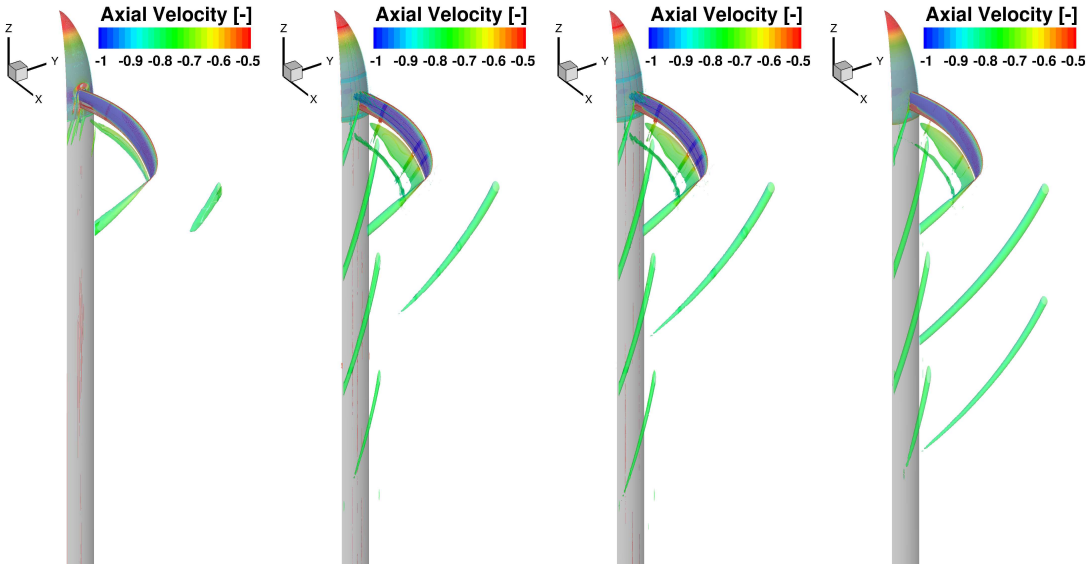

(a) B0. (b) B1. (c) B2. (d) B2a.

Figure 6.2: Mesh properties analysis: wake visualisation via iso-surfaces of Q criterion (non-dimensional value of 0.05) colored by non-dimensional axial velocity. *(Part 1/2) - IMPACTA Baseline blade.*

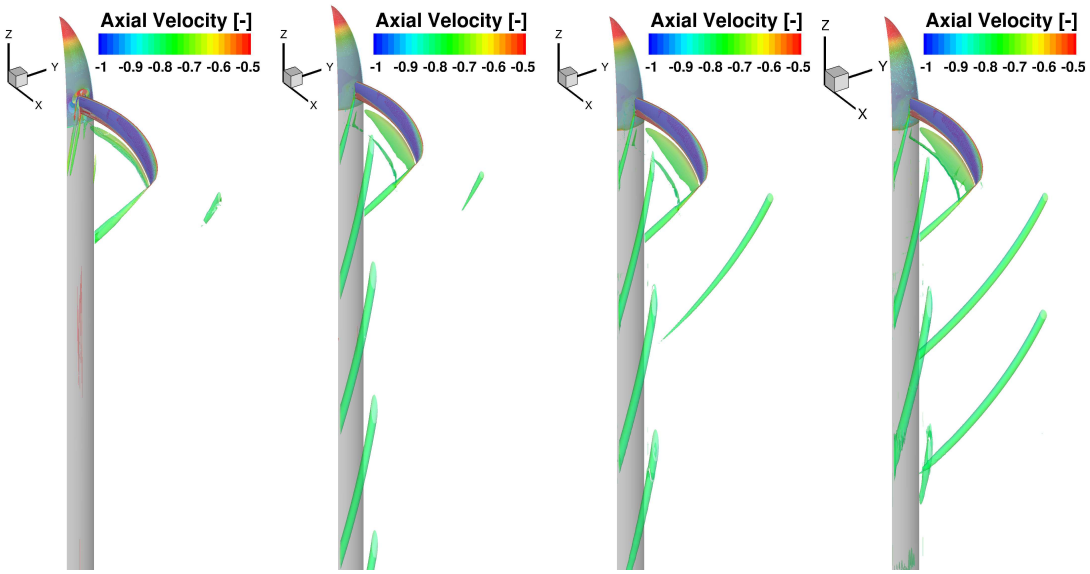

(e) O0. (f) O1. (g) O2a. (h) O2b.

Figure 6.2: Mesh properties analysis: wake visualisation via iso-surfaces of Q criterion (non-dimensional value of 0.05) colored by non-dimensional axial velocity. *(Part 2/2) - IMPACTA Offloaded-Tip blade.* Only small differences are seen between predictions of matched and chimera grids (the root vortex being generated by the root cut-out in the latter). Increasing the spatial resolution allows to preserve the propeller wake for longer distances in its down-stream propagation.

Test ID	ΔC_T	ΔC_P
B1	-1.3%	-0.28%
O1	-2.72%	-1.65%

Table 6.3: Blade cut-out effect on loads predictions: comparison against matched grid cases B0 and O0.

operates at slower RPM, is preserved for a shorter distance down-stream, compared to the Baseline.

6.1.3 Acoustic Results Presentation

Figure 6.3 presents, as an example, the SPL spectra at two points on the idealised fuselage (see Section 5.4.1 for definition) for the Baseline design.

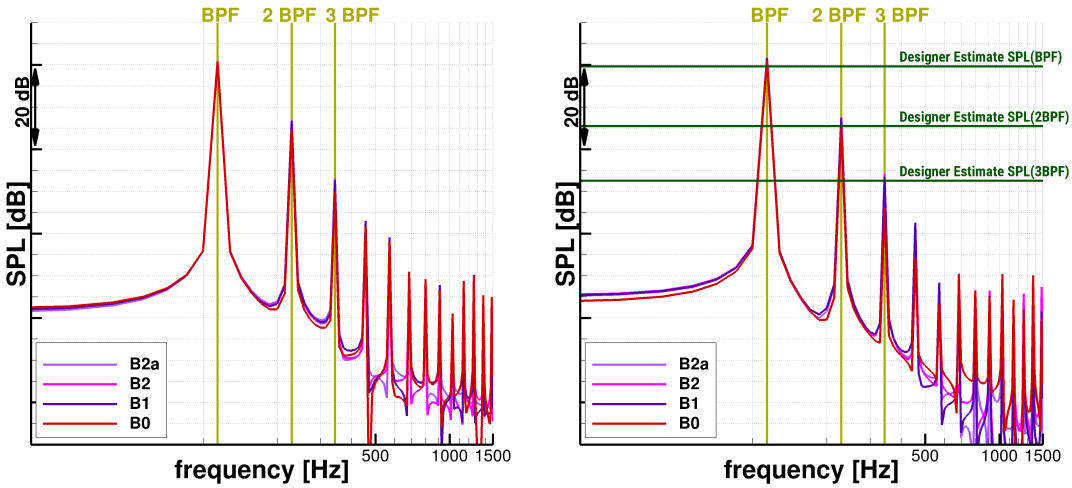

(a) Probe A.

(b) Probe B.

Figure 6.3: Mesh properties analysis: SPL spectra for the Baseline IMPACTA blade at two locations on the idealised fuselage near the propeller plane. See Figure 5.6 for the specific probe location. At these positions, differences in the predictions between the various grids are small for the second tone and significant for third and fourth tone. The main parameter affecting the predictions appears the regularity of the mesh.

Figure 6.4 shows the directivity analysis of the lower harmonics, up to the 4^{th}, on the idealised fuselage for the Baseline and the Offloaded-Tip blades. It is noted that, being the simulated flow conditions ideal, a smooth and regular trend of the SPL is expected.

6.1.4 Regularity of the Mesh Discussion

To study the effect of the regularity of the computational mesh on the numerical predictions, test cases B0, B1 and B2, for the Baseline, and O0 and O1, for the Offloaded-Tip blades, are compared.

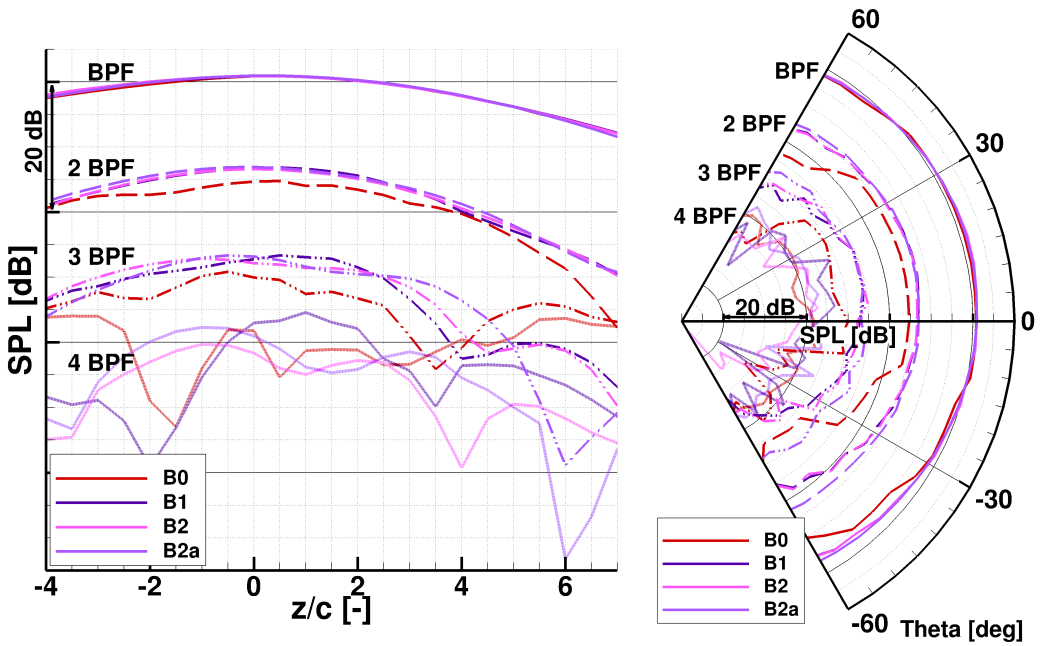

(a) $SPL(z_f), \Theta = 0$ deg. (b) $SPL(\Theta), z_f = 0$ c.

Figure 6.4: Mesh properties analysis: SPL trends on the idealised fuselage (see Figure 5.6). First four harmonics represented. *(Part 1/2) - IMPACTA Baseline blade.*

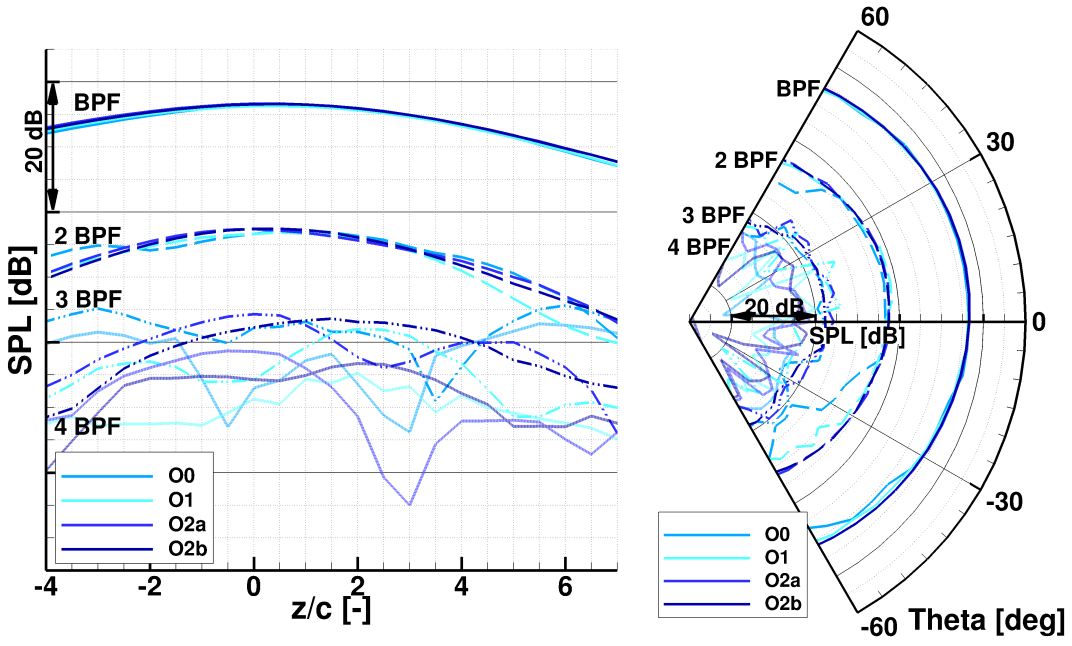

(c) $SPL(z_f), \Theta = 0$ deg. (d) $SPL(\Theta), z_f = 0$ c.

Figure 6.4: Mesh properties analysis: SPL trends on the idealised fuselage (see Figure 5.6). First four harmonics represented. *(Part 2/2) - IMPACTA Offloaded-Tip blade.* Both density and regularity of the mesh are shown to be important for accurate sound levels and directivities predictions, their importance increasing as the harmonic order and the distance increase. The resolution of grids G0/G1 appears adequate only for estimates at the BPF, whereas the density of G2a and G2b are needed for 2BPF and 3BPF, respectively.

Regarding the wake predictions (Figure 6.2), no major differences are noted, especially between azimuthally uniform and non-uniform grids. A slightly smaller tip vortex diameter is observed in the results of the chimera regular grids with respect to the distorted matched grids.
Regarding acoustics (Figures 6.3 and 6.4), appreciable differences are seen between the predictions of the matched and the chimera grids, from the 2^{nd} tone up. These differences increase with increasing harmonic order, since the higher the frequency, the lower the pressure perturbation amplitude, and therefore the bigger the effect of the numerical dissipation. The regular cell distribution in the background of the chimera meshes, compared to the distorted cells of the matched grid, allows for higher accuracy of the computational scheme, and less dissipation of the sound waves. This is visible in the estimated SPL values and the directivity trends. Differences between azimuthally uniform and non-uniform grids (tests B1 and B2) are minimal for the first and second tones, and become notable from the third tone. This is however mainly due to the different number of points per wavelength in the azimuthal direction.
The mesh regularity is therefore seen to be important for good sound level predictions, especially for the higher propeller harmonics and for larger distances from the propeller plane. The advantage of the reduced numerical dissipation of the regular grids appears bigger than the penalty introduced with the chimera interpolation.

6.1.5 Mesh Density Discussion

To study the impact of the mesh density on the numerical predictions, test cases B2 and B2a, for the Baseline, and O1, O2a and O2b, for the Offloaded-Tip blades, are compared.
Notable differences are observed in the propeller wake resolution (Figure 6.2), with almost one blade passage more, captured on grid G2a with respect to grid G2, and an additional one on grid G2b compared to grid G2a.
Analysing the SPL spectra at various points on the idealised fuselage (Figures 6.3 and 6.4), it can be seen that:

1. Almost no difference is visible in the BPF tone estimates of the different grids, indicating that the coarser grid yet has a sufficient spatial resolution.

2. Small differences are observed for the 2BPF tone, only at the largest distances from the blade tip, between the predictions of grids G2a and G2b, almost equivalent to each other, against grids G1/G2. So, for a first estimate of the sound level up to the 2^{nd} harmonic, the density of G2a is enough.

3. Grids G1 and G2 appear not sufficient for the 3BPF, away from the propeller axis. Grid G2a shows as well axial and azimuthal trends more irregular than the expected. Grid G2b seems more adequate for the evaluation of the 3^{rd} tone.

4. Even the finer grid, G2b, did not show smooth values for the 4BPF, particularly in the estimate of the SPL azimuthal trend on the fuselage.

Overall, a larger effect of the numerical errors (dissipation and dispersion) is seen as the propagation distance increases. The required minimum number of points per wavelength is observed to get bigger as the harmonic order increases, because of the larger impact of the numerical dissipation on perturbations of lower amplitude.

6.2. Computational Scheme Analysis: MUSCL4 vs MUSCL

To verify if the spatial 4^{th} oder accurate MUSCL4 scheme [211] is beneficial for propeller noise estimates, some of the previous tests were repeated with it. Its description and implementation in HMB3 are reported in Section 2.2.4. The use of a higher-order computational scheme may reduce the required mesh density, thanks to its smaller dissipation and dispersion errors. It can therefore be advantageous if the cost reduction, due to the smaller grid size, is bigger than the CPU penalty introduced by the computation of the additional higher-order terms.

6.2.1 Numerical Setup

Table 6.4 summarises the performed simulations.

Test ID	Grid	IMPACTA Blade	MUSCL corresponding Test
B1M4	G1	Baseline	B1
O1M4	G1	Offloaded-Tip	O1
O2aM4	G2a	Offloaded-Tip	O2a
O2bM4	G2b	Offloaded-Tip	O2b

Table 6.4: Computational scheme analysis: test cases simulated using the MUSCL4 scheme.

It is noted that MUSCL4 was active only on the background grid, whereas MUSCL was used in the foreground grid. This was done since no significant differences were expected in the solutions of the two schemes in that area, because of the intrinsically required blade mesh density and of the small distance from the sound source.
All computations were carried out starting from unperturbed free-stream conditions, as done for the MUSCL simulations, and the same CFL number was employed. A similar number of steps was needed to achieve convergence. Results are thus compared after the same number of steps, for more consistency.

6.2.2 Aerodynamic Predictions Comparison

Figure 6.5 compares the propeller vortical structures resolved by the MUSCL and MUSCL4 schemes, on the three different grid employed. Iso-surfaces of Q criterion, as well as contours of vorticity magnitude, are presented.
MUSCL4 shows longer-preserved blade tip, and root, vortices, with dissimilarities against MUSCL that are bigger on the coarser grid and decrease as the mesh density increases. This is because the finer the spatial discretisation, the smaller the numerical dissipation, and therefore the smaller the differences in accuracy between the predictions of the two schemes. Compared to MUSCL, MUSCL4 resolves 2 blade passages more on grid G1, and approximately 1.5 more on grid G2a, yielding on the second a similar solution to that obtained on grid G2b. Almost no difference is observed between MUSCL and MUSCL4 results on grid G2b. The vortex cores predicted by MUSCL4 also show a smaller diameter, and higher values of vorticity, compared to MUSCL results, because of the lower dispersion of the scheme.
Although the MUSCL4 scheme is active only on the background grid, the blade loads are expected to differ from MUSCL results, because of the improvements in the wake resolution and induced flow. As an example, Table 6.5 thus presents a comparison of the propeller performance for the test cases carried out on grid G1, where the bigger difference in the wake predictions between the two schemes is observed. Estimates of thrust and power agree within less than 1%, showing that the MUSCL scheme is enough for evaluating the propeller performance.

Test ID	ΔC_T	ΔC_P
B1M4	+0.49%	+0.59%
O1M4	+0.51%	+0.63%

Table 6.5: MUSCL4 loads predictions evaluation: comparison against MUSCL results.

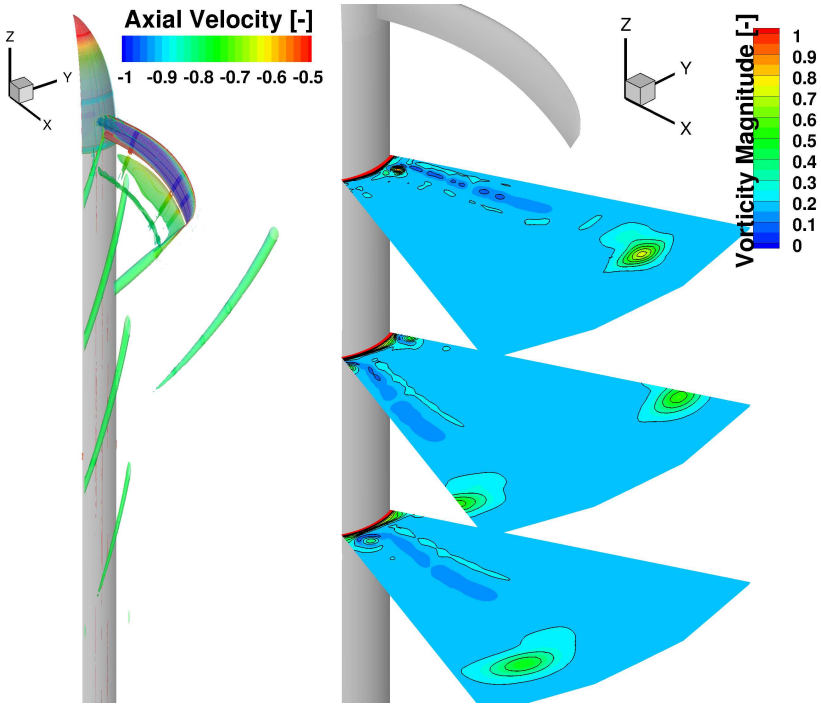

(a) B1. (b) B1.

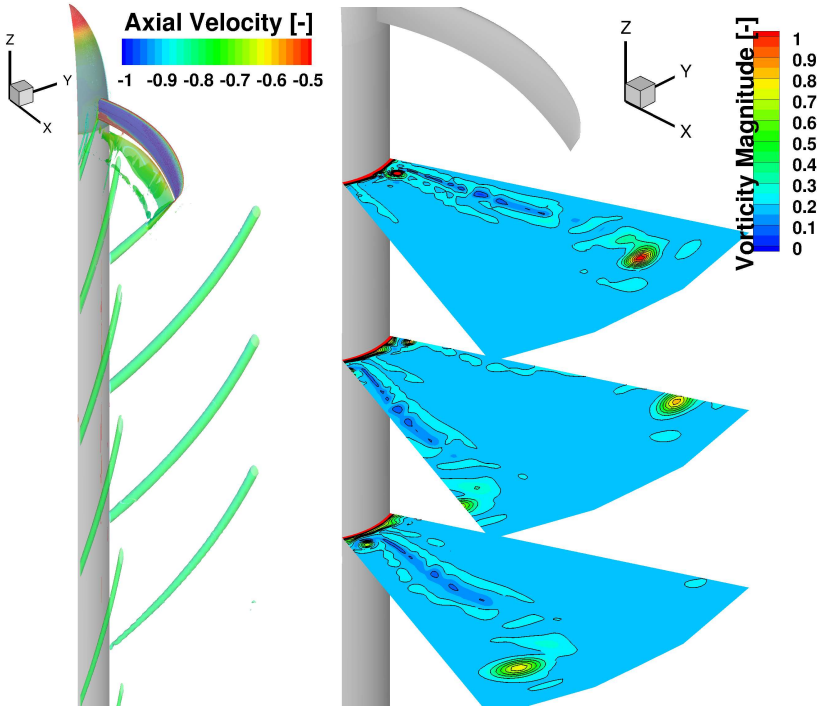

(c) B1M4. (d) B1M4.

Figure 6.5: Computational scheme analysis: propeller vortical structures visualisation. (a), (c) Iso-surfaces of Q criterion (non-dimensional value of 0.05) colored by non-dimensional axial velocity. (b), (d) Vorticity magnitude contours at $0.5R$, $1R$, and $1.5R$ down-stream the propeller rotational plane. *(Part 1/3) - Grid G1, IMPACTA Baseline blade.*

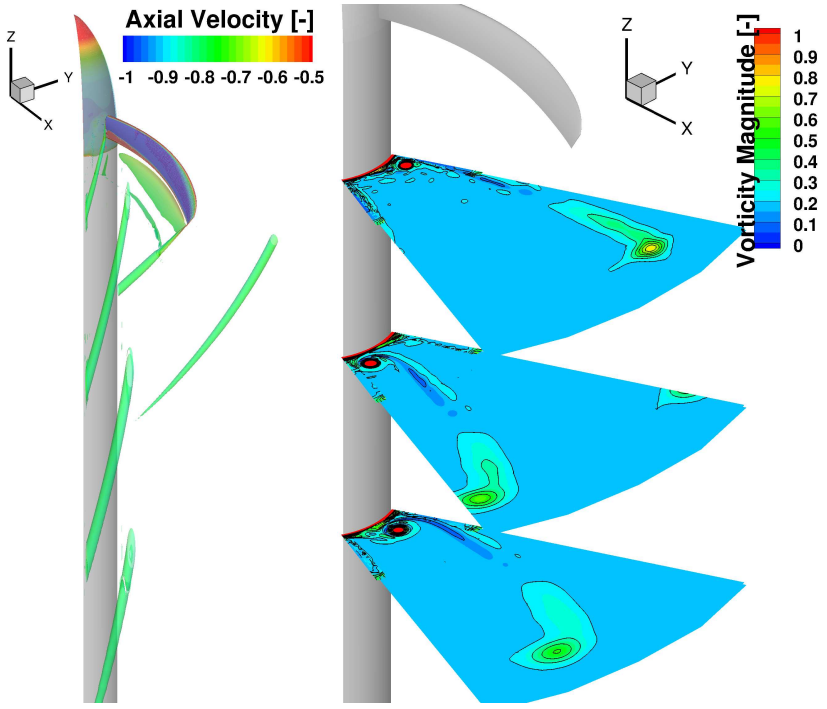

(c) O2a. (d) O2a.

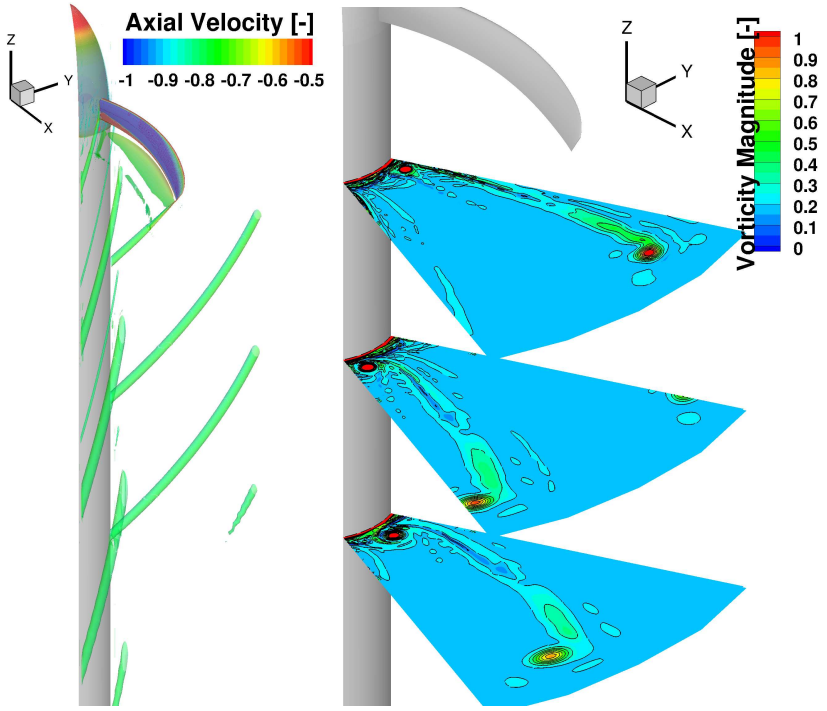

(e) O2aM4. (f) O2aM4.

Figure 6.5: Computational scheme analysis: propeller vortical structures visualisation. (a), (c) Iso-surfaces of Q criterion (non-dimensional value of 0.05) colored by non-dimensional axial velocity. (b), (d) Vorticity magnitude contours at $0.5R$, $1R$, and $1.5R$ down-stream the propeller rotational plane. *(Part 2/3) - Grid G2a, IMPACTA Offloaded-Tip blade.*

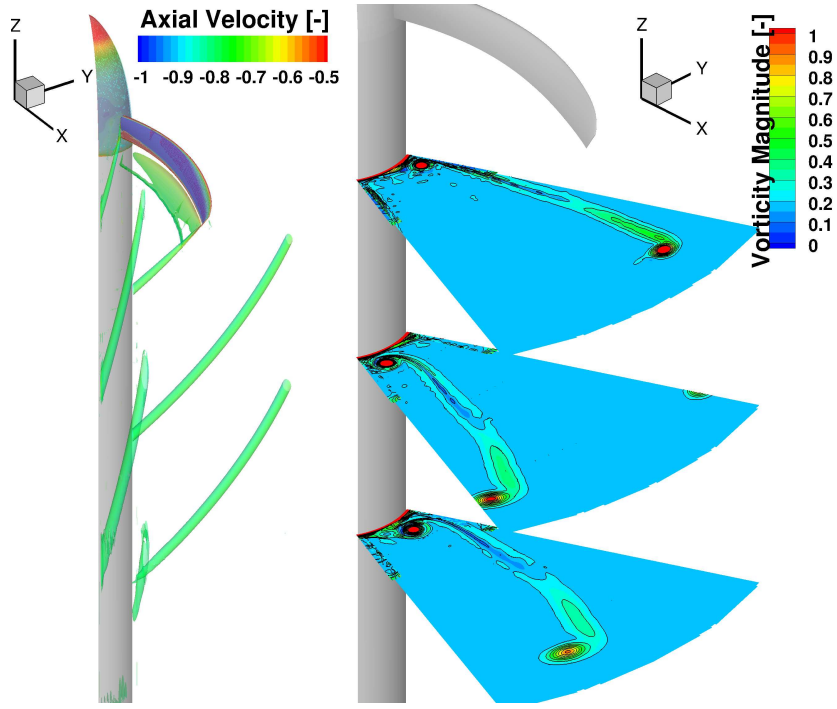

(e) O2b. (f) O2b.

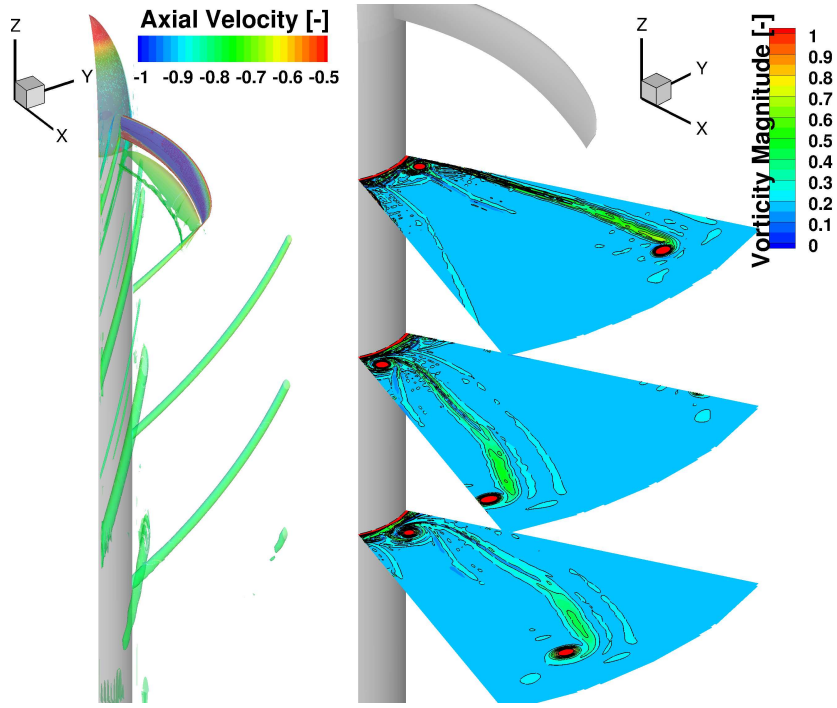

(g) O2bM4. (h) O2bM4.

Figure 6.5: Computational scheme analysis: propeller vortical structures visualisation. (a), (c) Iso-surfaces of Q criterion (non-dimensional value of 0.05) colored by non-dimensional axial velocity. (b), (d) Vorticity magnitude contours at $0.5R$, $1R$, and $1.5R$ down-stream the propeller rotational plane. *(Part 3/3) - Grid G2b, IMPACTA Offloaded-Tip blade.* MUSCL4 shows longer-preserved vortices, the differences with MUSCL decreasing as the mesh density increases because of the smaller effect of the numerical dissipation. It also predicts a smaller vortex core diameter, and higher values of vorticity, because of the lower numerical dispersion.

6.2.3 Acoustic Predictions Comparison

Figure 6.6 presents the SPL trends of the lower harmonics on the idealised fuselage (see Section 5.4.1 for definition) for the Baseline and Offloaded-Tip blades.

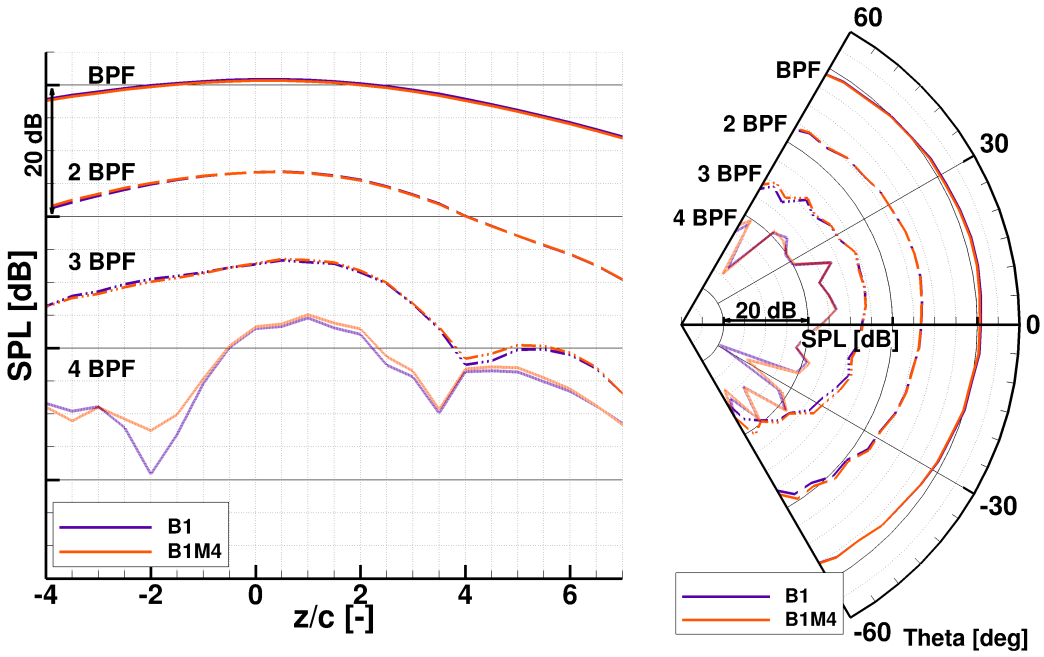

(a) Grid G1: $SPL(z_f), \Theta = 0$ deg.

(b) Grid G1: $SPL(\Theta), z_f = 0$ c.

Figure 6.6: Computational scheme analysis: SPL trends on the idealised fuselage (see Figure 5.6). First four harmonics represented. *(Part 1/2) - IMPACTA Baseline blade.*

On grid G1 the acoustic predictions of MUSCL and MUSCL4 schemes appear almost equivalent, even if the tip vortex resolution of the two solutions greatly differs (see Figure 6.5 as example). Small differences are seen only for the 3^{rd} and 4^{th} tones, especially for the Offloaded-Tip blade whose sound wave amplitudes are smaller. Larger differences, and from the 2^{nd} tone up, are instead seen in the SPL estimates obtained on the finer grids G2a and G2b. However, discrepancies between the predictions of the two schemes are only of fews dBs, and the maximum sound levels in the vicinity of the blade can be adequately determined by MUSCL up to the 3^{rd} harmonic. Therefore, to assess the acoustic footprint of the main propeller tones in its vicinity, even more in the case of a comparative study, the use of MUSCL4 was not beneficial, because of the higher computational cost without an increase in accuracy.

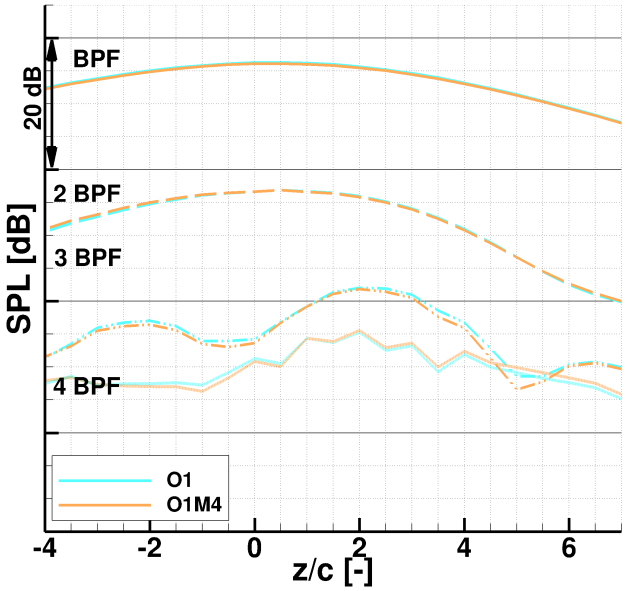

(c) Grid G1: $SPL(z_f), \Theta = 0$ deg.

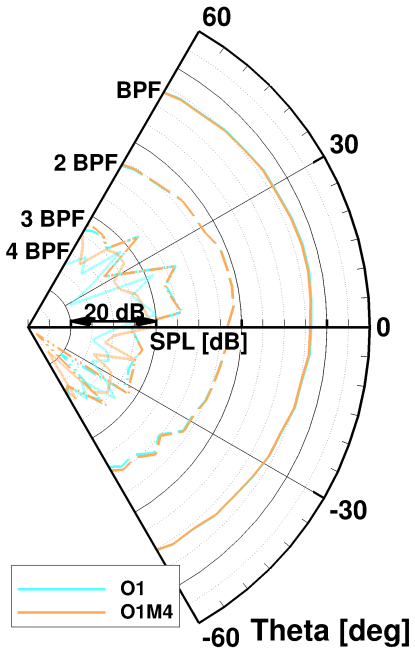

(d) Grid G1: $SPL(\Theta), z_f = 0$ c.

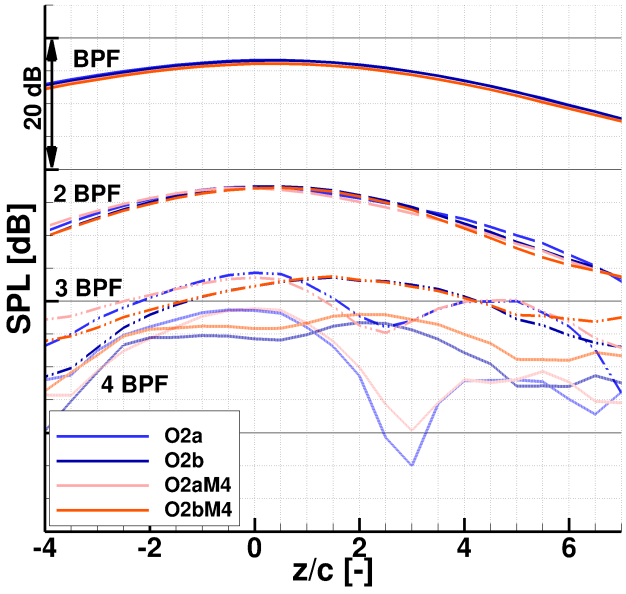

(e) Grids G2a and G2b: $SPL(z_f), \Theta = 0$ deg.

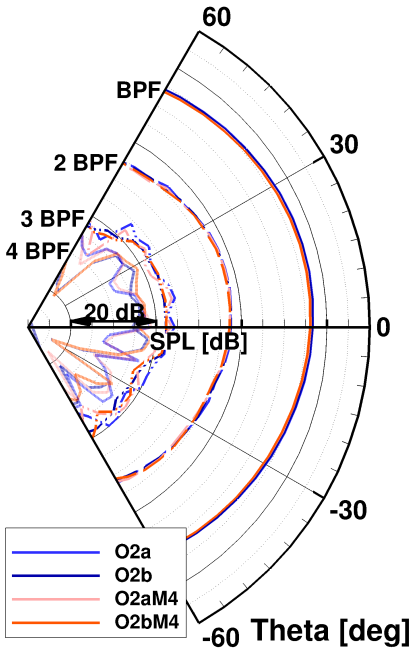

(f) Grids G2a and G2b: $SPL(\Theta), z_f = 0$ c.

Figure 6.6: Computational scheme analysis: SPL trends on the idealised fuselage (see Figure 5.6). First four harmonics represented. *(Part 2/2) - IMPACTA Offloaded-Tip blade.* On grid G1, MUSCL and MUSCL4 give almost identical results, with small differences for 3^{rd} and 4^{th} tones, especially for the Offloaded-Tip blade whose sound wave amplitudes are smaller. On grids G2a and G2b, differences between the two schemes are larger and appear from the 2^{nd} tone up. Overall, MUSCL is seen adequate to estimate the maximum sound levels in the blade vicinity up to the 3^{rd} tone.

To assess its effectiveness at larger distances, some analysis points have been arranged on a cylinder extending from $10c$ up-stream to $20c$ down-stream of the propeller plane, with a radial distance of $0.5R$ to $2R$ away from the blade tip. Figure 6.7 presents the

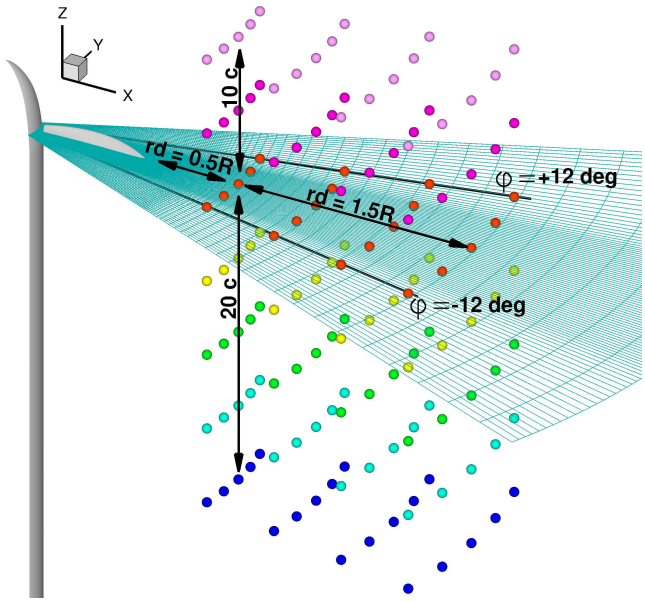

Figure 6.7: Analysis points for the assessment of MUSCL4 scheme further away than the idealised fuselage.

locations of the selected 140 points, and the local cylindrical system of reference (rd, φ, Z) adopted. This survey was carried out using grid G1. Figures 6.8 and 6.9 show the comparison of the SPL spectra for a sweep in the axial, radial and azimuthal directions among the analysis points. In general it is noted that:

1. at equal tone, the farther away we move from the blade, the bigger the differences between the estimates obtained with the two schemes;

2. the higher the harmonic order, the smaller the distance at which the differences appear.

MUSCL and MUSCL4 predictions agree well, up to the 3^{rd} tone, for distances smaller than $1R$ from the propeller plane in the axial direction, and up to $2R$ from the propeller axis in the radial direction. Differences are instead observed for larger distances, where the effect of the numerical dissipation of the scheme becomes significant. No significant differences between the estimates of the two schemes are seen by varying the azimuthal location, at fixed radial and axial coordinates. Yet, in the area analysed ($-12 \leq \varphi \leq +12$ deg) the grid density is uniform, and sufficiently fine, for reliable SPL predictions for the first three harmonics, even at radial distances of $1.5R$ from the blade tip.

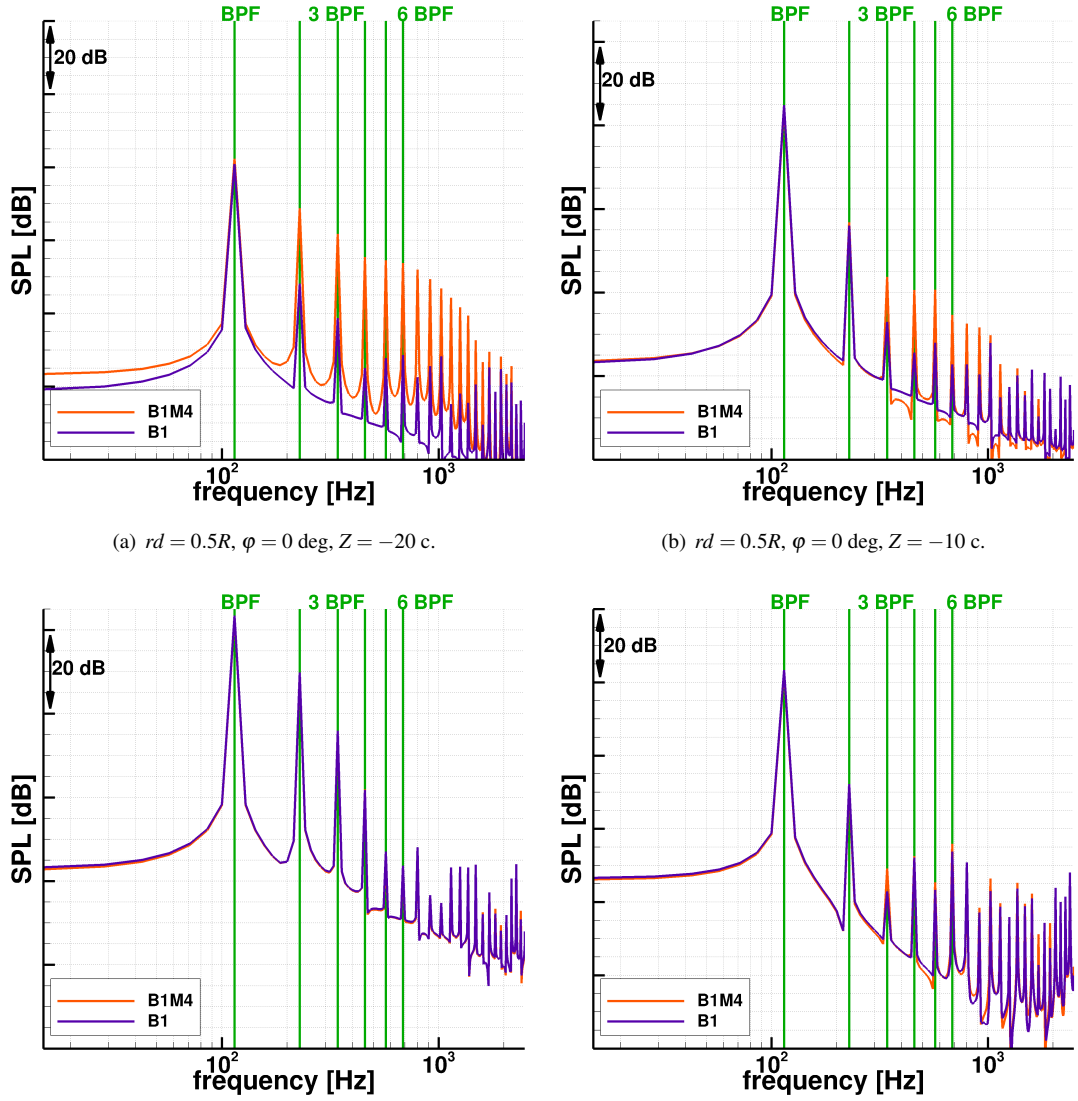

(a) $rd = 0.5R$, $\varphi = 0$ deg, $Z = -20$ c.

(b) $rd = 0.5R$, $\varphi = 0$ deg, $Z = -10$ c.

(c) $rd = 0.5R$, $\varphi = 0$ deg, $Z = 0$ c.

(d) $rd = 0.5R$, $\varphi = 0$ deg, $Z = +10$ c.

Figure 6.8: Computational scheme analysis: SPL spectra survey on axial sweep (tests B1 vs B1M4). Refer to Figure 6.7 for the analysis point locations. *(Part 1/2)*

6.2.4 Conclusive Remarks

Summarising, the MUSCL4 scheme applied to an isolated propeller in axial flight with a BPF of approximately 100 Hz showed, with respect to the original MUSCL scheme, the following:

(a) the ability of preserve the blade tip vortex for considerably longer distances downstream, and a better resolution of the vortex core, even on coarse/medium grids of 10-20 M cells;

(b) a small increase (within 1%) of the propeller thrust and power estimates, as a

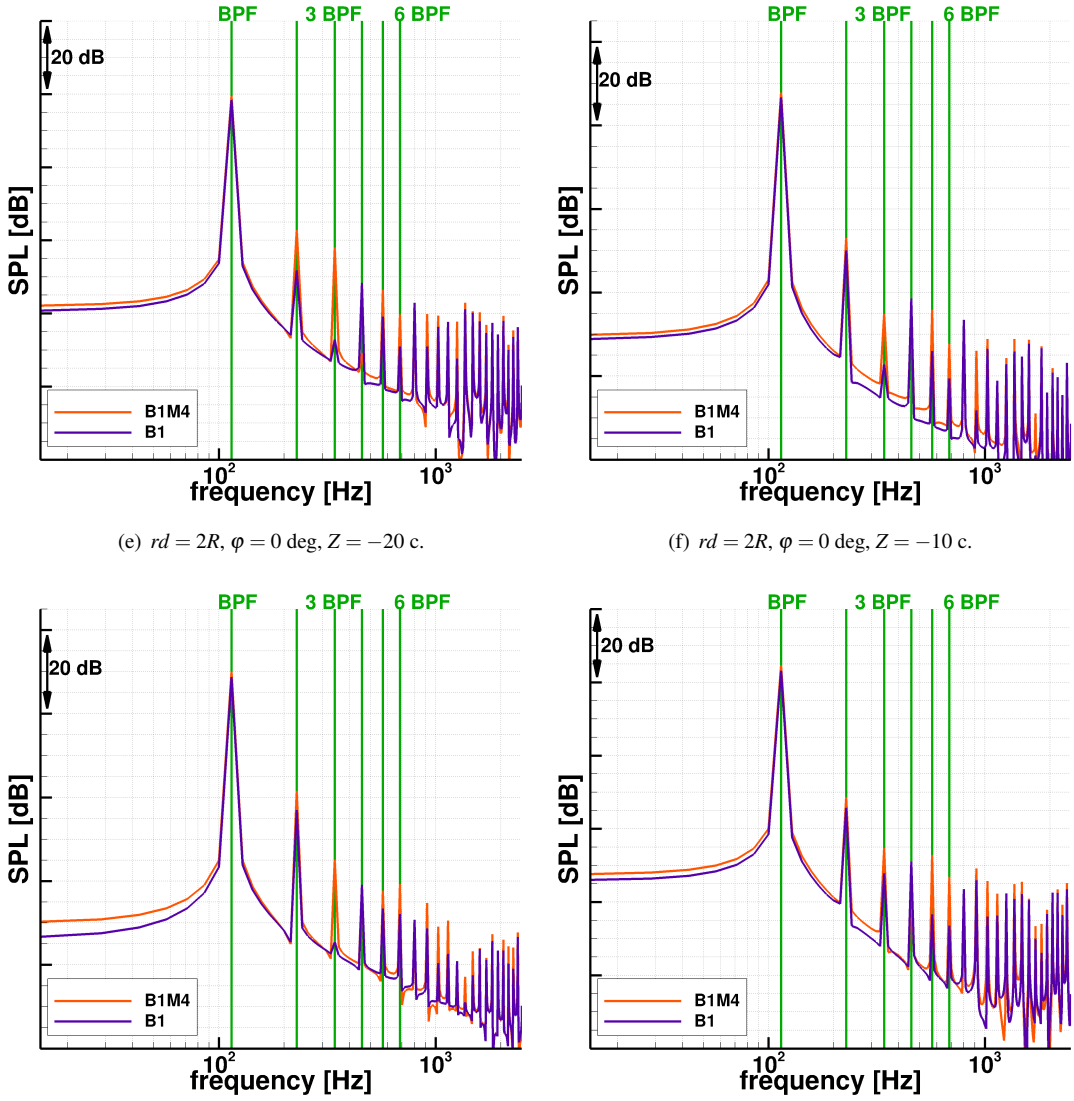

(e) $rd = 2R$, $\varphi = 0$ deg, $Z = -20$ c.

(f) $rd = 2R$, $\varphi = 0$ deg, $Z = -10$ c.

(g) $rd = 2R$, $\varphi = 0$ deg, $Z = 0$ c.

(h) $rd = 2R$, $\varphi = 0$ deg, $Z = +10$ c.

Figure 6.8: Computational scheme analysis: SPL spectra survey on axial sweep (tests B1 vs B1M4). Refer to Figure 6.7 for the analysis point locations. *(Part 2/2)* MUSCL and MUSCL4 predictions agree well, up to the 3^{rd} tone, for distances smaller than $1R$ from the propeller plane. At equal tone, the farther away from the blade, the bigger the differences between the two schemes. The higher the tone, the smaller the distance at which the differences appear.

consequence of the improved wake resolution;

(c) improvements in the sound predictions, thanks to the lower numerical dispersion and dissipation:

(c1) on coarse/medium grids, only for higher harmonics and large propagation distances;

(c2) on fine grids only, from the 4^{th} harmonic in the vicinity of the propeller blade.

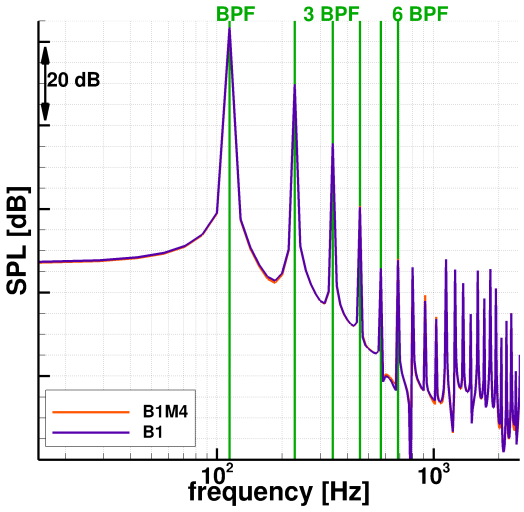

(a) $rd = 0.5R$, $\varphi = -12$ deg, $Z = 0$ c.

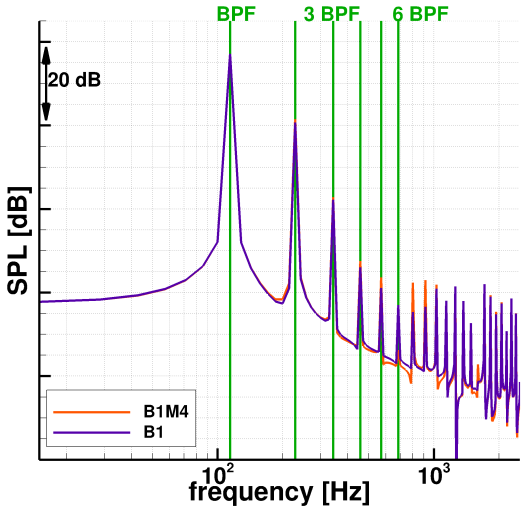

(b) $rd = 1.0R$, $\varphi = -12$ deg, $Z = 0$ c.

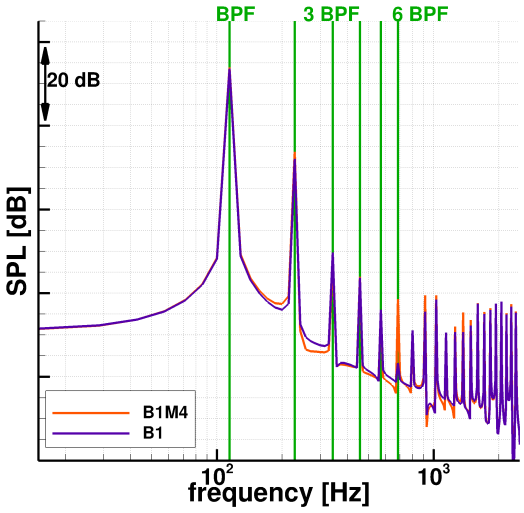

(c) $rd = 1.5R$, $\varphi = -12$ deg, $Z = 0$ c.

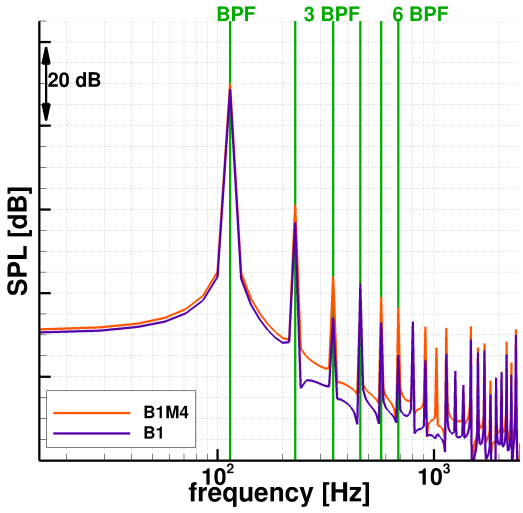

(d) $rd = 2.0R$, $\varphi = -12$ deg, $Z = 0$ c.

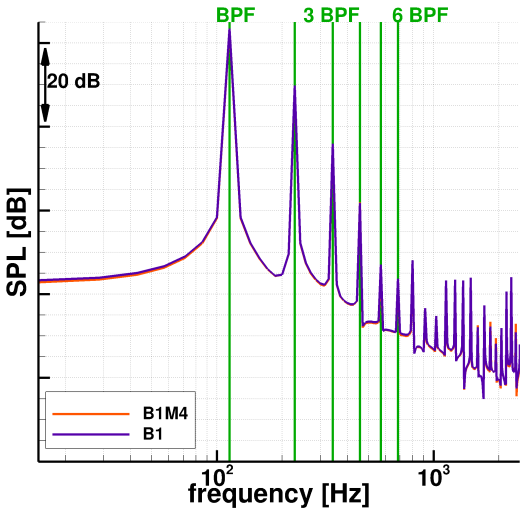

(e) $rd = 0.5R$, $\varphi = 0$ deg, $Z = 0$ c.

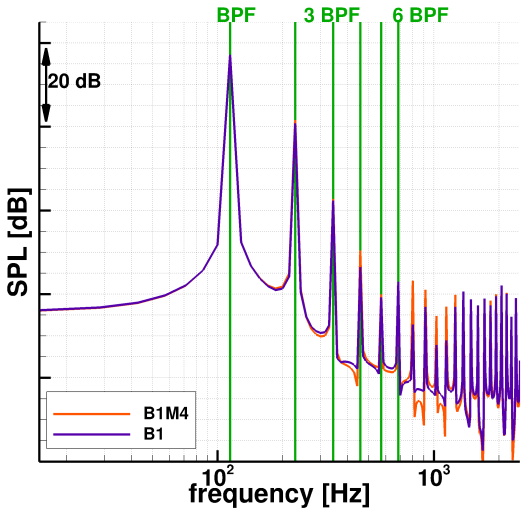

(f) $rd = 1.0R$, $\varphi = 0$ deg, $Z = 0$ c.

Figure 6.9: Computational scheme analysis: SPL spectra survey on radial, and azimuthal, sweep (tests B1 vs B1M4). Refer to Figure 6.7 for the analysis point locations. *(Part 1/2)*

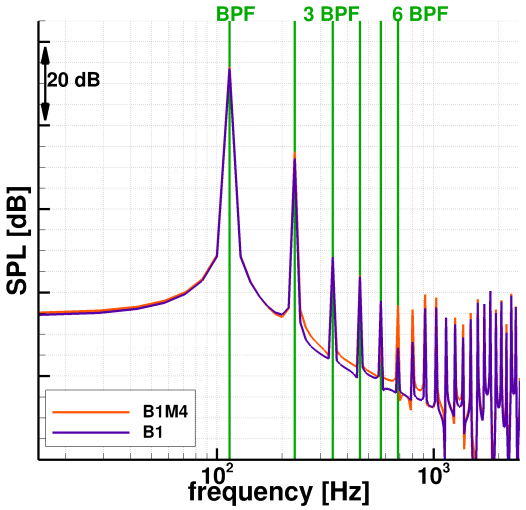

(g) $rd = 1.5R$, $\varphi = 0$ deg, $Z = 0$ c.

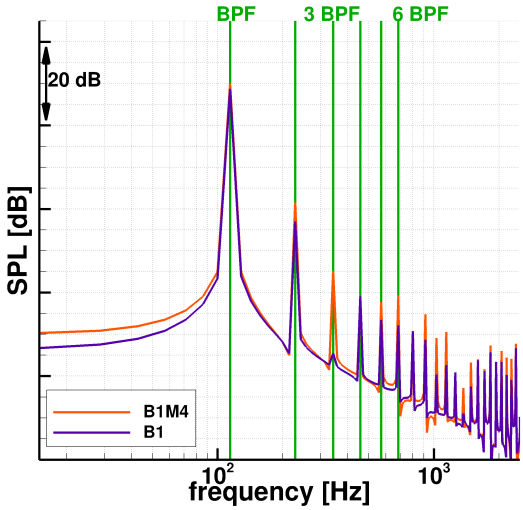

(h) $rd = 2.0R$, $\varphi = 0$ deg, $Z = 0$ c.

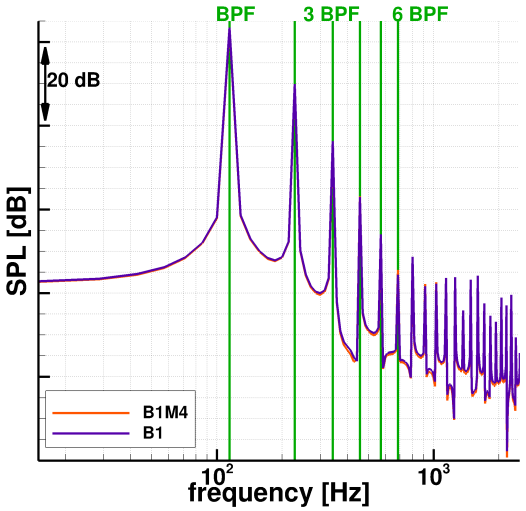

(i) $rd = 0.5R$, $\varphi = +12$ deg, $Z = 0$ c.

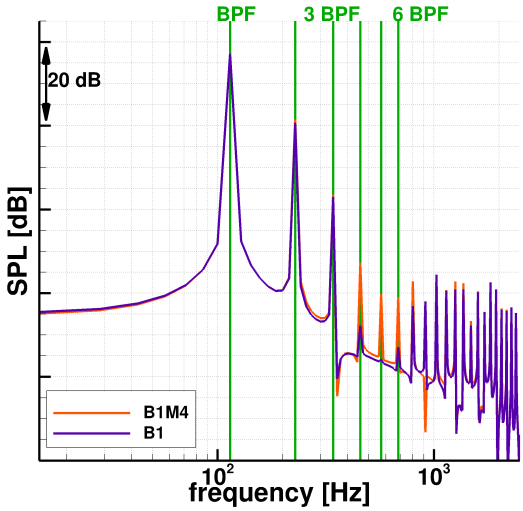

(j) $rd = 1.0R$, $\varphi = +12$ deg, $Z = 0$ c.

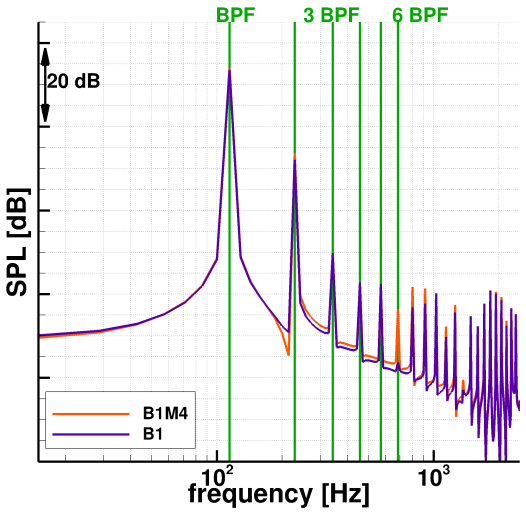

(k) $rd = 1.5R$, $\varphi = +12$ deg, $Z = 0$ c.

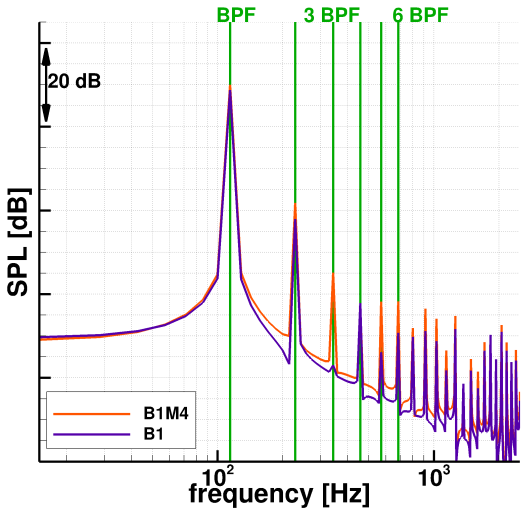

(l) $rd = 2.0R$, $\varphi = +12$ deg, $Z = 0$ c.

Figure 6.9: Computational scheme analysis: SPL spectra survey on radial, and azimuthal, sweep (tests B1 vs B1M4). Refer to Figure 6.7 for the analysis point locations. *(Part 2/2)* MUSCL and MUSCL4 predictions agree well up to $2R$ from the propeller axis, for all azimuthal positions tested (yet, the grid density is uniform and sufficiently fine for $-12 \leq \varphi \leq +12$ deg).

Therefore, for acoustic predictions in the vicinity of a modern propeller, as it is the case of interest in this research, the use of the MUSCL scheme is more adequate than MUSCL4, because of its lower computational cost.
It is noted that a central scheme, as opposed to an up-wind as MUSCL4, and schemes with an order higher than 4 (e.g. (W)ENO [263, 264] or DRP [265] schemes) may be computationally more advantageous than the 2^{nd} order MUSCL [57, 56].

6.3. Investigation of Different Turbulence Models

An accurate prediction of the propeller wake unsteadiness, and turbulence, is essential to capture noise broadband sources. URANS equations are effective in estimating the tonal noise content, but destroy the wake unsteady features, because of their high turbulent eddy viscosity, and rely on a complete statistic model of the turbulent scales. More advanced CFD techniques are therefore needed to resolve the propeller sound spectrum at high frequencies. Consequently, the objective is to assess two different methods of the hybrid LES-RANS family, the SAS [226] and the DES in its original formulation [239], for propeller acoustics. The first is a 2^{nd} generation URANS method, whereas the second is a hybrid model using an interfacing coupling strategy. Underlying principles, equations, and strengths of these two models are described in Section 2.3. As reference, they are compared against the results of an unsteady $k-\omega$ SST [215] simulation, since this is the RANS method on which both SAS and DES are founded.

6.3.1 NACA0012-Infinite Wing Preliminary Study

A preliminary study was carried out on an infinite wing to assess, and compare, the behavior of the different turbulence models considered.

Numerical Setup

A NACA 0012 airfoil is employed. The computational domain is extended for a quarter of the chord in the span-wise direction, and periodic boundary conditions are applied to the lateral planes. A standard "C" topology, extended up to the far-field, is adopted to generate the computational grid, as shown in Figure 6.10. The mesh counts 400 points around the airfoil, and 18 along the wing span. The maximum grid spacing in the wake region is of $0.015c$, where c is the airfoil chord, up to approximately $10c$ away from the trailing edge. Overall, the grid has approximately 7.2M cells. Flow conditions are presented in Table 6.6.

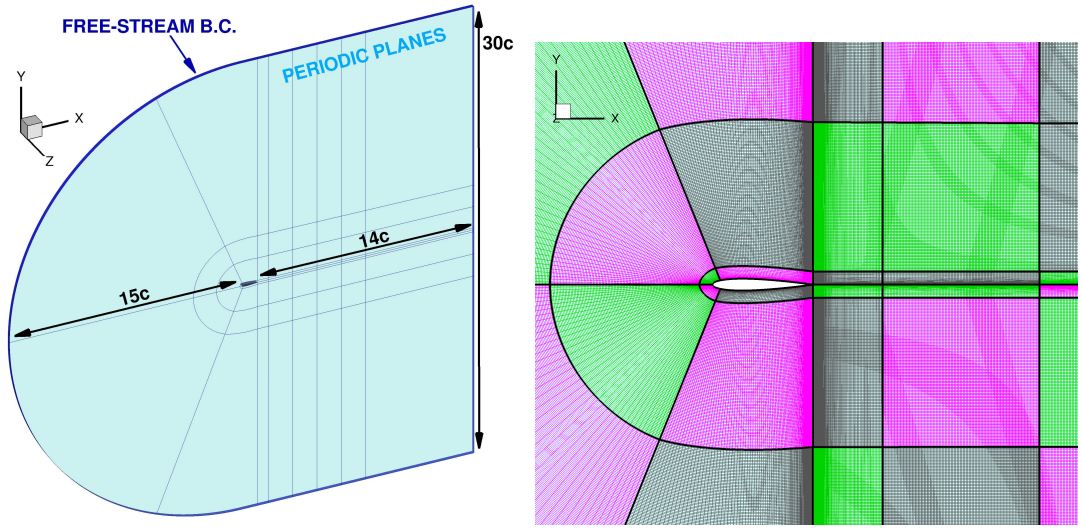

(a) Grid layout with dimensions. c is the airfoil chord. (b) Block topology and mesh visualisation around the airfoil.

Figure 6.10: NACA0012 infinite wing grid.

Unsteady simulations with the $k-\omega$ SST, the SAS, and the DES turbulence models were performed using 50 steps per flow particle passage over the wing chord.

Free-stream Mach M_∞	0.5
Free-stream Reynolds Re	1.0e6
Airfoil incidence	5 deg

Table 6.6: NACA0012 infinite wing flow conditions.

Models Behavior Assessment

Models Activation

Figure 6.11 shows where the SAS and DES models are switched on, i.e. where the first activates its scale adaptive capability, and where the second operates in its LES mode. The visualised trends are in agreement with the theoretical formulation of the two methods.

The additional source term of the SAS is seen active only in a narrow region near the wake axis. Only here the flow is unstable enough to trigger the eddy viscosity adaptation to the locally resolved flow turbulent structures. The magnitude of Q_{SAS} is large for the first chord down-stream the trailing edge, and then decays fast while increasing the distance.

The DES model behaves as LES on a more radially-extended area of the airfoil wake compared to the SAS, and for larger distances down-stream. The switch between

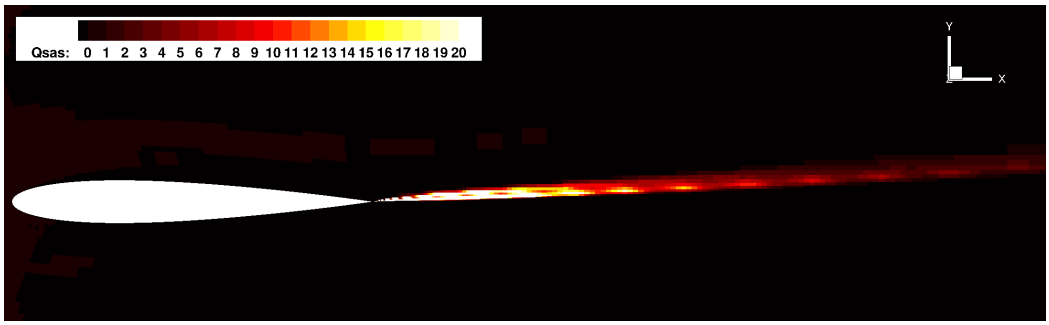

(a) SAS: additional source term for ω, Q_{SAS}, visualisation.

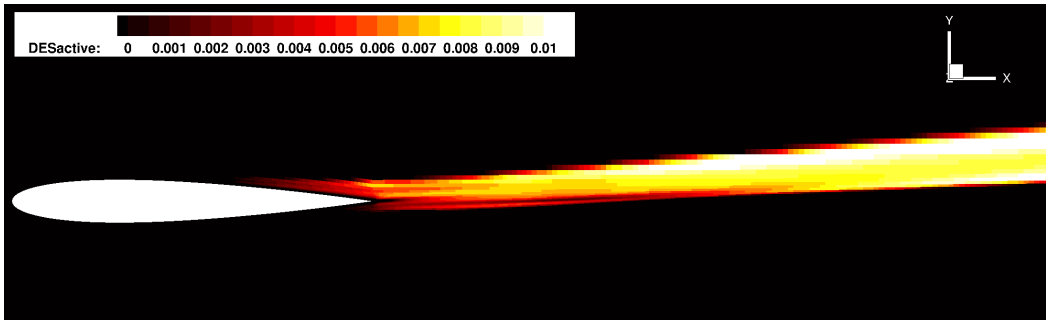

(b) DES: LES mode switch on visualisation.

Figure 6.11: SAS and DES model capability activation. Contours by cell average flood values. The scale-resolving mode of the two models is active only in the airfoil wake, for the DES method on a wider and longer region. The difference is due to the different definition of switching criterion.

the two DES modus operandi is dependent from the cell size, and not only from physical/numerical parameters of the flow. It is this fundamental difference in the switching-criterion choice that causes the important dissimilarities in the identification of the scale-resolving zones between the two models. It is noted that the LES mode in the DES appears also active on a small area above the boundary layer of the airfoil upper surface, near the trailing edge. This is connected to a small flow detachment generated because of the airfoil positive angle of attack.
In the other regions, the two models work as the original $k-\omega$ SST.

Eddy Viscosity

The effect of the two methods can be evaluated from the lowering of the turbulent eddy viscosity μ_T, that corresponds to a larger range of resolved turbulent length scales. Figure 6.12 presents a visualisation of the ratio between the turbulent and the laminar viscosity (*Ret*), for the three simulations. Compared to the SST, both advanced models shows smaller values of μ_T in the airfoil wake. The SAS has similar levels very close to the airfoil trailing edge, where, despite the high values of the additional ω source term Q_{SAS}, the overall energy balance does not greatly change. Its effectiveness then

increases as the distance down-stream increases: the *Ret* in the wake is reduced by approximately 25% at $0.5c$ from the trailing edge, and by 36% at $1c$, with respect to the SST. The DES shows a significant decrease in the turbulent eddy viscosity levels, even very close to the airfoil trailing edge. Around 75% and 82% reduction is seen in *Ret* values, compared to the SST, at $0.5c$ and $1c$ from the airfoil trailing edge, respectively. The observed important reduction of μ_T at large distances from the trailing edge is in agreement with the previous visualisations (Figure 6.11(b)), indicating the LES mode still active thanks to the small cells size.

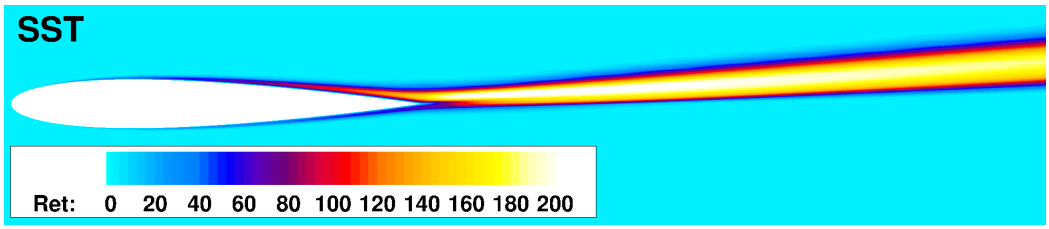

(a) SST.

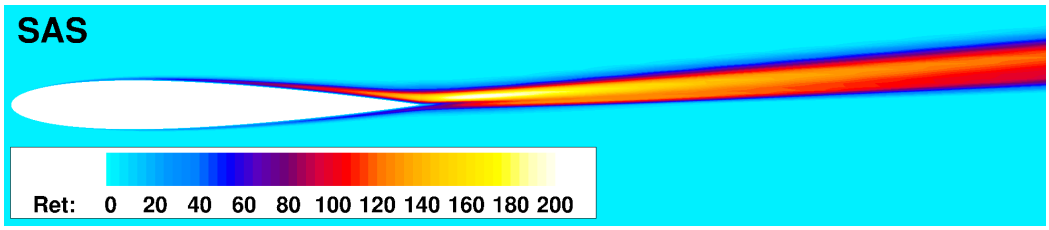

(b) SAS.

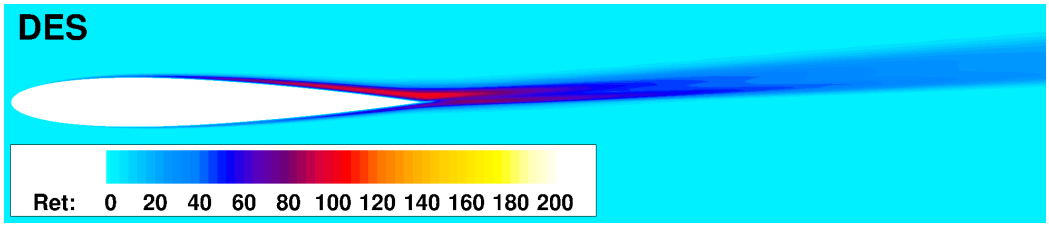

(c) DES.

Figure 6.12: SST, SAS and DES models comparison: visualisation of the turbulent eddy viscosity ratio $Ret = \frac{\mu_T}{\mu}$ in the airfoil wake. Both advance models show a notable reduction of μ_T compared to the RANS method (by 36% and 82% the SAS and the DES respectively, $1c$ down-stream the trailing edge), thus allowing to resolve a larger part of the turbulent spectra.

Wing Wake Prediction

To compare the airfoil wake prediction of the three methods, the profiles of the velocity U and the modelled turbulent kinetic energy k are shown in Figure 6.13, for different down-stream stations from the trailing edge to $8c$ away. Profile shapes, and location of the peaks, are observed to be the same for the three turbulence models, at all stations. The SST shows the highest velocities in the airfoil wake, whereas the DES displays

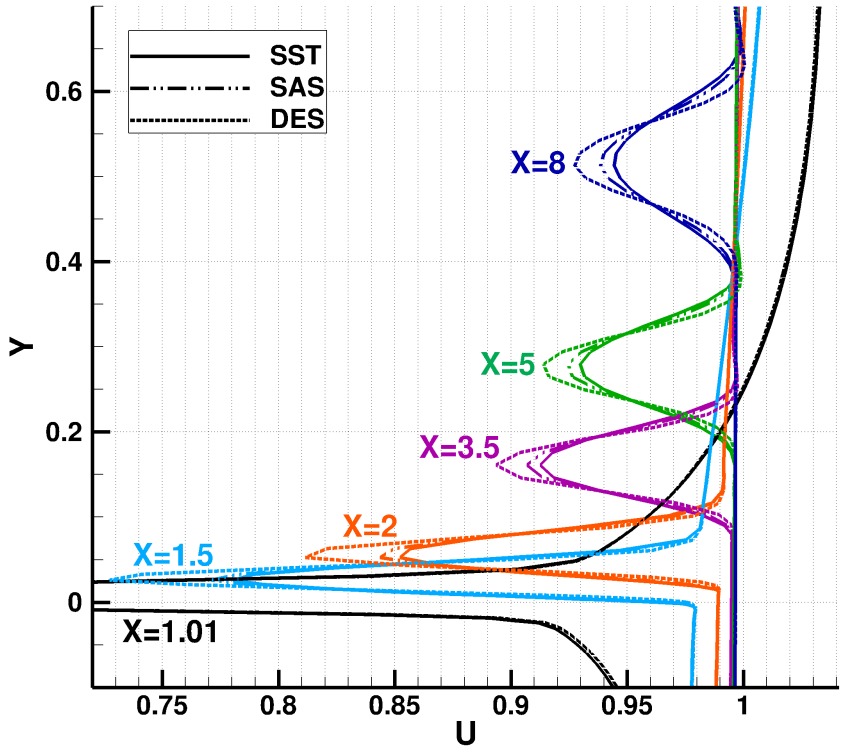

(a) Non dimensional velocity U.

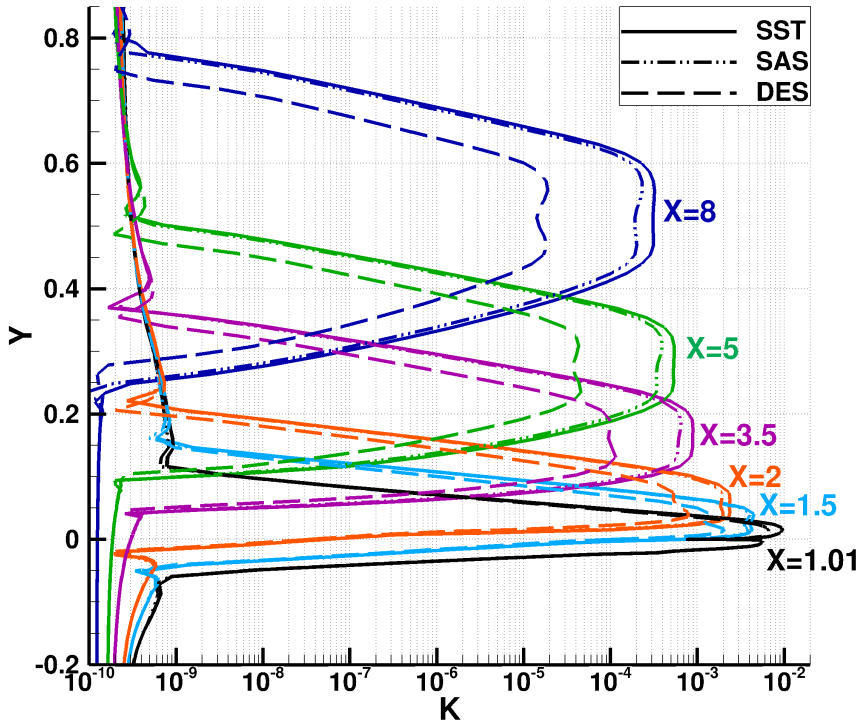

(b) Non dimensional turbulent kinetic energy k (logarithmic x-axis used for visualisation convenience).

Figure 6.13: SST, SAS and DES models comparison: velocity and modelled turbulent kinetic energy profiles in the airfoil wake. X=1 is the trailing edge coordinate. All three turbulence models predict the same profile shape and peaks location, at all stations. The SAS shows similar levels of k compared to the SST, while the DES a considerable reduction.

the slowest. In agreement with the methods' theory, the modelled kinetic energy is larger for the RANS model, and decreases for the SAS and, in a greater way, for the DES. The SAS predictions are very close to the SST. They show almost identical results up to $2c$ away from the airfoil trailing edge, and differ down-stream mainly only for the maximum U and k values. Bigger differences appear instead in the DES predictions. The double peak in the k profile is more pronounced, compared to the SST and the SAS results. Moreover, from approximately $3.5c$, and further down-stream the trailing edge, the DES shows a narrow wake.

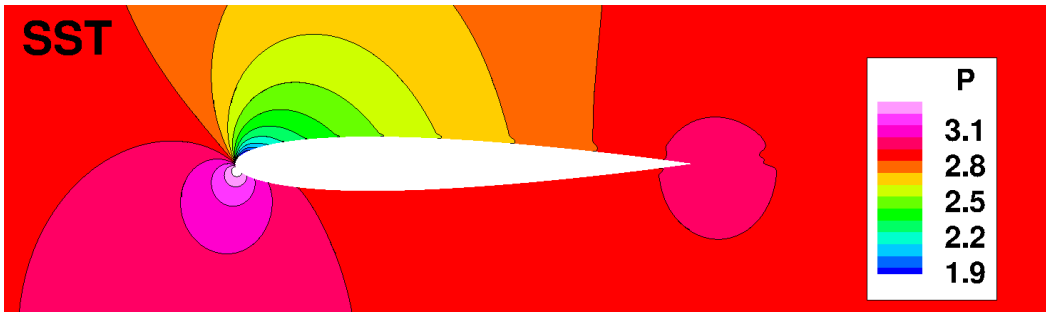

(a) SST.

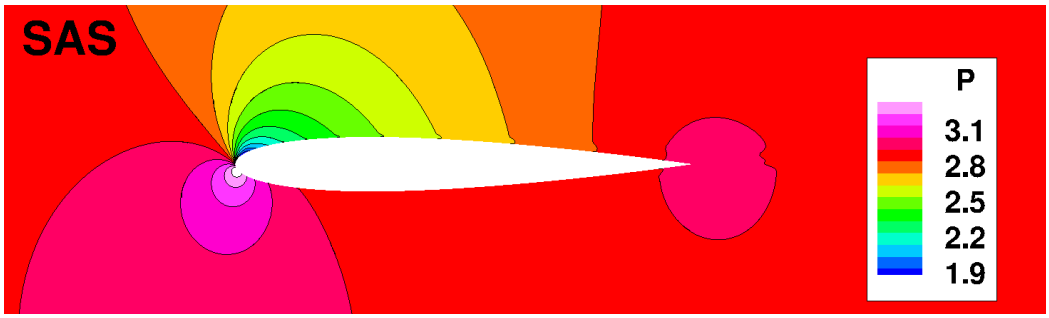

(b) SAS.

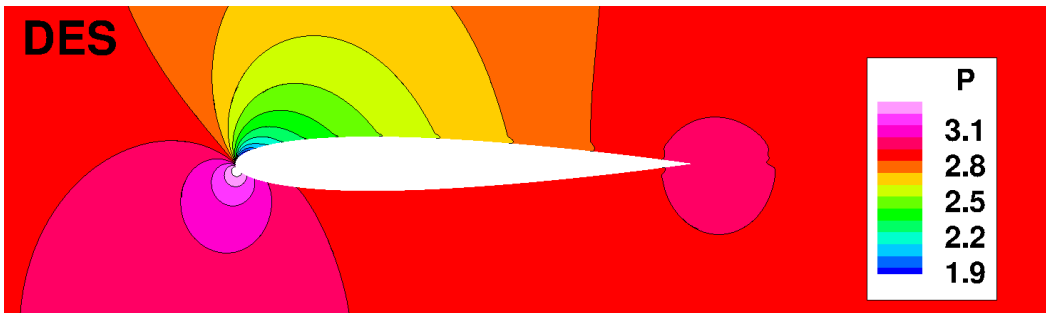

(c) DES.

Figure 6.14: SST, SAS and DES models comparison: non-dimensional pressure field visualisation. All three models give very similar predictions around the airfoil, small differences appearing on the upper surface towards the trailing edge. Considerable dissimilarities are only in the wake, the DES showing a smaller defect.

Wing Loading Prediction

The resulting differences, between the three simulations, in the wing loading predictions are reported in Table 6.7. The SAS gives lift and drag coefficients lower than the

Model	Lift Coefficient	Drag Coefficient
SST	0.1520	0.00360
SAS	0.1510	0.00357
DES	0.1485	0.00354

Table 6.7: SST, SAS and DES models comparison: airfoil force coefficients predictions.

SST by 0.6% and 1.1%, respectively. The estimates of the DES differ from the SST by approximately -2% for both force coefficients. The airfoil pressure field is presented in Figure 6.14 for the three simulations. Looking at it, the differences in the total wing loading appear mainly due to the dissimilarities in the pressure defect of the airfoil wake, and, to a less extent, to the differences observed on the upper airfoil surface toward the trailing edge.

6.3.2 IMPACTA Propeller Flow Predictions

To comprehensively assess the predictions of SAS and DES models, different test cases were run varying the time-step size, as summarised in Table 6.8.

Test ID	Turbulence Model	Time Resolution	Mesh Properties
SST1	$k-\omega$ SST	1 deg per step	Max Grid Spacing = $0.015c$, $y^+ \leq 1$, hyperbolic expansion law in boundary layer (ratio 1.1-1.13)
SAS1	$k-\omega$ SST SAS	1 deg per step	
SAS05	$k-\omega$ SST SAS	0.5 deg per step	
DES1	DES with $k-\omega$ SST	1 deg per step	
DES05	DES with $k-\omega$ SST	0.5 deg per step	
DES025	DES with $k-\omega$ SST	0.25 deg per step	
DES01	DES with $k-\omega$ SST	0.1 deg per step	

Table 6.8: Turbulence models analysis: computational test cases.

Considered temporal resolutions ranged from 1 propeller rotational degree to 0.1 degrees: initially, simulations were performed using time-steps of 1 and 0.5 degrees; the effect of further refinement in time was then investigated for the DES model. Note that all discretisations correspond to Nyquist frequencies in the broadband noise range: the largest, with 360 steps resolved per propeller revolution, gives a Nyquist frequency of approximately 2500 Hz.

The Baseline blade in cruise axial flight ($M_\infty = 0.5$, $RPM = 856.14$) is employed for all test cases of this analysis (refer to Table 5.1 for all the details about geometric and

operational parameters).
The SST simulation was started from unperturbed free-stream conditions using the first half of propeller revolution to smoothly accelerate the blade from zero to full-speed. A converged SST solution was then employed as initial condition for the SAS and DES computations. The original MUSCL scheme was used in all cases.

Computational Grid

Due to the need of restrain the mesh size, the adopted strategy was to generate an over-set grid with a foreground mesh containing the propeller blade and near-wake region. This way, without introducing a second chimera level, the spatial resolution was kept suitably fine in the area of interest. Layout, dimensions and boundary conditions are shown in Figure 6.15. The classic "C-H" topology was again used for the blade grid. From preliminary estimates of the flow, a maximum cell spacing equal to $0.015c$ was chosen for the foreground grid, yielding approximately 57M cells in it, and approximately 163M cells overall. This resolution corresponds to almost 100 points per wave-length for the frequency of 1kHz, and almost 40 points at 2.5 kHz.

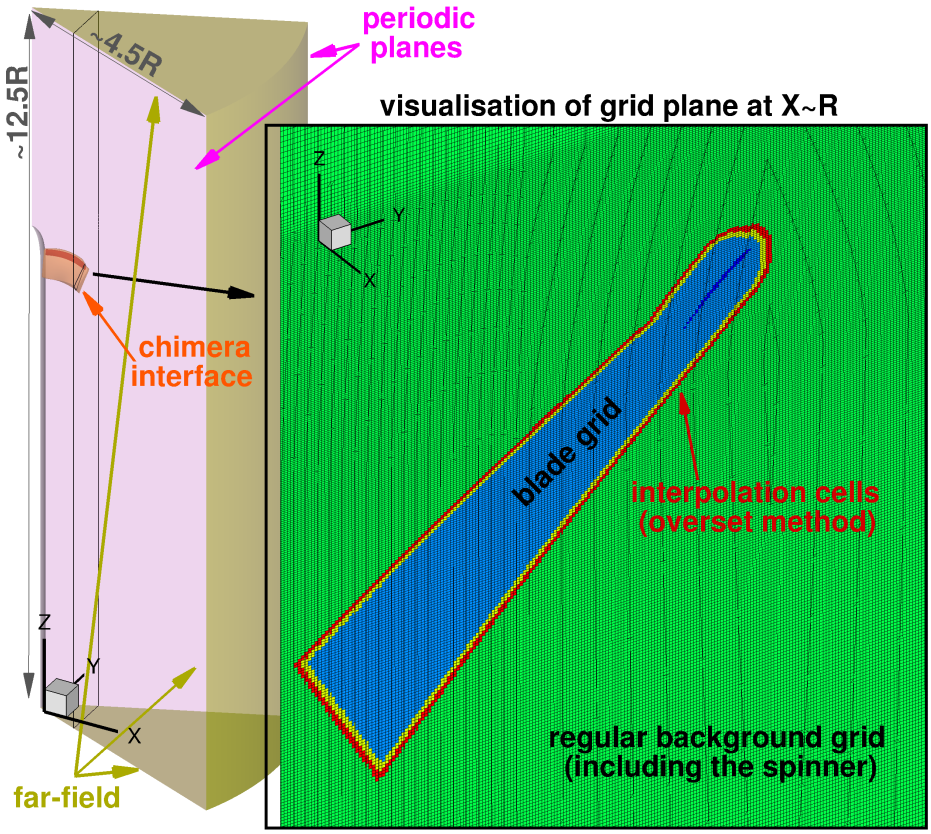

Figure 6.15: Single-blade IMPACTA Baseline propeller grid employed for the turbulence study.

Numerical probes are included in the near-wake, to record the pressure time evolution

at each simulated step. In particular, 42 probes are placed from $0.6R$ to the tip, at distances of $0.1c$, $0.5c$ and $1c$ from the blade trailing edge. Figure 6.16 shows their positions. It is noted that they are associated with a cell center, thus following rigidly the blade in its rotation.

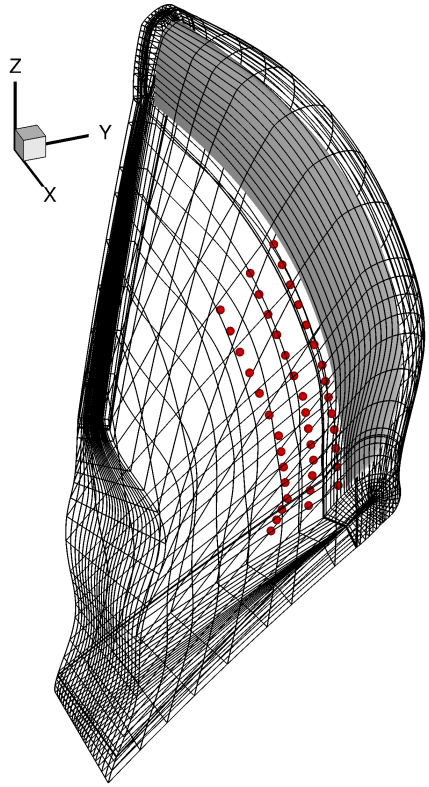

Figure 6.16: Localisation of the numerical probes employed in the turbulence study.

SAS and DES Predictions Discussion

SAS and DES Activation

Figure 6.17 shows where the additional ω source term of the SAS model Q_{SAS} (see Equation 2.31) is active in the flow, whereas the region in which its magnitude is big enough to invert the sign of the balance between production and destruction is visualised in Figure 6.18. The two visualisations refer to the SAS05 case, but the scenario is similar for the SAS1, since between the two simulations only the values of Q_{SAS} slightly differ, not the area of the flow where it is positive. The model is seen to operate using its scale adaptive capability in the near wake mainly, yielding a change in the ω balance from the root up to approximately $0.77R$, and in the tip vortex. The Q_{SAS} term is positive also in small regions near the blade surface on the pressure side and near the leading edge, at some outboard stations. Here, however, its magnitude is

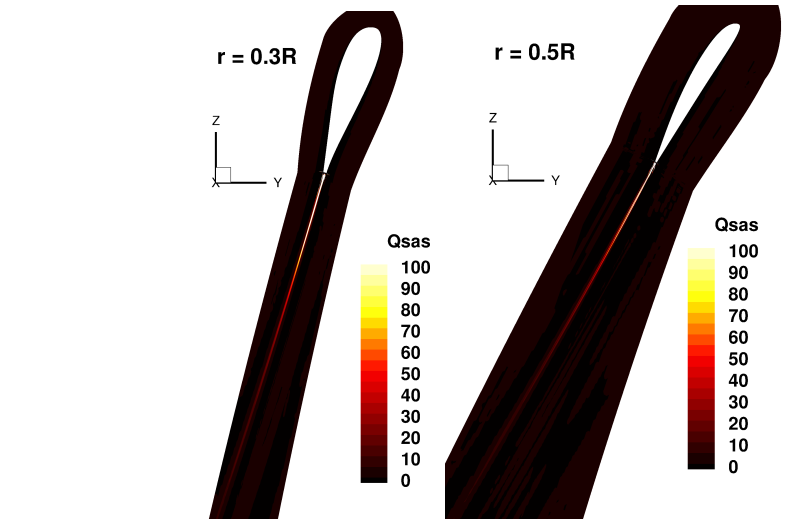

(a) $r = 0.3R$.

(b) $r = 0.5R$.

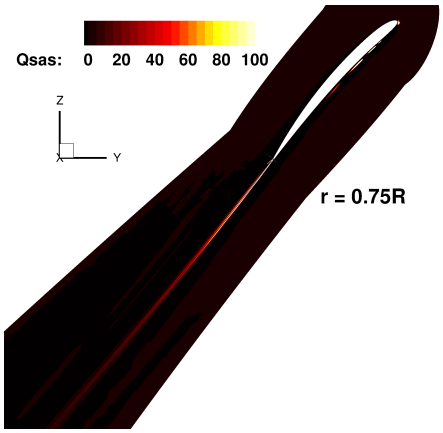

(c) $r = 0.75R$.

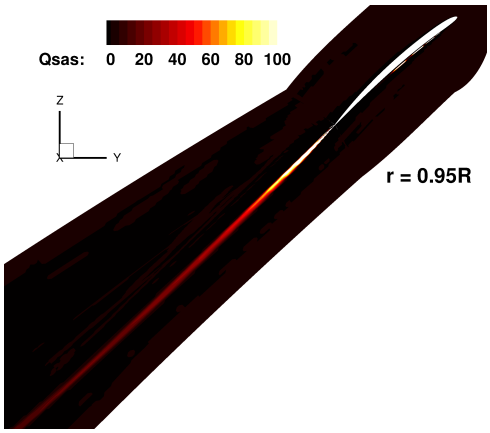

(d) $r = 0.95R$.

Figure 6.17: SAS05: visualisation of the additional source term for ω, Q_{SAS}, at various span-wise stations along the blade. $Q_{SAS} = 0$ denotes a RANS behavior of the model. The scale adaptive capability of the model is mainly active in the near wake in proximity of the wake axis.

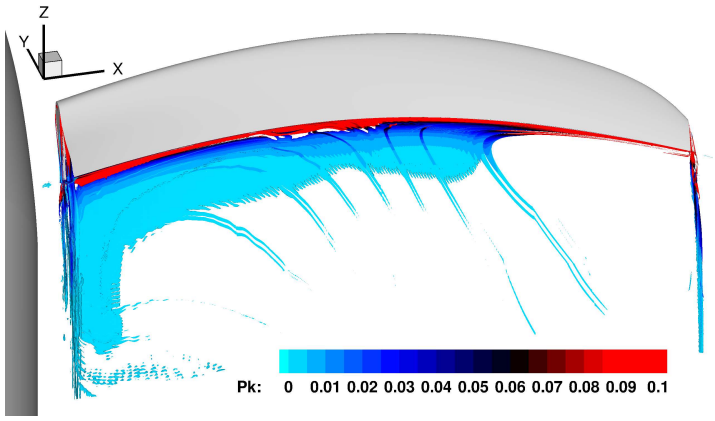

Figure 6.18: SAS05: visualisation of SAS source term "effectiveness", i.e. ω production/destruction balance changed (iso-surfaces at 0.01), colored by non-dimensional k production term. Q_{SAS} has a magnitude such to modify the ω energy balance from the blade root up to $\sim 0.77R$ close to the trailing edge, and in the tip vortex for longer down-stream distances.

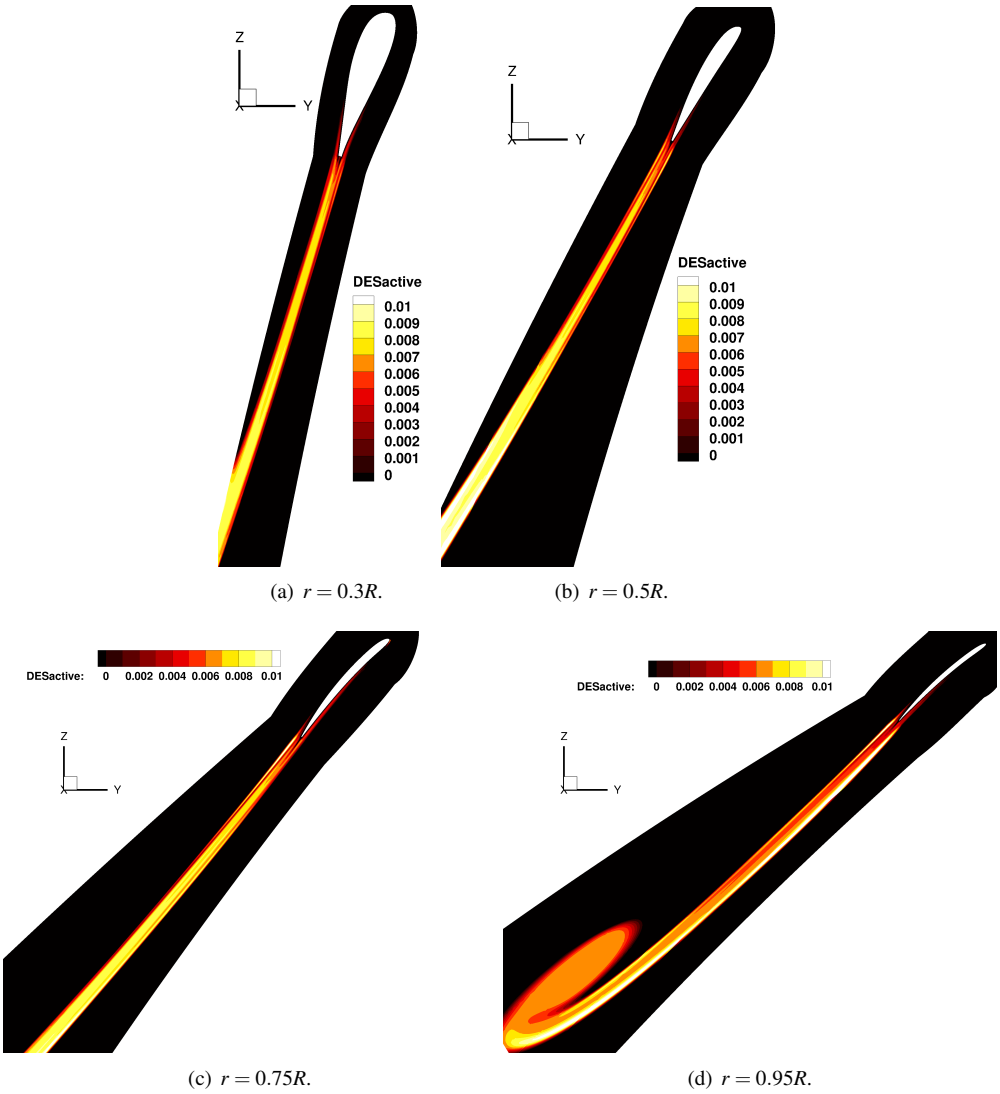

(a) $r = 0.3R$. (b) $r = 0.5R$.

(c) $r = 0.75R$. (d) $r = 0.95R$.

Figure 6.19: DES05: visualisation of regions where the LES mode is switch on. The DES operates in its scale-resolving mode on a wider area of the wake and for longer distances down-stream, compared to the SAS.

relatively small compared to the production and destruction terms, and thus the equilibrium of ω is not effectively modified.

Figure 6.19 shows where the DES model switches to LES mode for different span-wise stations along the blade. As before, the visualisation is done for the DES05 case, but it is qualitatively representative of DES1 as well. The LES capability appears active in the blade wake, on a wider area and for longer down-stream, compared to where the SAS is operational. The DES acts as LES also near the blade trailing edge on both suction and pressure sides, just outside the boundary layer inside which it behaves like URANS. The length of this activity zone varies with the span-wise location, however, it does not extend so up-stream to reach where the Q_{SAS} term was positive. The DES model is also active in a small region near the leading edge around $0.75R$, as was the

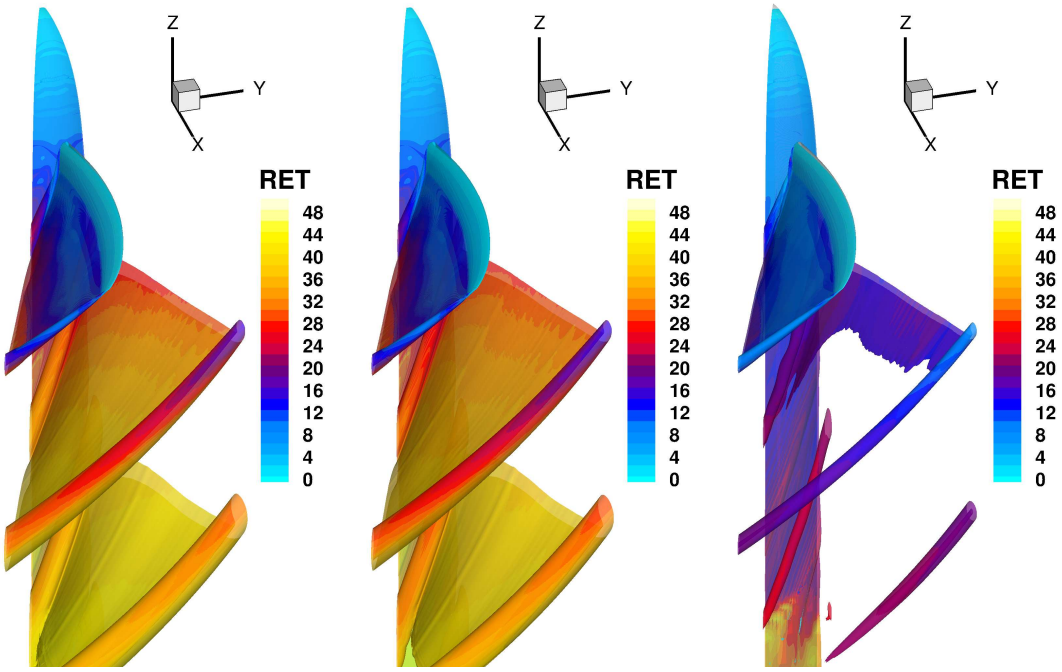

(a) SST1. (b) SAS1. (c) DES1.

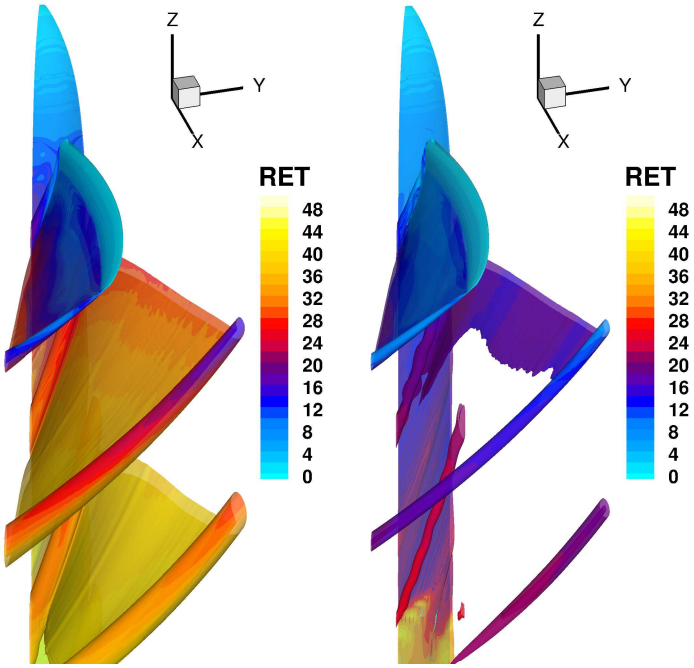

(d) SAS05. (e) DES05.

Figure 6.20: SST, SAS and DES comparison: blade wake prediction. Iso-surfaces of modelled turbulent kinetic energy k (non-dimensional value of 50) colored by eddy viscosity ratio $Ret = \frac{\mu_T}{\mu}$. The SAS shows very similar levels of k compared to the SST, whereas the DES reduces it considerably. Thus it is expected that only the latter will be able to extend significantly the resolved frequency range of the turbulence spectra.

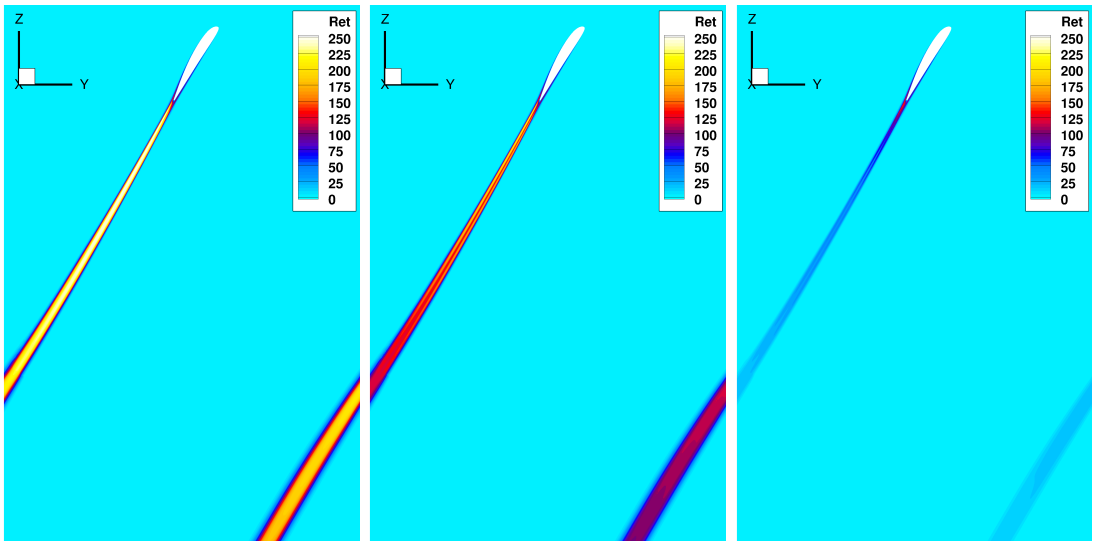

(a) SST1. (b) SAS1. (c) DES1.

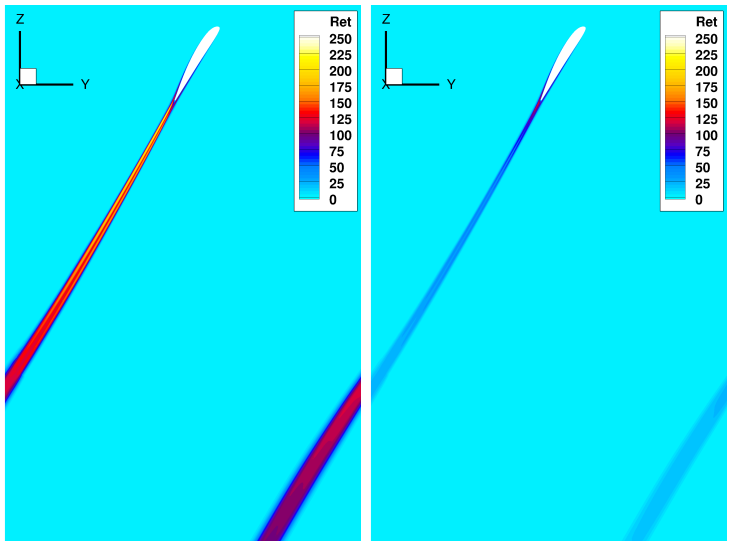

(d) SAS05. (e) DES05.

Figure 6.21: SST, SAS and DES comparison: visualisation of the turbulent eddy viscosity ratio $Ret = \frac{\mu_T}{\mu}$ at the blade mid-span. Both advanced models reduce μ_T, the DES displaying up to 50% less than SST. The smaller time step seems to not affect the behaviour of the SAS, whereas to slightly lower μ_T in the DES.

case for the SAS model. Finally, the large circular area of LES activity seen in the wake at $0.95R$ corresponds to the blade tip vortex.

To evaluate the effect of the two advanced turbulence models in comparison to the URANS, Figures 6.20 and 6.21 show iso-surfaces of modelled kinetic energy k and contours of turbulent Reynolds Ret, respectively.

The SAS simulations actually show lower turbulent eddy viscosity in the wake sheet with respect to the SST. However, the turbulent kinetic energy still appears very similar to the URANS results. Also, almost no differences are observed between the cases

SAS1 and SAS05.
The DES model yields considerably less modelled turbulent kinetic energy and lower turbulent eddy viscosity, the latter reaching reductions up to 50% compared to URANS. Small, but noticeable, differences are seen between the simulations with time-steps of 1 and 0.5 degrees. The use of the smaller time-step gives a further decrease in the turbulent eddy viscosity.
The maximum *Ret* occurs close to the trailing edge in the case of the DES model, where it operates as URANS, and slightly down-stream for SST and SAS.

Blade Wake Prediction

To compare the three models regarding the predictions of the blade wake and the vortical structures, Figures 6.22 and 6.23 show iso-surfaces of Q criterion and vorticity contours down-stream the propeller plane, respectively. SAS1 results are very similar to SST1, with small differences visible only in the root vortex resolution and slightly higher vorticity values in the vortex cores, especially from the third blade passage.
Longer vortex filaments are observable in the DES1 solution, along the whole blade span, even close to the blade root where SST1 and SAS1 do not show structures of that strength. Vorticity levels are slightly higher than SAS1 predictions, whereas no significant difference is seen in the core dimensions of the main vortices. SAS05 and SAS1 predictions mainly differ only around $R/2$ near the blade trailing edge, where the smaller time-step gives more irregular vortical structures. Structures of similar character appear in the DES05 solution as well. The latter shows also few small differences with respect to DES1 toward the blade tip. Further away from the blade trailing edge, no major differences are displayed between simulations performed with 1 and 0.5 degrees per time step, and the same observations hold in the comparison SAS/DES vs SST results.

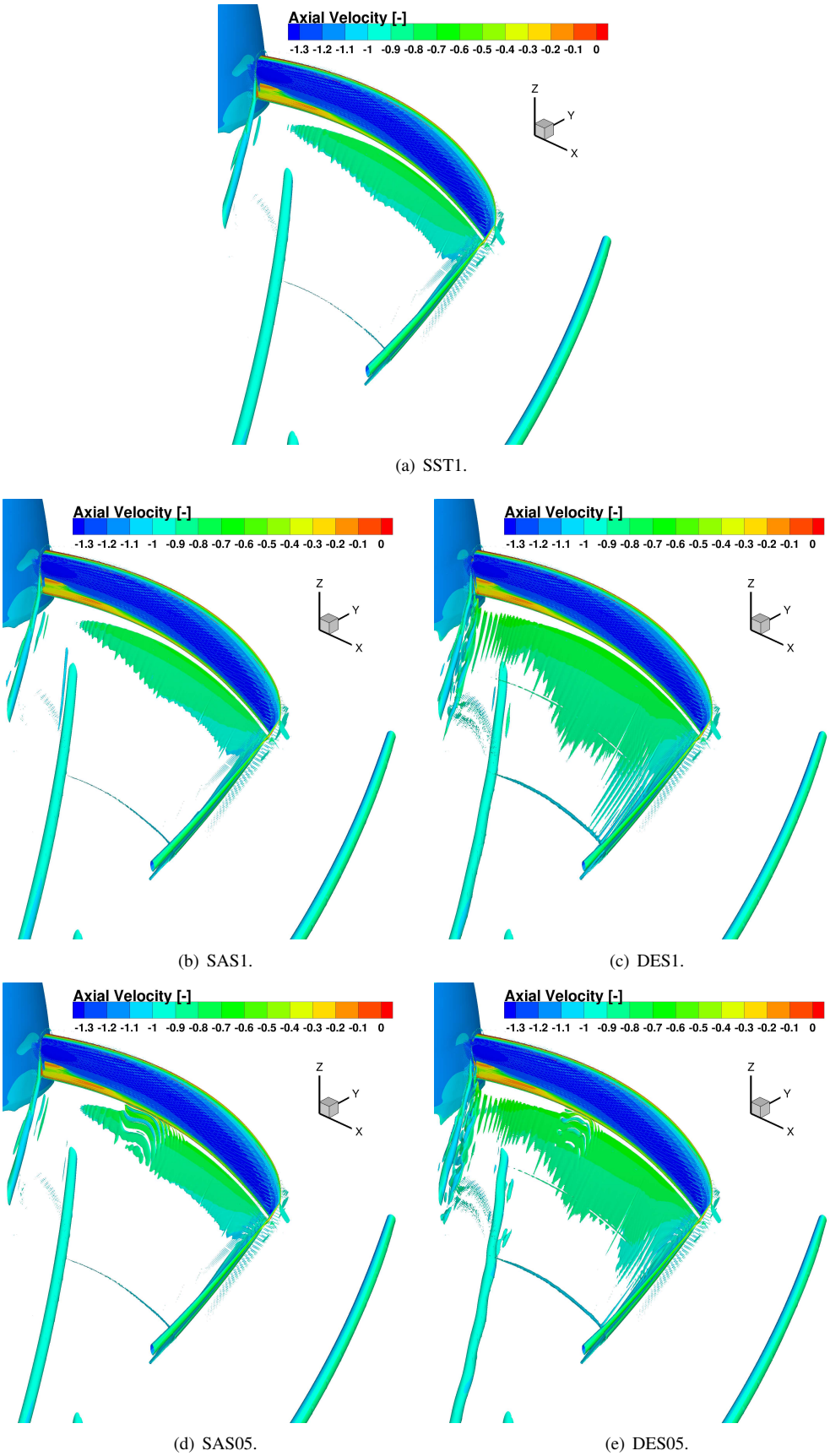

(a) SST1.

(b) SAS1.

(c) DES1.

(d) SAS05.

(e) DES05.

Figure 6.22: SST, SAS and DES comparison: blade wake prediction. Iso-surfaces of Q criterion (non-dimensional value of 0.1) colored by non-dimensional axial velocity. SAS1 prediction is very similar to SST1, with small differences only in the root vortex resolution. DES1 shows longer vortex filaments, along the whole blade span. The smaller time-step yields more irregular vortical structures near the blade trailing edge around mid-span, for both SAS and DES models.

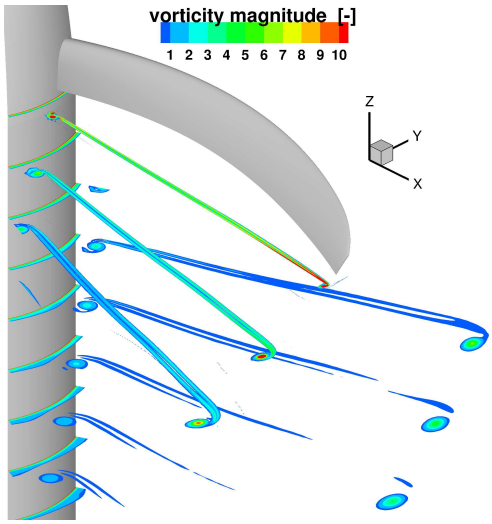

(a) SST1.

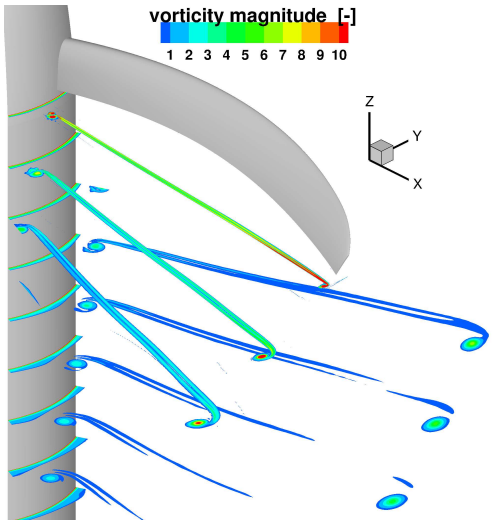

(b) SAS1.

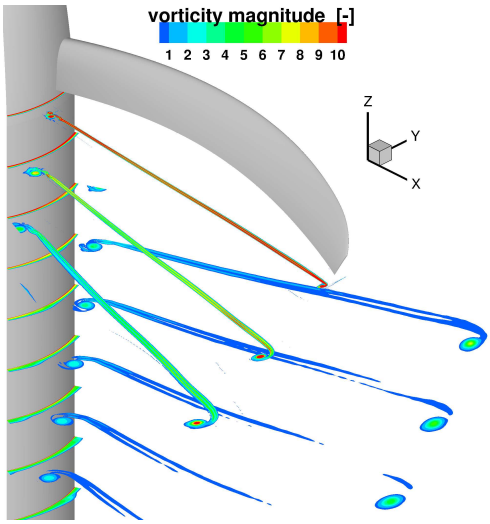

(c) DES1.

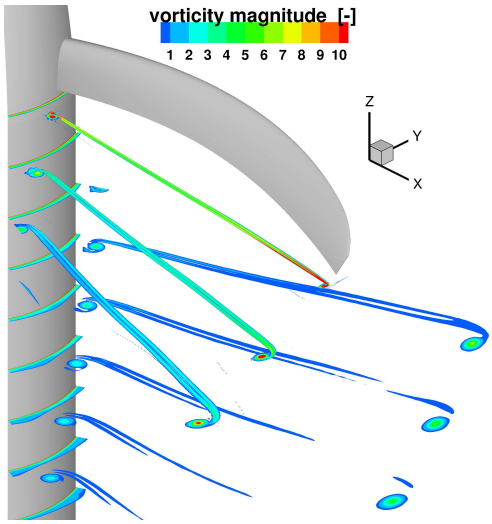

(d) SAS05.

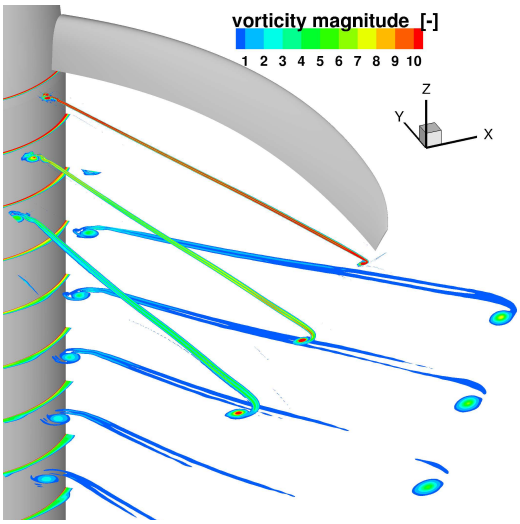

(e) DES05.

Figure 6.23: SST, SAS and DES comparison: blade wake prediction. Vorticity magnitude contours from $1c$ to $R/2$ down-stream the propeller rotational plane. SAS1 shows slightly higher vorticity values in the vortex cores compared to SST1, especially from the third blade passage. DES1 displays significantly higher vorticity along the whole span, and no differences in core dimensions.

Blade Loading Predictions

Span-wise loading predictions are compared in Figure 6.24 for the three models. Overall estimates of the propeller thrust and power are compared in Table 6.9. Blade forces and moment agree very well between all test cases. Very small discrepancies are seen only in the load peaks and near the blade root, with the DES model yielding the lower estimates as in the preliminary case of the infinite-wing. Overall, the propeller performance is predicted by all models within less than 1%, with differences between simulations using time-steps of 1 and 0.5 degrees of approximately $0.14-0.15\%$ and $0.13-0.14\%$ for thrust and power, respectively.

Test ID	ΔC_T	ΔC_P
SAS1	-0.17%	-0.21%
DES1	-0.58%	-0.71%
SAS05	-0.03%	-0.08%
DES05	-0.44%	-0.57%

Table 6.9: SAS and DES loads predictions evaluation: comparison against SST results.

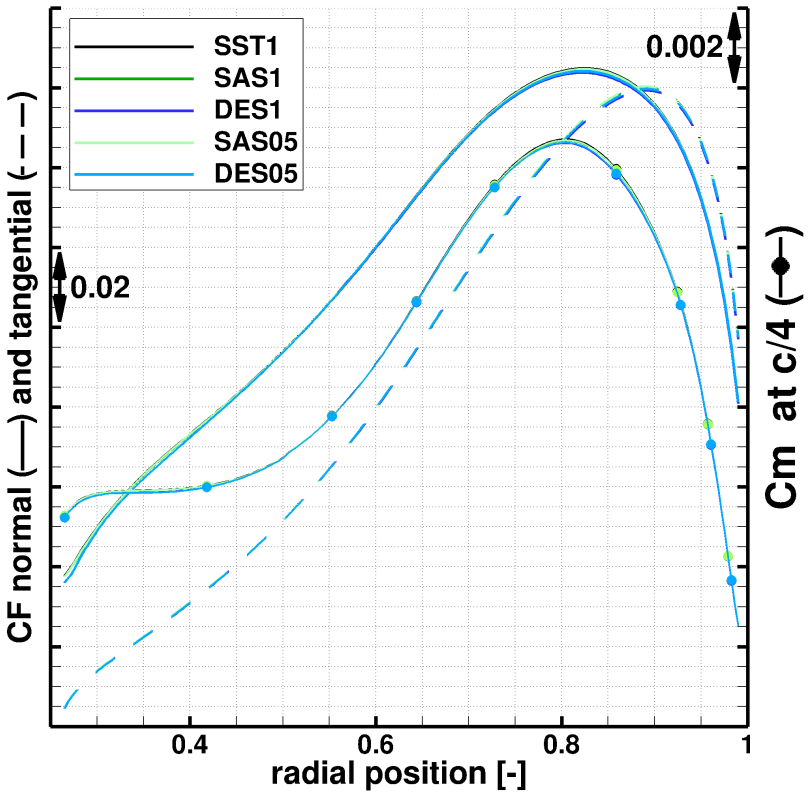

Figure 6.24: SST, SAS and DES comparison: blade span-wise loading distribution. All three models give close results. Very small discrepancies appear only in the load peaks and near the blade root, the DES yielding lower estimates. The time-step choice does not influence importantly the predictions.

Unsteady Pressure Predictions

SAS and DES unsteady pressure results are compared against the SST solution. The time signals of the unsteady pressure for some locations in the near-wake, and the corresponding power spectral density (PSD), are presented in Figures 6.25 and 6.26, respectively. Data are taken from the numerical probes (Figure 6.16 shows their positions), for a full propeller revolution. The main 4-per-rev oscillation is detectable

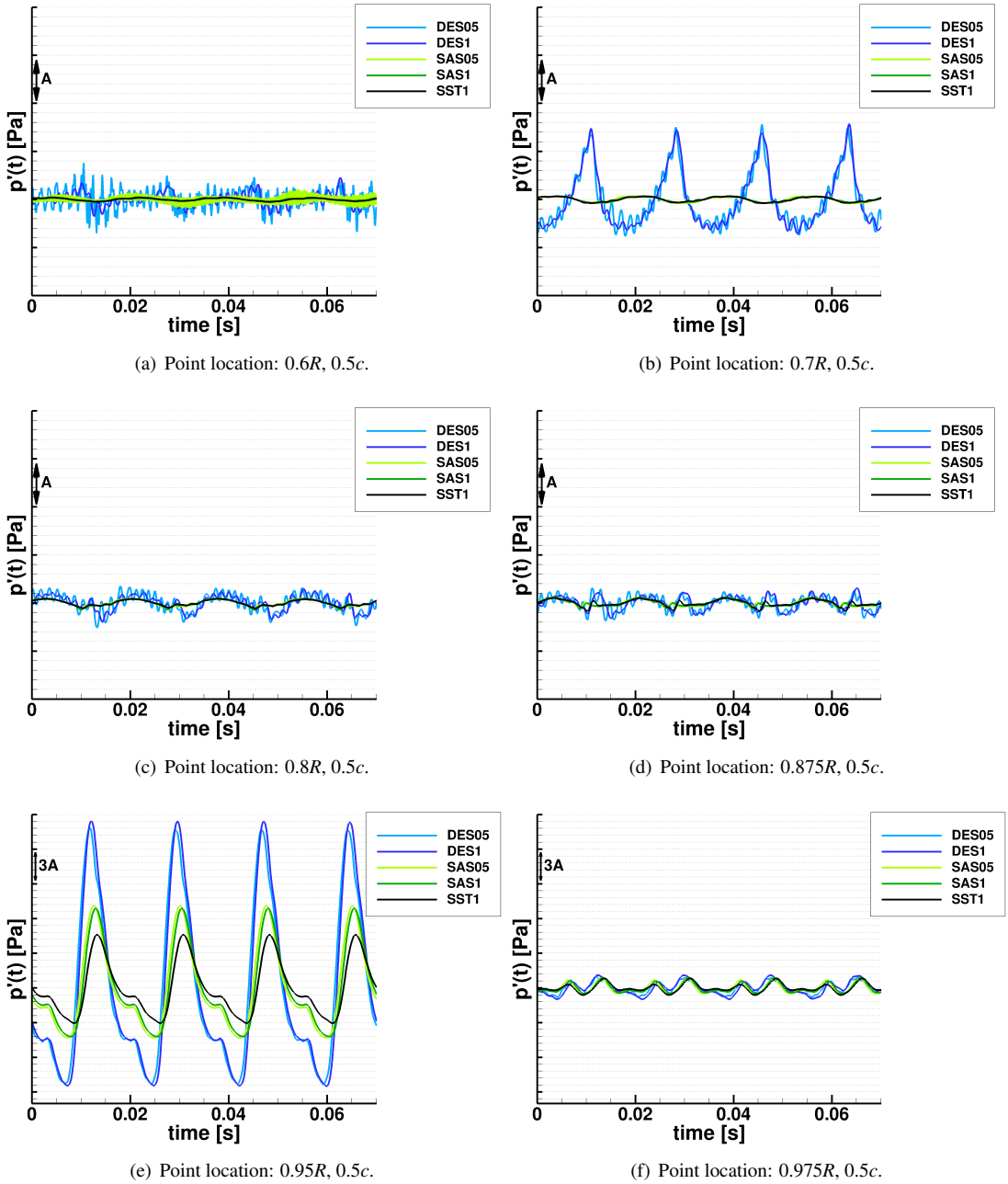

(a) Point location: 0.6R, 0.5c.

(b) Point location: 0.7R, 0.5c.

(c) Point location: 0.8R, 0.5c.

(d) Point location: 0.875R, 0.5c.

(e) Point location: 0.95R, 0.5c.

(f) Point location: 0.975R, 0.5c.

Figure 6.25: SST, SAS and DES comparison: unsteady pressure signals, for one propeller revolution, in the blade near-wake. *Part 1/2 - Radial sweep.*

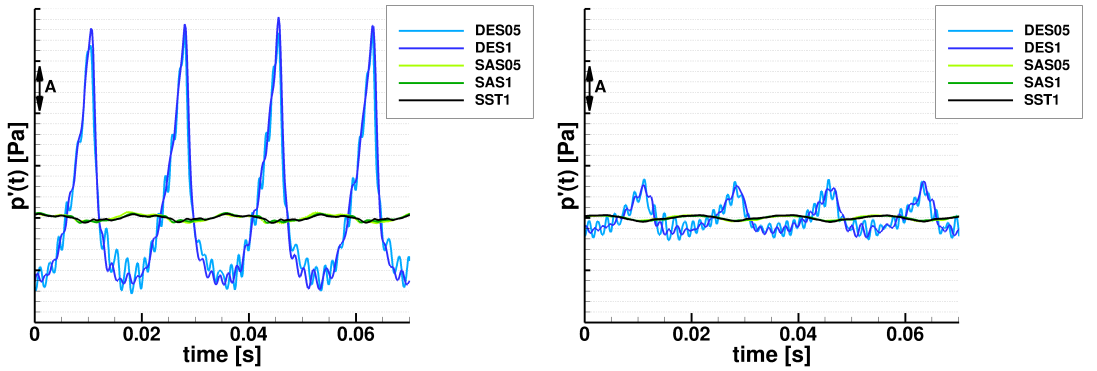

(g) Point location: 0.7R, 0.1c.

(h) Point location: 0.7R, 1c.

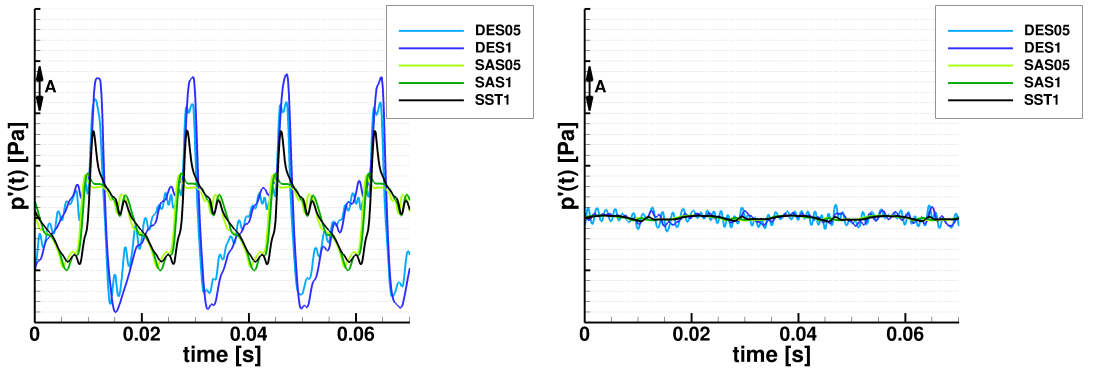

(i) Point location: 0.875R, 0.1c.

(j) Point location: 0.875R, 1c.

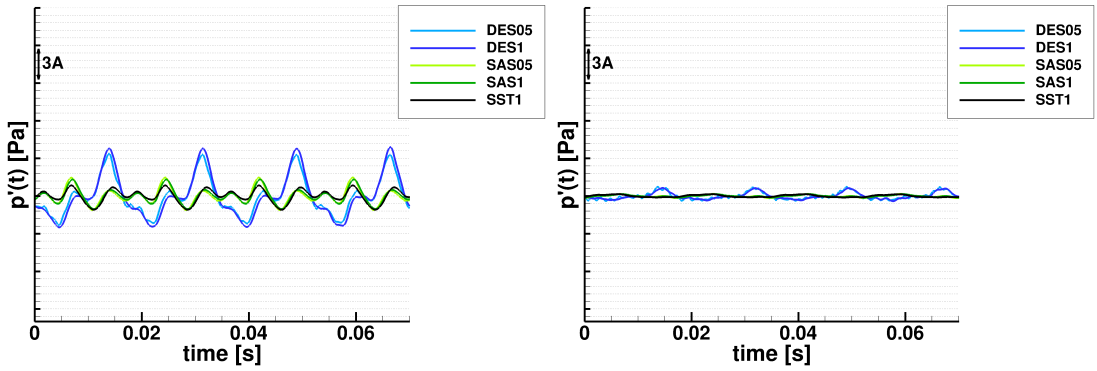

(k) Point location: 0.975R, 0.1c.

(l) Point location: 0.975R, 1c.

Figure 6.25: SST, SAS and DES comparison: unsteady pressure signals, for one propeller revolution, in the blade near-wake. *Part 2/2 - Stream-wise sweep.* The main 4-per-rev oscillation is due to the interaction with the wake of the preceding blade, the largest amplitude caused by the tip vortex around 0.95R. At a fixed span-wise station, the fluctuation amplitude decreases with increasing the distance from the trailing edge. The SAS is similar to SST, apart from a larger fluctuation amplitude at 0.95R. The DES shows a significantly larger fluctuation amplitude, at 0.7R, 0.95R and close to the trailing edge, and smaller oscillations on top of the main cycle up to 0.9R.

in all signals, thus giving the first harmonic at a frequency equal to BPF/2, and also all its multiples in the spectra. This is associated to the interaction with the wake of the preceding blade. The largest oscillation amplitude, amongst the analysed locations, is predicted by all methods at approximately $0.95R$, just inboard of the blade tip vortex, because of the encounter with the preceding blade tip vortex. In general, as expected, for a fixed span-wise station, the fluctuation amplitude decreases with increasing the distance from the blade trailing edge. The differences in the predictions between the three turbulence models vary in character depending on the location.

The SAS model gives results quite similar to the SST. Only at $0.95R$ a larger amplitude of the pressure fluctuations, and a related $\sim$1 dB increase in the PSD of the first two harmonics, are visible. This is probably due to the different resolution of the blade tip vortex due to the activation of the Q_{SAS} term (see Figure 6.18). Differences between SAS1 and SAS05 simulations are very small. The finer time resolution predicted high-frequency content at $0.6R$, where smaller vortical structures were observed (see Figure 6.22). Few distinct higher frequencies are also visible in the spectra.

The unsteady pressure predicted by DES displays oscillations of significantly larger amplitude, compared to SAS and SST, at $0.7R$, $0.95R$, and close to the blade trailing edge (probes at $0.1c$). Moreover, the DES pressure signals at stations up to $0.9R$ are more "lively" than SAS and SST: high-frequency oscillations are seen on top of the main fluctuations. These oscillations are predicted by both DES1 and DES05 computations, and are not a simple binary step-to-step fluctuation of the solver output - in the magnification of the pressure time history reported in Figure 6.27 as example, it is visible that they are resolved by 9 points in the case of DES1, and around 15 in the case of DES05. Furthermore, they appear quite regular in character, and exhibit coherence between nearby probes. This suggests that the origin of these oscillations may be physical and not numerical. DES05 predicts a higher frequency and a slightly larger magnitude for these fast oscillations, with respect to DES1. It is noted that this is the only significant difference between results of DES1 and DES05, as it can also be seen in the PSD spectra, that differ only at high frequencies. Looking at the unsteady pressure spectra, it appears that these oscillations are not connected to a single tone. On the contrary, their energy content is spread over more adjacent frequencies. This generates, compared to SST and SAS, a more continuous spectrum at high frequencies, with a peak at the frequency corresponding to the fast fluctuations observed in the time signals. This is the most evident qualitative difference amongst the acoustic predictions of three turbulence models. In fact, at lower frequencies (approximately up to 3BPF), where the spectra exhibit more distinct and isolated harmonics, the results of the dif-

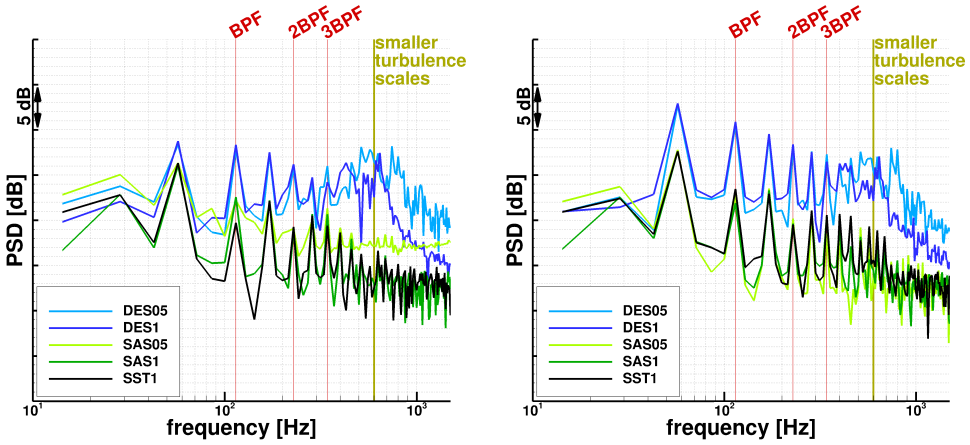

(a) Point location: 0.6R, 0.5c.

(b) Point location: 0.7R, 0.5c.

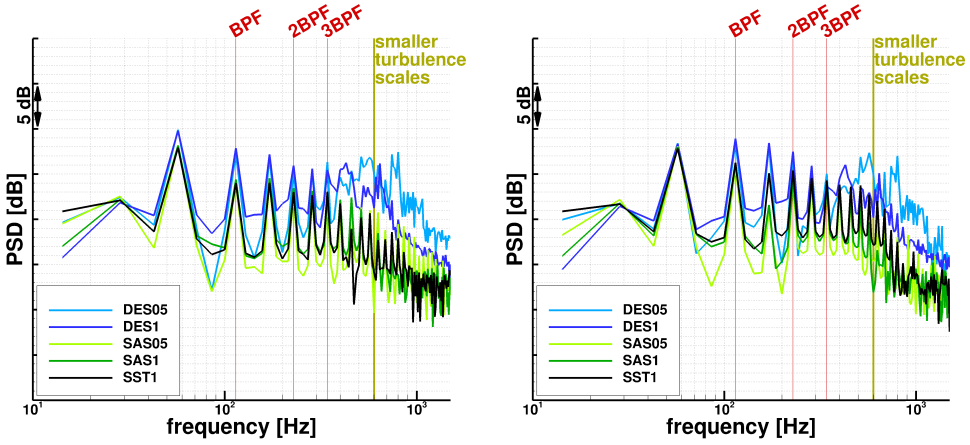

(c) Point location: 0.8R, 0.5c.

(d) Point location: 0.875R, 0.5c.

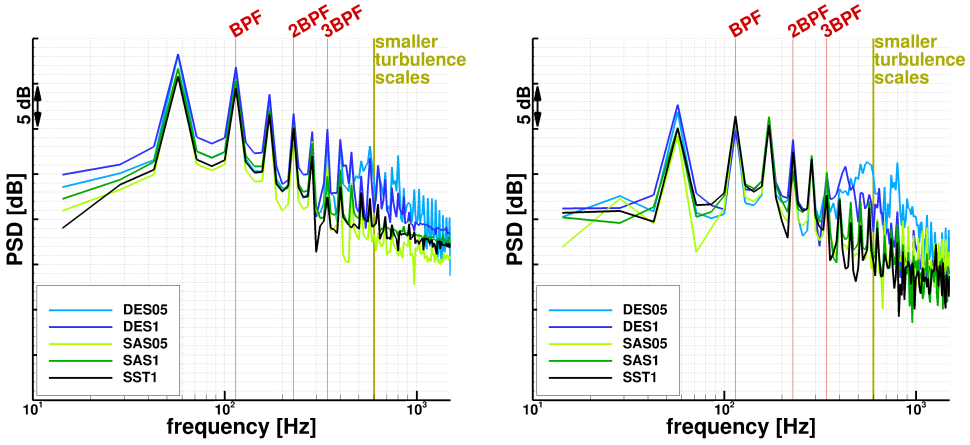

(e) Point location: 0.95R, 0.5c.

(f) Point location: 0.975R, 0.5c.

Figure 6.26: SST, SAS and DES comparison: PSD of the unsteady pressure in the blade near-wake. *Part 1/2 - Radial sweep.*

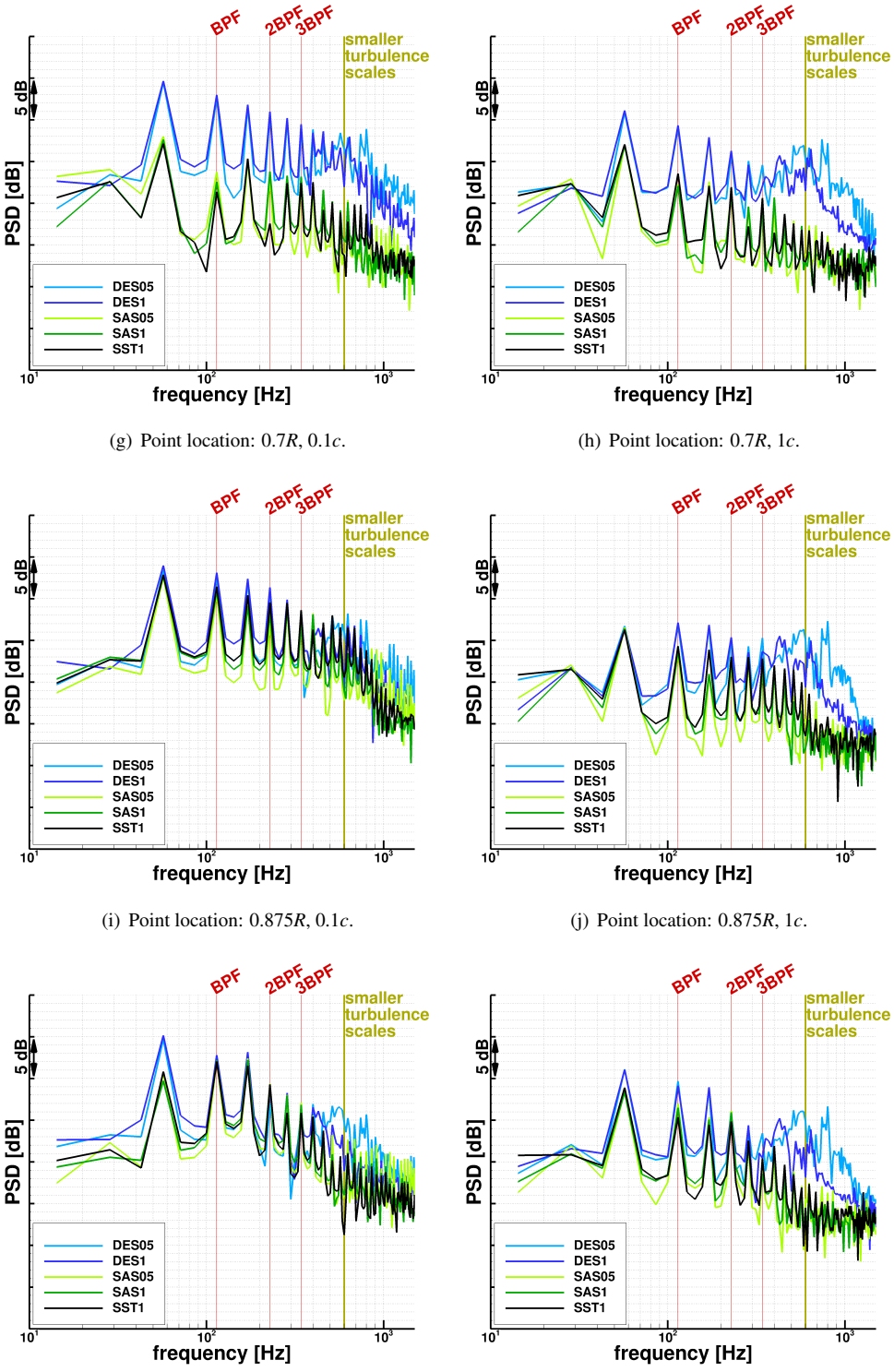

(g) Point location: 0.7R, 0.1c.

(h) Point location: 0.7R, 1c.

(i) Point location: 0.875R, 0.1c.

(j) Point location: 0.875R, 1c.

(k) Point location: 0.975R, 0.1c.

(l) Point location: 0.975R, 1c.

Figure 6.26: SST, SAS and DES comparison: PSD of the unsteady pressure in the blade near-wake. *Part 2/2 - Stream-wise sweep.* SAS spectra is very similar to SST, for all positions and all frequencies, the only difference being a $\sim$1 dB increase of the first two tones at 0.95R connected to the activation of Q_{SAS} in the tip vortex. SAS05 differs from SAS1 just for the presence of few high frequencies at 0.6R, where smaller vortical structures were observed. DES shows some differences in magnitude at low frequencies compared to SST and SAS (larger for inboard stations), and more content at high frequencies, with a peak comprising more frequencies corresponding to the fast fluctuations observed in the time signals. The finer time-step yields a higher frequency and a slightly larger magnitude for this high-frequency peak.

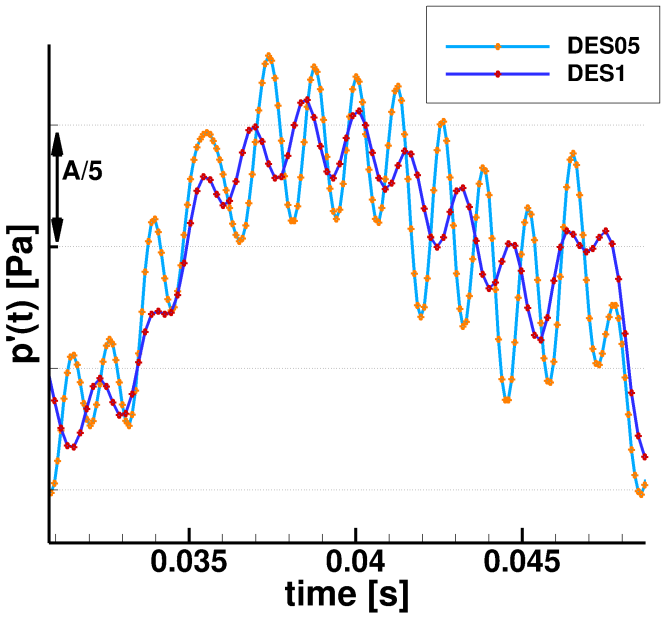

Figure 6.27: DES results investigation: detail of the unsteady pressure signal of probe located at (0.8R, 0.5c), for both DES1 and DES05. High-frequency oscillations predicted by the model are resolved by more than 8 points, are regular in character, and do not show a smaller amplitude with a finer time-step, thus suggesting a physical origin more than a numerical one.

ferent methods only vary in magnitude. The PSD estimated by DES is overall louder than those predicted by URANS models, the largest differences occurring at inboard blade stations, up to around 0.85R. toward the blade tip, the fast oscillations in the DES unsteady pressure signals have smaller amplitude, and the related high-frequency PSD contribution is less important with respect to that of the low-frequency tonal part of the spectra. At these blade stations, apart from the main 4-per-rev cycle, fluctuations two and three times faster can be observed in the pressure time histories. These are captured by the SST and SAS models as well.

Investigation of DES Results

To try to interpret the fast unsteady pressure oscillations appearing in the near-wake of the DES simulations, the flow-field was first analysed in more detail. A time refinement study was after carried out.

Flow Analysis

The local flow at different span-wise stations (0.5R, 0.7R and 0.95R) is investigated here. Figure 6.28 shows the velocity and pressure fields, at a fixed instant in time. At the inboard stations (Figures 6.28(a) and 6.28(b)), a pair of counter-rotating vortices is formed in the recirculation region that originates behind the thick trailing edge of the blade. Because of the inflow incidence, the two vortices are not symmetric, especially

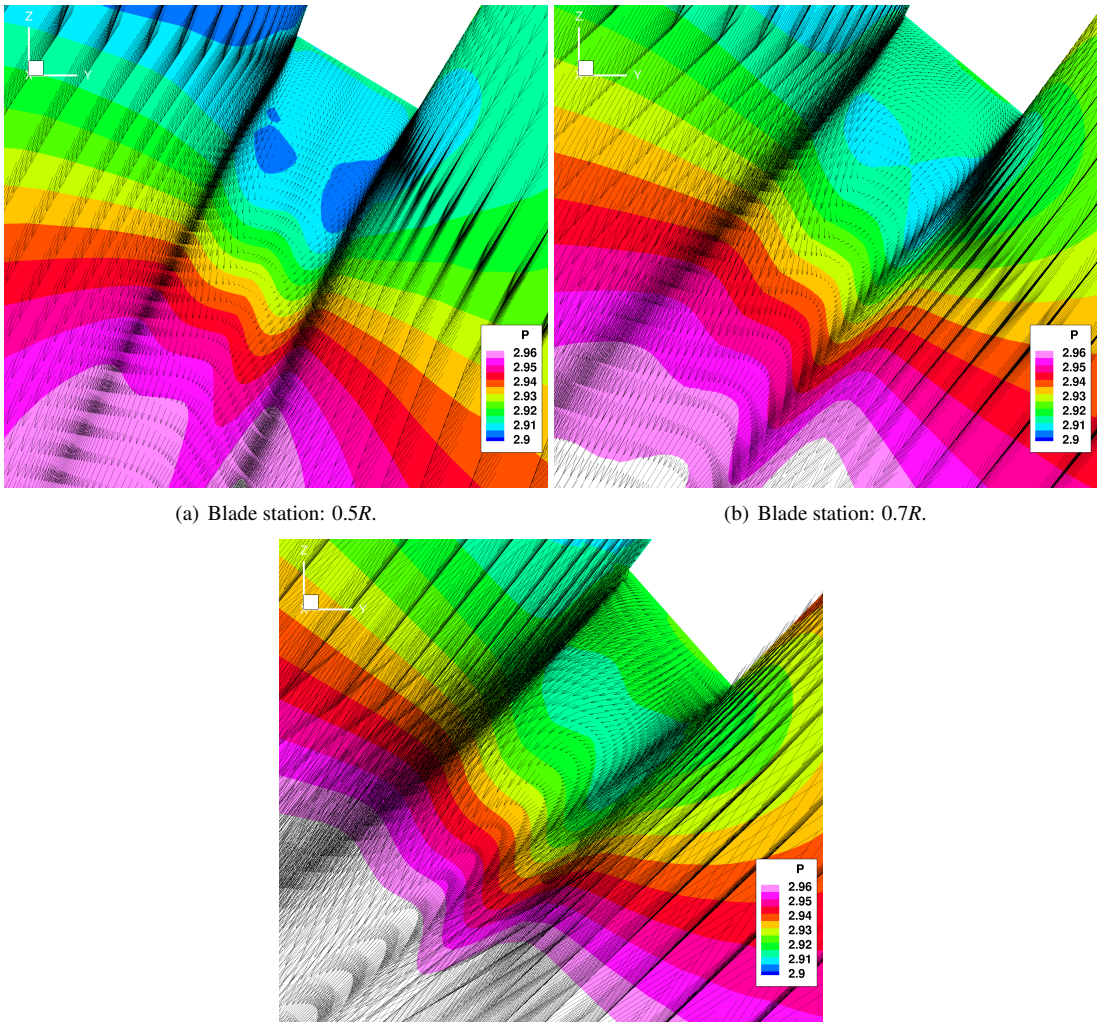

(a) Blade station: 0.5R.

(b) Blade station: 0.7R.

(c) Blade station: 0.95R.

Figure 6.28: DES trailing edge flow investigation: pressure contours and local velocity vectors. Inboards, a pair of not symmetric counter-rotating vortices is formed in the recirculation region originating behind the thick trailing edge. At blade tip, the flow is instead dominated by the tip vortex. No vortex-shedding is visible.

moving toward the blade tip. This can be easily seen from the position of the stagnation point on the trailing edge surface. At the considered instant, the aft vortex has the core slightly closer to the trailing edge, and a more circular shape. No vortex-shedding is visible in the wake. On the contrary, at 0.95R (Figure 6.28(c)) the strength of the tip vortex does not allow the generation of the recirculation bubble with the two counter-rotating vortices. This is consistent with the observed pressure signal recorded by the probes near the tip, which do not exhibit high-frequency oscillations (see Figures 6.25(e) and 6.25(f)).

To further analyse the behavior of the flow near the trailing edge, the local flow field has been plotted at different time instants for all the three considered span-wise stations.

Figures 6.29-6.31 present the vorticity contours and pressure iso-lines for the $0.5R$, $0.7R$ and $0.95R$ span-wise sections, at different blade azimuthal positions.

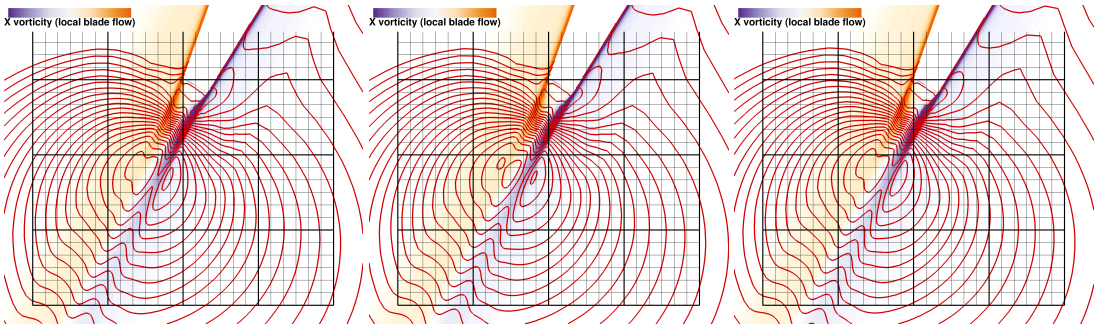

(a) Blade azimuthal position: 315 deg. (b) Blade azimuthal position: 321 deg. (c) Blade azimuthal position: 327 deg.

Figure 6.29: DES05 trailing edge flow - time visualisation via contours of local span-wise vorticity ω_x and iso-lines of pressure at $0.5R$. The high pressure peak down-stream the recirculation region is seen to pulse with time, causing periodic oscillations of the pressure field.

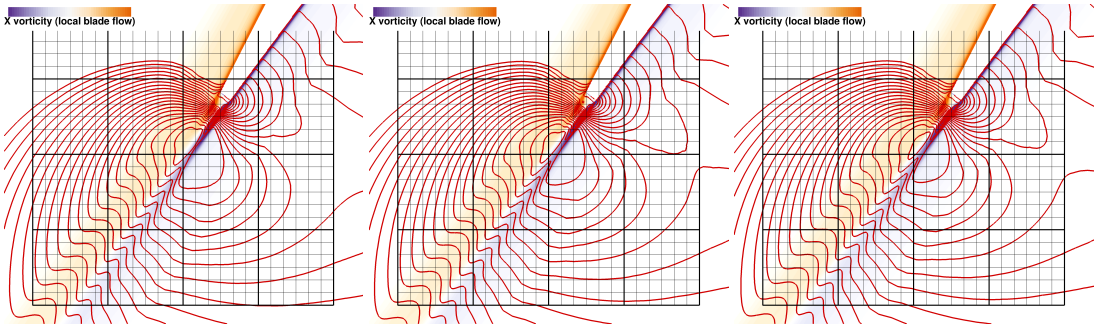

(a) Blade azimuthal position: 315 deg. (b) Blade azimuthal position: 321 deg. (c) Blade azimuthal position: 327 deg.

Figure 6.30: DES05 trailing edge flow - time visualisation via contours of local span-wise vorticity ω_x and iso-lines of pressure at $0.7R$. The cyclical movement of the pressure iso-lines towards and away the trailing edge observed at $0.5R$ is still present here, although with smaller displacements.

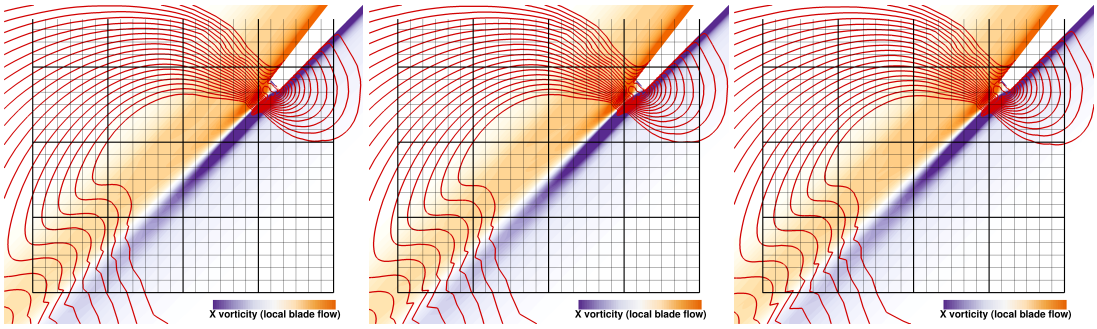

(a) Blade azimuthal position: 315 deg. (b) Blade azimuthal position: 321 deg. (c) Blade azimuthal position: 327 deg.

Figure 6.31: DES05 trailing edge flow - time visualisation via contours of local span-wise vorticity ω_x and iso-lines of pressure at $0.95R$. At this location, the tip vortex dominates the flow dynamics and no periodic pressure oscillations are visible in the near-wake.

Looking at the blade near-wake at $0.5R$ and $0.7R$ (Figures 6.29 and 6.30), the high pressure peak down-stream the recirculation region is seen to pulse with time. This makes move the pressure iso-lines in the wake cyclically toward and away the trailing edge, and leads to oscillations in the pressure field on the airfoil suction side close to the trailing edge. These pressure oscillations get smaller moving outboard along the blade span, until they vanish at about $0.95R$ (Figure 6.31), where the tip vortex dominates the the flow dynamics. The fast pressure fluctuations recorded by the numerical probes in the near-wake at inboard stations can be therefore explained by the pulsation of the high pressure center at the back of the trailing edge. This is, in turn, likely due to the small unsteady structures developing behind the thick trailing edge of the blade, where turbulence and three-dimensional effects may play a significant role.
The difference in the predicted oscillations frequency between DES1 and DES05 results is likely due to a better resolution of the flow dynamics thanks to the smaller time-step, and/or to an incomplete convergence of the computations.
Note that the SAS and SST simulations do not show these fluctuations probably because these models predicts a higher eddy viscosity for the flow behind the trailing edge, which prevents the development of turbulent structures at this small scale and damps high-frequency unsteadiness.

Simulations Time Resolution Refinement

A second set of DES simulations was carried out to study the effect of the time discretisation on the high-frequency pressure oscillations. Additional computations were thus performed using a time resolution equivalent to 0.25 and 0.1 degrees of propeller azimuth. Both simulations were started using the DES05 final flow-field as initial condition.
Unsteady pressure time histories and PSDs relative to the last half-revolution are shown in Figures 6.32 and 6.33, for all the considered temporal resolutions at some blade span-wise stations. The DES025 and DES01 results display the fast pressure oscillations already observed in the solutions obtained with the larger time-steps. In these cases, however, fast pressure fluctuations are also present at $0.95R$. As seen by analysing DES1 and DES05, a finer time resolution leads to larger pressure fluctuations magnitude, and also to a higher frequency of the associated peak in the spectrum. This trend is confirmed by comparing DES01 and DES025 (see Figure 6.34), but the difference is much smaller, especially in terms of amplitude, suggesting that the convergence of the temporal discretisation is nearly achieved.

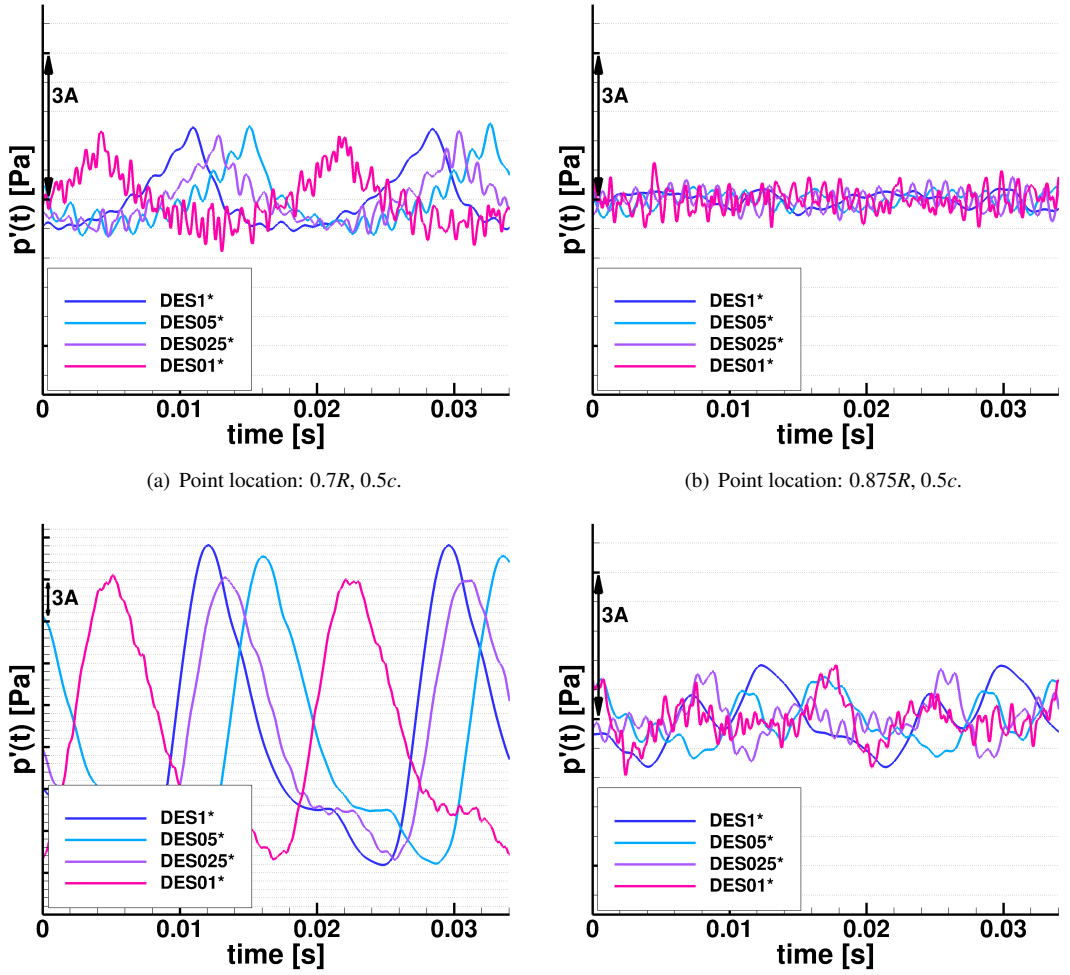

(a) Point location: 0.7R, 0.5c.

(b) Point location: 0.875R, 0.5c.

(c) Point location: 0.95R, 0.5c.

(d) Point location: 0.975R, 0.5c.

Figure 6.32: DES time refinement analysis: unsteady pressure signals in the blade near-wake for half propeller revolution. Note that the phase shift between the signals of the various cases is only due to the different simulation angles range presented. Also DES025 and DES01 display the fast oscillations obtained with the larger time-steps, and exhibit them at 0.95R as well.

6.3.3 Conclusive Remarks

The presented results allow to draw some conclusions about the capability of the considered methods to capture the blade wake unsteadiness and the flow turbulent dynamics beyond tonal content. The following was achieved:

1. The second generation URANS method SAS does not appear to be effective, because it fails to capture the high-frequency flow structures. It is possible that a finer time discretisation than the one used here (i.e. 0.5 propeller rotational degrees) allows for a better resolution of the small scales. However, its computational cost is larger than that of DES, making the approach less preferable.

2. The hybrid URANS-LES method DES yields a near-wake unsteady pressure

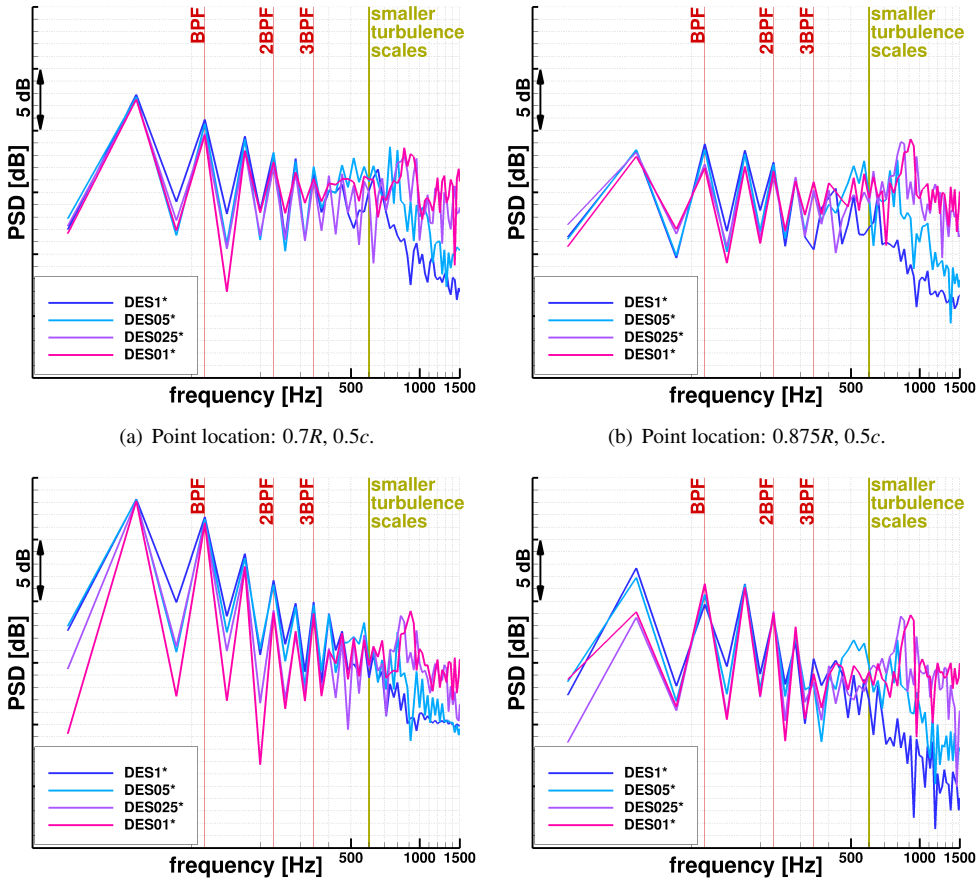

(a) Point location: 0.7R, 0.5c.

(b) Point location: 0.875R, 0.5c.

(c) Point location: 0.95R, 0.5c.

(d) Point location: 0.975R, 0.5c.

Figure 6.33: DES time refinement analysis: PSD of the unsteady pressure in the blade wake. The finer the time-step, the higher the peak frequency and the larger the magnitude predicted.

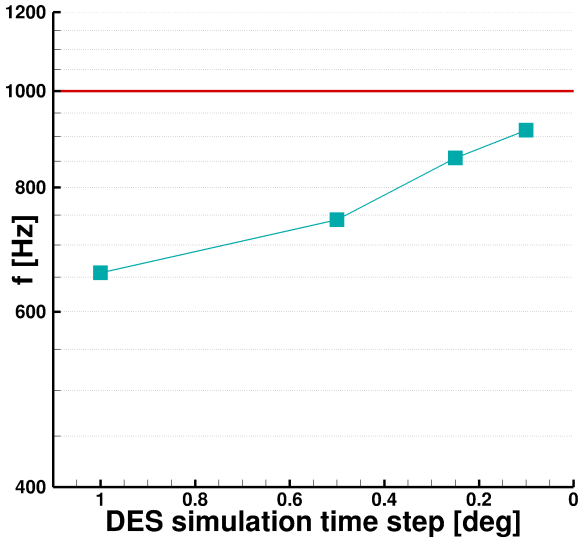

Figure 6.34: DES time refinement analysis: peak frequency of pressure oscillations related to small turbulent scales captured by DES as function of the time-step size of the simulation. The time-step size is seen to be critical for accurate predictions of trailing-edge noise. The choice of 0.1 deg of propeller rotation appears not far from convergence, but still not adequate.

spectrum more rich and continuous at high frequencies, with a clearly identifiable peak approaching 1 kHz as the time resolution gets finer, which is typical of trailing edge noise. Both space and time discretisations are equally important to accurately resolve this part of the spectrum.

These findings are in agreement with the conclusions of the European project DESider [266], which stated that the SAS model is more suitable for strongly unstable flows, whereas the DES model is more appropriate in the case of less unstable flows. This is because the scale-resolving mode of the SAS is not triggered if the flow is not sufficiently unsteady and separated.

Chapter 7

Co-rotating *vs* Counter-rotating Turboprop Layouts*

In this Chapter, the near sound field of a complete twin-engine turboprop aircraft with different propeller installation layouts is studied. This aims to assess the impact of "handedness", i.e. co-rotation vs counter-rotation, on the airplane acoustics. Unsteady RANS simulations are used to directly analyse the fuselage exterior noise, whereas experimental transfer functions are employed to estimate the interior cabin sound levels.

Co-rotating propellers and counter-rotating configurations with top-in and top-out rotation are considered. The last option is known to be more aerodynamically efficient[267]. The main advantages of counter-rotating propellers are the natural balance of roll and yaw moments, and of the P-factor. So, no engine is critical in this layout[268]. For these reasons, they are sometimes employed on military aircraft, of which a recent example is the A400M military transport aircraft. Civil turboprops adopt, instead, co-rotating propellers (see Table 7.1) because of lower maintenance costs and logistic reasons, since only one type of spares engines, gearbox and blades are required.

The two propellers are always assumed to be synchronised, i.e. their RPM precisely match, as it is usually done to improve passenger and crew comfort. This is because an audible vibration arises when the propellers do not turn with the same angular velocity. The two propellers are also considered in phase at this stage, i.e. $\psi_s = 0$ deg. A study of synchrophasing is presented in Chapter 8.

It is emphasised that the goal of the present research is not to estimate the absolute noise levels of each propeller installation options, but to carry out a relative study to

* The work presented in this Chapter is published in G. Chirico *et al.* , "Propeller installation effects on turboprop aircraft acoustics", *Journal of Sound and Vibration*,Vol. 424 (2018), pp. 238–262, doi:10.1016/j.jsv.2018.03.003

Aircraft	Category	Layout	Synch.
Bombardier Dash8 Q400	Civil	CO	YES
ATR 72	Civil	CO	YES
Fokker F50	Civil	CO	YES
Saab 2000	Civil	CO	YES
Fairchild-Dornier 328	Civil	CO	YES
Piper PA-44 Seminole	Civil	CNT	YES
Lockheed C-130J Super Hercules	Military	CO	YES
Lockheed P-3 Orion	Military	CO	YES
Alenia C-27J Spartan	Military	CO	YES
Airbus A400M Atlas	Military	CNT (on each wing)	YES
Bell Boeing V-22 Osprey	Military	CNT	NO

Table 7.1: Configuration of the main turboprop, with tractor propellers, and tilt-rotor aircraft currently operating, or of the recent past: CO = co-rotating propellers, CNT = counter-rotating propellers.

find if one configuration is acoustically advantageous with respect to the others.

7.1. Numerical Setup

The airplane considered in this analysis is a twin-engined turboprop, with a standard commercial high-wing design and a capacity of around 70-80 passengers, similar to the ATR72, the Bombardier Dash 8 series or the Fokker 50. The aircraft computational geometry is shown in Figure 7.1, along with its dimensions. It is a generic shape adopted in the IMPACTA project[8, 9]. No geometry simplifications were made, except for the lack of the horizontal and vertical tail surfaces that is not altering the cabin noise.

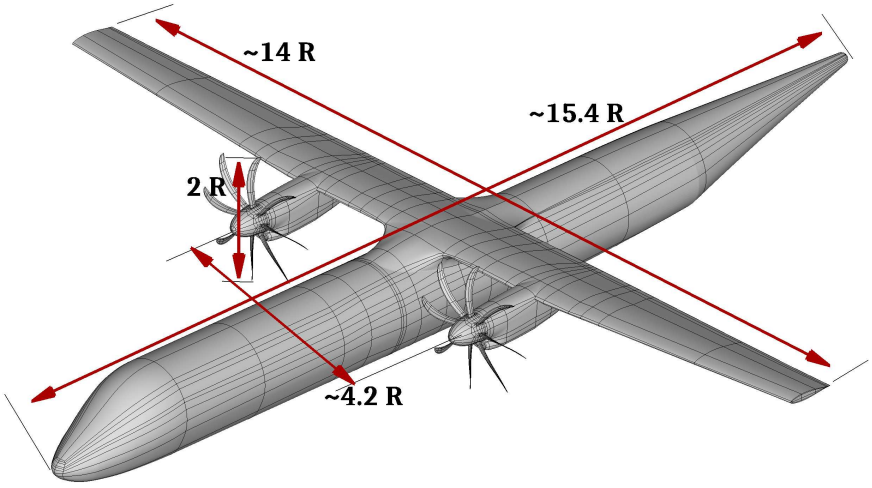

Figure 7.1: Turboprop computational geometry with dimensions as function of the propeller radius R.

The propeller employed is the Baseline design of the IMPACTA propeller (see Chapter

5 for a detailed description). Geometric parameters and flight cruise conditions are reported in Table 7.2. A cruise flight is here considered, since it is usually the longest segment of the aircraft route where propellers are the major noise source. It is noted that results may differ in climb, because of the different propeller operating conditions.

Radius R	2.21 m	Free-stream Mach number M_∞	0.5
Root chord c	0.213 m	Thrust line incidence	-2 deg
Pitch angle (0.7R)	$\sim 51^\circ$	Helical Mach number (0.95R)	0.789
Angular velocity	$\sim$850 RPM	Tip Reynolds number Re_{TIP}	1.24e06
Required Thrust	7852 N	Altitude	7620 m

Table 7.2: IMPACTA Baseline propeller parameters and nominal cruise operating conditions.

7.1.1 Test Cases

The following three options are considered:

1. Co-rotating propellers **(CO)**: conventional layout for civil aircraft with both propellers rotating clockwise as viewed from the rear - Figure 7.2(a);
2. Counter-rotating top-in propellers **(CNTI)**: port propeller rotating clockwise and starboard propeller counterclockwise as viewed from the rear, thus both propellers approach the fuselage when moving down-wards - Figure 7.2(b);
3. Counter-rotating top-out propellers **(CNTO)**: opposite of **CNTI**, port propeller rotating counterclockwise and starboard propeller clockwise as viewed from the rear, thus both propellers approach the fuselage when moving up-wards - Figure 7.2(c).

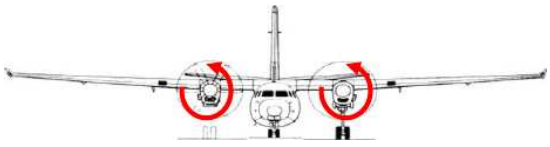

(a) **CO** - co-rotating.

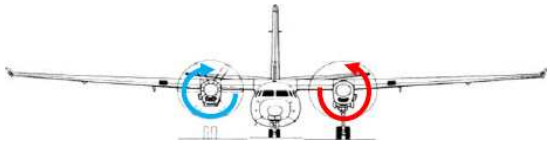

(b) **CNTI** - counter-rotating top-in.

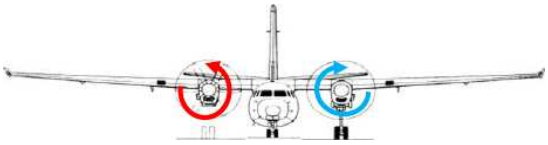

(c) **CNTO** - counter-rotating top-out.

Figure 7.2: Definition of the turboprop layouts considered. The aircraft sketch used to create these figures represents a Fokker 50 and was taken from [269].

Systems of Reference Definition

For convenience, a cylindrical system of reference is introduced to present data on the aircraft fuselage. The fuselage azimuthal coordinate Θ goes clockwise as viewed from the front of the aircraft, as defined in Figure 7.3. The longitudinal axis X is parallel to the fuselage center-line, positive in the flow direction, and with its origin at the propeller rotational plane.

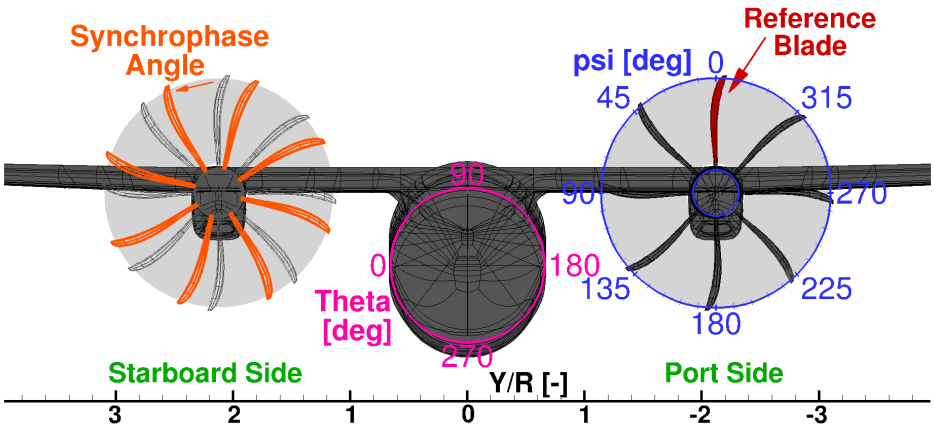

Figure 7.3: Definition of reference blade, blade azimuth angle ψ (increasing with the propeller rotation, regardless of the direction), fuselage azimuth angle Θ, and positive synchrophasing angle ψ_s (shifted blades in orange).

7.1.2 Computational Grids

Multi-block structured grids, generated with the ICEM-Hexa™ software of ANSYS, were employed. A fully-matched body-fitted mesh was built around the whole aircraft, adopting an "O" grid topology surrounding the surfaces of fuselage, wings and nacelles. Special attention was paid to have a good quality mesh in areas proved critical in preliminary tests, such as the fuselage-wing junction. Propellers are included in the airplane grid using the sliding plane technique[241] which allows for the relative motion and the exchange of information between the two meshes with a set of pre-calculated interpolation weights. The grids for all different cases were thus obtained just selecting the appropriate propellers during the assembling process. The aircraft mesh is then immersed, with the chimera over-set method[242], in a regular background grid which extends until the far-field. The layout of the complete grid, as well as block topology and mesh, are visualised in Figure 7.4. The aircraft grid was prepared for half of the model and then mirrored, to ensure perfect symmetry of the computational domain. Similarly, the propeller meshes were generated by copy-rotating a single-blade grid, mirroring in the case of opposite propeller rotation.

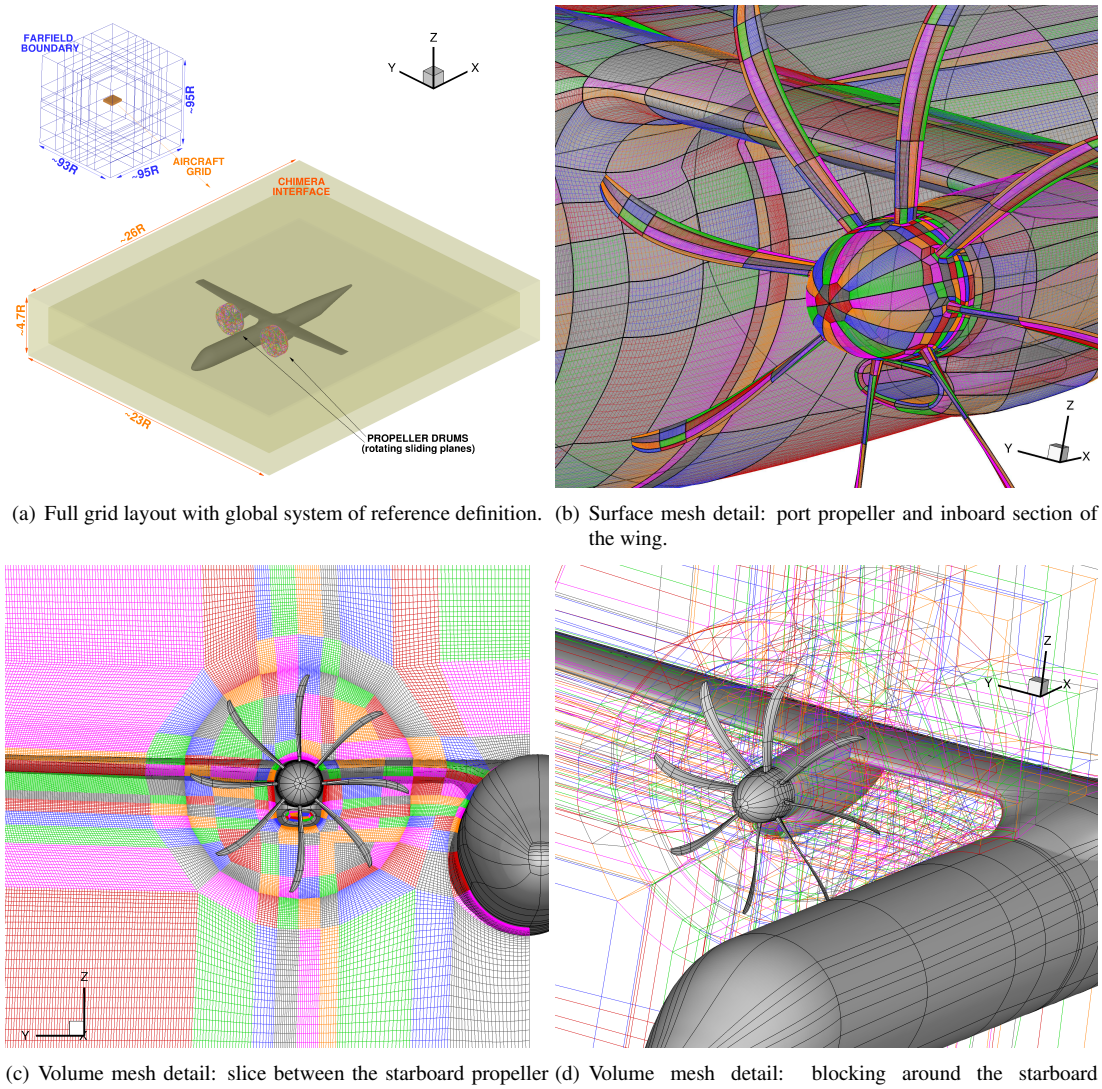

(a) Full grid layout with global system of reference definition.

(b) Surface mesh detail: port propeller and inboard section of the wing.

(c) Volume mesh detail: slice between the starboard propeller and the wing (frontal view).

(d) Volume mesh detail: blocking around the starboard propeller.

Figure 7.4: High-wing twin-engined turboprop aircraft: grid visualisation.

Overall, the full grid counts 13326 blocks and 170 million cells, of which 132 million belong to the airplane mesh and 16.5 million to each propeller. In the region of interest, the adopted spatial resolution has a maximum mesh spacing of $c/4$. This guarantees, at the operating conditions analysed, a minimum of 17 points per wave length for the third propeller tone, which was found adequate for near-field predictions in solver validation studies carried out on an isolated propeller.

Boundary Conditions

The aircraft surfaces are treated as solid walls. At the inlet boundaries, which are located far enough from the engine intakes, a surface pressure equal to the free-stream value is imposed and other variables are extrapolated. Free-stream boundary

conditions are applied on the external boundaries of the computational domain.

7.1.3 Simulations Details

Simulations were performed solving URANS equations, as the most efficient CFD method able to capture the propeller tonal noise, which is the main contribution to the overall interior noise. No attempt was made at this stage to study the broadband noise content. The $k-\omega$ SST turbulence model[215] was employed to close the equations. Computations were started for all cases from unperturbed free-stream flow conditions, accelerating gradually the propeller up to the cruise angular velocity in the first half of propeller revolution. A temporal resolution of 1 degree of propeller azimuth, i.e. 360 steps per propeller revolution, was chosen to guarantee smooth and fast convergence at each time-step of the simulation. The resulting Nyquist frequency allows to solve up to frequencies well above the third propeller tone. Using 17 computing nodes, each with two 2.1 GHz 18-core Intel Xeon E5-2695 series processors, one complete propeller revolution took 66 hours. Four full propeller revolutions were run before reaching an adequate convergence of the global flow-field in the region of interest for the analysis. Numerical probes are also included in the simulations to directly record the time pressure signal on the fuselage in the main propeller region of influence, from 1 R upstream the propeller plane to the wing junction area (see Figure 7.5). For monitoring purposes, additional probes are located along some span-wise wing stations and the engine intake.

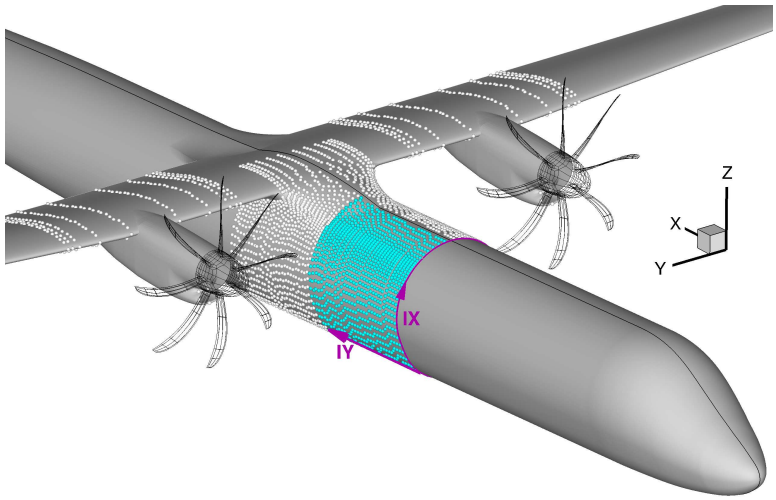

Figure 7.5: Locations of the numerical probes employed for the aircraft noise study, in light-blue those used as input to the transfer functions in the interior noise estimation.

Main parameters of the computational setup are summarised in Table 7.3.

Free-stream reference Mach number M_∞	0.5
Free-stream reference Reynolds number Re_∞	0.99e06
Maximum grid spacing in region of interest Δs	$c/4$
Boundary layer mesh parameters	$y^+ \leq 1$, hyperbolic points distribution with stretching ratio from 1.12 to 1.14
CFD method	URANS ($k-\omega$ SST)
Temporal resolution Δt	1 deg of propeller rotation

Table 7.3: Computational setup's main parameters for the IMPACTA aircraft simulations.

7.2. Aerodynamic Analysis

To show the complex characteristics of the flow-field generated from the interaction of the tractor propellers with the airframe, in Figure 7.6 the vortical structures are shown for the co-rotating layout. The adopted mesh resolution preserves the propellers' wake up to the aircraft tail. The interaction of the blade tip vortices with the wing is well captured by the CFD simulation which is able to show the different flow features of the flow-field in the case of inboard-up or -down propeller rotation. The vortices generated from the wing tips, the nacelles and the inclination of the aft fuselage are also visible.
Figure 7.7 presents a visualisation of the mean pressure field around the aircraft, in particular on a transversal plane at approximately $1R$ behind the propeller plane and on a longitudinal plane at spinner height. The average was computed over a quarter of a propeller revolution, using the volume CFD solution at all solved time steps. Pressure perturbations caused by the presence of the lifting wing and the thrusting propellers are well represented by the numerical results. The high-pressure bubble generated at the aircraft nose in the case of a subsonic motion is also captured, and observed as well at the tip of the spinners. The pressure field is, as expected, symmetric for the counter-rotating layouts, while starboard and port side are significantly dissimilar.
Appreciable differences, amongst the three configurations, appear only in the vicinity of the propeller, and particularly under the wing. The pressure field shows higher levels and steeper gradients on the up-stroking blade side, i.e. inboard for a top-out propeller rotation and outboard for a top-in propeller rotation. In the latter case, the depression zone that develops around the lower part of the nacelle is also more extended inboard, and reaches the fuselage surface.

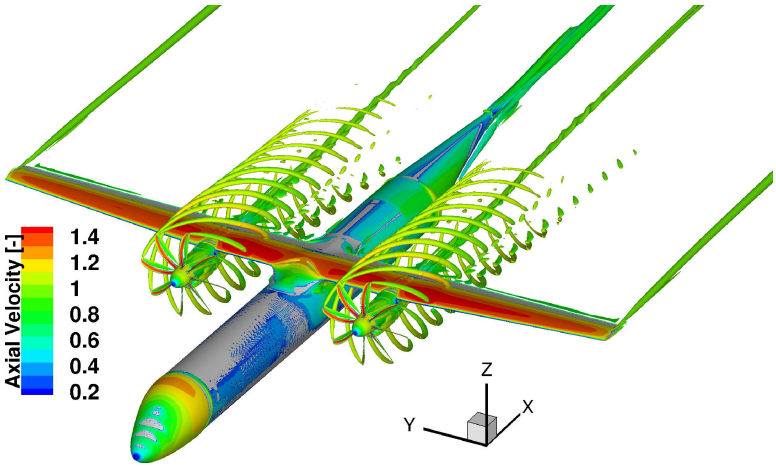

(a) Iso-surfaces of Q, colored by non dimensional axial velocity.

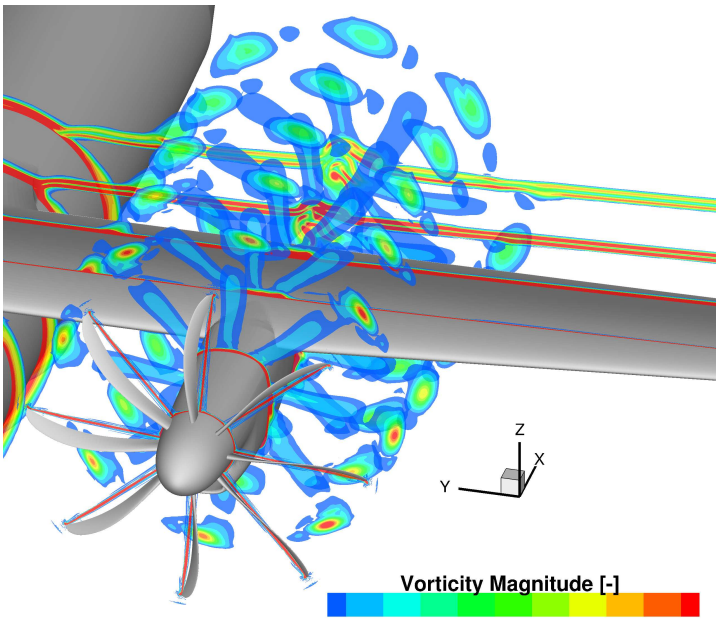

(b) Vorticity contours down-stream the port propeller.

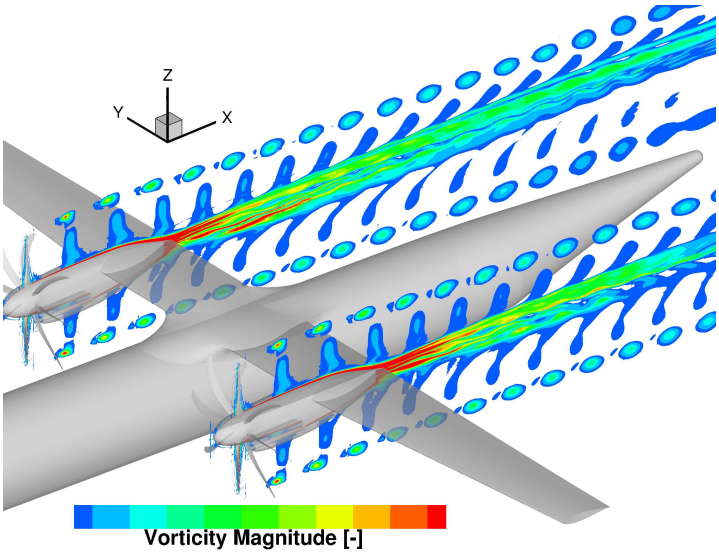

(c) Vorticity contours on the propellers longitudinal symmetry planes.

Figure 7.6: Visualisation of instantaneous vortical structures for the **CO** case: $\psi_b = 90$ deg. The mesh density allows to preserve the propeller wake up to approximately the aircraft tail and to resolve well the interaction tip vortices-wing.

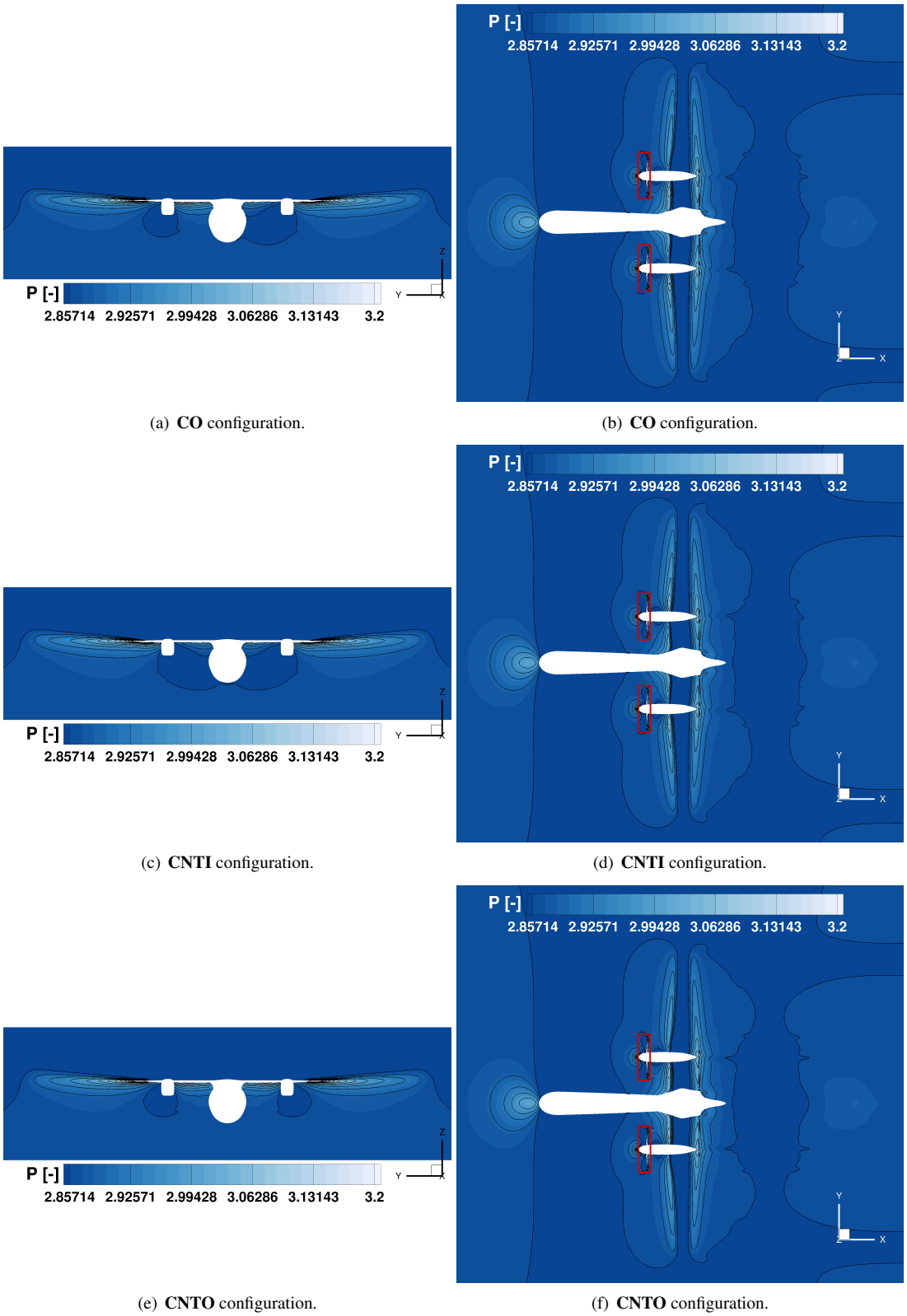

(a) **CO** configuration.

(b) **CO** configuration.

(c) **CNTI** configuration.

(d) **CNTI** configuration.

(e) **CNTO** configuration.

(f) **CNTO** configuration.

Figure 7.7: Averaged pressure field visualisation: comparison between the different installation configurations. Transversal plane at $\sim 1R$ behind the propeller plane on the left, longitudinal plane at propeller spinner height on the right (in red, the boundary of the rotating propeller grids). Counter-rotating configurations exhibits a symmetric pressure field. Differences between the different layouts appear only in the vicinity of the propellers. Higher pressure levels and steeper gradients are seen on the up-stroking blade side. For a top-in rotational direction, the area of low pressure around the nacelle extends up to the fuselage.

7.2.1 Aircraft Trimming Discussion

Because of the lack of the horizontal and vertical tail surfaces in the computational geometry, it was not expected to achieve a complete trim state in the flight direction. A small thrust surplus with respect to the aircraft drag was in effect found for the nominal conditions simulated (see Table 7.2). However, mean wing and propeller loads are suitably representative of cruise conditions. Therefore, being primarily interested in a comparative study among the different installation layouts, no attempt to trim the aircraft by changing the blade pitch was carried out. A discrepancy of less than 0.03% in the total propellers thrust was registered between all cases analysed and this was considered enough to achieve relative data with satisfactory accuracy.
The side force Fy and roll moment Mx, scaled with the port propeller thrust T_p and torque Q_p, respectively, are reported in Table 7.4 to quantify the natural aircraft equilibrium state, i.e. without any control surfaces. The co-rotating configuration shows unbalanced forces and moments, and is likely to result in considerably more trim drag. This is not the case for the counter-rotating layouts because of their symmetry.

	CO	**CNTI**	**CNTO**
Fy/T_p	21.303	0.046	0.001
Mx/Q_p	89.195	0.0215	0.0003

Table 7.4: Aircraft equilibrium state for the different installation layouts with no control surfaces active. Fy is the resultant side force, Mx the resultant roll moment, T_p and Q_p the thrust and torque of the port propeller.

7.2.2 Aircraft Loads Analysis

Figure 7.8 shows the average surface pressure distribution on the aircraft for the various configurations. The influence of the propeller on the wing loading is clearly visible, causing a modification of the pressure distribution on the wing region affected by the propeller slipstream. The effect depends on the rotational direction of the propeller: the wing experiences a loading increase on the propeller up-wash side and a decrease on the propeller down-wash side. In the case of propeller top-out rotation, the suction area on the wing inboard upper surface is observed to extend up to the wing-fuselage junction.
A comparison of the average span-wise normal pressure loading for the different configurations is presented in Figure 7.9. The reference line representing the clean aircraft case (no propeller installed) allows to distinguish the effects of the nacelle and that of the propellers. The lift gain and reduction due to the propeller swirl that modifies the local wing angle of attack in the propeller region of influence is evident.

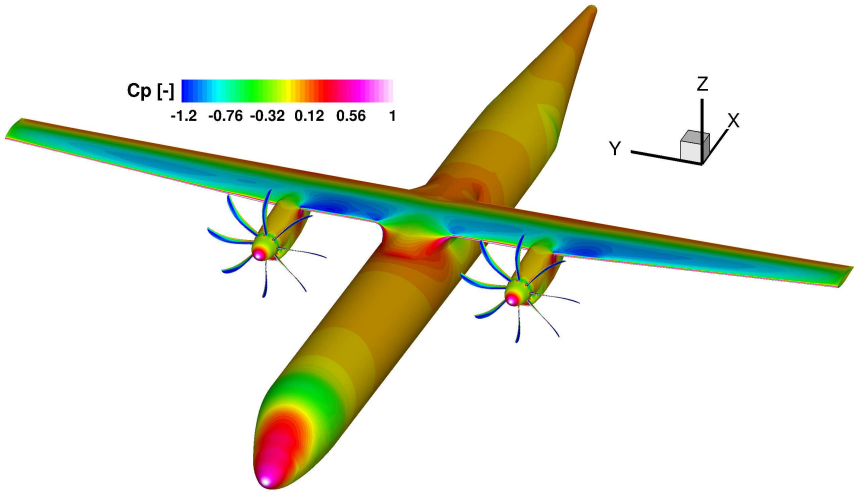

(a) **CO** configuration.

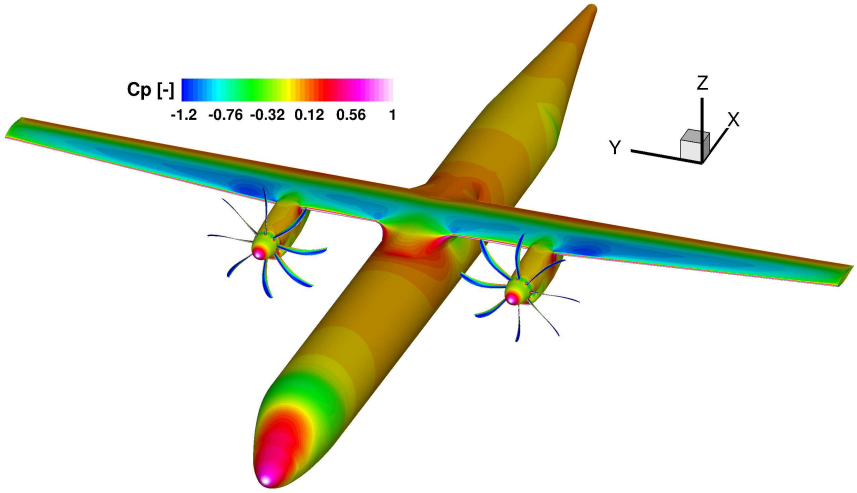

(b) **CNTI** configuration.

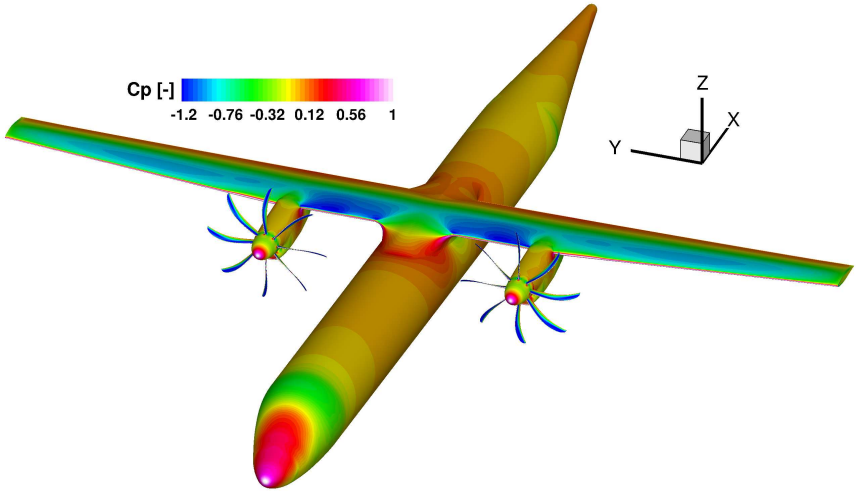

(c) **CNTO** configuration.

Figure 7.8: Averaged pressure loading on the aircraft. The propellers clearly affect the wing loading, generating an increase on the up-wash side and a decrease on the down-wash side.

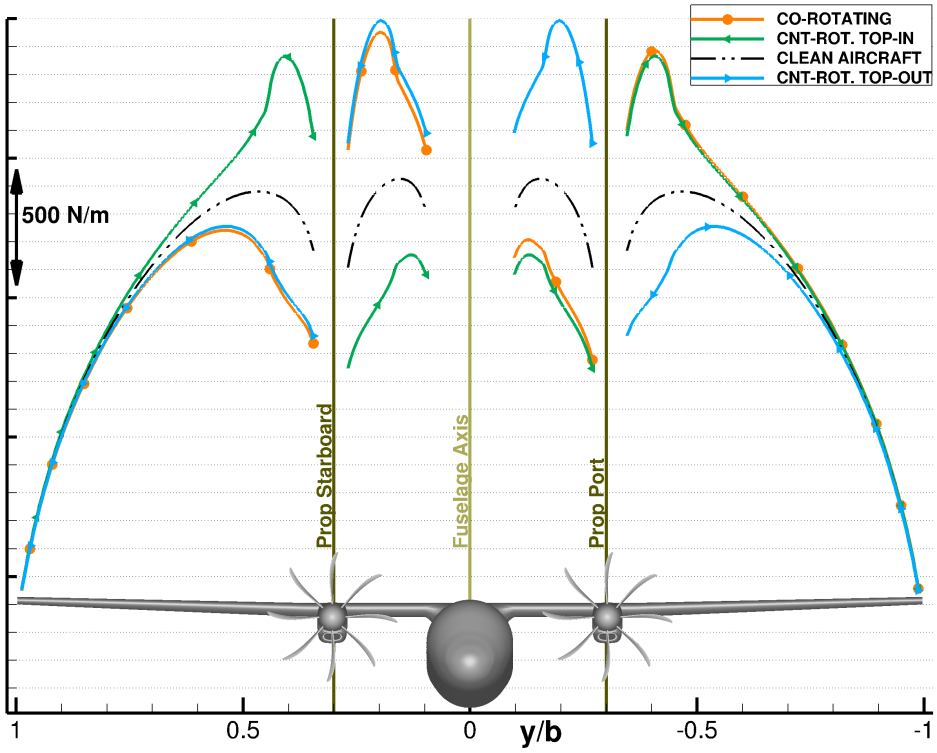

Figure 7.9: Span-wise normal averaged pressure force distribution over the wing: comparison between different layouts and clean aircraft as reference. The three configurations provide overall a similar lift, the gain/reduction due to the propeller swirl being important. Span-wise differences are noted up to mid-span for the same propeller rotation between co-and counter-rotating layouts, indicating the need of considering both propellers for accurate load distribution predictions.

Small differences are also visible in the loads of the inboard wing, up to around mid-span, for the same propeller rotation in the case of co-rotating and counter-rotating layouts. This suggests that for accurate load predictions both propellers must be considered, studying an isolated wing with a propeller may not be enough. Overall, the total average lift of the three configurations is quite similar: the counter-rotating top-in option gives 1.16% less than the co-rotating option, while the counter-rotating top-out option 1.19% more. As a measure of the aerodynamic efficiency, Table 7.5 presents the lift over drag ratio for each installation layouts. In line with previous studies[267], the counter-rotating top-out configuration appears to be the best design choice from the aerodynamic point of view. This is mainly due to the reduction of the drag pressure component (-0.81% with respect to the co-rotating case), in conjunction with the above mentioned lift increase.

	CO	**CNTI**	**CNTO**
Lift/Drag	20.334	20.178	20.663

Table 7.5: Aerodynamic efficiency† for the different installation layouts.

7.2.3 Propeller Loads Analysis

The presence of the nacelle and the wing also affects the propeller, yielding a periodic blade load variation during a propeller revolution. To visualise the effects of the installation, Figure 7.10 shows the propeller loads as function of the blade azimuthal position ψ for the co-rotating layout. Thrust and torque coefficients display the lar-

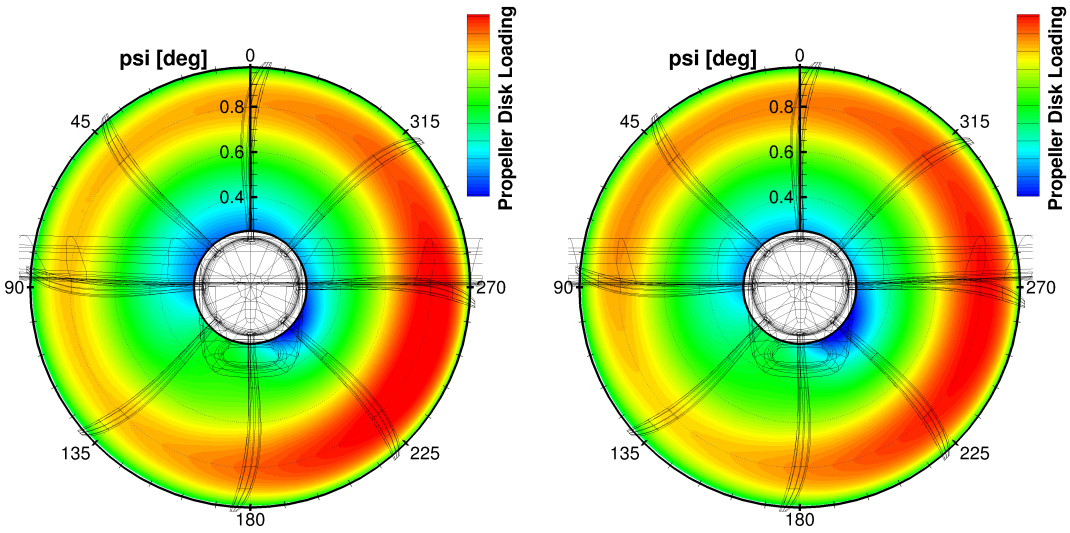

(a) Disc thrust loading for the starboard propeller, i.e. inboard-up rotating propeller (frontal view).

(b) Disc thrust loading for the port propeller, i.e. inboard-down rotating propeller (frontal view).

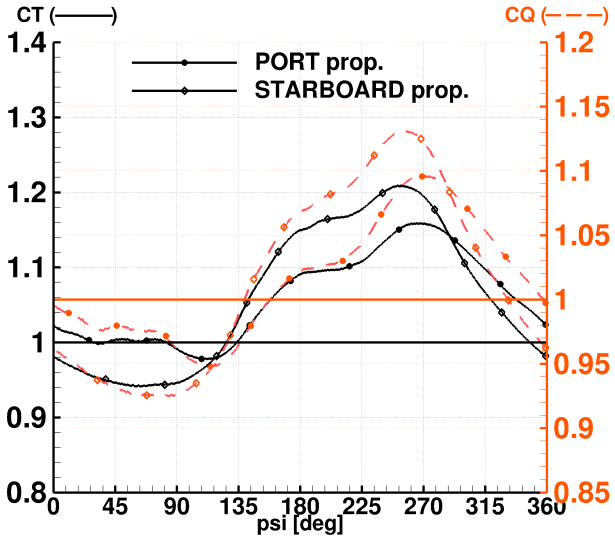

(c) Thrust and torque coefficients progress during a full propeller revolution for one blade. Results are scaled with respect to the corresponding values for the isolated propeller in axial flight.

Figure 7.10: Installation effects on the propeller for the **CO** case. Nacelle and wing cause a periodic variation in the blade loading. The negative incidence of the rotational axis makes the up-stroking blade more loaded, thus louder noise is expected to be emitted on this side of the propeller.

gest deviations from isolated axial flight values as the blade passes in front of the wing. Any deviation from symmetry observed between the up- and down-stroking blades is due both to the asymmetric wing profile and the lack of axial propeller inflow. In particular, because of the negative incidence of the propeller rotational axis (see Table 7.2), the up-stroking blade experiences a higher local angle of attack, thus resulting in higher loads. It is therefore expected that the inboard-up propeller installation option generates louder loading noise.

Overall, the propeller installed at the tested fixed-pitch cruise conditions gives about $2.7\% - 2.8\%$ more thrust than the propeller in isolation at axial flight conditions, with a penalty in the efficiency of about $0.6\% - 0.7\%$ due to an increase in torque of about 3.4%. The inboard-up layout shows a slightly higher propeller efficiency, although propeller operating conditions do not vary significantly between inboard-up or inboard-down rotation cases.

7.3. Acoustic Analysis

7.3.1 Aircraft External Sound Field

Figure 7.11 shows the instantaneous unsteady pressure field for the different layouts, on transversal and longitudinal planes. The adopted mesh resolution captures the pressure perturbations generated by the propeller blade tips and the propagation of the associated acoustic waves further down-stream, up until the rear end of the fuselage. The interaction of the sound waves with the wings is visible. Noise travelling in the up-stream direction, as well as emitted from the back of the nacelles, can be also noticed. As for the aerodynamics, the acoustic field for the counter-rotating configurations is symmetric, whereas differences between the port and starboard sides are evident for co-rotating propellers. The pressure perturbations generated by the interaction of the blade tip vortices with the wing leading-edge appear significantly larger on the up-stroking blade side. This is because of the higher loading of both propeller blade and wing. Moreover, from time visualisations (see, as an example, Figure 7.12 for co-rotating propellers), the associated sound waves are seen to be reflected by the nacelle and to interfere constructively with the direct sound field generated by the propeller rotation. Perturbations of larger amplitude thus result in the wing-fuselage junction area for inboard-up propeller rotation. In the case of co-rotating propellers, the wave front propagating up-stream after the reflection on the fuselage starboard wall is also seen considerably stronger. By contrast, for counter-rotating top-out propellers some favorable, i.e. destructive, acoustic interferences yield smaller amplitudes. Therefore,

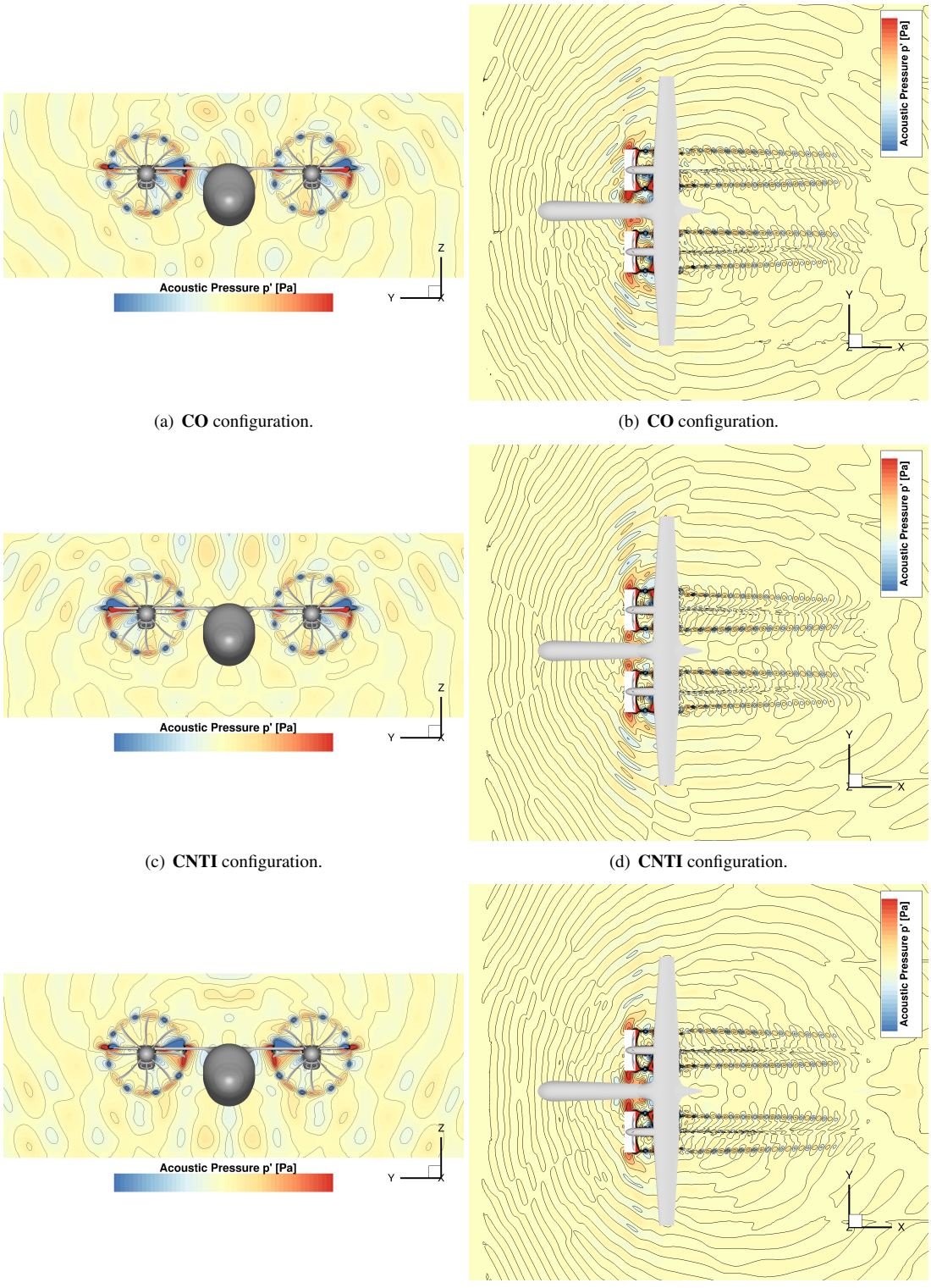

(a) **CO** configuration.

(b) **CO** configuration.

(c) **CNTI** configuration.

(d) **CNTI** configuration.

(e) **CNTO** configuration.

(f) **CNTO** configuration.

Figure 7.11: Instantaneous unsteady pressure field visualisations: comparison between the different installation configurations, $\psi_b = 90$ deg. Transversal plane at $\sim 1R$ behind the propeller plane on the left, longitudinal plane at propeller spinner height on the right. Perturbations due to the tip vortices are resolved up to the fuselage rear end. Their interaction with the wing leading edge is significantly stronger on the up-stroking blade side. Noise directed up-stream is also visible.

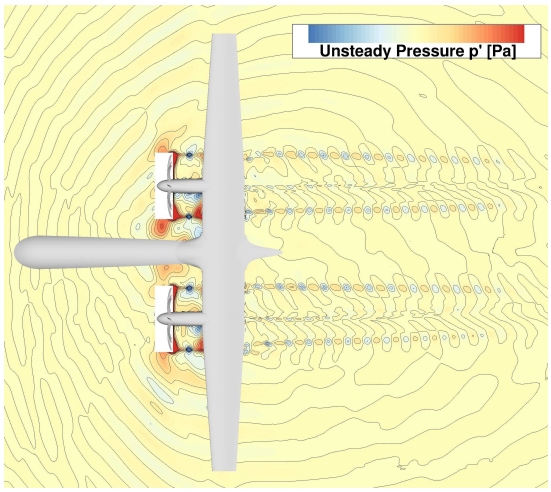

(a) $\psi_b = 45$ deg.

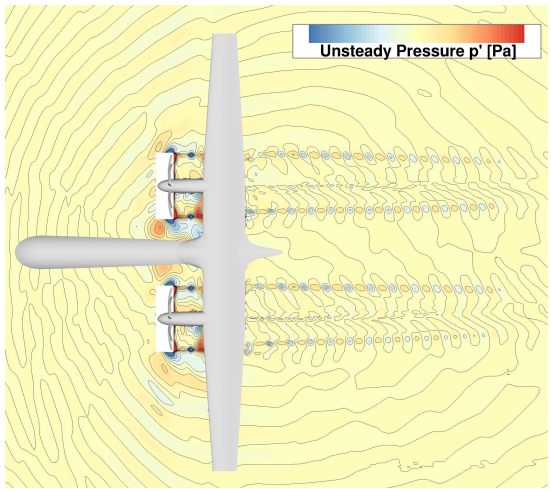

(b) $\psi_b = 48$ deg.

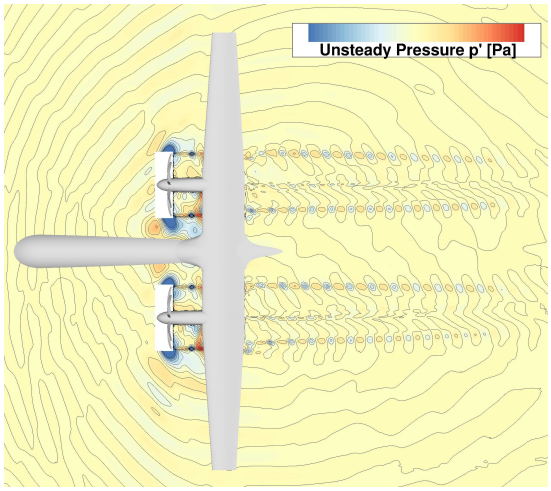

(c) $\psi_b = 51$ deg.

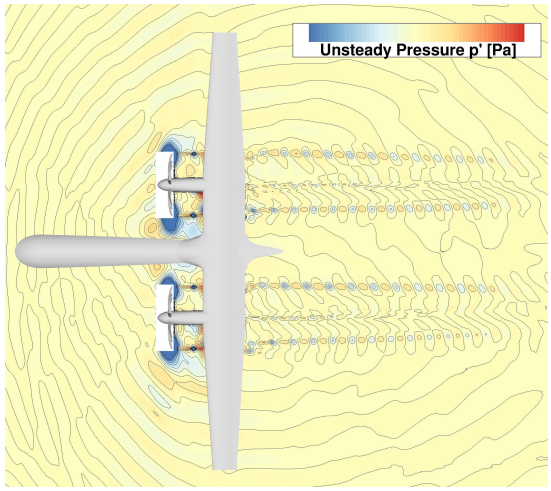

(d) $\psi_b = 54$ deg.

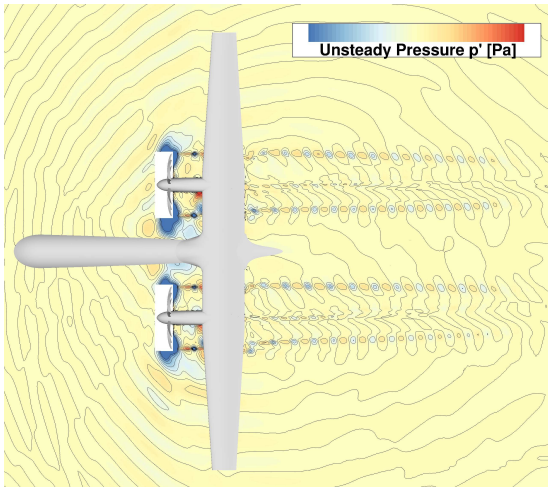

(e) $\psi_b = 57$ deg.

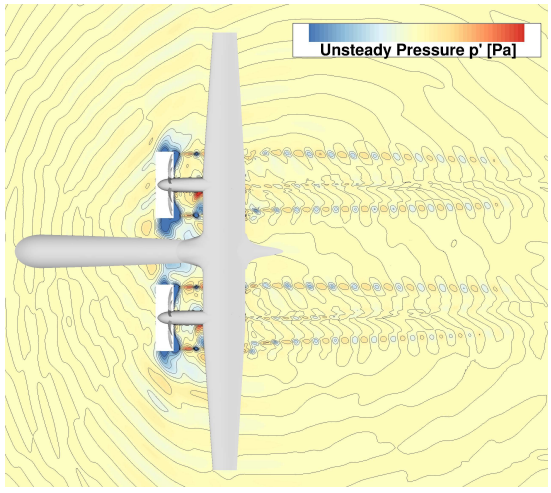

(f) $\psi_b = 60$ deg.

Figure 7.12: Unsteady pressure field time visualisation for the **CO** layout over one blade passage: longitudinal plane at propeller spinner height. *(Part 1/3)*

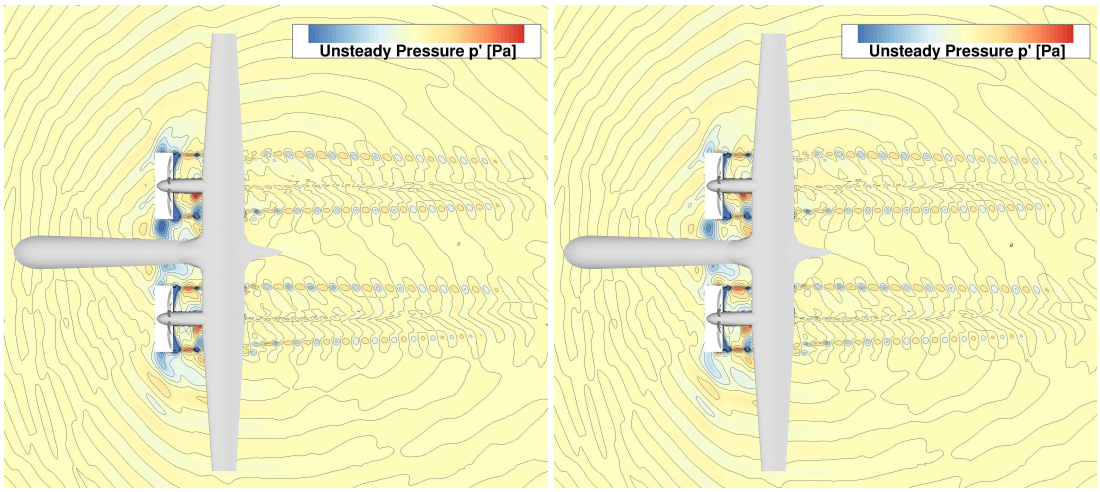

(g) $\psi_b = 63$ deg. (h) $\psi_b = 66$ deg.

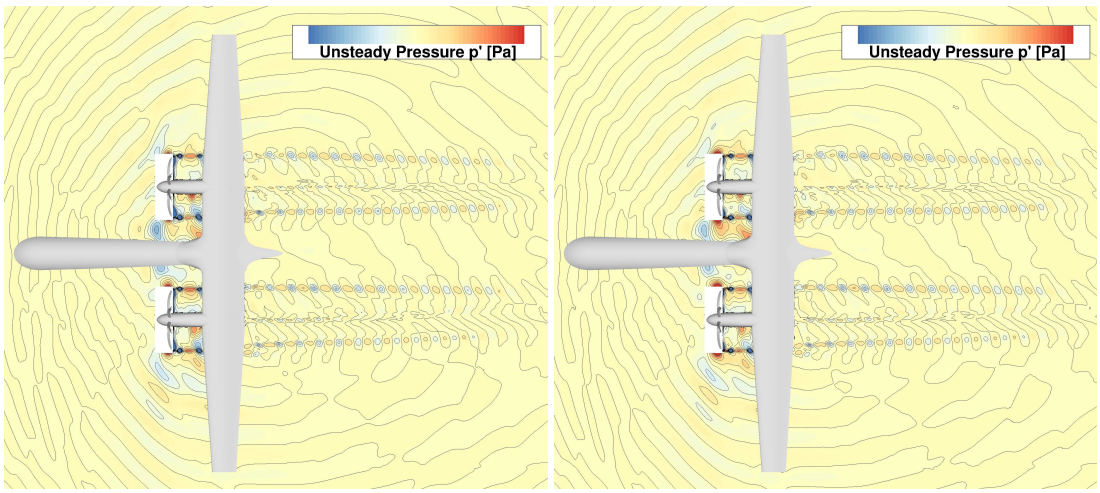

(i) $\psi_b = 69$ deg. (j) $\psi_b = 72$ deg.

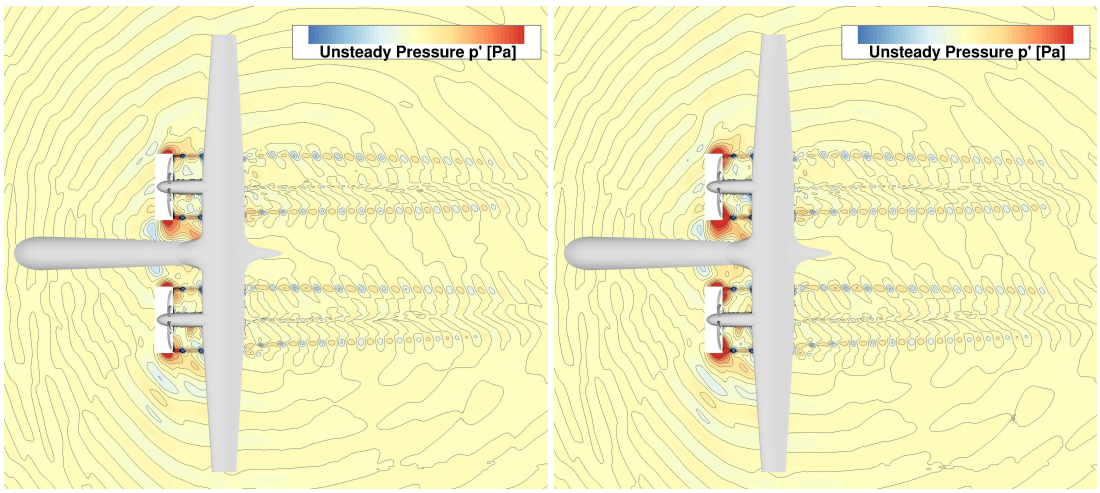

(k) $\psi_b = 75$ deg. (l) $\psi_b = 78$ deg.

Figure 7.12: Unsteady pressure field time visualisation for the **CO** layout over one blade passage: longitudinal plane at propeller spinner height. *(Part 2/3)*

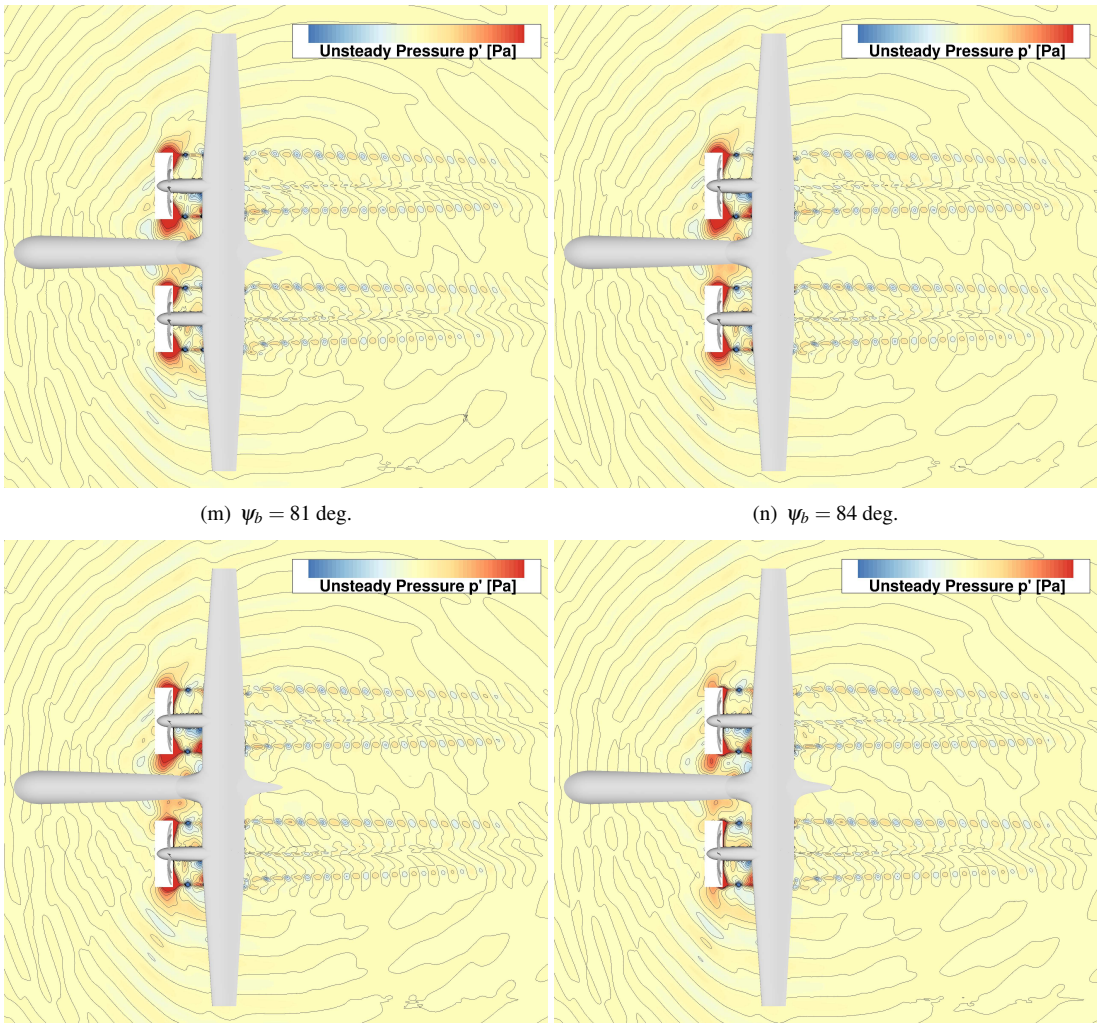

(m) $\psi_b = 81$ deg. (n) $\psi_b = 84$ deg.

(o) $\psi_b = 87$ deg. (p) $\psi_b = 90$ deg.

Figure 7.12: Unsteady pressure field time visualisation for the **CO** layout over one blade passage: longitudinal plane at propeller spinner height. *(Part 3/3)* Sound waves generated at the wing leading edge on the up-stroking blade side are reflected by the nacelle and interfere constructively with the direct sound field generated by the propeller, thus louder noise is expected in the cabin for an inboard-up rotation.

louder noise is expected in the aircraft cabin when the propeller rotates inboard-up, especially in the case of a co-rotating propellers layout.

The unsteady pressure distribution on the aircraft at a fixed instant, and the resulting overall sound pressure levels, are shown in Figures 7.13 and 7.14, respectively. The pressure perturbations due to the impact of the propeller wake on the wing leading edge are visible. Differences between the wing side in the propeller up-wash and that in the propeller down-wash are evident. As expected from the acoustic field analysis, the first shows fluctuations of larger amplitude. It also produces, in the case of inboard-up propeller rotation, a large area of high noise on the wing's lower surface, near the

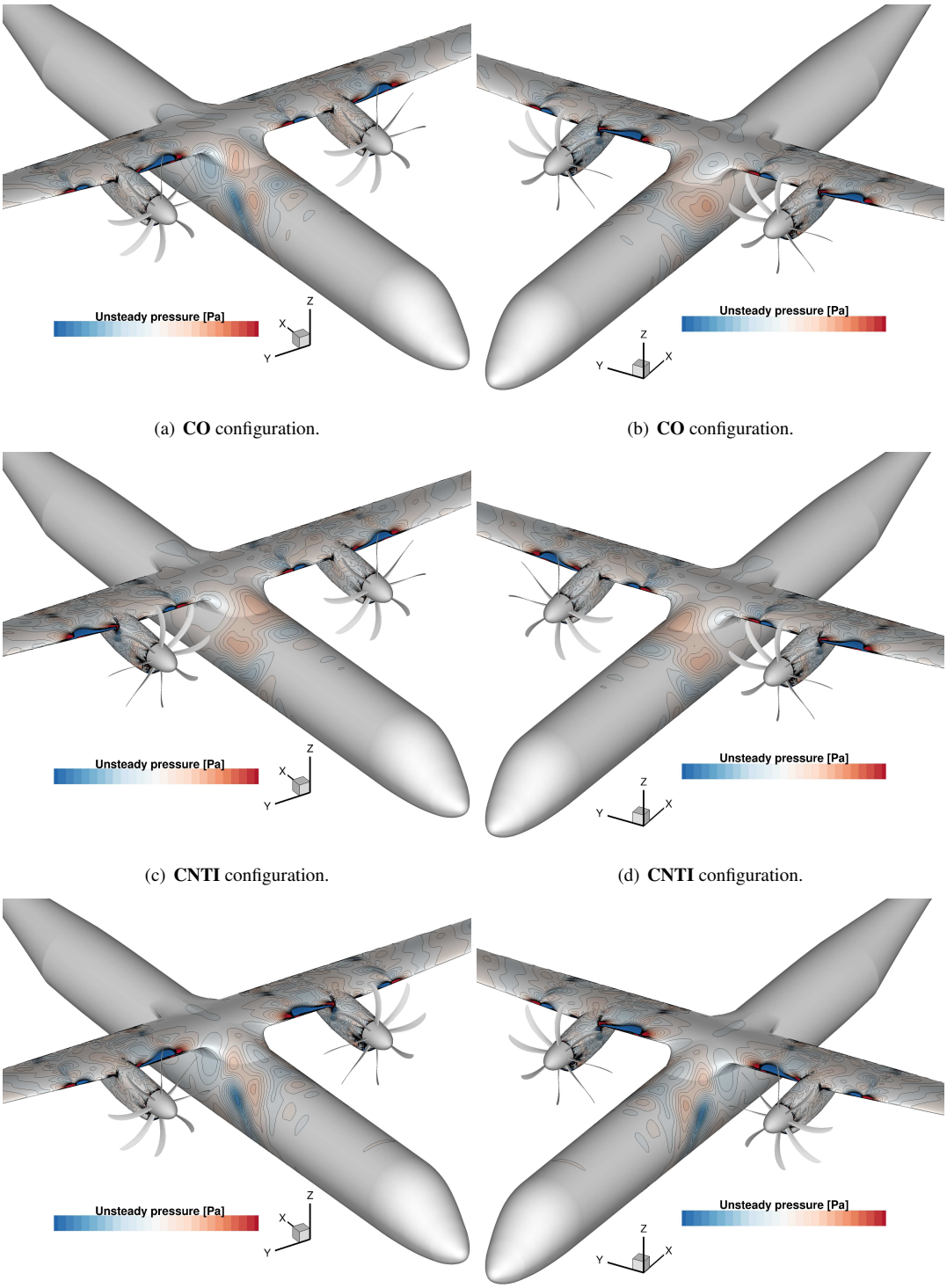

(a) **CO** configuration.

(b) **CO** configuration.

(c) **CNTI** configuration.

(d) **CNTI** configuration.

(e) **CNTO** configuration.

(f) **CNTO** configuration.

Figure 7.13: Unsteady pressure field on the aircraft, instantaneous visualisation ($\psi_b = 90$ deg) for the different layouts. View of the starboard side on the left and of the port side on the right. On the aircraft fuselage, significant fluctuations are observed in proximity of the propeller plane, from about one propeller radius up-stream up to the wing trailing edge station. On the wing, the impact of the propellers' wake appear the main source of perturbations, with big differences between up-wash and down-wash sides.

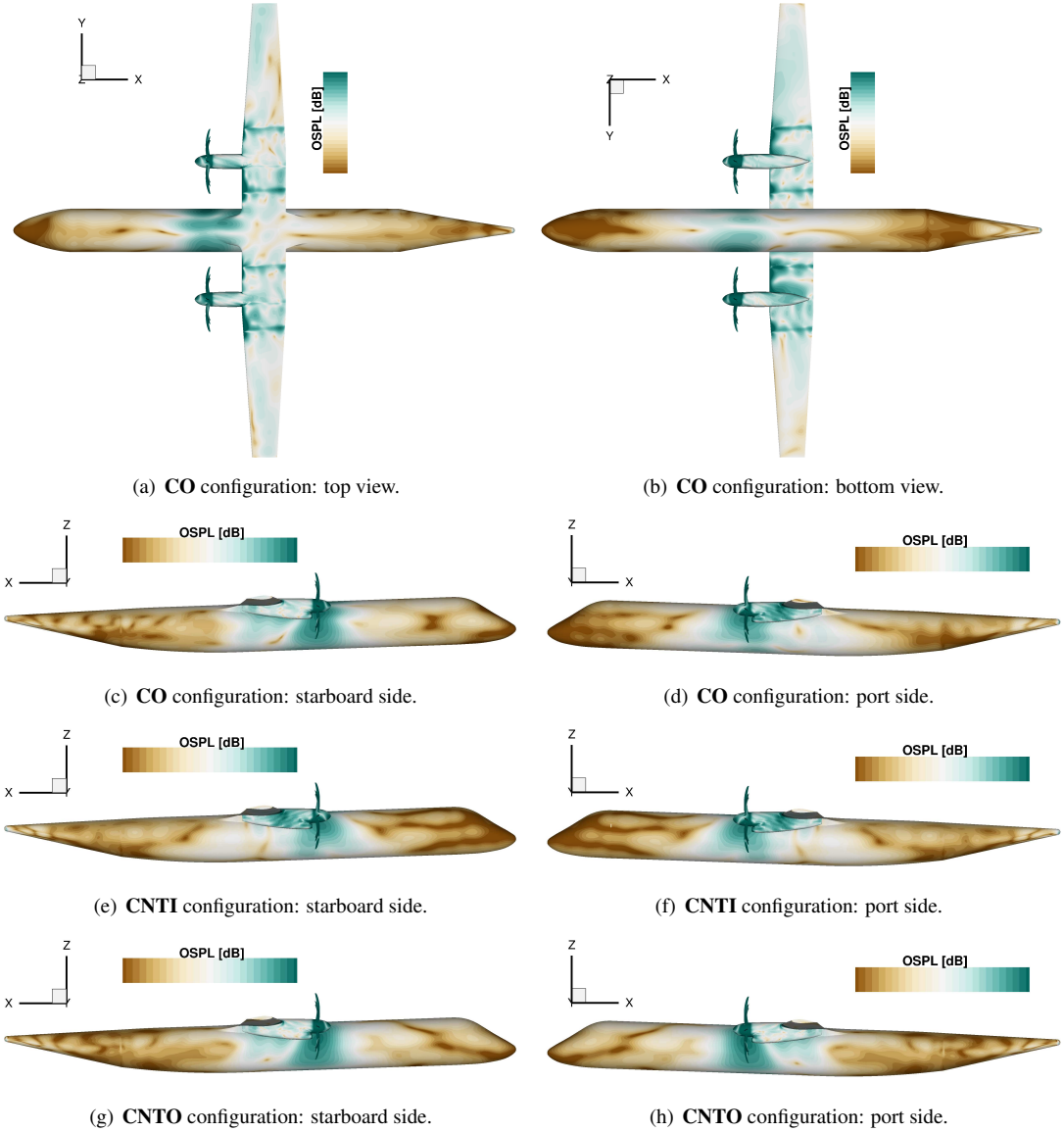

(a) **CO** configuration: top view.

(b) **CO** configuration: bottom view.

(c) **CO** configuration: starboard side.

(d) **CO** configuration: port side.

(e) **CNTI** configuration: starboard side.

(f) **CNTI** configuration: port side.

(g) **CNTO** configuration: starboard side.

(h) **CNTO** configuration: port side.

Figure 7.14: OSPL on the aircraft external surface for the different turboprop layouts: noise estimate from URANS results over a quarter of propeller revolution. Color scale range equal to 45 dB. The highest sound levels on the fuselage occur in correspondence of the propeller plane, the inboard-down rotation appearing beneficial. Port and starboard sides display a symmetric noise field for counter-rotating layouts. Differences are seen between different layouts for same rotational direction, showing the importance of the acoustic interferences between the various noise sources. A large area of high noise is noted on the wing's lower surface near the nacelle attachment in the case of an inboard-up propeller rotation, which may induce strong vibrations.

nacelle attachment. Footprints of the tip blade vortices can also be noted on the wing, on both the upper and the lower wing surfaces, at the boundary of the propeller slipstream. In agreement with the experimental findings of Sinnige *et al.* [270], these are seen to be the dominant source of pressure fluctuations on the wing. Pressure fluctuations associated with the blade root vortices are also solved by the simulation

and noticeable on the front part of the nacelles.

On the aircraft fuselage, significant pressure perturbations, and thus the highest sound levels, are observed in proximity of the propeller plane, from about one propeller radius up-stream up to the wing trailing edge station. The aircraft port and starboard sides display, as expected, a symmetric noise field for the counter-rotating propellers layouts, while differ for the co-rotating configuration. Differences in the OSPL distribution between the cases of inboard-up and inboard-down rotating propeller are evident, the second option appearing beneficial. Differences can also be seen in the unsteady pressure and OSPL on the fuselage for the same propeller rotation but for different installation options. See, for example, on the port side the differences between co-rotating and counter-rotating top-in layouts, in Figures 7.14(d) and 7.14(f), and on the starboard side between co-rotating and counter-rotating top-out layouts, in Figures 7.14(c) and 7.14(g). This proves that the interaction of the acoustic fields of the two propellers is important and that the CFD method is able to resolve it.

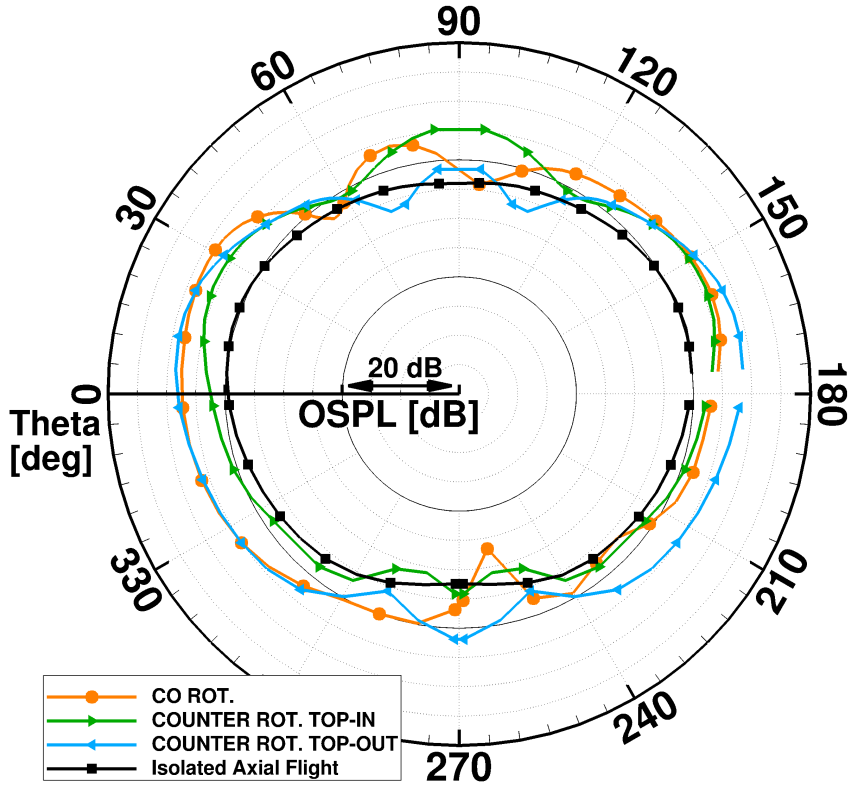

Figure 7.15: OSPL distribution as function of the fuselage azimuth Θ at the propeller plane: comparison between the different propeller installation layouts and the isolated propeller in axial flight. Noise estimate from numerical probe data over one full propeller revolution. Refer to Figure 7.3 for the azimuthal coordinate definition. The actual installed conditions modify importantly the noise field generated by the propeller, yielding on the fuselage higher levels and an irregular distribution. Differences between the various layouts are important and can reach up to 5 or 6 dB.

Data acquired by numerical probes is used for a more effective quantitative comparison between the different turboprop configurations. Figure 7.15 shows the OSPL distribution as a function of the fuselage azimuth at the propeller plane. The results for the isolated propeller in axial flight are also reported as reference.
The differences between isolated and installed propeller cases are substantial. The first shows a regular distribution on the fuselage, whereas in the installed cases the interaction of the sound fields of the two propellers and the presence of the airframe lead to an irregular noise pattern and higher noise. Results of the isolated propeller significantly underestimate the installed OSPL (up to 9 dB for positions at the passengers head height), without showing a constant shift in the predictions. Therefore, the computationally cheap simulation of a steady single blade in axial flight is not suitable for evaluating the actual sound levels on a flying aircraft.
The installed propeller cases show a local OSPL reduction around $\Theta \sim$ 55-70 deg and $\Theta \sim$ 95-120 deg, with the location of the minimum depending on the installation layout adopted. The resulting lobe at the top of the fuselage is centered in the cases of counter-rotating propellers, i.e. the maximum is at $\Theta = 90$ deg, and moved towards the side of the inboard-up rotating propeller in the case of a co-rotating configuration. Some irregularities in the OSPL trend in the installed cases are also observed in the lower part of the fuselage (240 deg $\leq \Theta \leq$ 300 deg). In the central part of the fuselage, where the aircraft masks the sound field of the second propeller, the noise distribution appears quite smooth. A noise maximum is seen around the location of minimum distance between propeller and fuselage, whose position depends on the propellers configuration. A smooth reduction follows going towards the bottom of the fuselage. Remarkable differences between the various installation layouts are noted and can reach up to 5 or 6 dB at certain azimuthal locations. As anticipated from the acoustic field analysis, the inboard-up propeller direction yields higher sound levels than the inboard-down. The co-rotating configuration exhibits a OSPL distribution very similar to that of counter-rotating top-out propellers on the starboard side for $\Theta \leq 25$ deg, and to that of counter-rotating top-in propellers on the port side for $\Theta \geq 145$ deg, because of the fuselage masking effect. Large differences are instead noted in the top area of the fuselage. There the sound waves from the two propellers interfere, creating a different acoustic field depending on the installation option.
To investigate more in depth the differences between the various layouts, Figure 7.16 shows the unsteady pressure waveforms recorded by some numerical probes on the fuselage, for certain angular positions at the propeller plane. Pressure time signals presented span over one propeller revolution. A predominant eight-period oscillation

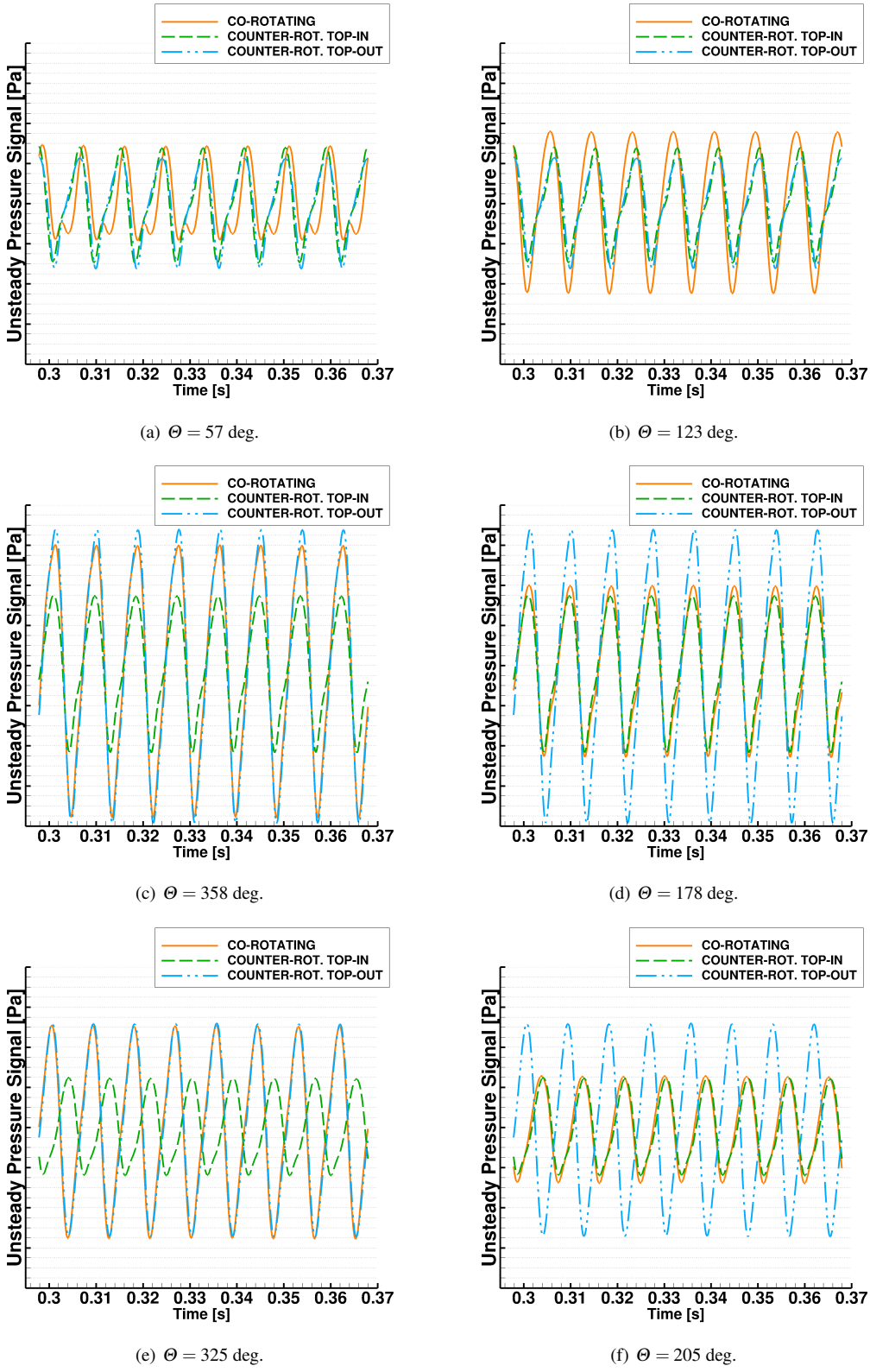

(a) $\Theta = 57$ deg.

(b) $\Theta = 123$ deg.

(c) $\Theta = 358$ deg.

(d) $\Theta = 178$ deg.

(e) $\Theta = 325$ deg.

(f) $\Theta = 205$ deg.

Figure 7.16: Unsteady pressure waveforms on the aircraft fuselage at the propeller plane, for some angular positions: comparison between the different propeller installation layouts. Signal length corresponding to one propeller revolution. Data from numerical probes for the last full propeller revolution run. See Figure 7.3 for the azimuthal coordinate definition. A predominant eight-period oscillation related to the blade passing is visible. The frequency at 2BPF becomes evident when favorable interferences, probably with waves emitted by the airframe, occur.

related to the blade passing frequency is visible as expected. The symmetry of the acoustic field for the counter-rotating layouts can also be observed.

The pressure time histories at $\Theta = 57$ deg (Figure 7.16(a)), where the OSPL has a local minimum for the co-rotating propellers, actually show a smaller fluctuation amplitude for this layout. The presence of the second harmonic frequency can be seen as well. This indicates that the sound waves propagating from the propeller to the fuselage wall undergo some favorable interactions with other sound waves. These are most likely waves emitted by the airframe, since the sound travelling time from the wing leading edge to the fuselage is close to the blade passing time. At the same azimuthal location on the port side (Figure 7.16(b)), the scenario for the co-rotating configuration is different: the pressure history displays a smooth sinusoidal trend with a larger amplitude than the other layouts, and thus the loudest noise. Counter-rotating propellers do not show significant differences at these two locations, and their signals slightly lead on the starboard side while slightly lag on the port side, compared to the co-rotating one. It is also observed a flattening of the sinusoidal signal after the low-picks for about half of the oscillation amplitude for both counter-rotating propeller cases. This suggests the existence of acoustic interferences between various sound sources.

Near the fuselage center-line (Figures 7.16(c) and 7.16(d)) the main difference between the three installation options is the magnitude of the pressure fluctuations, significantly larger in the case of inboard-up propeller rotation. No difference in phase is detectable between the three pressure histories. The signal flattening after the low-picks appears at this azimuthal position only in the case of inboard-down propeller rotation, i.e. for the counter-rotating top-in layout on both fuselage sides and for the co-rotating layout on the starboard side, but covering a smaller part of the signal.

At lower fuselage positions (Figures 7.16(e) and 7.16(f)), differences both in amplitude and phase between inboard-up and inboard-down rotating propeller cases are significant. The flattening of the signal progressively reduces moving towards the bottom of the fuselage, disappearing faster in the co-rotating propeller case.

As shown in Figure 7.15, at the propeller rotational plane, the counter-rotating top-out layout appears overall the loudest option, while the counter-rotating top-in layout appears the quietest. To evaluate overall the acoustics of the various configurations, in Figure 7.17 the sound levels on the aircraft fuselage are compared at different stations in the area where the higher OSPL is observed.

Going form the propeller rotational plane up-stream (Figures 7.17(a),7.17(c) and 7.17(e)), the OSPL distribution shows the same trend, with a maximum around the

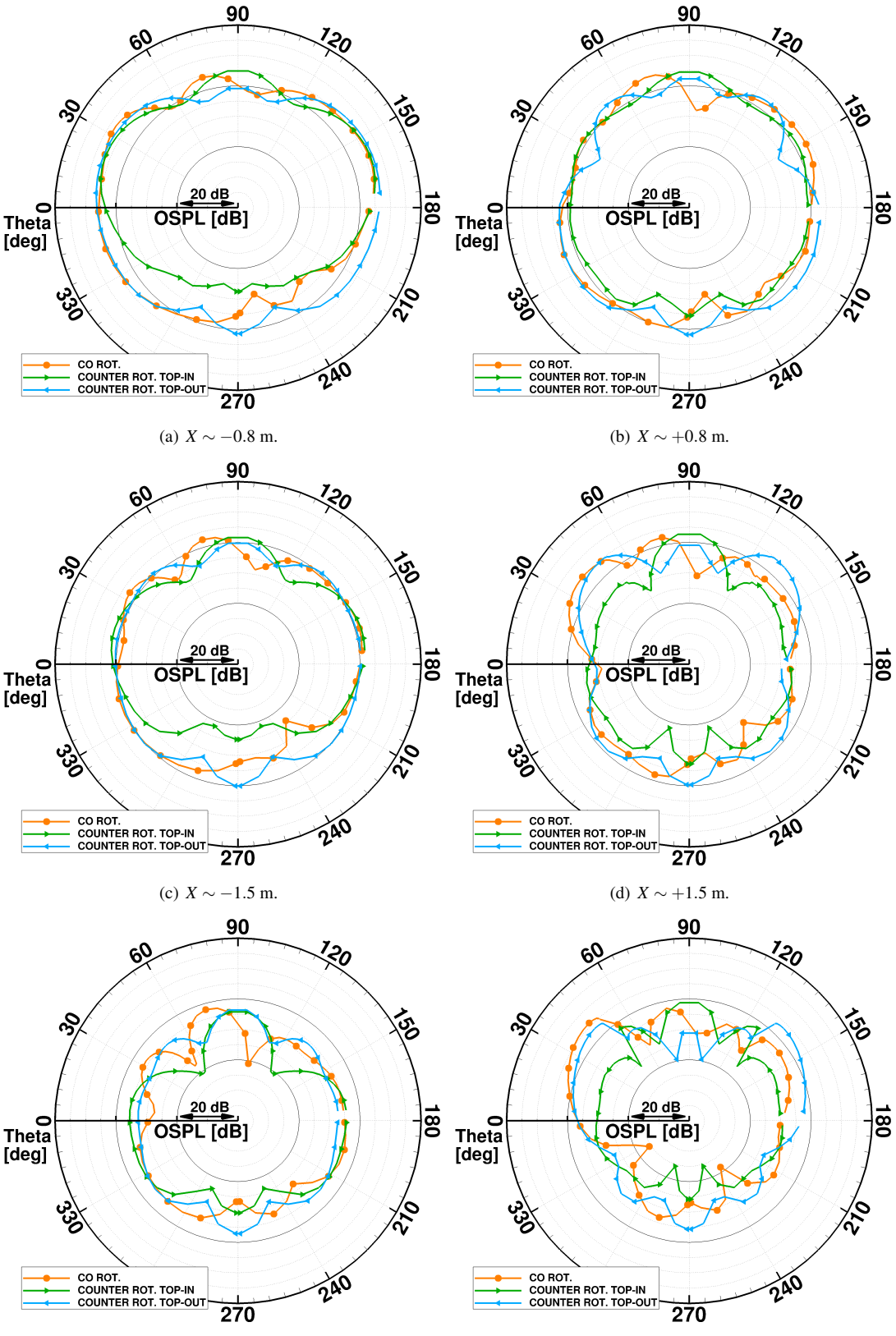

(a) $X \sim -0.8$ m.

(b) $X \sim +0.8$ m.

(c) $X \sim -1.5$ m.

(d) $X \sim +1.5$ m.

(e) $X \sim -2.2$ m.

(f) $X \sim +2.2$ m.

Figure 7.17: OSPL on the fuselage as a function of the angular position at various fuselage stations: comparison between the different propeller installation layouts. Noise estimate from numerical probe data over one full propeller revolution. Refer to Figure 7.3 for the azimuthal coordinate definition. Differences between the various layouts mainly appear down-stream the propeller plane, where the interactions between the sound emitted by the propellers and by the airframe play an important role. The **CNTI** options yield lower noise levels.

points closer to the propellers, two local minima at about $\Theta \sim 60$ and $100/120$ deg for co- and counter-rotating propellers respectively, a lobe at the top of the fuselage, and a noise reduction at the bottom. The larger the distance from the propeller plane, the lower the noise, as could be expected. The local noise reduction increased as well. The differences between the different layouts in the OSPL trend in the upper fuselage area become more significant, the counter-rotating top-in configuration showing the quietest noise. In the lower area of the fuselage, instead, less differences are noted among the various configurations further away the propeller rotational plane. For up-stream distances greater than R/2 (Figures 7.17(c) and 7.17(e)) the pick of the upper lobe tends to the same sound level in the cases of counter-rotating layouts, while near the propeller rotational plane a difference up to 5 dB is predicted, in favor of the counter-rotating top-out option. Moreover, at these distances, the co-rotating propeller configuration shows a second local minimum of the OSPL on the starboard side around $\Theta \sim 5$ deg which is not present in the other two installation options and makes this layout the quietest at this specific location.

Down-stream the propeller rotational plane (Figures 7.17(b),7.17(d) and 7.17(f)), due to the airframe sound waves emissions/reflections and connected interactions with the incoming ones, the OSPL distribution on the fuselage is different than ahead of the propeller plane, and its azimuthal trend becomes more irregular. Besides the points of local minimum defining the lobe at the top of the fuselage, other OSPL valleys can be seen on the upper-half of the fuselage creating one couple of additional lateral lobes, or two in proximity of the wing junction. The magnitude and the azimuthal positions of the main lateral lobes peak, as well as their extension, are shown to vary with the fuselage station. Increasing the distance from the propeller rotational plane, the dissimilarities in the OSPL predicted for the various layouts become larger and substantial: up to 10 dB of difference are observable for some azimuthal locations around $R/2$ away from the propeller plane (Figure 7.17(d)) and up to 15 dB about one radius away (Figure 7.17(f)). The counter-rotating top-in option appears overall the quietest, even though the counter-rotating top-out configuration shows significantly lower noise for the top lobe. Inboard-up rotating propellers yield to lateral lobes considerably louder, and covering a larger fuselage surface, than inboard-down rotating propellers. Moreover, the lateral lobe on the side of the inboard-up rotating propeller is observed to have higher OSPL in the case of co-rotating propellers with respect to counter-rotating top-out propellers. This suggests a detrimental acoustic interaction in the first case. The noise attenuation moving away from the propeller rotational plane is in general less than that observed going up-stream, because of the airframe reflections.

An exception is the counter-rotating top-in layout that exhibits, at equal distances from the propeller plane, lower OSPL down-stream than up-stream. As for fuselage stations ahead of the propeller plane, the local point of OSPL reduction in the half-lower part of the starboard side is more pronounced for the co-rotating propeller configuration. Finally, it is pointed out that at the locations of the OSPL local minimum of all fuselage stations, the frequency of the second tone is also observable in the pressure signals, indicating that important noise cancellations are generated by the interactions of propeller and airframe sound waves.

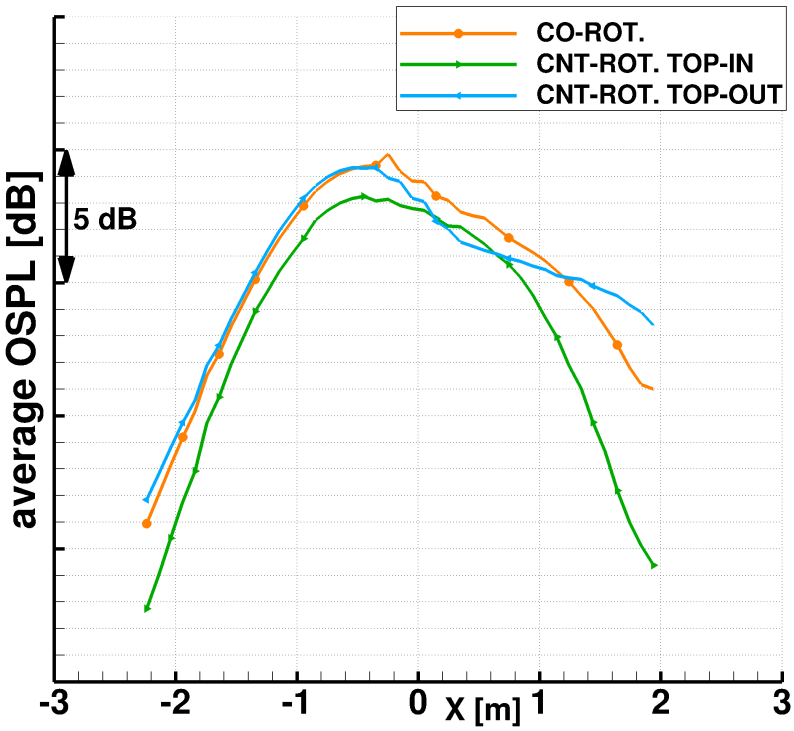

Figure 7.18: Azimuthally-averaged OSPL distribution as function of the fuselage longitudinal axis X: comparison between the different propeller installation layouts. Noise estimate from numerical probe data over one full propeller revolution. **CNTI** propellers are clearly the best option for all longitudinal positions. **CNTO** propellers are slightly louder than **CO** ahead of the propeller plane, but overall quieter behind it.

Figure 7.18 compares, for the three installation options, the distribution of the average OSPL along the airplane longitudinal axis. The azimuthal-average OSPL value, for each fuselage station, was computed including only the data of the upper surface region, while disregarding the area below the cabin floor (i.e. $212 \leq \Theta \leq 328$ deg, approximately). The top-in configuration appears the quietest, with a mean reduction of ~ 2 dB, and a maximum difference of more than 6 dB towards the fuselage-wing junction, with respect to co-rotating propellers. The top-out rotation option shows slightly higher noise levels than the co-rotating layout, up-stream the propeller plane

up to approximately 1 blade chord ahead. Moving further back, its OSPL longitudinal trend differs significantly from the other two configurations: a steeper reduction is observed up to approximately 1 blade chord behind, resulting in the lowest OSPL levels at that location; a decrease of only 3 dB is instead registered from there to the wing station, where the noise levels are almost 9 dB and 2.5 dB higher than counter-rotating top-in and co-rotating propellers, respectively. Overall, the counter-rotating top-out layout appears the loudest option.

7.3.2 Cabin Interior Noise

Cabin internal noise for an example passenger located on the starboard side of the airplane, slightly ahead of the propeller rotational plane on the second seat from the window, is evaluated. The experimental transfer functions determined by NLR within the IMPACTA project (refer to Section 3.2 for all details) are used for this estimate. CFD data from the numerical probes located in the area covered by the measurements (see Figure 7.5) are taken as input, employing the pressure history recorded over the last entire propeller revolution run.

As an example of the TF application, the unsteady pressure amplitude maps in the frequency domain, outside and inside the fuselage shell, are presented in Figure 7.19 for the fundamental harmonic. The modifications of the pressure field going through the fuselage shell, and the non-uniformity of the transmission losses of the aircraft structure, are noticeable. On the outside, marked differences are observed depending on the propeller rotation, the inboard-up case yielding fluctuations of higher amplitude, and over a larger area of the fuselage surface. On the inside, by contrast, the unsteady pressure amplitude presents similar characteristics for all propeller installation layouts. Because of the filtering properties of the aircraft structure, differences of the various configurations inside concern mainly the pressure oscillations magnitude.

The resulting pressure histories for the test passenger is shown in Figure 7.20(a), together with the signals at the same fuselage station and the same height on the external fuselage surface. The amplitude of the pressure fluctuations decreases considerably between outside and inside the aircraft cabin. In the transmission across the fuselage shell, the acoustic perturbations are reduced by around $17 - 20$ times.

Differences in the pressure oscillations among the various layouts are maintained, and are of the same order as those outside. The counter-rotating top-in configuration shows the smaller pressure fluctuations magnitude, indication of quieter sound levels. Counter-rotating top-out and co-rotating propellers display very similar pressure signals, the clear differences in the exterior acoustic field being probably attenuated

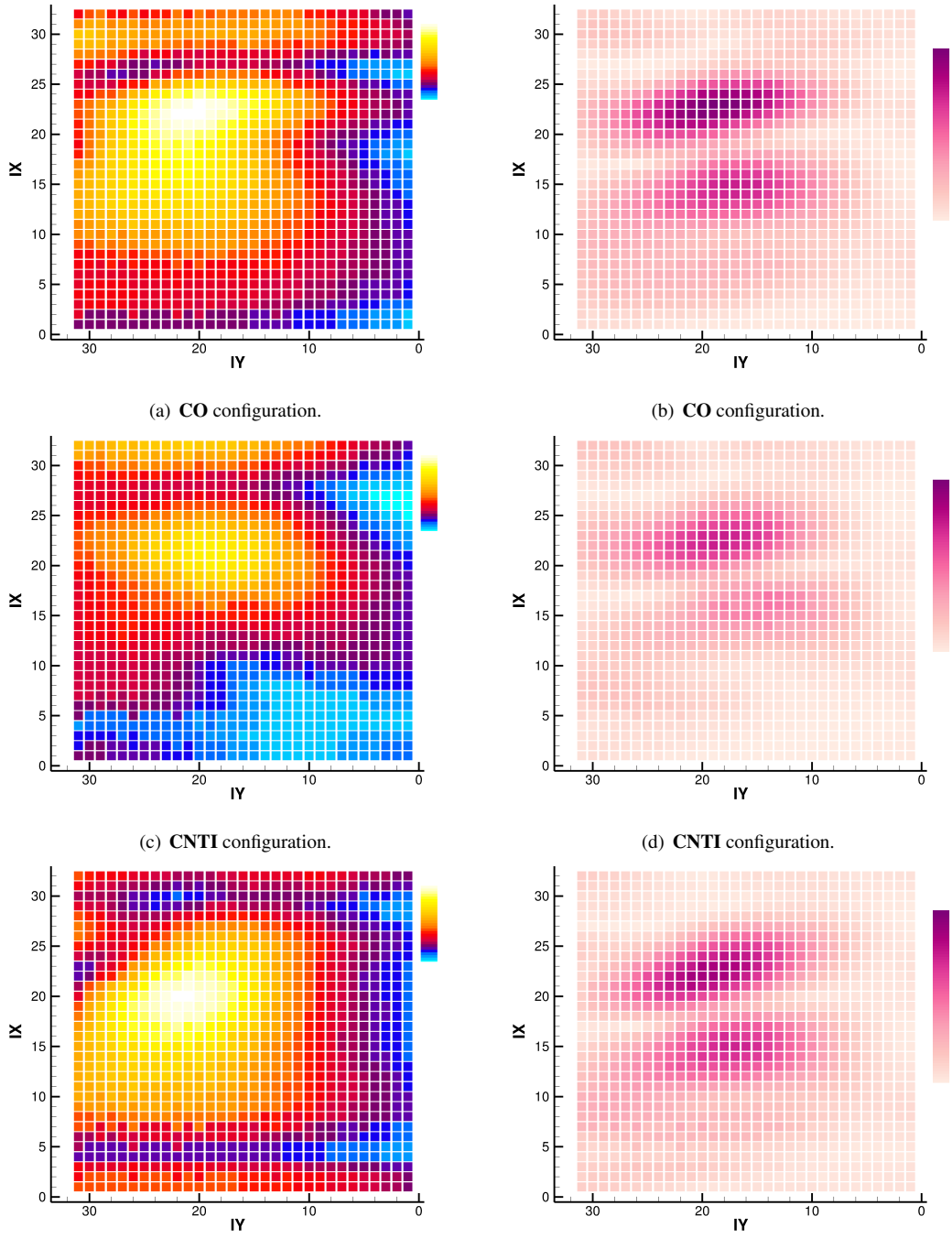

(a) **CO** configuration.

(b) **CO** configuration.

(c) **CNTI** configuration.

(d) **CNTI** configuration.

(e) **CNTO** configuration.

(f) **CNTO** configuration.

Figure 7.19: Transfer functions application for the different installation layouts: unsteady pressure amplitude maps at $f = \text{BPF}$ on the fuselage exterior surface (on the left) and the corresponding internal one (on the right). Please refer to Figure 7.5 for the definition of the coordinate IX and IY used for the plots, and for the TF area location. Despite the large differences in the impinging pressure field, the three layouts exhibit, inside, a similar noise distribution as effect of the structural filtering.

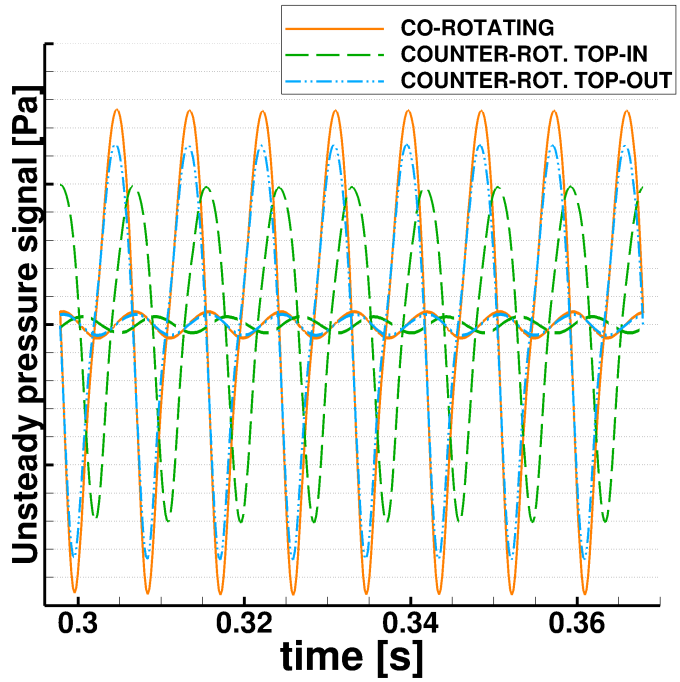

(a) Unsteady pressure signal (thick lines) compared with the one at the same height on the external fuselage surface (thin lines).

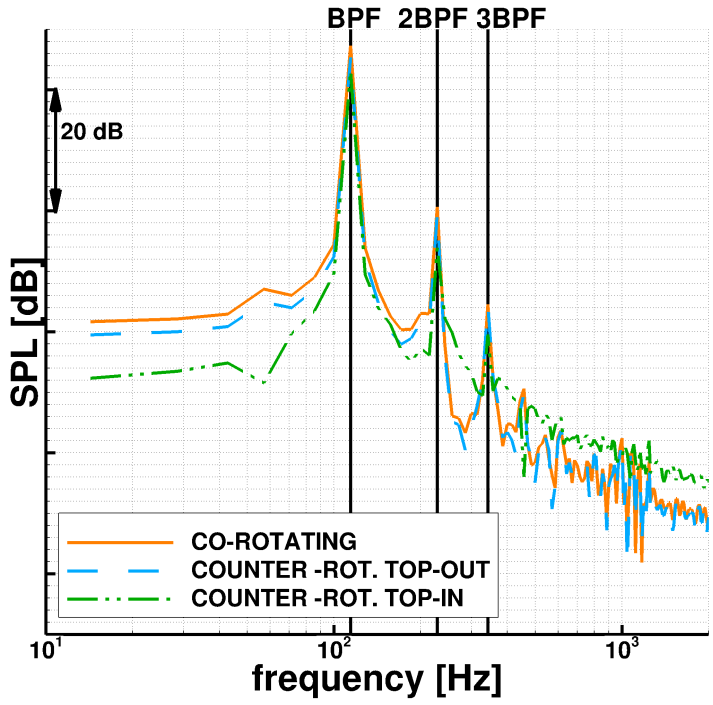

(b) Sound Pressure Level spectra in the frequency domain.

Figure 7.20: Cabin interior sound evaluation using experimental TF: comparison between the different propeller installation options. Data refer to a passenger located on the starboard side of the airplane, slightly ahead of the propeller rotational plane (see Figure 3.2(a)). In the transmission across the fuselage, the acoustic perturbations are reduced by $17-20$ times, but differences between the different layouts are maintained. The **CNTI** option appears the quietest, while the **CO** the loudest.

in the transmission through the fuselage. The sound spectra for the test passenger are reported in Figure 7.20(b). The tone at the blade passing frequency dominates the noise content. Components at the second and third propeller harmonics are also visible in the spectra. The counter-rotating top-in configuration appears to be the quietest, while the co-rotating the loudest. At the fundamental frequency, the predicted SPL for the co-rotating layout is around 2 and 4 dB higher than the counter-rotating top-out and top-in options, respectively. At 2 BPF, differences between co-rotating and counter-rotating top-out configurations become smaller, whereas the counter-rotating top-in option shows a benefit of more than 6 dB.

7.4. Conclusive Remarks

Significant differences in the exterior acoustic field between co- and counter-rotating propellers are observed. These differences remain audible in the aircraft cabin, although significantly attenuated by the fuselage shell filtering. Overall, at cruise condition with in-phased propellers, the counter-rotating top-out layout displays the best aerodynamic efficiency (in line with previous studies), whereas the counter-rotating top-in configuration is shown to be the best from the acoustic point of view. The propeller inboard-up rotation produces louder noise than the inboard-down direction because of the higher blade loading on the fuselage side. In addition, constructive interferences occur between direct propeller sound waves and noise emitted, as well as reflected, from the airframe, making the co-rotating installation option the loudest. Acoustic interferences between propellers and airframe appear in general to play an important role in the resulting sound field, showing the need to simulate the whole configuration to achieve accurate in flight noise estimates.

Chapter 8

Propellers Synchrophasing Analysis*

As shown in the previous Chapter, for the cruise conditions analysed, counter-rotating top-in propellers are acoustically better than co-rotating, in terms of near-field and cabin noise. Therefore, since civil turboprop aircraft usually adopt a co-rotating layout, propeller synchrophasing is now investigated, to assess if a **CO** configuration can be quieter than the **CNTI**.
Synchrophasing had previously proved effective in reducing vibration and noise levels[176, 177, 174, 175, 186], but there is still no complete understanding of its physics in presence of the airframe, and no thorough comparative study was carried out. The use of CFD enables to investigate the whole acoustic near-field that is generated from out-of-phase propellers, analysing the physics and assessing the possible noise benefits of this strategy. Various propeller synchrophasing angles were considered, and the different cases are compared regarding both exterior and interior sound levels.
Additional simulations were also conducted applying synchrophasing to the **CNTI** layout, to evaluate its effectiveness for this configuration, and potentially achieve larger noise reductions due to rotation direction and blade shift, together.

8.1. Test Cases and Numerical Setup

The IMPACTA aircraft with Baseline propellers at cruise conditions is again considered (see Section 7.1 for the details). The port propeller is taken as master, and the starboard propeller blades lead those of the port propeller, for a positive blade shift. Refer to Figure 7.3 for the notation used here. Typical synchrophasing angles for twin-engined turboprops are between 10 and 15 degrees[4]. Here, four synchrophasing

* Part of the work presented in this Section is published in G. Chirico *et al.* ,"Propeller installation effects on turboprop aircraft acoustics", *Journal of Sound and Vibration*,Vol. 424 (2018), pp. 238–262, doi:10.1016/j.jsv.2018.03.003

angles were initially tested for the **CO** configuration ($\psi_s = 5, 10, 15$ and 30 deg), one more ($\psi_s = 21$ deg) was added after the analysis of these first results. Two synchrophasing angles were studied for the **CNTI** configuration ($\psi_s = -5$ and -21 deg). Table 8.1 summarises all the cases simulated. Note that, since the propeller has eight blades, the maximum possible blade shift is equal to $\psi_s = 22.5$ deg. A larger angle is equivalent to a negative synchrophasing angle, e.g. $\psi_s = 30$ deg $\equiv -15$ deg.

Layout	**CO**					**CNTI**	
Synchrophasing ψ_s	+5 deg	+10 deg	+15 deg	+21 deg	+30 deg	-5 deg	-21 deg
Test ID	**CO5**	**CO10**	**CO15**	**CO21**	**CO30**	**CNTI5**	**CNTI21**

Table 8.1: Test cases for the propeller synchrophasing analysis.

Computational grids are identical to those used in the propeller "handedness" study of Chapter 7 (see Section 7.1.2 in particular). The grids for the different cases were simply created by applying a rotation to the starboard propeller drum by the desired synchrophasing angle during the mesh-assembling process.
URANS simulations were performed using the $k-\omega$ SST turbulence model[215] with a time resolution equivalent to 1 degree of propeller azimuth, as for the previous study. Computations were started from unperturbed free-stream flow conditions and run for six propeller revolutions to achieve an adequate flow convergence.
The summary of the main computational parameters is reported in Table 7.3.

8.2. Aerodynamic Analysis

For brevity, aerodynamic considerations are here omitted, since these were extensively discussed in the previous part of the study (see Section 7.2). It is only noted that:

(a) All synchrophased configurations provide a total thrust and lift that differ by less than -0.09% and $+0.14\%$ respectively, compared to the corresponding case with propellers in phase. A small increase in the aircraft effeciency is observed (see Table 8.2), due to the small increase in lift combined with a small decrease in drag.

(b) The mean pressure field developed around the airplane does not show appreciable differences compared to the in-phase operating case.

(c) Interestingly, for some synchrophasing angles, the loads fluctuations on the starboard wing display not only a phase shift, but also a different magnitude.

	CO	**CO5**	**CO10**	**CO15**	**CO21**	**CO30**	**CNTI**	**CNTI5**	**CNTI21**
Lift/Drag	20.324	20.361	20.361	20.359	20.364	20.359	20.171	20.212	20.211

Table 8.2: Aerodynamic efficiency for the various synchrophasing cases.

8.3. Acoustic Analysis for Co-rotating Layout

8.3.1 Aircraft External Sound Field

The OSPL distribution on the aircraft fuselage is shown in Figure 8.1 for the synchrophasing angles considered. Although the general trend of the noise field

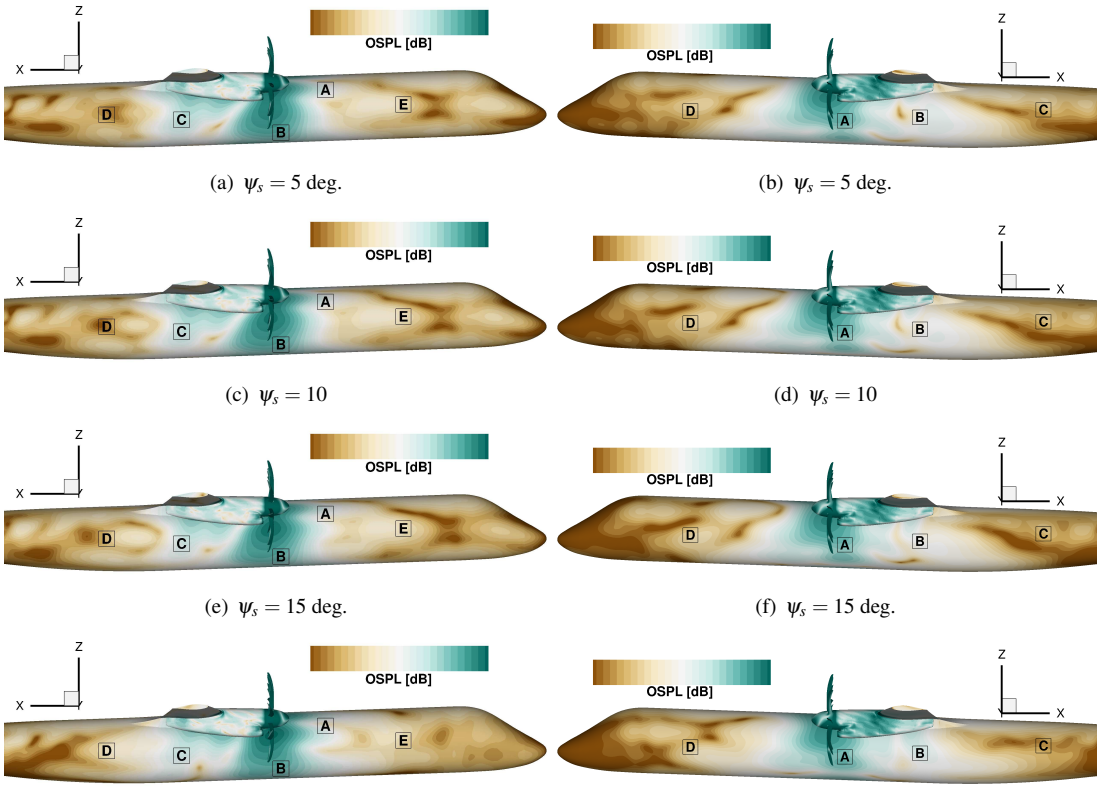

(a) $\psi_s = 5$ deg. (b) $\psi_s = 5$ deg.

(c) $\psi_s = 10$ (d) $\psi_s = 10$

(e) $\psi_s = 15$ deg. (f) $\psi_s = 15$ deg.

(g) $\psi_s = 30$ deg. (h) $\psi_s = 30$ deg.

Figure 8.1: OSPL on the aircraft external surface for the different **CO** synchrophasing cases: noise estimate from URANS results over a quarter of propeller revolution. Color scale range equal to 45 dB. Aircraft starboard side on the left and port side on the right. Refer to Figure 7.14 for the case of propellers in phase. The general trend remains substantially the same, but some small variations in levels and extension of the high noise lobes can be observed (in particular on the starboard side).

remains substantially the same, some differences can be observed. On the starboard side, there is a slight change in the azimuthal position and extent of the longitudinal noise lobe (A). The main noise lobe (B) is also seen to vary its size and the azimuthal location of its peak. No significant differences are noted in the fuselage region below

the wing (C), while sound levels and the position of the noise minimum behind the wing (D) are altered depending on the synchrophasing angle. In the fuselage frontal area (E), a similar noise pattern is observed for all cases, with only small variations in sound levels, apart from the **CO30** that shows an OSPL distribution considerably different.

Smaller differences are registered on the port side among the cases of **CO5**, **CO10** and **CO15**, whereas the choice of **CO30** results in a more extended area of high noise in the vicinity of the propeller plane (A) and a different OSPL pattern at the back (C) and front (D) of the fuselage. Finally, since the OSPLs of **CO15** and **CO30**, i.e. $\psi_s = -15$ deg equivalently, are dissimilar, the developed acoustic field depends on the magnitude of the blade shift and also on the sign of the shift (leading or lagging) of the starboard propeller.

Data from the fuselage numerical probes are used to have a more precise quantitative assessment of the several shift angle choices. Figure 8.2 presents the OSPL as a fun-

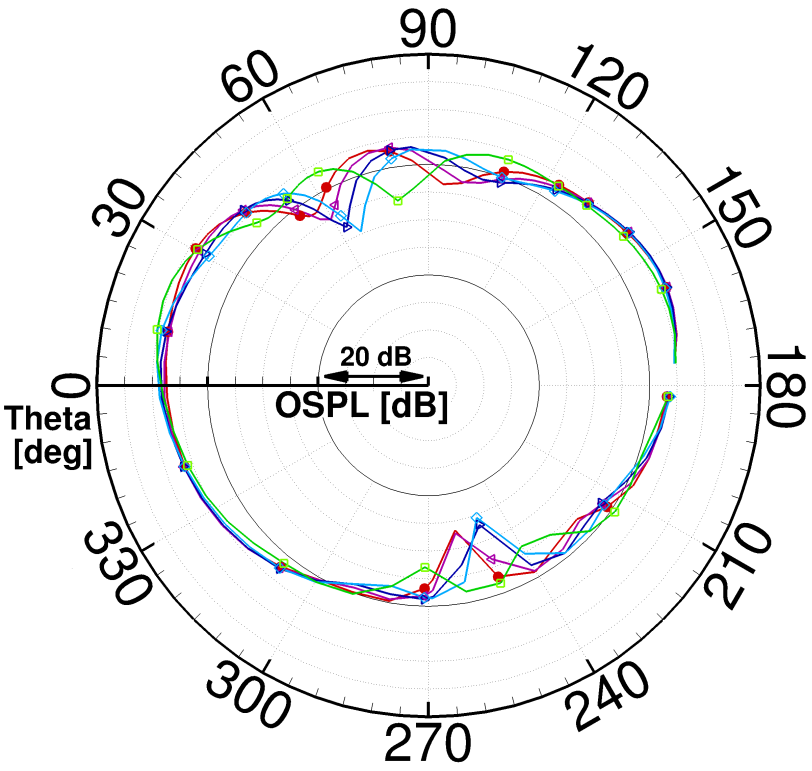

(a) $X \sim 0.0$ m.

Figure 8.2: OSPL around the fuselage at various stream-wise stations: comparison between the different **CO** synchrophasing cases. Noise estimate from numerical probe data over one full propeller revolution. Refer to Figure 7.3 for the azimuthal coordinate definition. Legend: red plain circles - **CO**; purple left triangles - **CO5**; blue right triangles - **CO10**; cyan diamonds - **CO15**; light green squares - **CO30**. *(Part 1/3: propeller plane)* The main effect of the positive synchrophasing angle appears to be a shift of the noise pattern towards slightly larger fuselage azimuthal angles.

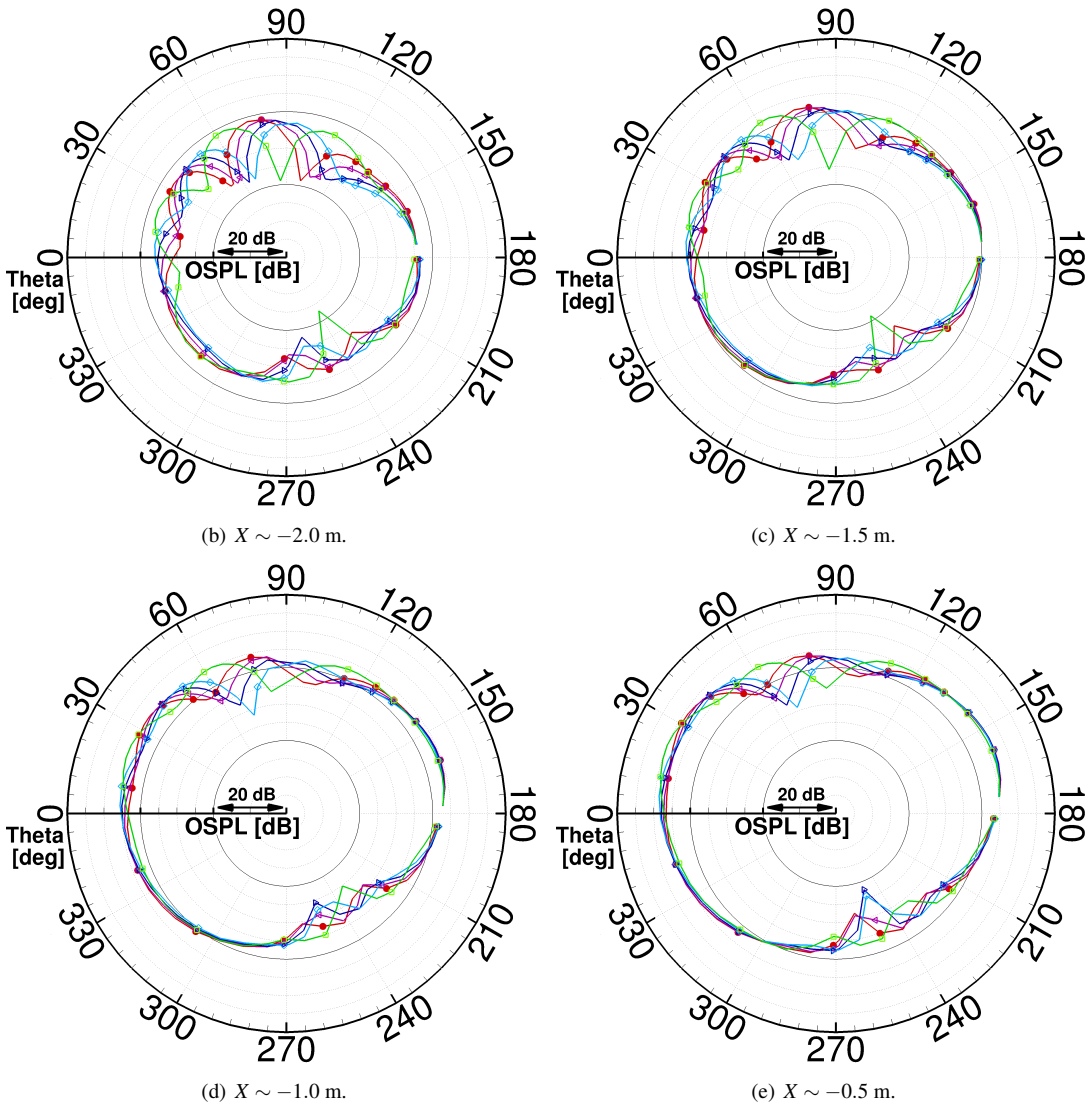

(b) $X \sim -2.0$ m. (c) $X \sim -1.5$ m.

(d) $X \sim -1.0$ m. (e) $X \sim -0.5$ m.

Figure 8.2: OSPL around the fuselage at various stream-wise stations: comparison between the different **CO** synchrophasing cases. Noise estimate from numerical probe data over one full propeller revolution. Refer to Figure 7.3 for the azimuthal coordinate definition. Legend: red plain circles - **CO**; purple left triangles - **CO5**; blue right triangles - **CO10**; cyan diamonds - **CO15**; light green squares - **CO30**. *(Part 2/3: up-stream the propeller plane)* Maximum levels differ at most of 2 dB, while minimum up to 5 dB, indicating stronger destructive interferences.

ction of the fuselage azimuthal position, at different longitudinal stations. The corresponding data for the case of propellers in phase are included for comparison. In general, the main effect of the positive synchrophasing angle appears to be a shift of the noise pattern towards slightly larger fuselage azimuthal angles, as can be seen looking at the position of the noise lobe on the upper part of the fuselage.

For fuselage stations ahead of the propeller, and up to around one propeller radius behind it, the differences in the sound levels of the noise maximum are at most of 2 dB. Bigger differences are observed regarding the points of minimum noise. The configurations with synchrophasing show reductions of up to 5 dB more than the in-

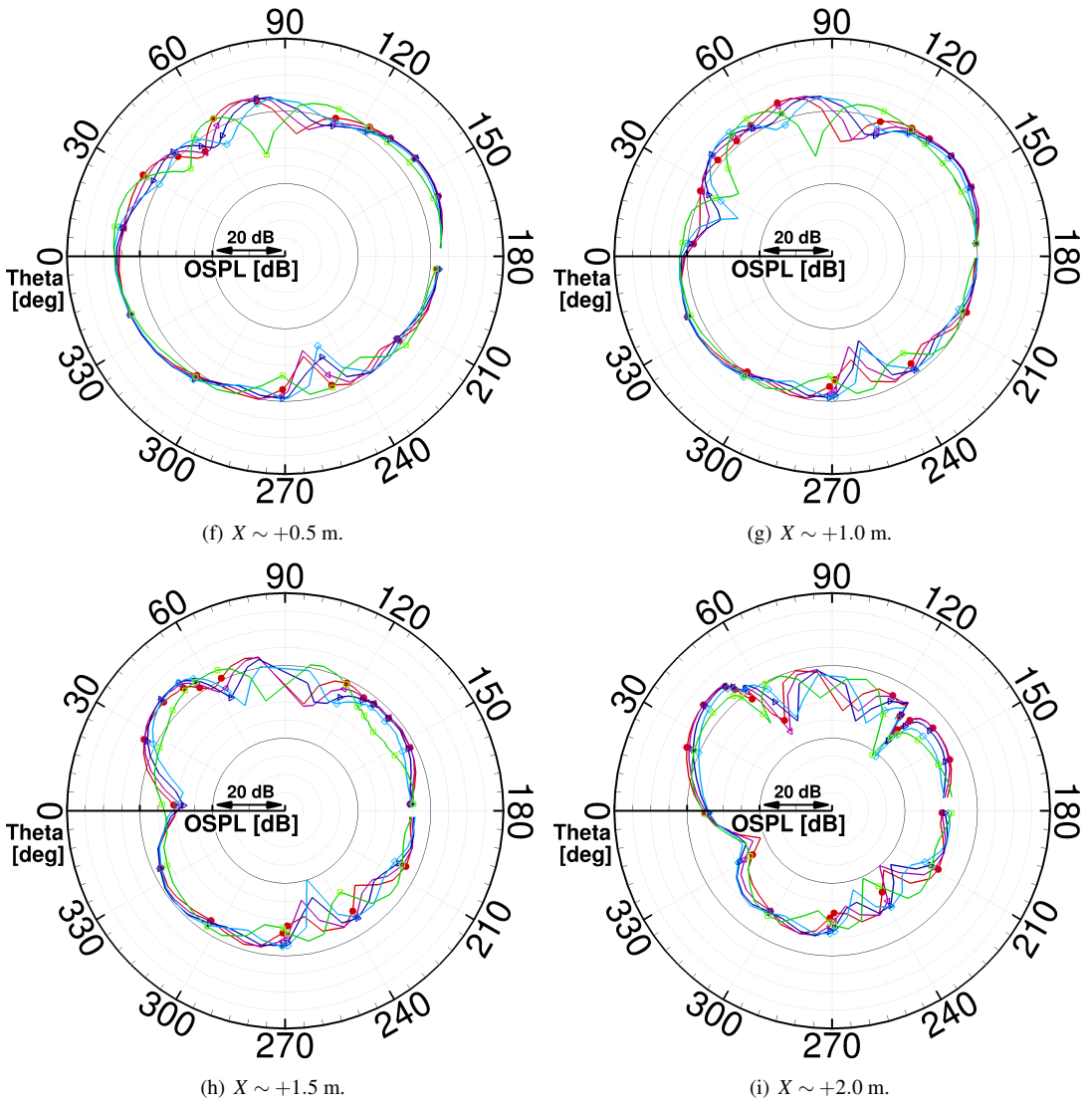

(f) $X \sim +0.5$ m. (g) $X \sim +1.0$ m.

(h) $X \sim +1.5$ m. (i) $X \sim +2.0$ m.

Figure 8.2: OSPL around the fuselage at various stream-wise stations: comparison between the different **CO** synchrophasing cases. Noise estimate from numerical probe data over one full propeller revolution. Refer to Figure 7.3 for the azimuthal coordinate definition. Legend: red plain circles - **CO**; purple left triangles - **CO5**; blue right triangles - **CO10**; cyan diamonds - **CO15**; light green squares - **CO30**. *(Part 3/3: down-stream the propeller plane)* For distances larger than $1R$, synchrophasing has a larger effect, indicating that it affects not only the interferences between propellers' sound fields, but also, and in greater ways, those between propellers direct sound field and airframe emitted noise. Maximum levels of both starboard and port lobes decrease with a positive increase of the shift angle.

phase case, indicating a stronger noise destructive interference.

Further back, where the noise on the fuselage is also affected by the acoustic waves generated by the interactions with the airframe, the noise distribution is seen to vary more considerably between the various test cases. The maximum sound levels of the upper-lateral lobes, both on the starboard and port sides, decrease with a positive increase of the synchrophasing angle.

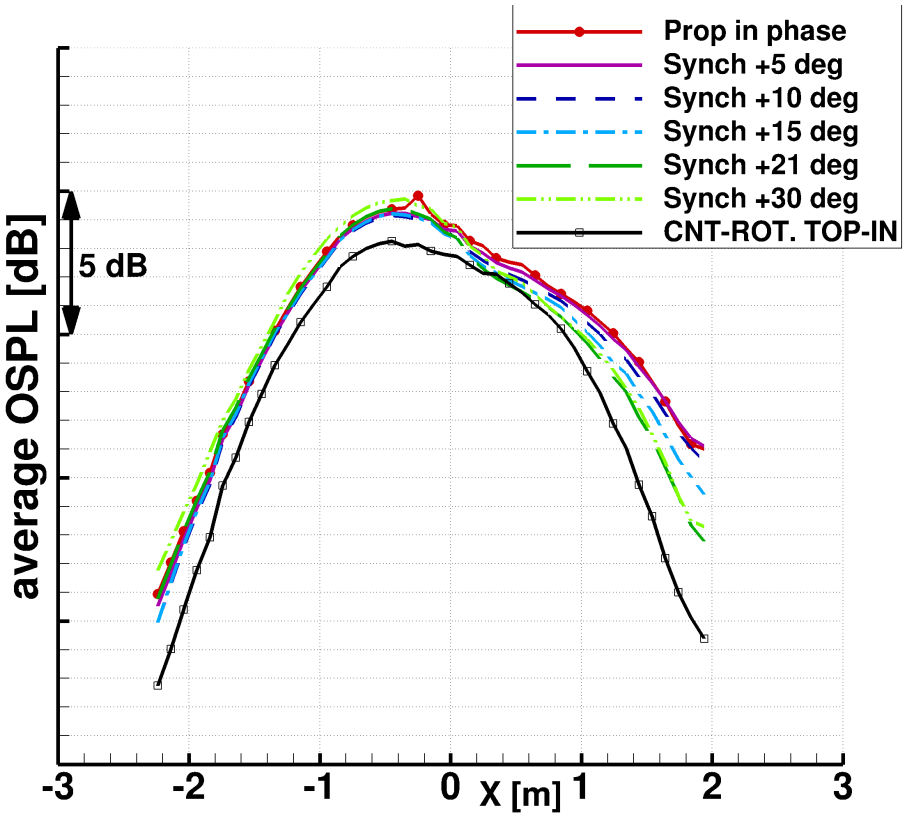

Figure 8.3: OSPL averaged over the fuselage azimuth Θ, in the passengers area, as a function of the fuselage longitudinal position: comparison between the different **CO** synchrophasing cases, and **CNTI** layout as a reference. Noise estimate from numerical probe data over one full propeller revolution. Ahead of the propeller plane all cases appear very similar. Behind, the larger the synchrophasing angle (up to the maximum blades relative shift), the larger the noise reduction. None of the synchrophasing angles allow to achieve the lower **CNTI** noise levels.

To overall assess the acoustics of the various options, Figure 8.3 shows the trend of the OSPL along the aircraft longitudinal axis, averaged over the azimuth. Only the upper surface of the fuselage, i.e. the area above the cabin floor, was here considered. Ahead of the propeller tip plane, all cases present very similar noise values, with some differences just for distances larger than one propeller diameter. Only the case of **CO30**, where the starboard propeller is leading the port one, yields slightly but noticeable higher OSPL for the whole front part of the aircraft fuselage. The almost null effect of synchrophasing up-stream the propeller plane may be due to the fact that the main noise propagation direction here is observed to be out-board.

Behind the propeller plane, the effect of the blade shift is more considerable, and differences between the various configurations increase the closer we are to the wing-fuselage junction. This may indicate that synchrophasing modifies not only the acoustic interference that develops between the sound fields of the two propellers, but also, and in greater ways, the interference of the propellers direct sound fields with the one produced from the interactions with the airframe. It is therefore crucial, when

studying the optimum synchrophasing angle numerically, to include the airframe in the simulations. Any tested synchrophasing angle had a beneficial effect in this area of the fuselage, with noise reductions of up to 1 dB about half radius away from the propeller plane and up to about 2 dB one radius away. Larger synchrophasing angles provide larger noise reductions. The OSPL decrease is seen to be non-linear with the synchrophasing angle.
The choice of **CO15** appears, overall, the quietest amongst those considered.
The same graph also shows the OSPL trend for the **CNTI** layout, which was proven the quietest option in the first analysis. It can be seen that, at all fuselage stations, no synchrophasing angle applied to the **CO** configuration is able to achieve a noise reduction equal to that obtained by the top-in propellers rotation.

CO5	**CO10**	**CO15**	**CO30**	**CNTI**
-0.16 dB	-0.365 dB	-0.55 dB	-0.36 dB	-2.17 dB

Table 8.3: OSPL average value for the fuselage region from 1 radius ahead the propeller tip plane to the wing-fuselage junction for the different **CO** synchrophasing cases: relative value with respect to the **CO** case. Value of **CNTI** layout reported as reference. Data from numerical probes over the last full propeller revolution. The lower part of the fuselage (below an ideal cabin floor) was not considered.

Table 8.3 reports the overall (i.e. for the fuselage region from 1 radius ahead the propeller tip plane to the wing-fuselage junction) noise benefit that are attained with synchrophasing, compared to in-phase propellers. The value for the counter-rotating top-in propellers layout is reported as a target. All synchrophasing angles analysed lead to a reduction in the OSPL. If the gain obtained by a choice of **CO5** appears almost negligible, with **CO15** it is possible to achieve a noise reduction of more than 0.5 dB with respect to in-phase propellers. The option of **CO30** seem to not be optimal because the considerably larger gain provided in the area between the propeller plane and the wing-fuselage junction is balanced by the increase in the sound levels ahead the propeller plane.

Looking at the average OSPL as a function of the synchrophasing angle, it can be thought that a choice closer to the maximum possible blade shift, i.e. $\psi_s \sim 22.5$ deg, may yield larger noise reductions. For this reason an additional simulation was performed with $\psi_s = 21$ deg. This choice was made considering the capability of current synchrophaser systems of maintaining a shift angle within ± 1 deg, to ensure that the starboard propeller is always leading with respect to the port one.
The azimuth-average OSPL along the fuselage, reported in Figure 8.3, displays significant benefits behind the propeller plane, showing similar sound levels to the

CO30 case, and a trend very close to that of propellers in phase ahead of the propeller plane.

Overall, the choice of **CO21** deg appears the quietest co-rotating configuration, leading to a noise reduction of 0.7 dB with respect to phased propellers. However, it is noted that the acoustic gains achieved by synchrophasing are significantly lower than that obtained by the counter-rotating top-in layout.

8.3.2 Cabin Interior Noise

The SPL for the first three propeller harmonics and the OSPL that would be heard by the passenger example are presented, for all **CO** synchrophasing cases, in Figure 8.4 and Table 8.4, respectively. Data of **CNTI** and **CNTO** are also reported for comparison. Co-rotating in phase propellers appear the loudest option, whereas the counter-rotating top-in configuration the quietest, at this flight condition and this passenger location. **CNTI** propellers exhibit significant noise reductions at the three first tones, yielding an OSPL decrease of more than 4 dB.

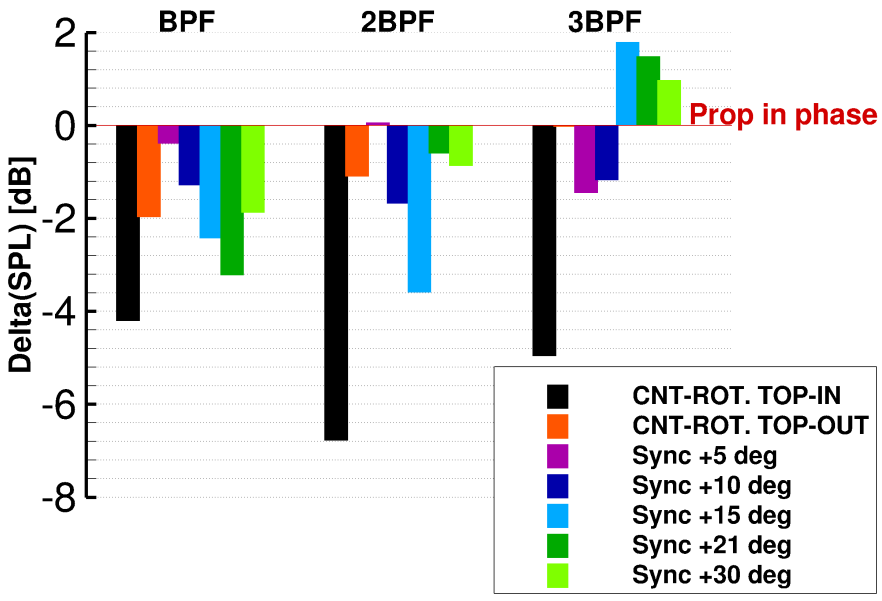

Figure 8.4: Cabin interior sound evaluation, for the example passenger, using experimental TF: SPL for first, second and third tone. Comparison between the different **CO** synchrophasing cases. Relative data with respect to the case with co-rotating phased propellers. Results for **CNTI** and **CNTO** configurations, with propellers in phase, are reported as reference. See Figure 3.2(a) for the passenger location. Synchrophasing appears significantly beneficial, the best angle depending on the frequency. **CNTI** is however the quietest option for all three harmonics.

Synchrophasing is also beneficial regarding cabin noise (apart from the case of **CO5** that is almost not affected), even if the differences that appear on the external surface of the fuselage are not very strong. The only phase angle to exhibit a sound levels

reduction at all first three harmonics is $\psi_s = 10$ deg. However, it results overall noisier than larger synchrophasing angles, because its noise reduction for the first tone is significantly weaker. $\psi_s = 21$ deg displays the larger reduction at the first harmonic

CNTI	CNTO	CO5	CO10	CO15	CO21	CO30
-4.21 dB	-1.97 dB	-0.39 dB	-1.29 dB	-2.42 dB	-3.21 dB	-1.87 dB

Table 8.4: Cabin interior OSPL evaluation, for the example passenger, using experimental TF: comparison between the different **CO** synchrophasing cases. Relative data with respect to the case with co-rotating phased propellers. Results for **CNTI** and **CNTO** configurations, with propellers in phase, are reported as reference. See Figure 3.2(a) for the passenger location.

(-3.2 dB with respect to phased propellers), while $\psi_s = 15$ deg appears the best for the second harmonic (-3.6 dB with respect to phased propellers). Results therefore show that the optimum angle choice depends on the harmonic frequency, the larger noise reduction for the BPF occurring close to the maximum blade shift and the higher the tone the smaller the angle. Overall, the **CO21** configuration provides a noise reduction of more than 3 dB, mainly thanks to the reduction of the first harmonic SPL. This is the most favorable angle amongst those analysed regarding both exterior and interior noise for **CO** propellers. Smaller angles are less effective, whereas larger angles seem not ideal because of the sound levels increase ahead of the propeller plane.
Finally, it is interesting to note that even the counter-rotating top-out layout, which has both propellers rotating inboard-up, shows lower noise levels than co-rotating phased propellers. This suggests the development of some destructive interferences in the counter-rotating case between the sound fields of the two propellers that do not occur in the co-rotating case. The pressure disturbance which travels ahead from the fuselage surface at the height of the propeller plane is also seen to be smaller in the external acoustic field visualisations as seen in Figure 7.11(f).

8.4. Acoustic Analysis for Counter-rotating Top-In Layout

8.4.1 Aircraft External Sound Field

Having introduced a shift of the starboard propeller blades, the generated acoustic field is no longer symmetric with respect to the longitudinal symmetry plane of the aircraft. As can be seen from the visualisation of the instantaneous unsteady pressure field in Figure 8.5, the cabin is not anymore invested simultaneously by peaks and valleys of the sound waves of the two propellers. Some differences between the test cases can also be observed near the port propeller, indicating that synchrophasing affects the acoustic field of the whole aircraft. In particular, a pressure perturbation of larger

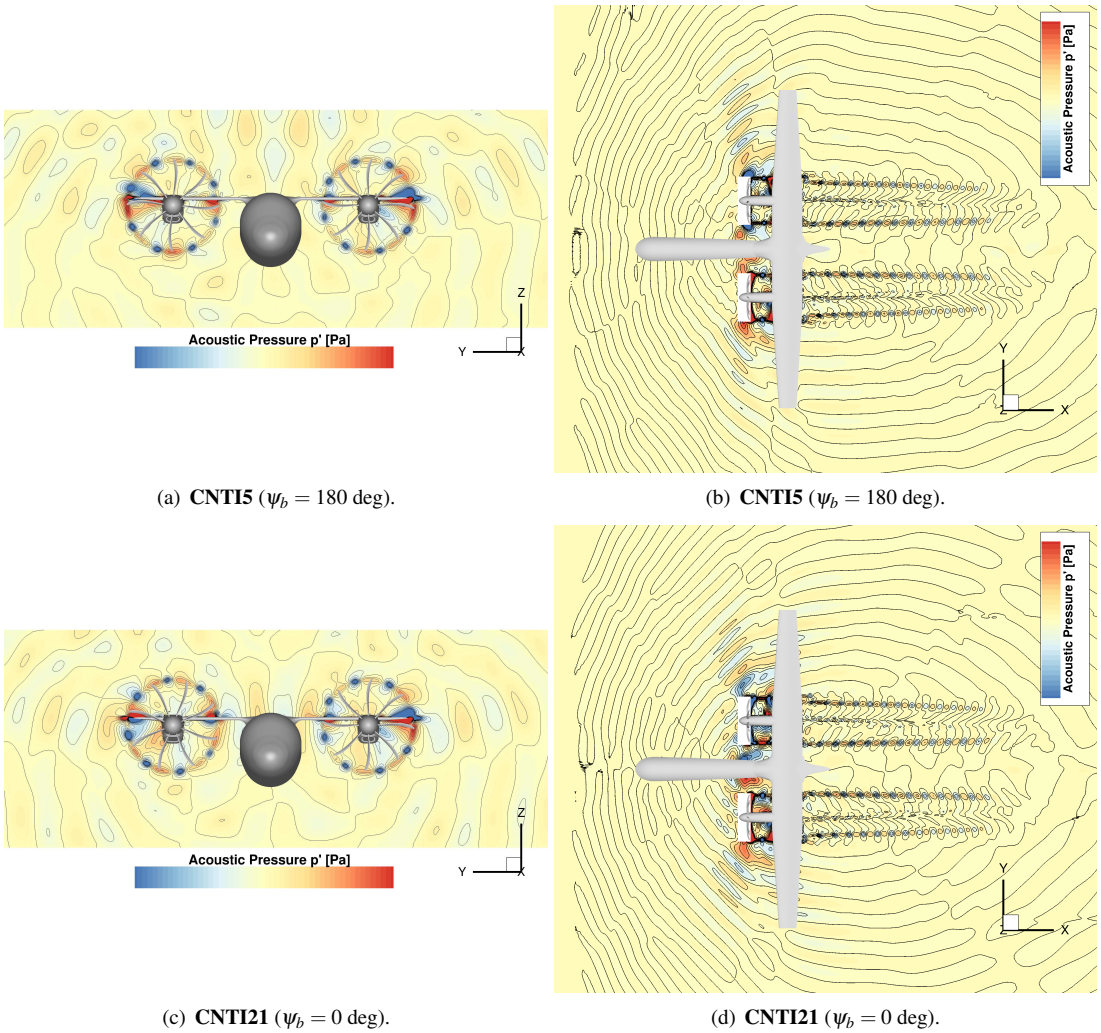

(a) **CNTI5** ($\psi_b = 180$ deg).

(b) **CNTI5** ($\psi_b = 180$ deg).

(c) **CNTI21** ($\psi_b = 0$ deg).

(d) **CNTI21** ($\psi_b = 0$ deg).

Figure 8.5: Instantaneous unsteady pressure field visualisation for the different **CNTI** synchrophasing cases. Transversal plane at $\sim 1R$ behind the propeller plane on the left, longitudinal plane at propeller spinner height on the right. Refer to Figures 7.11(c) and 7.11(d) for the **CNTI** case. Having introduced the blades shift, the acoustic field is no longer symmetric. Differences between the various cases are noted also on the port side, indicating that synchrophasing affects the overall sound field around the aircraft.

magnitude appears for the **CNTI21** case in the area between the port propeller and the fuselage.

Data from the fuselage numerical probes are used to evaluate the noise levels on the aircraft's external surface. In Figure 8.6 the OSPL azimuthal distribution is presented at various fuselage longitudinal stations. Results of the **CO** and **CO21** cases are reported in the same picture for comparison.

The **CNTI5** case shows an OSPL distribution very similar to the **CNTI** case, both up-stream and down-stream the propeller plane up to approximately $R/2$. Apart from the movement of the upper noise lobe towards the port side, only small differences are

observed in the sound levels of the lateral-upper lobes, showing a slight reduction on the port side and a slight increase on the starboard side. Larger variations, up to 5 dB, with the same trend appear further down-stream towards the wing junction.

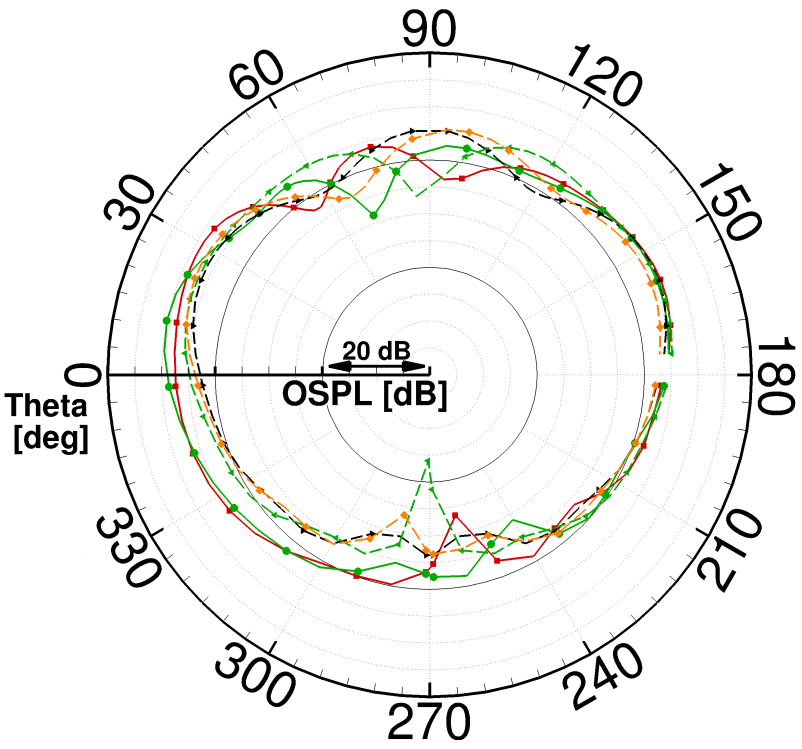

(a) $X \sim 0.0$ m.

Figure 8.6: OSPL around the fuselage at various stream-wise stations: comparison between the different **CNTI** synchrophasing cases. Noise estimate from numerical probe data over one full propeller revolution. Refer to Figure 7.3 for the azimuthal coordinate definition. Legend: red squares - **CO**; green circles - **CO21**; black left triangles - **CNTI**; orange diamonds - **CNTI5**; green right triangles - **CNTI21**. *(Part 1/3: propeller plane)* **CNTI5** differs from **CNTI** almost only for the small movement of the upper lobe towards the port side. **CNTI21** shows on the contrary a quite dissimilar OSPL distribution, the upper lobe split in two and a pronounced noise minimum at the bottom. These main characteristics are maintained at all fuselage stations.

The **CNTI21** option exhibits instead a remarkably different OSPL distribution compared to the **CNTI** case, at all fuselage stations. The upper high noise lobe is divided in two lobes almost symmetric to the aircraft mid-plane (the relative noise valley is at $\Theta \sim 85$ deg). A very pronounced low peak at the fuselage bottom ($\Theta \sim 270$ deg) is also formed. Regarding the noise upper lateral lobes, it can be observed that: *(i)* up-stream the propeller plane, the OSPL of the **CNTI21** case is very close to that of the **CNTI** configuration, with slightly lower sound levels, on both starboard and port sides, increasing the distance from the propeller plane; *(ii)* at the propeller plane and down-stream, the **CNTI21** shows higher sound levels than the **CNTI** and **CNTI5** cases, on the starboard and port sides, with larger differences the larger the distance

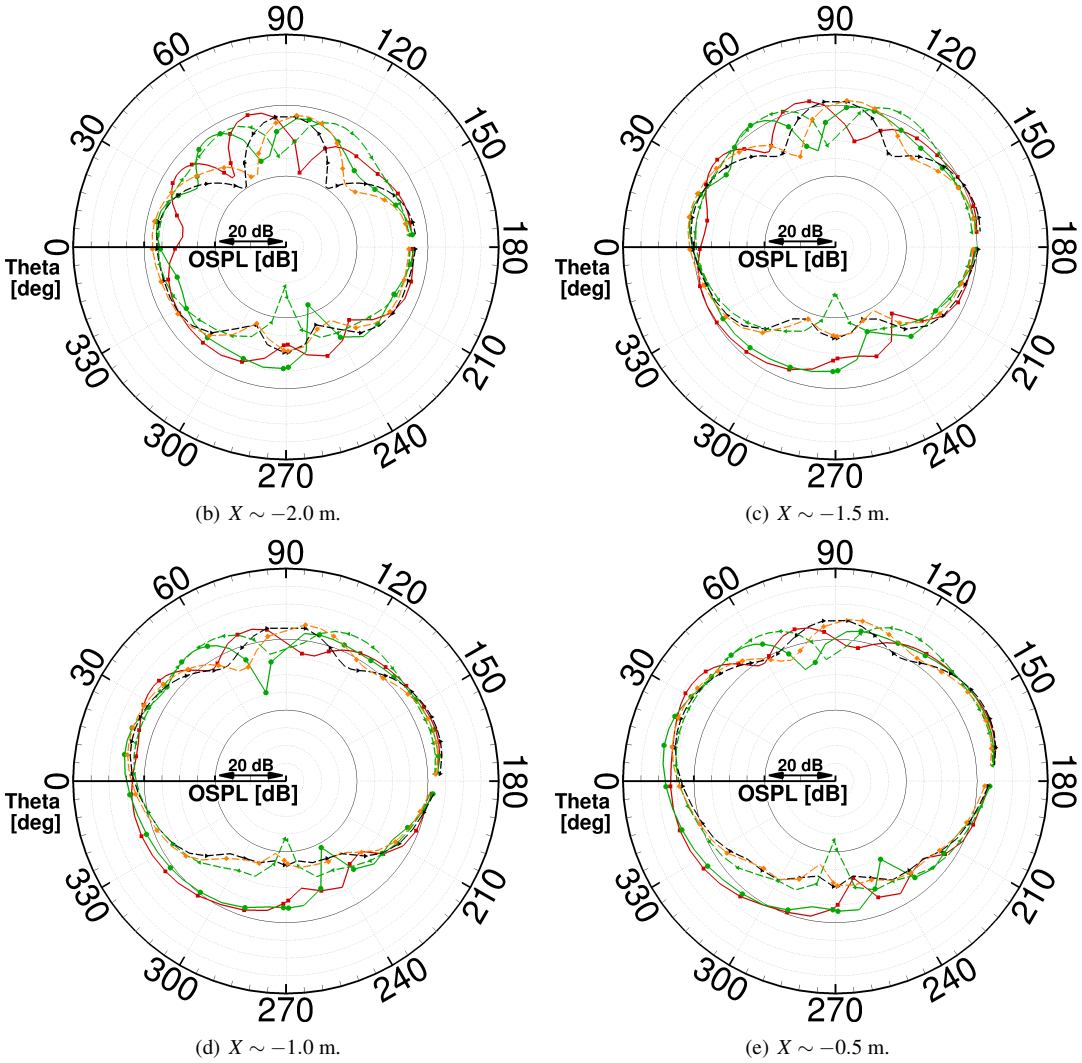

(b) $X \sim -2.0$ m. (c) $X \sim -1.5$ m.

(d) $X \sim -1.0$ m. (e) $X \sim -0.5$ m.

Figure 8.6: OSPL around the fuselage at various stream-wise stations: comparison between the different **CNTI** synchrophasing cases. Noise estimate from numerical probe data over one full propeller revolution. Refer to Figure 7.3 for the azimuthal coordinate definition. Legend: red squares - **CO**; green circles - **CO21**; black left triangles - **CNTI**; orange diamonds - **CNTI5**; green right triangles - **CNTI21**. *(Part 2/3: up-stream the propeller plane)* Both **CNTI5** and **CNTI21** exhibit lateral lobes very similar to **CNTI**: the first showing a slight reduction on the port side and a slight increase on the starboard side, the second lower levels on both sides. These differences increase increasing the distance from the propeller plane.

from the propeller plane, up to more than 6 dB at approximately $1R$ away. It is noted that, down-stream the propeller plane, the **CNTI21** sound levels of the port lobe are similar to the **CO** case.

The trend of the average OSPL along the fuselage of the different **CNTI** cases is presented in Figure 8.7 and compared against the **CO** and the **CO21** options. The **CNTI5** appears almost equivalent to the **CNTI** configuration, the higher and lower OSPL values on the starboard and port sides respectively, compensating each other for the most part of the fuselage. Only up-stream the propeller plane, for distances bigger

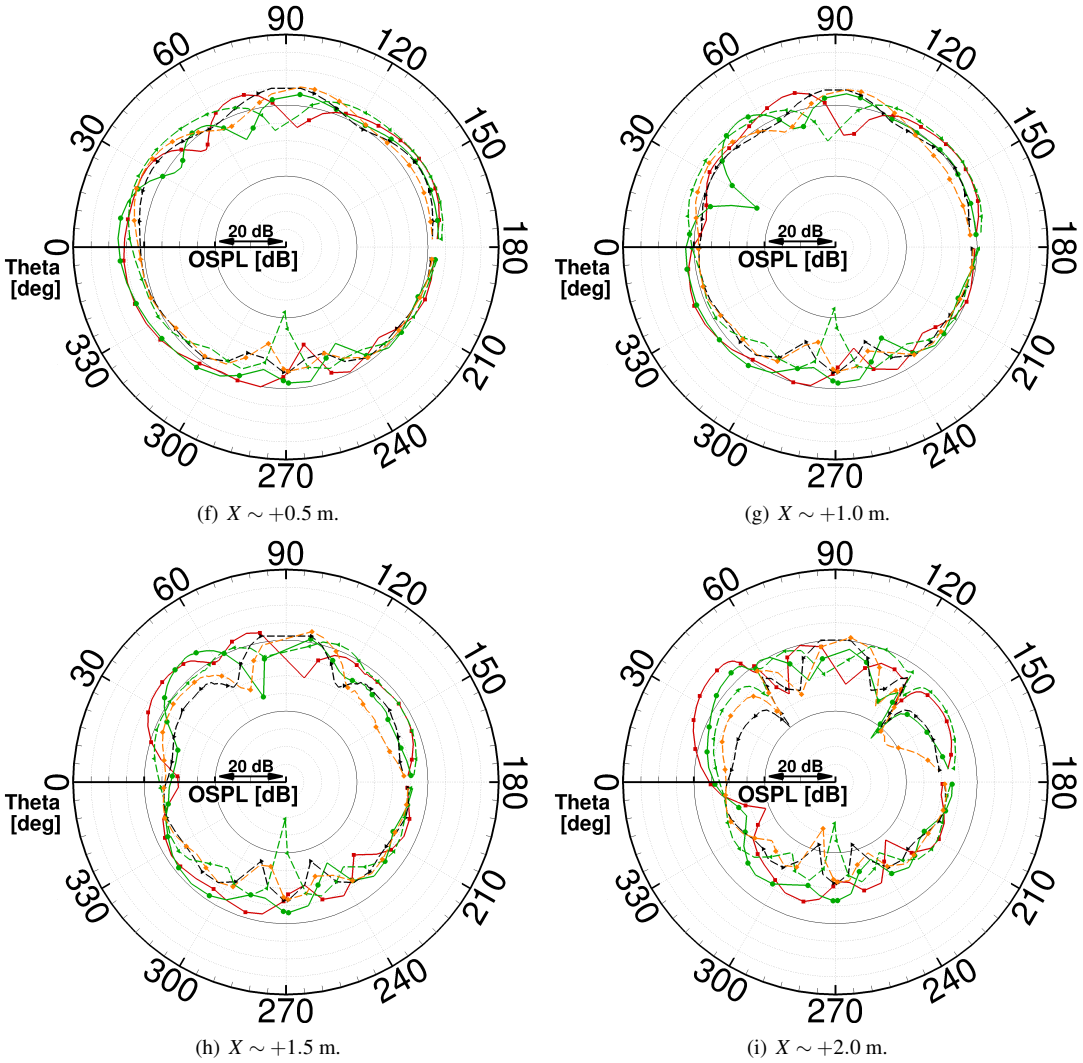

(f) $X \sim +0.5$ m. (g) $X \sim +1.0$ m.

(h) $X \sim +1.5$ m. (i) $X \sim +2.0$ m.

Figure 8.6: OSPL around the fuselage at various stream-wise stations: comparison between the different **CNTI** synchrophasing cases. Noise estimate from numerical probe data over one full propeller revolution. Refer to Figure 7.3 for the azimuthal coordinate definition. Legend: red squares - **CO**; green circles - **CO21**; black left triangles - **CNTI**; orange diamonds - **CNTI5**; green right triangles - **CNTI21**. *(Part 3/3: down-stream the propeller plane)* **CNTI5** differs significantly from **CNTI** only for distances larger than $R/2$. **CNTI21** is noisier than **CNTI** and **CNTI5** on both sides, the noise levels increasing as the the distance from the propeller plane increases. Its port lobe is comparable with that of **CO**.

than 1.5 m, the **CNTI5** configuration shows louder noise levels, with a maximum difference of 1 dB at the further up-stream position considered in the analysis. A narrow area of lower noise in instead observed towards the wing-fuselage junction.

The **CNTI21** case, on the other hand, results significantly noisier than the quietest **CNTI** configuration, with a longitudinally-average discrepancy of approximately +2.7 dB and maximum OSPL differences of about +5 dB at fuselage stations $\pm 1R$ from the propeller plane. The **CNTI21** case is also louder than the **CO** configuration up to approximately 1.2 m down-stream the propeller plane, and than the **CO21** option for

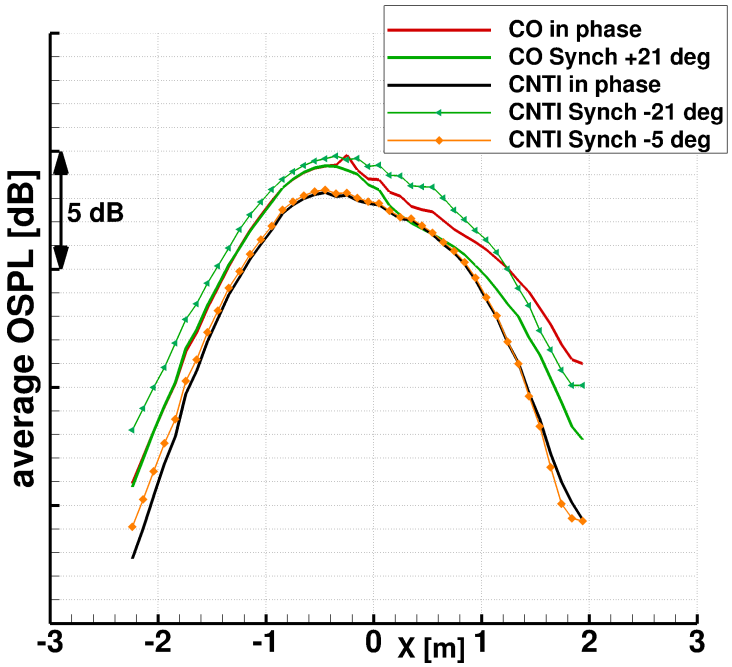

Figure 8.7: OSPL averaged over the fuselage azimuth Θ, in the passengers area, as a function of the fuselage longitudinal position: comparison between the different **CNTI** synchrophasing cases. **CO** and **CO21** configurations reported as a reference. Noise estimate from numerical probe data over one full propeller revolution. **CNTI5** appears overall almost equivalent to **CNTI**. **CNTI21** results instead the worse choice, being louder than **CO** as well.

all fuselage stations considered, with local differences up to +2 dB.

8.4.2 Cabin Interior Noise

Pressure time histories recorded by the numerical probes on the starboard fuselage (see Figure 7.5) are used as input to the transfer functions to estimate the cabin sound levels for the example passenger considered (refer to Figure 3.2(a)). Figure 8.8 presents the SPL of the first three harmonics. With respect to the **CNTI** case, the **CNTI5** option shows a louder first tone ($\sim$ +1.4 dB), but quieter second and third tones. The considerably large reduction at the third tone with the choice of $\psi_s = -5$ deg appears mainly due to the transformation of the phase during the passage into the fuselage shell more than the transmission loss. The **CNTI21** option yield instead an increase of both first ($\sim$ +1.7 dB) and second tones, and the same noise level at the third tone, compared to the **CNTI** case. It can also be noted that all **CNTI** tested configurations display a significant SPL reductions for all the first three harmonics compared to the **CO** case. Table 8.5 reports the OSPL at the example passenger location of the different test cases with respect to the **CNTI** option, which is shown to be the quietest mainly thanks to the lowest SPL at the blade passing frequency. The **CNTI5** option yields louder interior noise than the **CNTI** by more than 1 dB, though its external sound levels are very close

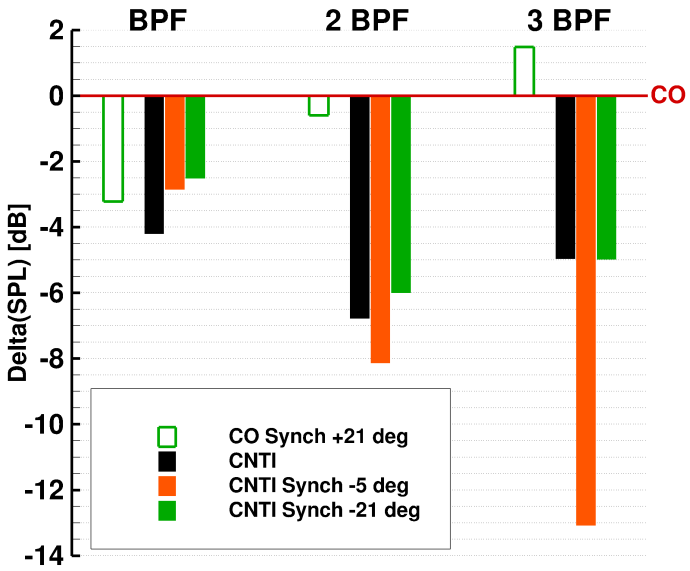

Figure 8.8: Cabin interior sound evaluation, for the example passenger, using experimental TF: SPL for first, second and third tone. Comparison between the different **CNTI** synchrophasing cases. Relative data with respect to the case with co-rotating phased propellers. Results for **CO21** configuration are reported as reference. See Figure 3.2(a) for the passenger location. The **CNTI** option appears the best for reducing the noise at the BPF, the **CNTI5** at 2BPF and 3BPF. The **CO** choice is seen to be the worse, with a penalty of more than 2 dB at the first harmonic.

(averaging along the fuselage axis a difference of +0.17 dB is registered). The **CNTI21** case, that displayed the highest sound levels on the outside of the fuselage, is noisier than the **CNTI** and **CNTI5** options. However, it is significantly quieter (more than 2.5 dB) than the **CO** configuration. It is also noted that the **CO21** case results quieter than the **CNTI5**, despite its OSPL on the external fuselage shows higher values.

CO	CO21	CNTI5	CNTI21
+ 4.21 dB	+1.00 dB	+1.35 dB	+1.68 dB

Table 8.5: Cabin interior OSPL evaluation, for the example passenger, using experimental TF: comparison between the different **CNTI** synchrophasing cases. Relative data with respect to the **CNTI** layout with phased propellers. Results for **CO21** configuration are also reported as reference. See Figure 3.2(a) for the passenger location.

8.5. Conclusive Remarks

The effect of propeller synchrophasing is shown important for the interior noise, and therefore must be considered when estimating actual cabin sound levels. Synchrophasing appears to have a significant favorable effect on a configuration with co-rotating propellers, yielding reductions in OSPL of more than 3 dB for a blade shift angle near the maximum possible (the best synchrophasing angles to decrease the SPL of

harmonics higher than the fundamental tone are instead smaller). The noise reduction appears to be mainly due to the different acoustic interferences that develop between propellers direct sound fields and waves emanating by the airframe, as well as to the different phase of the sound waves impinging on the fuselage. However, it is noted that despite the significant benefit of synchrophasing, co-rotating propellers remain louder than the counter-rotating top-in configuration with propellers in phase. The latter is seen to be the quietest choice, since, by contrast, synchrophasing on a counter-rotating top-in layout results in OSPL increase of more than 1 dB, at least for the shift angles tested.

Chapter 9

Conclusions and Future Work

Compared to turbofans, propeller-driven aircraft would be significantly advantageous for short/medium-range flights, thanks to their lower fuel consumption (nowadays attained at similar flight speeds), as well as the need of shorter runways and climbing/descent times. Their noise is however still high and must be reduced in line with the new aviation environmental targets. The present thesis covered therefore some aspects of turboprop near-field acoustics, aiming to improve our understanding of the actual sound field in-flight and to identify a quieter solution.
A modern propeller with eight blades of extremely low activity factor AF and operating at high loading conditions was considered for this study. Propeller designs, "handedness" for a typical twin-engined aircraft, and synchrophasing were analysed via Computational Fluid Dynamics. The flow solver HMB3 of the University of Glasgow was employed, after a preliminary validation for propeller aerodynamics and acoustics against the JORP and IMPACTA wind tunnel data.
The main findings of the dissertation are here detailed, followed by some recommendations for future work.

9.1. Conclusions

Various blade and hub designs were studied in isolation by means of RANS simulations, to find the quietest at source level.
A blade geometry that moved the loading span-wise inboard, thus off-loading the tip, and operates at lower RPM was found the best choice. OSPL reductions up to 6 dB were observed 1 m away from the blade tip, without severe performance penalty.
Hub configurations with different geometric periodicity led to a spread of the acoustic energy over more frequencies, but resulting in slightly higher sound levels. This could potentially be more pleasant to the human ear, however the transfer functions used to

evaluate cabin noise filtered the majority of the additional tones in the spectra.

A sensitivity analysis of the numerical approach was also performed, to assess the most suitable strategy for noise evaluation.
Density and regularity of the mesh were shown to be both important for accurate noise levels and directivity predictions, especially as the harmonic order and the distance from the propeller increase, because of the stronger effect of numerical dissipation and dispersion. The minimum number of points per wavelength depended on the computational scheme and the sound frequency: approximately 25 points were found enough for the BPF when MUSCL is employed.
The use of a 4^{th} order space-accurate MUSCL scheme was seen not computationally cost-effective for acoustics in the vicinity of the propeller, because of the grid resolution needed for flow predictions.
The scale-resolving models SAS and DES were compared to assess their capability of capturing the high-frequency part of the propeller sound spectrum. The first was seen not effective because the flow is not strongly unstable, the second appeared more suitable and showed the onset of trailing edge noise. The (U)RANS $k-\omega$ SST solution was confirmed adequate to estimate the propeller tonal noise.

The whole acoustic field of a twin-engined high-wing turboprop was examined using URANS computations, for both co- and counter-rotating propellers. Installations effects were thus analysed for the first time, for tonal noise, and the effect of synchrophasing could also be evaluated.
The need of simulating the whole airplane to accurately determine in-flight noise levels was confirmed: the acoustic interferences between the propellers sound waves and those emitted and reflected by the airframe were proven important.
At cruise conditions, with phased propellers, the counter-rotating top-in layout was found the quietest, with a OSPL reduction of more than 4 dB inside the cabin compared to the co-rotating configuration. The inboard-up propeller rotation yielded louder noise because of the higher blade loading on the fuselage side and because of constructive acoustic interferences.
In line with previous experimental and analytical studies, synchrophasing was shown to affect only slightly the exterior OSPL distribution and values, but to be rather effective in the cabin as a consequence of the phase variation occurring during the structure transmission. On co-rotating propellers, the interior OSPL could be lowered by more than 3 dB compared to in-phase propellers with a synchrophasing angle close

to the maximum relative blade shift. By contrast, and with symmetry, the best option for the counter-rotating top-in layout appeared to be in-phase propellers. It was also noted that the optimum synchrophasing angle depends on the harmonic considered, thus it could be thought to use it in conjunction with tunable vibration absorbers calibrated on other tones.

9.2. Future Work

Concerning the propeller design, future efforts should be directed toward the optimisation of the Off-loaded Tip blade as the most promising. RANS simulations could be used for this purpose, coupled to an optimisation strategy based on differential evolution (e.g. [112]) or on a quasi-Newton method using a discrete adjoint for the gradient computation (e.g. [271, 272]). Both aerodynamics and acoustics must be considered in the optimisation. This blade design should also be tested mounted on the aircraft, to evaluate its actual noise benefit in flight.
With regard to the CFD capability of high-frequency noise predictions, improved DES models should be tested. Recent progress in computing systems allows nowadays the resolution of such big computations. A systematic analysis of central 6-or-more accurate schemes should anyway be performed to quantify their benefit in terms of mesh size reduction, thus to limit the computational cost of these expensive simulations (or maximise the captured spectra on a given mesh). Additional extensive experimental data are nonetheless necessary to gain more insight in the noise generation mechanism, and to validate the numerical methods. A CFD solver output that would be also useful to investigate on this subject is the PSD of kinetic energy.
As for propeller installation, handedness and synchrophasing studies should be performed at take-off and landing regimes, thus to evaluate the best turboprop operating option regarding community noise as well. Finally, it would be very interesting to develop a vibro-acoustic model of the aircraft fuselage coupled with the CFD. This way, the assessment of the complete cabin sound field would be possible, and results could be also tailored on the actual airplane of interest. In addition, if the full aircraft is structurally modelled, the structure-borne noise could be also accounted for.

Bibliography

[1] M. Janic. *The sustainability of air transportation: a quantitative analysis and assessment*. Routledge, 2017. ISBN 9781351881395. URL https://www.taylorfrancis.com/books/9781351881395.

[2] M.S. Ryerson and M. Hansen. The potential of turboprops for reducing aviation fuel consumption. *Transportation Research Part D: Transport and Environment*, 15(6):305–314, 2010. ISSN 1361-9209. doi: https : / / doi . org / 10 . 1016 / j . trd . 2010 . 03 . 003. URL http://www.sciencedirect.com/science/article/pii/S1361920910000349.

[3] M. Smirti and M. Hansen. The potential of turboprops to reduce aviation fuel consumption. *University of California Transportation Center*, pages 1–13, 2009. URL https://escholarship.org/uc/item/5131891j. (UCTC Research Paper No. 883).

[4] Dowty Aerospace Propellers. URL http://dowty.com. (Accessed 23 February 2018).

[5] P. Argüelles, M. Bischoff, P. Busquin, B.A.C. Droste, R. Sir Evans, W. Kröll, J.L. Lagardere, A. Lina, J. Lumsden, D. Ranque, et al. European Aeronautics: a Vision for 2020 - Meeting Society's Needs and Winning Global Leadership. Technical report, European Commission, Directorate General for Research and Innovation - Advisory Council for Aeronautics Research in Europe, 2001. URL http://www.acare4europe.org/sites/acare4europe.org/files/document/Vision%202020_0.pdf.

[6] The High Level Group on Aviation Research: M. Darecki, C. Edelstenne, T. Enders, E. Fernandez, P. Hartman, J.-P. Herteman, M. Kerkloh, I. King, P. Ky, M. Mathieu, G. Orsi, G. Schotman, C. Smith, and J.-D. W*ö*rner. Flightpath 2050: Europe's vision for aviation. report of the high level group on aviation research. Technical report, ACARE (Advisory Council for Aeronautics Research in Europe) - Publications Office of the European Union, Luxembourg, 2011. URL http://ec.europa.eu/transport/sites/transport/files/modes/air/doc/flightpath2050.pdf.

[7] X. Huang, L. Sheng, and Y. Wang. Propeller synchrophase angle optimization of turboprop-driven aircraft—an experimental investigation. *Journal of Engineering for Gas Turbines and Power*, 136(11): 112606–1–112606–9, 2014. doi: 10.1115/1.4027644. URL http://dx.doi.org/10.1115/1.4027644.

[8] IMPACTA - IMproving the Propulsion Aerodynamics and aCoustics of Turboprop Aircraft. URL http://gtr.rcuk.ac.uk/project/506AE188-48A3-4C80-B96C-40E7120FFB75#. (Accessed 10 February 2018).

[9] N.W. Bown and A. Knepper. Aircraft ad Propulsion Design Requirements for the IMPACTA Project. Technical Report ITS 01675, Issue 3, Dowty Propellers (GE Aviation Systems Ltd), 2013.

[10] ARA - Aircraft Research Association. URL http://www.ara.co.uk. (Accessed 26 March 2018).

[11] Netherlands Aerospace Centre. URL http://www.nlr.org/. (Accessed 26 March 2018).

[12] CFD Laboratory - University of Glasgow. Modelling and simulation. URL https://www.gla.ac.uk/cfd. (Accessed 26 March 2018).

[13] B. Magliozzi, D. Hanson, and R. Amiet. Propeller and propfan noise. In *Aeroacoustics of Flight Vehicles: Theory and Practice. Volume1: Noise Sources. NASA Technical Report 90-3052.*, volume 1, pages 1–64. NASA, Langley Research Center, Hampton, VA, USA, 1991. URL https://ntrs.nasa.gov/archive/nasa/casi.ntrs.nasa.gov/19920001380.pdf.

[14] M. Carley and J.A. Fitzpatrick. Spectral conditioning of propeller noise from broadband sources. *Journal of sound and vibration*, 238(1):31–49, 2000. doi: 10.1006/jsvi.2000.3101.

[15] G. Müller and M. Möser. *Handbook of engineering acoustics*. Springer Science & Business Media, 2012. ISBN 978-3-642-43550-8.

[16] J.P. Yin, S.R. Ahmed, and W. Dobrzynski. New acoustic and aerodynamic phenomena due to non-uniform rotation of propellers. *Journal of sound and vibration*, 225(1):171–187, 1999. doi: https://doi.org/10.1006/jsvi.1999.2229.

[17] W. M. Dobrzynski, H. H. Heller, J. O. Powers, and J. E. Densmore. Propeller Noise Tests in the German-Dutch Wind Tunnel DNW. Technical Report DFVLR-IBc129-86/3, FAA-AEE 86-3 (AD-A174 977), DFVLR/FAA (Deutsche Forschungs-und Versuchsanstalt fuer Luft und Raumfahrt/Federal Aviation Administration), 1986.

[18] J. Obata, Y. Yosida, and S. Morita. Studies on the Sounds Emitted by Revolving Airscrews. Part I. Technical Report 79, Aeronautical Research Institute, Tokyo Imperial University, 1932. URL https://repository.exst.jaxa.jp/dspace/handle/a-is/11388.

[19] J. Obata and S. Morita. Studies on the Sounds Emitted by Revolving Airscrews. Part II. Experiments with Model Airscrews. In *Proceedings of the Physico-Mathematical Society of Japan. 3rd Series*, volume 14, pages 486–509. THE PHYSICAL SOCIETY OF JAPAN, The Mathematical Society of Japan, 1932. doi: 10.11429/ppmsj1919.14.0_486. URL https://www.jstage.jst.go.jp/article/ppmsj1919/14/0/14_0_486/_article.

[20] E.Z. Stowell and A.F. Deming. Vortex noise from rotating cylindrical rods. *The Journal of the Acoustical Society of America*, 7(3):190–198, 1936. doi: 10.1121/1.1915806. URL https://doi.org/10.1121/1.1915806.

[21] A. Skvortsov, K. Gaylor, C. Norwood, B. Anderson, and L. Chen. Scaling lays for noise generated by the turbulent flow around a slender body. In *Proceedings of the Undersea Defence Technology Conference, Cannes, France*, 2009.

[22] I. Proudman. The Generation of Noise by Isotropic Turbulence. *Proceedings of the Royal Society of London A: Mathematical, Physical and Engineering Sciences*, 214(1116):119–132, 1952. ISSN 0080-4630. doi: 10.1098/rspa.1952.0154.

[23] G.M. Lilley. The Radiated Noise From Isotropic Turbulence Revisited. Technical Report ICASE Report No. 93-75, NASA Contractor Report 1916547, NASA Langley Research Center, Hampton, Virginia, United States, December 1993. URL http://oai.dtic.mil/oai/oai?verb=getRecord&metadataPrefix=html&identifier=ADA276712.

[24] R. K. Amiet. Noise due to turbulent flow past a trailing edge. *Journal of sound and vibration*, 47(3):387–393, 1976. doi: 10.1016/0022-460X(76)90948-2.

[25] R.W. Paterson and R.K. Amiet. Noise of a Model Helicopter Rotor Due to Ingestion of Turbulence. Technical Report NASA CR-3213, NASA Langley Research Center; Hampton, VA, United States, November 1979. URL https://ntrs.nasa.gov/search.jsp?R=19800002821.

[26] M. Roger and S. Moreau. Back-Scattering Correction and Further Extensions of Amiet's Trailing-Edge Noise Model. Part I:Theory. *Journal of Sound and Vibration*, 286(3):477 – 506, 2005. ISSN 0022-460X. doi: https://doi.org/10.1016/j.jsv.2004.10.054. URL http://www.sciencedirect.com/science/article/pii/S0022460X04009356.

[27] M. Roger and S. Moreau. Back-Scattering Correction and Further Extensions of Amiet's Trailing-Edge Noise Model. Part II:Application. *Journal of Sound and Vibration*, 323(1):397 – 425, 2009. ISSN 0022-460X. doi: https://doi.org/10.1016/j.jsv.2008.11.051. URL http://www.sciencedirect.com/science/article/pii/S0022460X08010079.

[28] S. Moreau and M. Roger. Competing Broadband Noise Mechanisms in Low-Speed Axial Fans. *AIAA Journal*, 45(1):48–57, 2007. ISSN 0001-1452. doi: 10.2514/1.14583. URL https://doi.org/10.2514/1.14583.

[29] Y. Rozenberg. *Modélisation analytique du bruit aérodynamique à large bande des machines tournantes : utilisation de calculs moyennés de mécanique des fluides*. Theses, Ecole Centrale de Lyon, Laboratoire de Mecanique des Fluides et d'Acoustique (LMFA), December 2007. URL https://tel.archives-ouvertes.fr/tel-00678225.

[30] B. Magliozzi. Generalized Propeller Noise Estimating Procedure - Revision D. Technical report, Hamilton Standard Publication, 1971.

[31] M.H. Smith. A prediction procedure for propeller aircraft flyover noise based on empirical data. Technical Report SAE Technical Paper 810604, SAE International, 1981. URL https://www.sae.org/publications/technical-papers/content/810604/.

[32] W. Dobrzynski. A general prediction procedure for light propeller driven aeroplane flyover noise signatures. In *Proceedings of Inter-Noise 94: Noise - Quantity and Quality*, pages 271–274. Institute of Noise Control Engineering, 1994. URL http://elib.dlr.de/36220/.

[33] F.J.H. Lynam and H.A. Webb. The emission of sound by airscrews. Technical Report Technical Reports and Memoranda No. 624, Technical Report of the Advisory Committee for Aeorinautics for the Year 1918-1919 Vol. II, 1919.

[34] G.H. Bryan. The acoustics of moving sources with application to airscrews. Technical Report Technical Reports and Memoranda No. 684, Technical Report of the Advisory Committee for Aeorinautics for the Year 1920-1921 Vol. II, 1920.

[35] F.B. Metzger. A review of propeller noise prediction methodology: 1919-1994. Technical Report NASA-CR-198156, NAS 1.26:198156, NASA Langley Research Center, Hampton, VA, United States, 1995. URL https://ntrs.nasa.gov/search.jsp?R=19960008819.

[36] L. Gutin. On the Sound of a Rotating Propeller. Technical Report TM-1195, NACA-National Advisory Committee for Aeronautics., Langley Aeronautical Lab.; Langley Field, VA, United States, October 1948. URL https://ntrs.nasa.gov/search.jsp?R=20030068996.

[37] A.F. Deming. Noise from propellers with symmetrical sections at zero blade angle. Technical Report TN-605, NACA-National Advisory Committee for Aeronautics. Langley Aeronautical Lab.; Langley Field, VA, United States, 1937. URL https://ntrs.nasa.gov/search.jsp?R=19930081380.

[38] A.F. Deming. Propeller rotation noise due to torque and thrust. *The Journal of the Acoustical Society of America*, 12(1):173–182, 1940. doi: http://dx.doi.org/10.1121/1.1916089.

[39] M.J. Lighthill. On Sound Generated Aerodynamically. I. General Theory. *Proceedings of the Royal Society of London A: Mathematical, Physical and Engineering Sciences*, 211(1107):564–587, 1952. ISSN 0080-4630. doi: 10.1098/rspa.1952.0060.

[40] M.J. Lighthill. On Sound Generated Aerodynamically. II. Turbulence as a Source of Sound. *Proceedings of the Royal Society of London A: Mathematical, Physical and Engineering Sciences*, 222(1148):1–32, 1954. ISSN 0080-4630. doi: 10.1098/rspa.1954.0049.

[41] I.E. Garrick and C.E. Watkins. A theoretical study of the effect of forward speed on the free-space sound-pressure field around propellers. Technical Report TN-3018, NACA-National Advisory Committee for Aeronautics. Langley Aeronautical Lab.; Langley Field, VA, United States, 1954. URL https://ntrs.nasa.gov/search.jsp?R=19930092212.

[42] J.E. Ffowcs Williams and D.L. Hawkings. Sound Generation by Turbulence and Surfaces in Arbitrary Motion. *Philosophical Transactions of the Royal Society of London A: Mathematical, Physical and Engineering Sciences*, 264(1151):321–342, 1969. ISSN 0080-4614. doi: 10.1098/rsta.1969.0031. URL http://rsta.royalsocietypublishing.org/content/264/1151/321.

[43] N. Curle. The influence of solid boundaries upon aerodynamic sound. In *Proceedings of the Royal Society of London A: Mathematical, Physical and Engineering Sciences*, number 1187 in 231, pages 505–514. The Royal Society, 1955. doi: 10.1098/rspa.1955.0191. URL http://rspa.royalsocietypublishing.org/content/231/1187/505.

[44] F. Farassat. Theory of noise generation from moving bodies with an application to helicopter rotors. Technical Report NASA TR R-451, National Aeronautics and Space Administration, Washington, D.C., 1975. URL https://ntrs.nasa.gov/archive/nasa/casi.ntrs.nasa.gov/19760005740.pdf.

[45] F. Farassat and G.P. Succi. A review of propeller discrete frequency noise prediction technology with emphasis on two current methods for time domain calculations. *Journal of Sound and Vibration*, 71 (3):399–419, 1980. ISSN 0022-460X. doi: https://doi.org/10.1016/0022-460X(80)90422-8. URL http://www.sciencedirect.com/science/article/pii/0022460X80904228.

[46] F. Farassat. Linear acoustic formulas for calculation of rotating blade noise. *AIAA journal*, 19(9):1122–1130, 1981. doi: 10.2514/3.60051. URL https://doi.org/10.2514/3.60051.

[47] F. Farassat. The prediction of the noise of supersonic propellers in time domain - new theoretical results. In *8th Aeroacoustics Conference*. American Institute of Aeronautics and Astronautics, 1983. doi: 10.2514/6.1983-743. URL https://doi.org/10.2514/6.1983-743. AIAA Paper 83-0743.

[48] F. Farassat. The evolution of methods for noise prediction of high speed rotors and propellers in the time domain. In Anjaneyulu Krothapalli and Charles A. Smith, editors, *Recent Advances in Aeroacoustics*, pages 129–147, New York, NY, 1986. Springer New York. ISBN 978-1-4612-4840-8.

[49] F. Farassat, S.L. Padula, and M.H. Dunn. Advanced turboprop noise prediction based on recent theoretical results. *Journal of Sound and Vibration*, 119(1):53–79, 1987. ISSN 0022-460X. doi: https://doi.org/10.1016/0022-460X(87)90189-1. URL http://www.sciencedirect.com/science/article/pii/0022460X87901891.

[50] F. Farassat, M.H. Dunn, and P.L. Spence. Advanced propeller noise prediction in the time domain. *AIAA Journal*, 30(9):2337–2340, 1992. ISSN 0001-1452. doi: 10.2514/3.11224. URL https://doi.org/10.2514/3.11224.

[51] D.B. Hanson. Near-field frequency-domain theory for propeller noise. *AIAA journal*, 23(4):499–504, 1985. doi: 10.2514/3.8943. URL https://doi.org/10.2514/3.8943.

[52] D.B. Hanson and D.J. Parzych. Theory for noise of propellers in angular inflow with parametric studies and experimental verification. Technical Report CR-4499, E-7601, NAS 1.26:4499, NASA. Lewis Research Center, Washington, United States, 1993. URL https://ntrs.nasa.gov/search.jsp?R=19930015905.

[53] D.B. Hanson and B. Magliozzi. Propagation of propeller tone noise through a fuselage boundary layer. *Journal of Aircraft*, 22(1):63–70, 1985. doi: 10.2514/3.45081. URL https://doi.org/10.2514/3.45081.

[54] F. Farassat. Derivation of Formulations 1 and 1A of Farassat. Technical Report NASA/TM-2007-214853, L-19318, NASA Langley Research Center, Hampton, VA, United States, March 2007. URL https://ntrs.nasa.gov/search.jsp?R=20070010579.

[55] F Farassat. Acoustic radiation from rotating blades—the kirchhoff method in aeroacoustics. *Journal of sound and vibration*, 239(4):785–800, 2001. ISSN 0022-460X. doi: https://doi.org/10.1006/jsvi.2000.3221. URL http://www.sciencedirect.com/science/article/pii/S0022460X00932218.

[56] C.K.W. Tam. Computational aeroacoustics-issues and methods. *AIAA journal*, 33(10):1788–1796, 1995. doi: http://dx.doi.org/10.2514/3.12728.

[57] T. Colonius and S.K. Lele. Computational Aeroacoustics: Progress on Nonlinear Problems of Sound Generation. *Progress in Aerospace Sciences*, 40(6):345 – 416, 2004. ISSN 0376-0421. doi: http://dx.doi.org/10.1016/j.paerosci.2004.09.001.

[58] C.K.W. Tam. Recent advances in computational aeroacoustics. *Fluid dynamics research*, 38(9):591–615, 2006. doi: 10.1016/j.fluiddyn.2006.03.006. URL http://stacks.iop.org/1873-7005/38/i=9/a=A02.

[59] S.K. Lele and J.W. Nichols. A second golden age of aeroacoustics? *Philosophical Transactions of the Royal Society of London A: Mathematical, Physical and Engineering Sciences*, 372(2022), 2014. ISSN 1364-503X. doi: 10.1098/rsta.2013.0321. URL http://rsta.royalsocietypublishing.org/content/372/2022/20130321.

[60] P. Spalart, W.H. Jou, M.K. Strelets, and S.R. Allmaras. Comments on the Feasibility of LES for Wings, and on a Hybrid RANS/LES Approach. In *First AFOSR International Conference on DNS/LES, Columbus, OH*, August 1997.

[61] A.C. Bellcock and K.P. Rouser. Design of jet-blowing flow control for propeller boundary layer separation suppression. In *AIAA Information Systems-AIAA Infotech at Aerospace, 2018*, 2018. doi: 10.2514/6.2018-0749.

[62] T. Zimbelman and K.P. Rouser. A plasma flow control concept for propeller boundary layer separation suppression. In *AIAA Information Systems-AIAA Infotech at Aerospace, 2018*, number 209989, 2018. doi: 10.2514/6.2018-0748.

[63] L.F. Rego, L.T. Lima Pereira, and F. Catalano. Noise reductions on a pusher propeller configuration through pylon tangential blowing. In *2018 AIAA/CEAS Aeroacoustics Conference, AIAA AVIATION Forum*, 2018. doi: 10.2514/6.2018-4194. URL https://doi.org/10.2514/6.2018-4194.

[64] Y. Bury, A. Bordron, H. Belloc, and D. Prat. Cror-powerplant pylon wake mitigation for noise reduction through innovative blowing/suction-based active flow control system. In *34th AIAA Applied Aerodynamics Conference, AIAA AVIATION Forum*, 2016. doi: 10.2514/6.2016-3116. URL https://doi.org/10.2514/6.2016-3116.

[65] U. Emborg, F. Samuelsson, J. Holmgren, and S. Leth. Active and passive noise control in practice on the saab 2000 high speed turboprop. In *4th AIAA/CEAS aeroacoustics conference*, pages 1–5. American Institute of Aeronautics and Astronautics, 1998. doi: 10.2514/6.1998-2231. URL https://doi.org/10.2514/6.1998-2231.

[66] A. Paonessa, A. Sollo, M. Paxton, M. Purver, and C.F. Ross. Experimental active control of sound in the ATR 42. In *INTER-NOISE and NOISE-CON Congress and Conference Proceedings, NoiseCon93, Williamsburg VA*, volume 95, pages 225–230. Institute of Noise Control Engineering, 1993. (NASA STI/Recon Technical Report A).

[67] H. Breitbach, D. Sachau, and S. Böhme. Acoustic challenges of the A400M for active systems. In *Smart Structures and Materials 2006: Industrial and Commercial Applications of Smart Structures Technologies*, volume 6171, pages 6171041–6171048. International Society for Optics and Photonics, 2006. doi: 10.1117/12.658435. URL https://doi.org/10.1117/12.658435.

[68] M. Arena, A. De Fenza, M. Di Giulio, A. Paonessa, and F. Amoroso. Progress in studying passive and active devices for fuselage noise reduction for next generation turboprop. *CEAS Aeronautical Journal*, 8(2):303–312, 2017. ISSN 1869-5590. doi: 10.1007/s13272-017-0242-7. URL http://dx.doi.org/10.1007/s13272-017-0242-7.

[69] G.P. Succi, D.H. Munro, and J.A. Zimmer. Experimental verification of propeller noise prediction. *AIAA Journal*, 20(11):1483–1491, 1982. doi: 10.2514/3.51211. URL https://doi.org/10.2514/3.51211.

[70] D.C. Mikkelson, G.A. Mitchell, and L.J. Bober. Summary of recent nasa propeller research. Technical Report NASA-TM-83733, E-2216, NAS 1.15:83733, NASA Lewis Research Center; Cleveland, OH, United States, 1984. URL https://ntrs.nasa.gov/search.jsp?R=19840024274. (Conference paper prepared for the AGARD Fluid Dyn. Panel Meeting on Aerodyn. and Acoustics of Propellers, 1-4 Oct. 1984, Toronto (Canada)).

[71] J.H. Dittmar. A comparison between an existing propeller noise theory and wind tunnel data. Technical Report NASA-TM-81519, E-464, NASA Lewis Research Center; Cleveland, OH, United States, 1980. URL https://ntrs.nasa.gov/search.jsp?R=19800016608. (Document ID 19800016608).

[72] M. Nallasamy, R.P. Woodward, and J.F. Groeneweg. High-speed propeller performance and noise predictions at takeoff/landing conditions. *Journal of Aircraft*, 26(6):563–569, 1989. doi: 10.2514/3.45803. URL https://ntrs.nasa.gov/archive/nasa/casi.ntrs.nasa.gov/19880004578.pdf. (NASA Technical Memorandum 100267, AIAA-88-0264).

[73] R. Woodward. Measured noise of a scale model high speed propeller at simulated take-off/approach conditions. In *25th AIAA Aerospace Sciences Meeting*, pages 1–27. American Institute of Aeronautics and Astronautics, 1987. doi: 10.2514/6.1987-526. URL https://ntrs.nasa.gov/archive/nasa/casi.ntrs.nasa.gov/19870007155.pdf. (Paper AIAA-87-0526).

[74] J.H. Dittmar and D.B. Stang. Cruise noise of the 2/9th scale model of the Large-scale Advanced Propfan (LAP) propeller, SR-7A. Technical Report NASA-TM-100175, E-3746, NAS 1.15:100175, NASA Lewis Research Center; Cleveland, OH, United States, September 1987. URL https://ntrs.nasa.gov/archive/nasa/casi.ntrs.nasa.gov/19870018965.pdf.

[75] H. Gounet and S. Lewy. Prediction of a single-rotation prop-fan noise by a frequency domain scheme. In *ICAS, Congress, 15 th, London (UK)*, pages 1442–1450. International Council of the Aeronautical Sciences, 1986. URL http://www.icas.org/ICAS_ARCHIVE/ICAS1986/ICAS-86-3.10.2.pdf. Paper ICAS-86-3.10.2.

[76] C.K.W. Tam and M. Salikuddin. Weakly nonlinear acoustic and shock-wave theory of the noise of advanced high-speed turbopropellers. *Journal of Fluid Mechanics*, 164:127–154, 1986. doi: 10.1017/S0022112086002501. URL https://doi.org/10.1017/S0022112086002501.

[77] J.B.H.M. Schulten. Frequency-domain method for the computation of propeller acoustics. *AIAA journal*, 26 (9):1027–1035, 1988. doi: 10.2514/3.10008. URL https://doi.org/10.2514/3.10008.

[78] J.B.H.M. Schulten. Effects of asymmetric inflow on near-field propeller noise. *AIAA journal*, 34(2):251–258, 1996. doi: 10.2514/3.13058. URL https://doi.org/10.2514/3.13058.

[79] J.B.H.M. Schulten. Comparison of measured and predicted noise of the Brite-EuRam SNAAP advanced propellers. *3rd AIAA/CEAS Aeroacoustics Conference*, 1997. doi: 10.2514/6.1997-1709. URL https://doi.org/10.2514/6.1997-1709. (Paper AIAA-97-1709-CP).

[80] A.B. Parry and D.G. Crighton. Asymptotic theory of propeller noise. I-Subsonic single-rotation propeller. *AIAA journal*, 27(9):1184–1190, 1989. doi: 10.2514/3.10244. URL https://doi.org/10.2514/3.10244.

[81] D.G. Crighton and A.B. Parry. Asymptotic theory of propeller noise. II-Supersonic single-rotation propeller. *AIAA journal*, 29(12):2031–2037, 1991. doi: 10.2514/3.10838. URL https://doi.org/10.2514/3.10838.

[82] N. Peake and D.G. Crighton. An asymptotic theory of near-field propeller acoustics. *Journal of Fluid Mechanics*, 232:285–301, 1991. doi: 10.1017/S0022112091003695. URL https://doi.org/10.1017/S0022112091003695.

[83] W. Boyd and N. Peake. An approximate method for the prediction of propeller near-field effects. In *13th Aeroacoustics Conference, Tallahassee,FL (USA)*. American Institute of Aeronautics and Astronautics, 1990. doi: 10.2514/6.1990-3998. URL https://doi.org/10.2514/6.1990-3998.

[84] C.E. Whitfield, P.R. Gliebe, R. Mani, and P. Mungur. High Speed Turboprop Aeroacoustic Study (Single Rotation). Volume 1: Model Development. Final Report. Technical Report NASA-CR-182257-VOL-1, NAS 1.26:182257-VOL-1, General Electric Co.; Aircraft Engines.; Cincinnati, OH, United States, May 1989. URL https://ntrs.nasa.gov/search.jsp?R=19890014768. Document ID: 19890014768.

[85] C.E. Whitfield, R. Mani, and P.R. Gliebe. High Speed Turboprop Aeroacoustic Study (Single Rotation). Volume 2: Computer programs. Technical Report NASA-CR-185242, NAS 1.26:185242, General Electric Co.; Aircraft Engines.; Cincinnati, OH, United States, July 1990. URL https://ntrs.nasa.gov/search.jsp?R=19920022004. Document ID: 19920022004.

[86] T.S.L.S. Zandbergen, S. Sarin, and R. Donnelly. Experimental/theoretical investigation of the sound field of an isolated propeller, including angle of incidence effects. In *13th Aeroacoustics Conference, Tallahassee, FL (USA)*, pages 1–8, 1990. doi: 10.2514/6.1990-3952. URL https://doi.org/10.2514/6.1990-3952. (Paper AIAA-90-3952).

[87] H.H. Brouwer. On the use of the method of matched asymptotic expansions in propeller aerodynamics and acoustics. *Journal of Fluid Mechanics*, 242:117–143, 9 1992. ISSN 1469-7645. doi: 10.1017/S0022112092002301. URL http://journals.cambridge.org/article_S0022112092002301.

[88] N. Scrase and M. Maina. The evaluation of propeller aero-acoustic design methods by means of scaled-model testing employing pressure tapped blades and spinner. In *ICAS PROCEEDINGS*, pages 183–195. International Council of the Aeronautical Sciences, 1994. Paper ICAS-94-6.1.2.

[89] H. Gounet. Contribution to the study of light aircraft propeller noise. Technical Report NT 1982-8, ONERA, 1982.

[90] M.H. Dunn and F. Farassat. High-speed propeller noise prediction - a multidisciplinary approach. *AIAA journal*, 30(7):1716–1723, 1992. doi: 10.2514/3.11128. URL https://doi.org/10.2514/3.11128.

[91] D.M. Hanson and M.R. Fink. The importance of quadrupole sources in prediction of transonic tip speed propeller noise. *Journal of Sound and Vibration*, 62(1):19–38, 1979. ISSN 0022-460X. doi: 10.1016/0022-460X(79)90554-6. URL http://www.sciencedirect.com/science/article/pii/0022460X79905546.

[92] M. Carley. Sound radiation from propellers in forward flight. *Journal of sound and vibration*, 225(2):353–374, 1999. ISSN 0022-460X. doi: https://doi.org/10.1006/jsvi.1999.2284. URL http://www.sciencedirect.com/science/article/pii/S0022460X99922848.

[93] M. Carley. Propeller noise fields. *Journal of Sound and Vibration*, 233(2):255–277, 2000. ISSN 0022-460X. doi: https://doi.org/10.1006/jsvi.1999.2797. URL http://www.sciencedirect.com/science/article/pii/S0022460X99927979.

[94] C.J. Chapman. The structure of rotating sound fields. *Proceedings of the Royal Society of London A: Mathematical, Physical and Engineering Sciences*, 440(1909):257–271, 1993. ISSN 0962-8444. doi: 10.1098/rspa.1993.0015. URL http://rspa.royalsocietypublishing.org/content/440/1909/257.

[95] M. Van Dyke. Lifting-line theory as a singular-perturbation problem. *Journal of Applied Mathematics and Mechanics*, 28(1):90–102, 1964.

[96] M. Van Dyke. Perturbation methods in fluid mechanics/annotated edition. Technical Report NASA STI/Recon Technical Report A, Stanford University Stanford, Calif, 1975.

[97] K.D. Korkan, E. von Lavante, and L.J. Bober. Numerical evaluation of propeller noise including nonlinear effects. *AIAA Journal*, 24(6):1043–1045, 1986. doi: 10.2514/3.9386. URL https://doi.org/10.2514/3.9386.

[98] I. Lindblad. On the resolution of the nonlinear near field of a single-rotation propfan with a numerical solution of the euler equations. In *13th Aeroacoustics Conference,Tallahassee,FL,U.S.A.*, pages 21–25. American Institute of Aeronautics and Astronautics, 1990. doi: 10.2514/6.1990-3995. URL https://doi.org/10.2514/6.1990-3995. (Paper AIAA-90-3995).

[99] S. Meijer, I. Lindblad, and S. Wallin. Acoustic prediction for transonic propellers including nonlinear near-field effects. In *14th DGLR/AIAA Aeroacoustics Conference, Aachen, Germany*, volume 1, pages 388–395, 1992.

[100] B.G. Marinus, M. Roger, R. Van den Braembussche, and W. Bosschaerts. Truncated Method for Propeller Noise Prediction up to Low Supersonic Helical Tip Mach Numbers. In *15th AIAA/CEAS Aeroacoustics Conference (30th AIAA Aeroacoustics Conference)*. American Institute of Aeronautics and Astronautics, 2009. doi: 10.2514/6.2009-3330. URL https://doi.org/10.2514/6.2009-3330. (Paper AIAA 2009-3330).

[101] M. De Gennaro, D. Caridi, and M. Pourkashanian. Ffowcs William-Hawkings Acoustic Analogy for Simulation of NASA SR2 Propeller Noise in Transonic Cruise Condition. In *V ECCOMAS CFD*, pages 1–16. European Conference on Computational Fluid Dynamics, Lisbon (Portugal), 2010. ISBN 978-989-96778-1-4. URL http://http://pubdb.ait.ac.at/files/PubDat_AIT_129832.pdf.

[102] M. De Gennaro, D. Caridi, and C. De Nicola. Noise Prediction of NASA SR2 Propeller in Transonic Condition. *ICNAAM, Numerical Analysis and Applied Mathematics International Conference*, 1281:167–170, 2010. doi: 10.1063/1.3498163.

[103] K.S. Brentner and F. Farassat. Analytical Comparison of the Acoustic Analogy and Kirchhoff Formulation for Moving Surfaces. *AIAA Journal*, 36(8):1379–1386, 1998. ISSN 0001-1452. doi: 10.2514/2.558. URL https://doi.org/10.2514/2.558.

[104] C.H. Tan, K.S. Voo, W.L. Siauw, J. Alderton, A. Boudjir, and F. Mendonça. CFD Analysis of the Aerodynamics and Aeroacoustics of the NASA SR2 Propeller. In *ASME Turbo Expo 2014: Turbine Technical Conference and Exposition*, volume 2A:Turbomachinery, pages 1–11. American Society of Mechanical Engineers, 2014. ISBN 978-0-7918-4560-8. doi: 10.1115/GT2014-26779. URL http://dx.doi.org/10.1115/GT2014-26779. Paper GT2014-26779.

[105] J. Hambrey, M. Kotwicz Herniczek, D. Feszty, S. Meslioui, and J. Park. Comparison of Three Popular Methods for the Prediction of High Speed Propeller Noise. In *23rd AIAA/CEAS Aeroacoustics Conference, AIAA AVIATION Forum*, pages 1–12. American Institute of Aeronautics and Astronautics, 2017. doi: 10.2514/6.2017-4181. URL https://arc.aiaa.org/doi/pdf/10.2514/6.2017-4181.

[106] J. Hambrey, D. Feszty, S. Meslioui, and J. Park. Acoustic Prediction of High Speed Propeller Noise Using URANS and a Ffowcs Williams-Hawkings Solver. In *35th AIAA Applied Aerodynamics Conference, AIAA AVIATION Forum*, pages 1–9. American Institute of Aeronautics and Astronautics, 2017. doi: 10.2514/6.2017-3917. URL https://arc.aiaa.org/doi/pdf/10.2514/6.2017-3917.

[107] D. Hanson. Helicoidal surface theory for harmonic noise of propellers in the far field. *AIAA Journal*, 18(10):1213–1220, 1980. doi: 10.2514/3.50873. URL https://doi.org/10.2514/3.50873.

[108] M. Kotwicz Herniczek, D. Feszty, S.-A. Meslioui, and J. Park. Applicability of Early Acoustic Theory for Modern Propeller Design. In *23rd AIAA/CEAS Aeroacoustics Conference, AIAA AVIATION Forum*, pages 1–19. American Institute of Aeronautics and Astronautics, 2017. doi: 10.2514/6.2017-3865. URL https://arc.aiaa.org/doi/pdfplus/10.2514/6.2017-3865.

[109] F.W. Barry and B. Magliozzi. Noise detectability prediction method for low tip speed propellers. Technical Report HSER 5834, AFAPL-TR-71-37, UNITED TECHNOLOGIES CORP WINDSOR LOCKSCT HAMILTON STANDARD DIV, 1971. URL http://www.dtic.mil/dtic/tr/fulltext/u2/729432.pdf.

[110] D.B. Hanson. Sound from a propeller at angle of attack: a new theoretical viewpoint. In *Proceedings of the Royal Society of London A: Mathematical, Physical and Engineering Sciences*, volume 449, pages 315–328. The Royal Society, 1995. doi: 10.1098/rspa.1995.0046. URL http://rspa.royalsocietypublishing.org/content/449/1936/315.article-info.

[111] A. Giauque, B. Ortun, B. Rodriguez, and B. Caruelle. Numerical Error Analysis with Application to Transonic Propeller Aeroacoustics. *Computer and Fluids*, 69:20–34, 2012. ISSN 0045-7930. doi: https://doi.org/10.1016/j.compfluid.2012.07.022. URL http://www.sciencedirect.com/science/article/pii/S0045793012002903.

[112] B.G. Marinus, M. Roger, and R.A. Van de Braembussche. Aeroacoustic and Aerodynamic Optimization of Aircraft Propeller Blades. In *16th AIAA/CEAS Aeroacoustics Conference*, pages 1–17. American Institute of Aeronautics and Astronautics, 2010. doi: 10.2514/6.2010-3850. URL https://doi.org/10.2514/6.2010-3850. Paper AIAA 2010-3850.

[113] B.G. Marinus. Comparative Study of Effects of Sweep and Humps on High-Speed Propeller Blades. *AIAA Journal*, 52(4):739–746, 2014. doi: http://dx.doi.org/10.2514/1.J052833.

[114] R.P. Woodward and I.J. Loeffler. In-flight source noise of an advanced large-scale single-rotation propeller. *Journal of Aircraft*, 30(6):918–926, 1993. doi: 10.2514/3.46435. URL https://doi.org/10.2514/3.46435.

[115] R.P. Woodward and I.J. Loeffler. In-flight near-and far-field acoustic data measured on the Propfan Test Assessment (PTA) testbed and with an adjacent aircraft. Technical Report NASA-TM-103719, E-6402, NAS 1.15:103719, NASA Lewis Research Center; Cleveland, OH, United States, April 1993. URL https://ntrs.nasa.gov/archive/nasa/casi.ntrs.nasa.gov/19930017869.pdf.

[116] P. Spence and P.J.W. Block. Analysis of the PTA external noise data and comparison with predictions. In *13th Aeroacoustics Conference*, pages 1–24. American Institute of Aeronautics and Astronautics, 1990. doi: 10.2514/6.1990-3935. URL http://dx.doi.org/10.2514/6.1990-3935. (Paper AIAA-90-3935).

[117] B.H. Little, H.W. Bartel, N.N. Reddy, G. Swift, C.C. Withers, and P.C. Brown. Propfan test assessment (pta): Flight test report. Technical Report NASA-CR-182278, NAS 1.26:182278, LG89ER0026, Lockheed Aeronautical Systems Co.; Marietta, GA, United States, 1989. URL https://ntrs.nasa.gov/search.jsp?R=19900002422.

[118] B.H. Little, D.T. Poland, H.W. Bartel, C.C. Withers, and P.C. Brown. Propfan test assessment (pta). Technical Report NASA-CR-185138, NAS 1.26:185138, LG89ER0064, Lockheed Aeronautical Systems Co.; Marietta, GA, United States, 1989. URL https://ntrs.nasa.gov/search.jsp?R=19900002423.

[119] M.H. Dunn and G.M. Tarkenton. Computational methods in the prediction of advanced subsonic and supersonic propeller induced noise: ASSPIN users' manual. Technical Report NASA-CR-4434, NAS 1.26:4434, NASA. Langley Research Center, Washington, United States, 1992. URL https://ntrs.nasa.gov/search.jsp?R=19920012215.

[120] P. Spence. Development of a boundary layer noise propagation code and its application to advanced propellers. In *29th Aerospace Sciences Meeting*. American Institute of Aeronautics and Astronautics, 1991. doi: 10.2514/6.1991-593. URL https://doi.org/10.2514/6.1991-593.

[121] M. Nallasamy, E. Envia, B. Clark, and J.F. Groeneweg. Near-field noise of a single rotation propfan at an angle of attack. In *13th Aeroacoustics Conference*, pages 1–18, 1990. doi: http://dx.doi.org/10.2514/6.1990-3953. URL https://ntrs.nasa.gov/archive/nasa/casi.ntrs.nasa.gov/19910003003.pdf. (Paper AIAA-90-3953, NASA TM-103645).

[122] E Envia. Prediction of noise field of a propfan at angle of attack. Technical Report NASA-CR-189047, E-6645, NAS 1.26:189047, NASA, United States, October 1991. URL https://ntrs.nasa.gov/archive/nasa/casi.ntrs.nasa.gov/19920004541.pdf.

[123] M. Nallasamy and J.F. Groeneweg. Prediction of unsteady blade surface pressures on an advanced propeller at an angle of attack. *Journal of aircraft*, 27(9):789–803, 1990. doi: 10.2514/3.45939. URL https://ntrs.nasa.gov/archive/nasa/casi.ntrs.nasa.gov/19900003244.pdf. (Paper AIAA-89-1060, NASA TM-102374).

[124] M. Nallasamy and F. Groeneweg. Unsteady euler analysis of the flowfield of a propfan at an angle of attack. *Journal of Propulsion and Power*, 8(1):136–143, 1992. doi: 10.2514/3.23453. URL https://doi.org/10.2514/3.23453.

[125] P.J.W. Block. The effects of installation on single-and counter-rotation propeller noise. In *9th Aeroacoustics Conference*, pages 1–13. American Institute of Aeronautics and Astronautics, 1984. doi: 10.2514/6.1984-2263. URL https://doi.org/10.2514/6.1984-2263. (Paper AIAA-84-2263).

[126] P.J.W. Block. Installation noise measurements of model sr and cr propellers. Technical Report NASA-TM-85790, NAS 1.15:85790, NASA Langley Research Center; Hampton, VA, United States, 1984. URL https://ntrs.nasa.gov/archive/nasa/casi.ntrs.nasa.gov/19840017357.pdf.

[127] L. Heidelberg and R. Woodward. Advanced turboprop wing installation effects measured by unsteady blade pressure and noise. In *11th Aeroacoustics Conference*, pages 1–22. American Institute of Aeronautics and Astronautics, 1987. doi: 10.2514/6.1987-2719. URL https://ntrs.nasa.gov/archive/nasa/casi.ntrs.nasa.gov/19880000626.pdf. (Paper AIAA-87-2719, NASA TM-100200).

[128] A. Dumas and C. Castan. Aerodynamic Integration of High Speed Propeller on Aircraft Recent Investigations in European Wind Tunnels. In *21st ICAS Congress, Melbourne (Australia)*, pages 1–11. International Council of the Aeronautical Sciences, 1998. ISBN ISBN-10: 1-56347-287-2, ISBN-13: 978-1-56347-287-9. URL http://www.icas.org/ICAS_ARCHIVE/ICAS1998/PAPERS/5103.PDF. Paper ICAS-98-5.10.3.

[129] M. Amato, F. Boyle, J. Eaton, and P. Gardarein. Euler/Navier-Stokes simulation for propulsion airframe integration of advanced propeller-driven aircraft in the European Research Programs GEMINI/APIAN. In *21st ICAS Congress, Melbourne (Australia)*, pages 1–12. International Council of the Aeronautical Sciences, 1998. ISBN ISBN-10: 1-56347-287-2, ISBN-13: 978-1-56347-287-9. URL http://www.icas.org/ICAS_ARCHIVE/ICAS1998/PAPERS/5102.PDF. Paper ICAS 98-5.10.2.

[130] J.M. Bousquet and P. Gardarein. Improvements on computations of high speed propeller unsteady aerodynamics. *Aerospace science and technology*, 7(6):465–472, 2003. ISSN 1270-9638. doi: 10.1016/S1270-9638(03)00046-4. URL http://www.sciencedirect.com/science/article/pii/S1270963803000464.

[131] P. Crozier. APIAN installed tests in the ONERA S1MA wind tunnel. In *39th Aerospace Sciences Meeting and Exhibit*, pages 1–11. American Institute of Aeronautics and Astronautics, 2001. doi: 10.2514/6.2001-580. URL https://doi.org/10.2514/6.2001-580. (Paper AIAA-2001-0580).

[132] J. Frota and E. Maury. Analysis of APIAN high speed isolated test results - Acoustics and Aerodynamics. *Air and Space Europe*, 3(3):87–92, 2001. ISSN 1290-0958. doi: https://doi.org/10.1016/S1290-0958(01)90064-4. URL http://www.sciencedirect.com/science/article/pii/S1290095801900644.

[133] C. Polacsek, P. Spiegel, F. Boyle, J. Eaton, H. Brouwer, and R. Nijboer. Noise computation of high-speed propeller-driven aircraft. In *6th Aeroacoustics Conference and Exhibit*. American Institute of Aeronautics and Astronautics, 2000. doi: 10.2514/6.2000-2086. URL https://doi.org/10.2514/6.2000-2086. Paper AIAA-2000-2086.

[134] I. Samuelsson. Low speed wind tunnel investigation of propeller slipstream aerodynamic effects on different nacelle/wing combinations. In *ICAS, Congress, 16 th, Jerusalem (Israel)*, pages 1749–1765. International Council of the Aeronautical Sciences, 1988. URL http://www.icas.org/ICAS_ARCHIVE/ICAS1988/ICAS-88-4.11.1.pdf. Paper ICAS-88-4.11.1.

[135] I. Samuelsson. Experimental investigation of low speed model propeller slipstream aerodynamic characteristics including flow field surveys and nacelle/wing static pressure measurements. In *ICAS, Congress, 17 th, Stockholm (Sweden)*, pages 71–84. International Council of the Aeronautical Sciences, 1990. URL http://www.icas.org/ICAS_ARCHIVE/ICAS1990/ICAS-90-3.1.3.pdf. Paper ICAS-90-3.1.3.

[136] P. Lotsted. Propeller slip-stream model in subsonic linearized potential flow. *Journal of Aircraft*, 29(6): 1098–1105, 1992. doi: 10.2514/3.56865. URL https://doi.org/10.2514/3.56865.

[137] P. Lotsted. A propeller slipstream model in subsonic linearized potential flow. In *ICAS, Congress, 17 th, Stockholm (Sweden)*, pages 733–744. International Council of the Aeronautical Sciences, 1990. URL http://www.icas.org/ICAS_ARCHIVE/ICAS1990/ICAS-90-5.4.4.pdf. Paper ICAS-90-5.4.4.

[138] H.K. Tanna, R.H. Urrin, and H.E. Lumblee. Installation effects on propeller noise. *Journal of Aircraft*, 18 (4):303–309, 1981. doi: 10.2514/3.44703. URL https://doi.org/10.2514/3.44703.

[139] A.S. Aljabri. Prediction of propeller slipstream characteristics. *Lockheed-Georgia Company Engineering Rept. LG79ER0120*, 1979.

[140] B. Magliozzi. V/stol rotary propulsion systems noise prediction and reduction. *Dept. of Transportation, FAA Systems Research and Development Service Report FAA-RD-76-lt9, May*, 1976.

[141] S. Leth, F. Samuelsson, and S. Meijer. Propeller Noise Generation and its Reduction on the Saab 2000 High-Speed Turboprop. In *4th AIAA/CEAS Aeroacoustics Conference*, pages 457–463. American Institute of Aeronautics and Astronautics, 1998. doi: 10.2514/6.1998-2283. URL https://doi.org/10.2514/6.1998-2283. Paper AIAA-98-2283.

[142] T.S.L.S. Zandbergen, S. Sarin, and R. Donnelly. Propeller noise measurements in DNW on the fuselage of a twin engineaircraft model. In *9th Aeroacoustics Conference, Williamsburg, VA (USA)*, pages 1–10, 1984. doi: 10.2514/6.1984-2367. URL http://dx.doi.org/10.2514/6.1984-2367. (Paper AIAA-84-2367).

[143] G.P. Succi. Design of quiet efficient propellers. Technical Report SAE Technical Paper 790584, SAE International, 1979.

[144] J.B.H.M. Schulten. Aeroacoustics of wide-chord propellers in non-axisymmetric flow. In *9th Aeroacoustics ConferenceWilliamsburg, VA (USA)*, 1985. doi: 10.2514/6.1984-2304. URL https://doi.org/10.2514/6.1984-2304.

[145] J. Šulc, J. Hofr, and L. Benda. Exterior noise on the fuselage of light propeller driven aircraft in flight. *Journal of Sound and Vibration*, 84(1):105–120, 1982. ISSN 0022-460X. doi: https://doi.org/10.1016/0022-460X(82)90435-7. URL http://www.sciencedirect.com/science/article/pii/0022460X82904357.

[146] H.H. Hubbard and A.A. Regier. Free-space oscillating pressures near the tips of rotating propellers. Technical Report NACA Technical Report 996, National Advisory Committee for Aeronautics. Langley Aeronautical Lab.; Langley Field, VA, United States, 1950. URL https://ntrs.nasa.gov/search.jsp?R=19930092054. (Also bound with NACA Annual Report 36, p. 785-805).

[147] J.F. Groeneweg. Aeroacoustics of advanced propellers. In *ICAS, 27th Congress, Stockholm*, volume 1, pages 108–126, 1990. URL http://www.icas.org/ICAS_ARCHIVE/ICAS1990/ICAS-90-4.1.2.pdf. (Paper ICAS-90-4.1.2).

[148] R.A. Marretta, G. Davi', A. Milazzo, G. Lombardi, and M. Carley. A {PROCEDURE} {FOR} {THE} {EVALUATION} {OF} {INSTALLED} {PROPELLER} {NOISE}. *Journal of Sound and Vibration*, 244(4):697 – 716, 2001. ISSN 0022-460X. doi: http://doi.org/10.1006/jsvi.2000.3489. URL http://www.sciencedirect.com/science/article/pii/S0022460X00934898.

[149] E.J. Hall. Aerodynamic/aeroacoustic cfd analysis of advanced turbopropeller propulsion systems. In *Presentation Information from the SAE Workshop on Propeller Noise Prediction Methods*, 1994.

[150] A. Stuermer. Unsteady Euler and Navier-Stokes Simulations of Propellers with the Unstructured DLR TAU-Code. In *New Results in Numerical and Experimental Fluid Mechanics V*, pages 144–151. Springer, 2006. doi: 10.1007/978-3-540-33287-9_18.

[151] E.W.M. Roosenboom, A. Stürmer, and A. Schröder. Advanced experimental and numerical validation and analysis of propeller slipstream flows. *Journal of Aircraft*, 47(1):284–291, 2010. doi: http://dx.doi.org/10.2514/1.45961.

[152] Bouarfa Mohamed, Mathieu Jubera, Tanguy Duhil De Benaze, Grégoire Pont, and PIerre Brenner. Propeller simulations using an overset technique based on geometric intersections. In *35th AIAA Applied Aerodynamics Conference*, pages 1–23, 2017. doi: 10.2514/6.2017-3916. URL https://arc.aiaa.org/doi/pdf/10.2514/6.2017-3916.

[153] R. de Vries, T. Sinnige, B. Della Corte, F. Avallone, D. Ragni, G. Eitelberg, and L.L. Veldhuis. Tractor propeller-pylon interaction, part i: Characterization of unsteady pylon loading. In *55th AIAA Aerospace Sciences Meeting*, pages 1–16, 2017. doi: 0.2514/6.2017-1175. (Paper AIAA-2017-1175).

[154] C. Agostinelli, C.B. Allen, C. Liu, G. Ferraro, and A. Rampurawala. Propeller - wing interaction using rapid computational methods. In *31st AIAA Applied Aerodynamics Conference, Fluid Dynamics and Co-located Conferences*. American Institute of Aeronautics and Astronautics, 2013. doi: 10.2514/6.2013-2418. URL http://dx.doi.org/10.2514/6.2013-2418.

[155] C. Agostinelli, S. Simeone, A. Rampurawala, C.B. Allen, and F. Zhu. A fast approach to model the effects of propeller slipstream on wing load distribution. In *53rd AIAA Aerospace Sciences Meeting*, page 0028, 2015. doi: 10.2514/6.2015-0028. URL https://arc.aiaa.org/doi/abs/10.2514/6.2015-0028.

[156] M.D. Patterson, M.J. Daskilewicz, and B. German. Simplified aerodynamics models to predict the effects of upstream propellers on wing lift. In *53rd AIAA Aerospace Sciences Meeting*, page 1673, 2015. doi: 10.2514/6.2015-1673. URL https://arc.aiaa.org/doi/pdf/10.2514/6.2015-1673.

[157] J.A. Cole, M.D. Maughmer, G. Bramesfeld, and M.P. Kinzel. A higher-order free-wake method for propeller-wing systems. In *35th AIAA Applied Aerodynamics Conference*, page 3414, 2017. doi: 10.2514/6.2017-3414. URL https://arc.aiaa.org/doi/pdf/10.2514/6.2017-3414.

[158] L Müller, D Kožulović, and R Radespiel. Aerodynamic performance of an over-the-wing propeller configuration at increasing mach number. *CEAS Aeronautical Journal*, 5(3):305–317, 2014. ISSN 1869-5590. doi: 10.1007/s13272-014-0108-1. URL https://doi.org/10.1007/s13272-014-0108-1.

[159] L. Veldhuis, T. Stokkermans, T. Sinnige, and G. Eitelberg. Analysis of swirl recovery vanes for increased propulsive efficiency in tractor propeller aircraft. In *30th Congress of the International Council of the Aeronautical Sciences, ICAS 2016*. International Council of the Aeronautical Sciences, 2016. URL http://pure.tudelft.nl/ws/files/14199939/2016_0060_paper.pdf.

[160] C. Lenfers, N. Beck, and R. Radespiel. Numerical and experimental investigation of propeller slipstream interaction with active high lift wing. In *35th AIAA Applied Aerodynamics Conference - AIAA AVIATION Forum*, pages 1–14. American Institute of Aeronautics and Astronautics, 2017. doi: 10.2514/6.2017-3248. URL https://arc.aiaa.org/doi/pdf/10.2514/6.2017-3248.

[161] P. Della Vecchia, D. Malgieri, F. Nicolosi, and A. De Marco. Numerical analysis of propeller effects on wing aerodynamic: tip mounted and distributed propulsion. In *Aerospace Europe 6th CEAS Conference*, 2017.

[162] Ç. Atalayer, J. Friedrichs, and D. Wulff. Aerodynamic investigation of s-duct intake for high power turboprop installed on a channel wing. *The Aeronautical Journal*, 121(1242):1131–1146, 2017. doi: 10.1017/aer.2017.46. URL https://doi.org/10.1017/aer.2017.46.

[163] N. van Arnhem, T. Sinnige, T.C. Stokkermans, G. Eitelberg, and L.L. Veldhuis. Aerodynamic interaction effects of tip-mounted propellers installed on the horizontal tailplane. In *2018 AIAA Aerospace Sciences Meeting*, page 2052, 2018. doi: 10.2514/6.2018-2052. URL https://arc.aiaa.org/doi/pdf/10.2514/6.2018-2052.

[164] T.C. Stokkermans, N. van Arnhem, T. Sinnige, and L.L. Veldhuis. Validation and comparison of rans propeller modeling methods for tip-mounted applications. In *2018 AIAA Aerospace Sciences Meeting*, pages 1–22, 2018. doi: 10.2514/6.2018-0542. URL https://arc.aiaa.org/doi/pdf/10.2514/6.2018-0542.

[165] J. Dierke, R.A. Akkermans, J. Delfs, R. Ewert, et al. Installation effects of a propeller mounted on a wing with coanda flap. part ii: numerical investigation and experimental validation. In *20th AIAA/CEAS Aeroacoustics Conference - AIAA AVIATION Forum*. American Institute of Aeronautics and Astronautics, 2014. doi: https://doi.org/10.2514/6.2014-3189.

[166] R.A. Akkermans, M. Pott-Pollenske, H. Buchholz, J. Delfs, D. Almoneit, et al. Installation Effects of a Propeller Mounted on a High-Lift Wing with a Coanda Flap. Part I: Aeroacoustic Experiments. In *20th AIAA/CEAS Aeroacoustics Conference - AIAA AVIATION Forum*, pages 1–14. American Institute of Aeronautics and Astronautics, 2014. doi: 10.2514/6.2014-3191. URL https://doi.org/10.2514/6.2014-3191. Paper AIAA 2014-3191.

[167] D. Boots and D. Feszty. Numerical investigation of the effect of wing position on the aeroacoustic field of a propeller. In *52nd AIAA/SAE/ASEE Joint Propulsion Conference, AIAA Propulsion and Energy Forum*, pages 1–7. American Institute of Aeronautics and Astronautics, 2016. doi: 0.2514/6.2016-4801. URL https://arc.aiaa.org/doi/pdf/10.2514/6.2016-4801.

[168] P.T. Soderman and W. Clifton Horne. Acoustic and aerodynamic study of a pusher-propeller aircraft model. Technical Report NASA TP-3040, Ames Research Center, 1990. URL http://www.ivrp.pl/pafiledb/uploads/Pusher-Propeller.pdf.

[169] B. Della Corte, T. Sinnige, R. de Vries, F. Avallone, D. Ragni, G. Eitelberg, and L.L.M. Veldhuis. Tractor Propeller-Pylon Interaction, Part II: Mitigation of Unsteady Pylon Loading by Application of Leading-Edge Porosity. In *55th AIAA Aerospace Sciences Meeting, AIAA SciTech Forum*, 2017. doi: 10.2514/6.2017-1176. URL https://doi.org/10.2514/6.2017-1176.

[170] Dassault Systemes. SIMULIA PowerFLOW. URL https://exa.com/en/product/simulation-tools/powerflow-cfd-simulation. (Accessed 09/09/2018).

[171] F. Avallone, D. Casalino, and D. Ragni. Impingement of a propeller-slipstream on a leading edge with a flow-permeable insert: A computational aeroacoustic study. *International Journal of Aeroacoustics*, pages 1–25, 2018. doi: 10.1177/1475472X18788961. URL https://doi.org/10.1177/1475472X18788961.

[172] G. Brès, F. Pérot, and D. Freed. A Ffowcs Williams - Hawkings Solver for Lattice-Boltzmann Based Computational Aeroacoustics. In *16th AIAA/CEAS Aeroacoustics Conference, AIAA Aeroacoustics Conferences*, 2010. doi: 10.2514/6.2010-3711. URL https://doi.org/10.2514/6.2010-3711.

[173] T. Kletschkowski. *Adaptive Feed-Forward Control of Low Frequency Interior Noise*, chapter Active Noise Control in a Semi-closed Interior, pages 189–235. Springer Netherlands, Dordrecht, 2012. doi: 10.1007/978-94-007-2537-9_9. URL https://doi.org/10.1007/978-94-007-2537-9_9.

[174] C.R. Fuller. Noise control characteristics of synchrophasing. I-Analytical investigation. *AIAA journal*, 24 (7):1063–1068, 1986. doi: 10.2514/3.9392. URL https://doi.org/10.2514/3.9392.

[175] J.D. Jones and C.R. Fuller. Noise control characteristics of synchrophasing. II-Experimental investigation. *AIAA journal*, 24(8):1271–1276, 1986. doi: 10.2514/3.9431. URL http://dx.doi.org/10.2514/3.9431.

[176] J.F. Johnston, R.E. Donham, and W.A. Guinn. Propeller signatures and their use. *Journal of Aircraft*, 18 (11):934–942, 1981. doi: http://dx.doi.org/10.2514/3.57583.

[177] B. Magliozzi. Synchrophasing for cabin noise reduction of propeller-driven airplanes. In *8th Aeroacoustics Conference*, pages 1–7. American Institute of Aeronautics and Astronautics, 1983. doi: 10.2514/6.1983-717. URL https://doi.org/10.2514/6.1983-717. Paper AIAA-83-0717.

[178] D.M. Blunt. Altitude and airspeed effects on the optimum synchrophase angles for a four-engine propeller aircraft. *Journal of Sound and Vibration*, 333(16):3732–3742, 2014. ISSN 0022-460X. doi: https://doi.org/10.1016/j.jsv.2014.03.038. URL http://www.sciencedirect.com/science/article/pii/S0022460X14002399.

[179] D. Hammond, R. McKinley, and B. Hale. Noise Reduction Efforts for Special Operations C-130 Aircraft Using Active Synchrophaser Control. Technical report, Air Force Rsearch Lab,Wright Patterson AFB,OH,45433, 1998. URL http://www.dtic.mil/dtic/tr/fulltext/u2/a434029.pdf.

[180] F.G. Pla and G.C. Goodman. Method and apparatus for synchronizing rotating machinery to reduce noise, June 1993. URL https://www.google.com/patents/US5221185. US Patent 5221185.

[181] F.G. Pla. Method for reducing noise and/or vibration from multiple rotating machines, August 1998. URL https://www.google.com/patents/US5789678. US Patent 5789678.

[182] D. Kaptein. Propeller blade position controller, September 1996. URL https://www.google.com/patents/US5551649. US Patent 5551649, DE69526464D1, EP0663337B1.

[183] B. Magliozzi. Adaptive synchrophaser for reducing aircraft cabin noise and vibration, September 1995. URL https://patents.google.com/patent/WO1995022488A1/en. US Patent 5453943, WO1995022488A1.

[184] L.J. Eriksson. Active sound attenuation system with on-line adaptive feedback cancellation, June 1987. US Patent 4677677, CA1282161C.

[185] D.M. Blunt. *Optimisation and adaptive control of aircraft propeller synchrophase angles.* PhD thesis, School of Mechanical Engineering, The University of Adelaide, South Australia 5005, 2012. URL https://digital.library.adelaide.edu.au/dspace/bitstream/2440/75757/2/02whole.pdf. (Section 2.4).

[186] D.M. Blunt and B. Rebbechi. Propeller synchrophase angle optimisation study. In *13th AIAA/CEAS Aeroacoustics Conference (28th AIAA Aeroacoustics Conference)*, page 3584. American Institute of Aeronautics and Astronautics, 2007. doi: 10.2514/6.2007-3584. URL https://doi.org/10.2514/6.2007-3584. Paper AIAA 2007-3584.

[187] A. Knepper and N.W. Bown. IMPACTA Wind-Tunnel Instrumentation Specification. Technical Report ITS 01777, Issue 3, Dowty Propellers (GE Aviation Systems Ltd), 2014.

[188] G.N. Barakos, R. Steijl, K. Badcock, and A. Brocklehurst. Development of CFD Capability for Full Helicopter Engineering Analysis. In *31st European Rotorcraft Forum, Florence (Italy)*, pages 1–15, 2005. ISBN 9781617389566.

[189] R. Steijl, G. Barakos, and K. Badcock. A Framework for CFD Analysis of Helicopter Rotors in Hover and Forward Flight. *International Journal for Numerical Methods in Fluids*, 51(8):819–847, 2006. ISSN 1097-0363. doi: 10.1002/fld.1086. URL http://dx.doi.org/10.1002/fld.1086.

[190] S. Osher and S. Chakravarthy. Upwind Schemes and Boundary Conditions with Applications to Euler Equations in General Geometries. *Journal of Computational Physics*, 50(3):447–481, 1983. ISSN 0021-9991. doi: https://doi.org/10.1016/0021-9991(83)90106-7. URL http://www.sciencedirect.com/science/article/pii/0021999183901067.

[191] P.L. Roe. Approximate Riemann Solvers, Parameter Vectors, and Difference Schemes. *Journal of Computational Physics*, 43(2):357–372, October 1981.

[192] B. van Leer. Flux-vector Splitting for the Euler Equations. In *Eighth International Conference on Numerical Methods in Fluid Dynamics*, pages 507–512. Springer Berlin Heidelberg, 1997. ISBN 978-3-540-39532-4. doi: 10.1007/978-3-642-60543-7_5.

[193] G.D. van Albada, B. van Leer, and W.W. Roberts Jr. A Comparative Study of Computational Methods in Cosmic Gas Dynamics. In *Upwind and High-Resolution Schemes*, volume 2, pages 95–103. Springer Berlin Heidelberg, 1997. ISBN 978-3-642-60543-7. doi: 10.1007/978-3-642-60543-7_6. URL https://doi.org/10.1007/978-3-642-60543-7_6.

[194] A. Jameson. Time dependent calculations using multigrid, with applications to unsteady flows past airfoils and wings. In *10th Computational Fluid Dynamics Conference, Honolulu, HI, U.S.A*. American Institute of Aeronautics and Astronautics, 1991. doi: https://doi.org/10.2514/6.1991-1596.

[195] O. Axelsson. *Iterative Solution Methods*. Cambridge University Press, Cambridge, MA, 1994. ISBN 9780511624100. doi: 10.1017/CBO9780511624100. URL https://doi.org/10.1017/CBO9780511624100.

[196] E. Gabriel, G.E. Fagg, G. Bosilca, T. Angskun, J.J. Dongarra, J.M. Squyres, V. Sahay, P. Kambadur, B. Barrett, A. Lumsdaine, R.H. Castain, D.J. Daniel, R.L. Graham, and T.S. Woodall. Open MPI: Goals, concept, and design of a next generation MPI implementation. In *Proceedings, 11th European PVM/MPI Users' Group Meeting*, pages 97–104, Budapest, Hungary, September 2004. URL https://www.open-mpi.org/papers/euro-pvmmpi-2004-overview/euro-pvmmpi-2004-overview.pdf.

[197] Open MPI: Open Source High Performance Computing. URL https://www.open-mpi.org/.

[198] S.J. Lawson, M. Woodgate, R. Steijl, and G.N. Barakos. High Performance Computing for Challenging Problems in Computational Fluid Dynamics. *Progress in Aerospace Sciences*, 52: 19–29, July 2012. ISSN 0376-0421. doi: https://doi.org/10.1016/j.paerosci.2012.03.004. URL http://www.sciencedirect.com/science/article/pii/S0376042112000371. Applied Computational Aerodynamics and High Performance Computing in the UK.

[199] ARCHIE-WeSt: High Performance Computing for the West of Scotland, . URL https://www.archie-west.ac.uk/.

[200] Cirrus UK National Tier-2 HPC Service at EPCC. URL http://www.cirrus.ac.uk/.

[201] ARCHER UK National Supercomputing Service, . URL http://www.archer.ac.uk/.

[202] G.N. Barakos and M.A. Woodgate. KNL Performance Comparison: HMB, 2017. URL http://www.archer.ac.uk/community/benchmarks/archer-knl/KNL_perf_HMB.pdf.

[203] A. J. Jerri. The Shannon sampling theorem - Its various extensions and applications: A tutorial review. *Proceedings of the IEEE*, 65(11):1565–1596, 1977. doi: 10.1109/PROC.1977.10771.

[204] M. Biava and L. Vigevano. The effect of far-field boundary conditions on tip vortex path predictions in hovering. In *CEAS Aerospace Aerodynamics Research Conference, Cambridge*, pages 10–13, 2002.

[205] G.R. Srinivasan. A free-wake euler and navier-stokes cfd method and its application to helicopter rotors including dynamic stall. Technical Report ADA278000, JAI ASSOCIATES INC MOUNTAIN VIEW CA, 1993. URL http://www.dtic.mil/docs/citations/ADA278000.

[206] C.O.E. Burg. Higher order variable extrapolation for unstructured finite volume rans flow solvers. In *17th AIAA Computational Fluid Dynamics Conference - Fluid Dynamics and Co-located Conferences*. American Institute of Aeronautics and Astronautics, 2005. doi: https://doi.org/10.2514/6.2005-4999.

[207] H. Q. Yang, Z. J. Chen, A. Przekwas, and J. Dudley. A high-order cfd method using successive differentiation. *Journal of Computational Physics*, 281:690–707, 2015. doi: https://doi.org/10.1016/j.jcp.2014.10.046.

[208] H.Q. Yang and R.E. Harris. Vertex–centered, high-order schemes for turbulent flows. In *54th AIAA Aerospace Sciences Meeting - AIAA SciTech Forum*. American Institute of Aeronautics and Astronautics, 2016. doi: https://doi.org/10.2514/6.2016-1098.

[209] D. Mavriplis. Revisiting the least-squares procedure for gradient reconstruction on unstructured meshes. In *16th AIAA Computational Fluid Dynamics Conference - Fluid Dynamics and Co-located Conferences*. American Institute of Aeronautics and Astronautics, 2003. doi: https://doi.org/10.2514/6.2003-3986.

[210] A. Jimenez Garcia and G. N. Barakos. Implementation of high-order methods in the hmb cfd solver. In *73rd AHS International's Annual Forum and Technology Display*, 2017.

[211] A. Jimenez-Garcia and G.N. Barakos. Assessment of a high-order muscl method for rotor flows. *International Journal for Numerical Methods in Fluids*, 2018. ISSN 1097-0363. doi: 10.1002/fld.4492. URL http://dx.doi.org/10.1002/fld.4492.

[212] M. Breuer, D. Lakehal, and W. Rodi. *Flow around a Surface Mounted Cubical Obstacle: Comparison of Les and Rans-Results*, pages 22–30. Vieweg+Teubner Verlag, Wiesbaden, 1996. ISBN 978-3-322-89838-8. doi: 10.1007/978-3-322-89838-8_4. URL https://doi.org/10.1007/978-3-322-89838-8_4.

[213] J. Fröhlich and D. von Terzi. Hybrid les/rans methods for the simulation of turbulent flows. *Progress in Aerospace Sciences*, 44(5):349 – 377, 2008. ISSN 0376-0421. doi: https://doi.org/10.1016/j.paerosci.2008.05.001. URL http://www.sciencedirect.com/science/article/pii/S0376042108000390.

[214] J. Boussinesq. *Théorie de l'Écoulement Tourbillonant et Tumultueux des Liquides dans des Lits Rectilignes à Grande Section, Tome I-II (Theory of the swirling and turbulent flow of liquids in straight channels of large section, Volume I-II)*. Gaulthier-Villars, Paris, France, first edition, 1897.

[215] F.R. Menter. Two-Equation Eddy-Viscosity Turbulence Models for Engineering Applications. *AIAA Journal*, 32(8):1598–1605, August 1994. doi: 10.2514/3.12149. URL https://doi.org/10.2514/3.12149.

[216] D.C. Wilcox. Formulation of the k–x turbulence model revisited. *AIAA J*, 46(11):2823–2838, 2008.

[217] W.P Jones and B.E Launder. The prediction of laminarization with a two-equation model of turbulence. *International Journal of Heat and Mass Transfer*, 15(2):301 – 314, 1972. ISSN 0017-9310. doi: https://doi.org/10.1016/0017-9310(72)90076-2. URL http://www.sciencedirect.com/science/article/pii/0017931072900762.

[218] P. Bradshaw, D.H. Ferriss, and N.P. Atwell. Calculation of boundary-layer development using the turbulent energy equation. *Journal of Fluid Mechanics*, 28(3):593–616, 1967. doi: 10.1017/S0022112067002319. URL https://doi.org/10.1017/S0022112067002319.

[219] F. R. Menter. Zonal Two Equation k-omega Turbulence Models for Aerodynamic Flows. *AIAA Paper*, 23rd Fluid Dynamics, Plasmadynamics, and Lasers Conference(2906), 1993. doi: 10.2514/6.1993-2906. URL https://doi.org/10.2514/6.1993-2906.

[220] P.R. Spalart and C.L. Rumsey. Effective Inflow Conditions for Turbulence Models in Aerodynamic Calculations. *AIAA Journal*, 45(10):2544–2553, 2007. doi: 10.2514/1.29373. URL https://doi.org/10.2514/1.29373.

[221] NASA Langley Research Center. Turbulence Modeling Resource. URL https://turbmodels.larc.nasa.gov/index.html.

[222] A.K. Hellsten. New advanced kw turbulence model for high-lift aerodynamics. *AIAA journal*, 43(9):1857–1869, 2005. doi: 10.2514/1.13754. URL https://doi.org/10.2514/1.13754.

[223] S. Wallin and A.V. Johansson. An explicit algebraic reynolds stress model for incompressible and compressible turbulent flows. *Journal of Fluid Mechanics*, 403:89–132, 2000. doi: 10.1017/S0022112099007004.

[224] B. Chaouat. The state of the art of hybrid rans/les modeling for the simulation of turbulent flows. *Flow, Turbulence and Combustion*, 99(2):279–327, Sep 2017. ISSN 1573-1987. doi: 10.1007/s10494-017-9828-8. URL https://doi.org/10.1007/s10494-017-9828-8.

[225] F. R. Menter and Y. Egorov. The Scale-Adaptive Simulation Method for Unsteady Turbulent Flow Predictions. Part 1: Theory and Model Description. *Flow Turbulence Combust*, 85:113 – 138, 2010. doi: 10.1007/s10494-010-9264-5.

[226] Y. Egorov and F. R. Menter. Development and application of sst-sas turbulence model in the desider project. In *Advances in Hybrid RANS-LES Modelling*, pages 261–270. Springer, 2008.

[227] J. C. Rotta. *Ü*ber eine Methode zur Berechnung turbulenter Scherströmungen. *Aerodynamische Versuchsanstalt Göttingen Rept. 69A 14*, 1968.

[228] J.C. Rotta. *Turbulente Scherströmungen*, pages 127–186. Vieweg+Teubner Verlag, Wiesbaden, 1972. ISBN 978-3-322-91206-0. doi: 10.1007/978-3-322-91206-0_3. URL https://doi.org/10.1007/978-3-322-91206-0_3.

[229] F. R. Menter and Y. Egorov. A Scale Adaptive Simulation Model using Two-Equation Models. *43rd AIAA Aerospace Sciences Meeting and Exhibit*, 2005. doi: http://dx.doi.org/10.2514/6.2005-1095.

[230] A. Travin, M. Shur, M. Strelets, and P. Spalart. Detached-eddy simulations past a circular cylinder. *Flow, Turbulence and Combustion*, 63(1):293–313, 2000. ISSN 1573-1987. doi: 10.1023/A:1009901401183. URL https://doi.org/10.1023/A:1009901401183.

[231] Sir William Thomson F.R.S. Xlvi. hydrokinetic solutions and observations. *Philosophical Magazine*, 42(281):362–377, 1871. doi: 10.1080/14786447108640585. URL http://www.tandfonline.com/doi/abs/10.1080/14786447108640585.

[232] H.V. Helmholtz. Uber discontinuirliche flüssigkeits-bewegung, 1868.

[233] P.R. Spalart. Detached-Eddy Simulation. *Annual Review of Fluid Mechanics*, 41:181 – 202, 2009. doi: 10.1146/annurev.fluid.010908.165130.

[234] P. Spalart, S. Deck, M. L. Shur, K. D. Squires, M.K. Strelets, and A. Travin. A New Version of Detached-Eddy Simulation, Resistant to Ambiguous Grid Densities. *Theoretical and Computational Fluid Dynamics*, 20:181–195, 2006. ISSN 1432-2250. doi: 10.1007/s00162-006-0015-.

[235] M.L. Shur, P.R. Spalart, M.K. Strelets, and A.K. Travin. A hybrid rans-les approach with delayed-des and wall-modelled les capabilities. *International Journal of Heat and Fluid Flow*, 29(6):1638 – 1649, 2008. ISSN 0142-727X. doi: https://doi.org/10.1016/j.ijheatfluidflow.2008.07.001. URL http://www.sciencedirect.com/science/article/pii/S0142727X08001203.

[236] M.L. Shur, P.R. Spalart, M.K. Strelets, and A.K. Travin. An enhanced version of des with rapid transition from rans to les in separated flows. *Flow, turbulence and combustion*, 95(4): 709–737, 2015. ISSN 1386-6184. doi: https://doi.org/10.1007/s10494-015-9618-0. URL https://link.springer.com/article/10.1007/s10494-015-9618-0.

[237] M.L. Shur, P.R. Spalart, and M.K. Strelets. Jet noise computation based on enhanced des formulations accelerating the rans-to-les transition in free shear layers. *International Journal of Aeroacoustics*, 15(6-7):595–613, 2016. doi: https://doi.org/10.1177/1475472X16659388. URL http://journals.sagepub.com/doi/abs/10.1177/1475472X16659388.

[238] P.R. Spalart, S.R. Allmaras, et al. A one equation turbulence model for aerodynamic flows. *RECHERCHE AEROSPATIALE-FRENCH EDITION-*, pages 5–21, 1994.

[239] M. Strelets. Detached Eddy Simulation of Massively Separated Flows. In *AIAA 39th Aerospace Sciences Meeting and Exhibit, Reno, NV*, January 8–11 2001. AIAA-2001-0879.

[240] ANSYS ICEM CFD. URL http://www.ansys.com/Products/Other+Products/ANSYS+ICEM+CFD/. (Accessed 23/02/2016).

[241] R. Steijl and G. Barakos. Sliding Mesh Algorithm for CFD Analysis of Helicopter Rotor–Fuselage Aerodynamics. *International Journal for Numerical Methods in Fluids*, 58(5):527–549, 2008. ISSN 1097-0363. doi: 10.1002/fld.1757. URL http://dx.doi.org/10.1002/fld.1757.

[242] M. Jarwowsky, M.A. Woodgate, G. Barakos, and J. Rokicki. Towards Consistent Hybrid Overset Mesh Methods for Rotorcraft CFD. *International Journal for Numerical Methods in Fluids*, 74(8):543–576, 2014. ISSN 1097-0363. doi: 10.1002/fld.3861. URL http://dx.doi.org/10.1002/fld.3861.

[243] Technical Committee TC 29 (Electroacoustics). Electroacoustics–Sound Level Meters (IEC 61672). Technical report, International Electrotechnical Commission IEC, 2013. Part 1: Specifications (https://webstore.iec.ch/publication/5708), Part 2: Pattern evaluation tests (https://webstore.iec.ch/publication/5709), Part 3: Periodic tests (https://webstore.iec.ch/publication/5710).

[244] ICAO Committee on Aviation Environmental Protection (CAEP) Steering Group. Environmental technical manual. volume i: Procedures for the noise certification of aircraft. Technical Report 9501, AN/929, International Civil Aviation Organisation (ICAO), Canada H3C 5H7, 2015.

[245] Technical Committee ISO/TC 43 (Acoustics). Acoustics–Normal equal-loudness-level contours (ISO 226:2003). Technical report, International Organization for Standardization ISO, 2003. URL https://www.iso.org/standard/34222.html. Standard reviewed and confirmed in 2014.

[246] E.G.M. Geurts. IMPACTA Transmission functions generation - test and processing. Technical Report NLR-CR-2013-145, National Aerospace Laboratory NLR, 2013.

[247] L.M. Lyamshev. Theory of sound radiation by thin elastic shells and plates. *Sov. Phys. Acoust*, 5(4):431–438, 1960.

[248] D.G. MacMartin, G.L. Basso, and F.W. Slingerland. Aircraft fuselage noise transmission measurements using a reciprocity technique. *Journal of sound and vibration*, 187(3):467–483, 1995. doi: https://doi.org/10.1006/jsvi.1995.0536. URL https://www.sciencedirect.com/science/article/pii/S0022460X85705366.

[249] E.G. Williams. *Fourier acoustics: sound radiation and nearfield acoustical holography*. Academic press, 1999. ISBN 0-12-753960-3.

[250] A. Gomariz-Sancha, M. Maina, and A. J. Peace. Analysis of Propeller-Airframe Interaction Effects through a Combined Numerical Simulation and Wind-Tunnel Testing Approach. In *AIAA SciTech Forum, 53rd AIAA Aerospace Sciences Meeting, Kissimmee, Florida*, pages 1–19, 2015. doi: 10.2514/6.2015-1026. URL https://doi.org/10.2514/6.2015-1026. Paper AIAA 2015-1026.

[251] G.N. Barakos and C.S. Johnson. Acoustic comparison of propellers. *International Journal of Aeroacoustics*, 15(6-7):575–594, 2016. doi: 10.1177/1475472X16659214. URL https://doi.org/10.1177/1475472X16659214.

[252] D. C. Wilcox. Multiscale Model for Turbulent Flows. *AIAA Journal*, 26(11):1311–1320, November 1988. doi: http://dx.doi.org/10.2514/3.10042.

[253] J. Jeong and F. Hussain. On the Identification of a Vortex. *Journal of Fluid Mechanics*, 285:69–94, 1995. doi: 10.1017/S0022112095000462. URL https://doi.org/10.1017/S0022112095000462.

[254] P. Chakraborty, S. Balachandar, and R.J. Adrian. On the Relationships between Local Vortex Identification Schemes. *Journal of Computational Physics*, 535:189–214, 2005. doi: 10.1017/S0022112005004726. URL https://doi.org/10.1017/S0022112005004726.

[255] ARA Aircraft Research Association. Transonic Wind Tunnel Testing of ARA. URL http://www.ara.co.uk/services/experimental-aerodynamics/transonic-wind-tunnel-testing/. (Accessed 25/04/2018).

[256] S. Butterworth. On the theory of filter amplifiers. *Wireless Engineer*, 7(6):536–541, 1930.

[257] M.F. Heidmann. Interim prediction method for fan and compressor source noise. Technical Report NASA-TM-X-71763, E-8398, NASA Lewis Research Center; Cleveland, OH, United States, June 1975. URL https://ntrs.nasa.gov/search.jsp?R=19750017876.

[258] L. Bertsch, S. Guérin, G. Looye, and M. Pott-Pollenske. The parametric aircraft noise analysis module-status overview and recent applications. In *17th AIAA/CEAS Aeroacoustics Conference (32nd AIAA Aeroacoustics Conference)*, page 2855, 2011. doi: http://dx.doi.org/10.2514/6.2011-2855.

[259] W. Dobrzynski. Propeller noise reduction by means of unsymmetrical blade-spacing. *Journal of sound and vibration*, 163(1):123–126, 1993. doi: 10.1006/jsvi.1993.1152.

[260] Tecplot Inc. User's manual tecplot 360 ex 2016 release 2. Technical report, 2016.

[261] W. Dobrzynski. Ermittlung von emissionskennwerten für schallimmissionsrechnungen an landeplätzen. *Project Report, DLR-Interner Bericht. 129-94/17*, 1994.

[262] Aircraft Noise Committee. Estimation of the Maximum Discrete Frequency Noise from Isolated Rotors and Propellers. Technical Report Aerounautical Series 76020, ESDU, March 2011. URL https://www.esdu.com/cgi-bin/ps.pl?sess=uniglas_1180528132231hrl&t=doc&p=esdu_76020b. ISBN: 978 0 85679 157 4.

[263] A. Harten, B. Engquist, S. Osher, and S.R. Chakravarthy. Uniformly high order accurate essentially non-oscillatory schemes, III. In *Upwind and high-resolution schemes*, pages 218–290. Springer, 1987. ISBN 978-3-642-60543-7. doi: 10.1007/978-3-642-60543-7_12. URL https://doi.org/10.1007/978-3-642-60543-7_12.

[264] X.-D. Liu, S. Osher, and T. Chan. Weighted essentially non-oscillatory schemes. *Journal of computational physics*, 115(1):200–212, 1994. ISSN 0021-9991. doi: https://doi.org/10.1006/jcph.1994.1187. URL http://www.sciencedirect.com/science/article/pii/S0021999184711879.

[265] C.K.W. Tam and J.C. Webb. Dispersion-relation-preserving finite difference schemes for computational acoustics. *Journal of computational physics*, 107(2):262–281, 1993. ISSN 0021-9991. doi: https://doi.org/10.1006/jcph.1993.1142. URL http://www.sciencedirect.com/science/article/pii/S0021999183711423.

[266] W. Haase, M. Braza, and A. Revell. *DESider–A European Effort on Hybrid RANS-LES Modelling. Results of the European-Union Funded Project, 2004–2007*. Springer, Berlin, Heidelberg, 2009. doi: 10.1007/978-3-540-92773-0. URL https://link.springer.com/book/10.1007%2F978-3-540-92773-0#toc. (Part of the Notes on Numerical Fluid Mechanics and Multidisciplinary Design book series (NNFM, volume 103)).

[267] L.L.M. Veldhuis. Review of Propeller-Wing Aerodynamic Interference. In *ICAS - 24th International Congress of the Aeronautical Sciences, Yokohama (Japan)*, pages 1–21. International Council of the Aeronautical Sciences, 2004. ISBN ISBN 0-9533991-6-8. Paper ICAS 2004-6.3.1.

[268] SKYbrary. Critical Engine. URL https://www.skybrary.aero/index.php/Critical_Engine. (Accessed 10 February 2018).

[269] Airsoc.com. Fokker 50 Turboprop Regional Airliner. URL http://airsoc.com/articles/view/id/54f82b9c313944bf778b456a/fokker-50-turboprop-regional-airliner. (Accessed 23/08/2018).

[270] T. Sinnige, R. de Vries, B. Della Corte, F. Avallone, D. Ragni, G. Eitelberg, and L.L.M. Veldhuis. Unsteady pylon loading caused by propeller-slipstream impingement for tip-mounted propellers. *Journal of Aircraft*, 55(4):1065 – 1618, 2018. ISSN 0021-8669. doi: 10.2514/1.C034696. URL https://doi.org/10.2514/1.C034696.

[271] M. Biava, M. Woodgate, and G. Barakos. Fully Implicit Discrete-Adjoint Methods for Rotorcraft Applications. *AIAA Journal*, 54(2):735–749, 2016. ISSN 1097-0363. doi: 10.2514/1.J054006. URL https://arc.aiaa.org/doi/10.2514/1.J054006.

[272] M. Biava and G.N. Barakos. Optimisation of Ducted Propellers for Hybrid Air Vehicles Using High-Fidelity CFD. *The Aeronautical Journal*, 120(1232):1632–1657, 2016. doi: 10.1017/aer.2016.78.

[273] W.E. Zorumski and D.S. Weir. Aircraft Noise Prediction Program theoretical manual: Propeller aerodynamics and noise. Technical Report NASA-TM-83199-PT-3, L-15937, NAS 1.15:83199-PT-3, NASA Langley Research Center; Hampton, VA, United States, June 1986. URL https://ntrs.nasa.gov/archive/nasa/casi.ntrs.nasa.gov/19860015749.pdf. Document ID: 19860015749.

[274] IHS ESDU. URL https://www.esdu.com/cgi-bin/ps.pl?sess=unlicensed_1160313124023tmn&t=gen&p=home. Accessed 28/05/2018.

[275] Aircraft Noise Committee. Prediction of near-field and far-field harmonic noise from subsonic propellers with non-axial inflow. Technical Report Aerounautical Series 11005, ESDU, February 2018. URL https://www.esdu.com/cgi-bin/ps.pl?sess=uniglas_1180528172612crc&t=pdf&p=esdu_11005. ISBN: 978 1 86246 696 8.

Appendix A

Post-processing Codes for Noise Estimation

The main computer programs implemented to estimate exterior and interior noise from the CFD solutions are reported here. Please refer to Chapter 3 for all the details and the assumptions of the adopted approaches.

A.1. SPL Evaluation from RANS Computation of Single Blade

This code determines OSPL and SPL spectrum of a propeller in isolation at the desired locations. It takes in input the RANS solution of HMB3, the flow-field parameters, the positions of the analysis points, and the preferred sampling frequency. The program reconstructs first the equivalent pressure time histories that would be registered at the analysis points during one complete propeller revolution, and then estimates the sound levels. Tecplot is employed, in bash mode, for the pressure signals reconstruction, using the inverse-distance interpolation method, and to perform their FFT, with a rectangular window function. All the steps are automated within the Python script here reported.

Listing A.1: Program "SPLsteady.py"

```
# ================================================================================
# ================================================================================

USAGE = """-------------------------------------------------------
~ USAGE: input Parameters:
                          flowfile_steady (with location, without .plt)
                          number of blades (ie. the computational domain is 1/nb)
                          delta_angle per step
                          rho
                          v_tip
                          blade real radius
                          probes_file (with location)
                          number of probes
```

```
        outputs: 1) ./pressure_t/probes_XX.dat with dimensional pressure at each probe for each↩
              time step (if you want to animate how the pressure varies on th fuselage)
                 2) ./probes_pt.dat with acoustic pressure signal of each probe
                 3) ./OSPLprobes_pt.dat with the overall SPL
                 4) ./SPL_flowfile_steady with SPL vs frequency for each probe

       ATTENTION!!! use the directory created "pressure_t" just for the output of this script,
       DO NOT add anything else in there!!!!!!!!
-------------------------------------------------------------------
"""

# ================================================================================
# ================================================================================

import math
import os,sys

if (len(sys.argv) < 9):
  print "~ ERROR    ~ incorrect number of parameters"
  print "-----------------------------------------"
  print USAGE
  sys.exit()

flowfile_steady = sys.argv[1]
blade = int(sys.argv[2])
delta_angle = float(sys.argv[3])

rho = float(sys.argv[4])
v_tip = float(sys.argv[5])
radius_real = float(sys.argv[6])

probes_file = sys.argv[7]
n_probes = int(sys.argv[8])

if ((360.00 /blade) / delta_angle < 1):
  print " ~ ERROR - inconsistent parameters:"
  print " delta_angle bigger than period segment"
  print "-------------------------------------"
  sys.exit()

# ================================================================================
# extraction pressure on the desired location with Tecplot Macro
# ================================================================================

try:
    os.system('mkdir pressure_t')
except:
    pass

print "beginning extraction pressure signal with Tecplot macro"

# writing Tecplot macro
# ---------------------------------

def TecFlow(flowfile_steady,blade,rho,v_tip):

  # open file
  output = """#!MC 1410

$!VarSet |flow_file| = '"""+flowfile_steady+"""'
$!READDATASET  '"|flow_file|.plt"'
  READDATAOPTION = NEW
  RESETSTYLE = YES
  INCLUDETEXT = NO
  INCLUDEGEOM = NO
  INCLUDECUSTOMLABELS = NO
  VARLOADMODE = BYNAME
  ASSIGNSTRANDIDS = YES
  INITIALPLOTTYPE = CARTESIAN3D
  VARNAMELIST = '"X" "Y" "Z" "P"'

$!VARSET |Zones| = |NUMZONES|

"""
  # copy rotate to have the full propeller flowfield
  output = output+"""
$!VarSet |alpha| = (2*pi/"""+str(blade)+""")

$!ALTERDATA
  EQUATION = '{Xnew}={X}'
$!ALTERDATA
  EQUATION = '{Ynew}={Y}'
```

```
$!VarSet |blade_loop| = ("""+str(blade)+""" - 1)
$!VarSet |blade_index| = 1

$!LOOP |blade_loop|

$!VarSet |zone_index| = 1

$!LOOP |Zones|

$!VarSet |source| = (|zone_index|)
$!VarSet |dest|   = (|Zones|*|blade_index|+|zone_index|)
$!DUPLICATEZONES
  SOURCEZONES =  [|source|]
  DESTINATIONZONE = |dest|

$!VARSET |zone_index| += 1

$!ENDLOOP

$!VarSet |init| = (|Zones|*|blade_index|+1)
$!VarSet |end| = (|Zones|*(|blade_index|+1))
$!ALTERDATA  [|init|-|end|]
  EQUATION = '{Xnew}={X}*cos(|alpha|*|blade_index|)-{Y}*sin(|alpha|*|blade_index|)'
$!ALTERDATA  [|init|-|end|]
  EQUATION = '{Ynew}={X}*sin(|alpha|*|blade_index|)+{Y}*cos(|alpha|*|blade_index|)'
$!ALTERDATA  [|init|-|end|]
  EQUATION = '{X}={Xnew}'
$!ALTERDATA  [|init|-|end|]
  EQUATION = '{Y}={Ynew}'

$!VARSET |blade_index| += 1

$!ENDLOOP

"""
  # dimensional pressure
  output = output+"""
  $!ALTERDATA
  EQUATION = '{P} = {P} * ("""+str(rho)+""" * """+str(v_tip)+""" * """+str(v_tip)+""")'

"""
  return output

# probes zone loading and interpolation
def TecProbe(probes_file,delta_angle):

  output = """

$!VarSet |EndSourceZones| = |NUMZONES|
$!READDATASET  '"""+probes_file+"""'
  READDATAOPTION = APPEND
  RESETSTYLE = YES
  INCLUDETEXT = NO
  INCLUDEGEOM = NO
  INCLUDECUSTOMLABELS = NO
  VARLOADMODE = BYNAME
  ASSIGNSTRANDIDS = YES
  INITIALPLOTTYPE = CARTESIAN3D
  VARNAMELIST = '"X" "Y" "Z" "P" "Xnew" "Ynew" "V1" "V2" "V3"'

$!VarSet |p1| = |NUMZONES|
$!ALTERDATA [|p1|]
  EQUATION = '{X} = {V1}'
$!ALTERDATA [|p1|]
  EQUATION = '{Y} = {V2}'
$!ALTERDATA [|p1|]
  EQUATION = '{Z} = {V3}'

$!INVERSEDISTINTERPOLATE
  SOURCEZONES =  [1-|EndSourceZones|]
  DESTINATIONZONE = |p1|
  VARLIST =  [4]
  INVDISTEXPONENT = 3.5
  INVDISTMINRADIUS = 0
  INTERPPTSELECTION = OCTANTNPOINTS
  INTERPNPOINTS = 8

$!WRITEDATASET  "./pressure_t/probes_0.dat"
  INCLUDETEXT = NO
  INCLUDEGEOM = NO
  INCLUDECUSTOMLABELS = NO
```

```
  INCLUDEDATASHARELINKAGE = YES
  ASSOCIATELAYOUTWITHDATAFILE = NO
  ZONELIST =  [|p1|]
  VARPOSITIONLIST = [1-4]
  BINARY = NO
  USEPOINTFORMAT = YES
  PRECISION = 12
  TECPLOTVERSIONTOWRITE = TECPLOTCURRENT

$!VarSet |numb_steps_considered| = (((360 / """+str(blade)+""") / """+str(delta_angle)+""") - 1)

$!LOOP |numb_steps_considered|

$!VarSet |teta| = ("""+str(delta_angle)+"""*pi/180)
$!ALTERDATA [1-|EndSourceZones|]
   EQUATION = '{Xnew}={X}*cos(|teta|)-{Y}*sin(|teta|)'
$!ALTERDATA [1-|EndSourceZones|]
   EQUATION = '{Ynew}={X}*sin(|teta|)+{Y}*cos(|teta|)'
$!ALTERDATA [1-|EndSourceZones|]
   EQUATION = '{X}={Xnew}'
$!ALTERDATA [1-|EndSourceZones|]
   EQUATION = '{Y}={Ynew}'

$!INVERSEDISTINTERPOLATE
  SOURCEZONES =  [1-|EndSourceZones|]
  DESTINATIONZONE = |p1|
  VARLIST =  [4]
  INVDISTEXPONENT = 3.5
  INVDISTMINRADIUS = 0
  INTERPPTSELECTION = OCTANTNPOINTS
  INTERPNPOINTS = 8

$!WRITEDATASET  "./pressure_t/probes_|loop|.dat"
  INCLUDETEXT = NO
  INCLUDEGEOM = NO
  INCLUDECUSTOMLABELS = NO
  INCLUDEDATASHARELINKAGE = YES
  ASSOCIATELAYOUTWITHDATAFILE = NO
  ZONELIST =  [|p1|]
  VARPOSITIONLIST = [1-4]
  BINARY = NO
  USEPOINTFORMAT = YES
  PRECISION = 12
  TECPLOTVERSIONTOWRITE = TECPLOTCURRENT

$!ENDLOOP

"""
  return output

# ------------------------------------

macrofile = open('ExtractProbesSteadyBlade_python.mcr','w')
macrofile.write(TecFlow(flowfile_steady,blade,rho,v_tip)+TecProbe(probes_file,delta_angle))

macrofile.close()

# execution Tecplot macro
# ------------------------------------
os.system("tec360 -mesa -b ExtractProbesSteadyBlade_python.mcr")

print "Extraction Probes with Tecplot done"

# ======================================================================
# reconstruction signal probes - acoustic pressure
# ======================================================================

ofile = "probes_pt.dat"

files = os.listdir("./pressure_t/")
print "n files = ", len(files)


tag = [0 for x in range(len(files))]
j = 0

for ifile in files:
  tag[j] = int(ifile.split("probes_")[1].split(".dat")[0])
  j = j + 1

files_sorted = sorted(tag)
```

```
p_array = [[0 for x in range(len(files) + 1)]for y in range(n_probes)]
p_fluct = [[0 for x in range(len(files) + 1)]for y in range(n_probes)]

for j in range(len(files)):

  ifile = str("./pressure_t/probes_" + str(files_sorted[j]) + ".dat")
  infile = open(str(ifile),"r") # skip line header file
  for i in range(10):
     infile.readline()

  for i in range(n_probes):
    p_array[i][j] = float(infile.readline().split(" ")[4].split("\n")[0])

  infile.close()

for i in range(n_probes):
  p_array[i][len(files)] = p_array[i][0] # last point to close the period (= first point)

for i in range(n_probes):

  p_mean = sum(p_array[i]) / float(len(files) + 1)

  for j in range(len(files) + 1):
    p_fluct[i][j] = p_array[i][j] - p_mean
# ------------------------------------------------------------------

time = 0
dt = math.pi * delta_angle * radius_real / (180.00 * v_tip)

outfile = open(str(ofile),"w")

for n in range(blade):

  for i in range(len(files)):

     outfile.write(str(time))

     for k in range(n_probes):

       outfile.write(" " + str(p_fluct[k][i]))

     outfile.write("\n")

     time = time + dt

outfile.write(str(time)) # last point to close the period

for k in range(n_probes):

       outfile.write(" " + str(p_fluct[k][0]))

outfile.write("\n")
outfile.close()

# ------------------------------------------------------------------
# OVERALL SPL

ospl = [0 for x in range(n_probes)]
p_ref = 2.0e-05

for i in range(n_probes):

  var_p_fluct2 = 0
  for j in range(len(files) + 1):
    var_p_fluct2 = var_p_fluct2 + math.pow(p_fluct[i][j],2)

  ospl[i] = 10.0 * math.log10( (var_p_fluct2 / float(len(files) + 1)) / math.pow(p_ref,2) )

# ------------------------------------------------------------------

ifile = str("./pressure_t/probes_" + str(files_sorted[0]) + ".dat")
infile = open(str(ifile),"r") # skip line header file
for i in range(10):
   infile.readline()

ofile2 = str("OSPL" + ofile)
outfile = open(str(ofile2),"w")

for i in range(n_probes):
  line = infile.readline()
  outfile.write(line.split()[0] + " " + line.split()[1] + " " + line.split()[2] + " " + str(ospl↩
       [i]) + "\n")
```

```
outfile.close()

# ------------------------------------------------------------------
print "Acoustic pressure signal computed"
print "here with:", ofile, " and ", ofile2," !!!"

# ==================================================================
# FFT with Tecplot
# ==================================================================

# writing Tecplot macro
# ------------------------------------

def TecFFT(n_probes,var_in,var_out):

  # open file
  output = """#!MC 1410

$!READDATASET  '"./probes_pt.dat"'
  READDATAOPTION = NEW
  RESETSTYLE = YES
  VARLOADMODE = BYNAME
  ASSIGNSTRANDIDS = YES
  VARNAMELIST = '"""+str(var_in)+"""'

$!VarSet |varFFT| = ("""+str(n_probes)+""" + 1)

  $!FOURIERTRANSFORM
  INDEPENDENTVAR = 1
  WINDOWFUNCTION = RECTANGULAR
  DEPENDENTVARS =  [2-|varFFT|]
  SOURCEZONES =  [1]
  INCLUDECONJUGATES = NO
  OBEYSOURCEZONEBLANKING = NO
  REPLACEMATCHINGRESULTZONES = YES
  REPLACEMATCHINGRESULTVARIABLES = YES

  $!WRITEDATASET  "./FFTprobes_pt.dat"
  INCLUDETEXT = NO
  INCLUDEGEOM = NO
  INCLUDEDATASHARELINKAGE = YES
  ZONELIST =  [2]
  VARPOSITIONLIST =  ["""+str(var_out)+"""]
  BINARY = NO
  USEPOINTFORMAT = YES
  PRECISION = 9
  TECPLOTVERSIONTOWRITE = TECPLOTCURRENT

"""
  return output

# ------------------------------------

var_in = "\"V1\""
for i in range(n_probes):
  var_in = str(var_in + " \"V" + str(i+2) + "\"")

var_out = str(str(n_probes + 2) + "-" + str(n_probes+3))
for i in range(n_probes-1):
  var_out = str(var_out + "," + str((n_probes+3) + 3 * (i + 1)))

macrofile2 = open('FFTProbesSteadyBlade_python.mcr','w')
macrofile2.write(TecFFT(n_probes,var_in,var_out))

macrofile2.close()

# execution Tecplot macro
# ------------------------------------
os.system("tec360 -mesa -b FFTProbesSteadyBlade_python.mcr")

# ------------------------------------------------------------------
print "FFT - Acoustic pressure done"

# ==================================================================
# SPL computation
# ==================================================================

sig_length = float(360.0/delta_angle + 1)
fft_lenght = int((sig_length - 1)/2 + 1)
name = flowfile_steady.split("/")[-1]
ofile_spl = str("SPL_" + name + ".dat")
```

```
p_fluct = [[0 for x in range(fft_lenght)]for y in range(n_probes+1)]
spl = [[0 for x in range(fft_lenght)]for y in range(n_probes+1)]

header = 7 +  n_probes

infile = open("./FFTprobes_pt.dat","r") # skip line header file
for i in range(header):
   infile.readline()

for i in range(fft_lenght):

  line = infile.readline()

  for j in range(n_probes):
    p_fluct[j][i] = float(line.split()[j])

  p_fluct[n_probes][i] = float(line.split()[n_probes].split("\n")[0])

infile.close()

amplitude_factor = 2.0/sig_length
p_ref = 2.0e-05

for i in range(fft_lenght):

  spl[0][i] = p_fluct[0][i] # frequency

  for j in range(n_probes):

    spl[j+1][i] = 20.0 * math.log10((p_fluct[j+1][i] * amplitude_factor)/ p_ref)

outfile = open(str(ofile_spl),"w")

for i in range(fft_lenght):

   for j in range(n_probes):

       outfile.write(str(spl[j][i]) + " ")

   outfile.write(str(spl[n_probes][i]) + "\n")

outfile.close()

print "SPL computation done"

print "here with:", ofile_spl, " !!!"

# ------------------------------------------------------------------
# clean up
os.system("rm -f  ExtractProbesSteadyBlade_python.mcr")
os.system("rm -f  FFTProbesSteadyBlade_python.mcr")
os.system("rm -f  batch.log")
```

A.2. SPL Evaluation from Unsteady CFD Simulations

This Python script computes OSPL and SPL spectrum from the pressure signals recorded during an unsteady simulation by the numerical probes. In addition to the probe files and their position, the user needs to supply only the flowfield data and the desired signals parameters (lenght and starting time). The FFT is performed by Tecpolt, in bash mode, with a rectangular window function.

Listing A.2: Program “SPLunsteady.py”

```
USAGE = """-------------------------------------------------------------
~ USAGE: input Parameters:
```

```
                        probes_file_directory (with path and final / included)
                        first iteration of the signal to consider
                        steps considered in the signal
                        delta_angle per step
                        rho
                        mach st file
                        sound
                        RPM
                        file with probe locations (in format as .grd.probes, with only the ↩
                            probes you want)
                        root output name

        outputs: 1) ./probes_pt.dat with acoustic pressure signal of each probe
                 2) ./OSPLprobes_pt.dat with overall SPL at the probes analysed
                 3) ./SPL_probes_pt.dat with SPL vs frequency for each probe
-------------------------------------------------------------
"""

# ================================================================================
# ================================================================================

import math
import os,sys

if (len(sys.argv) < 11):
  print "~ ERROR    ~ incorrect number of parameters"
  print "-------------------------------------------"
  print USAGE
  sys.exit()

probes_file_directory = sys.argv[1]

it_start = int(sys.argv[2])
steps_sig = int(sys.argv[3])

delta_angle = float(sys.argv[4])

rho = float(sys.argv[5])
mach = float(sys.argv[6])
sound = float(sys.argv[7])
RPM = float(sys.argv[8])

ifile_location_probes = sys.argv[9]
root_out = sys.argv[10]

# ================================================================
# HMB Probes reading, cleaning up and extraxtion desired data
# ================================================================

s = steps_sig + 1 # (s simulations steps gives s + 1 data points)

conv_p = rho * mach * mach * sound * sound

ofile = str(root_out+"_probes_pt.dat")

# time vector computation
# ===========================

d_time = float(delta_angle) / (6 * RPM)
time = []

time_in = float(it_start) * d_time

for i in range(s):
  time.append((time_in + float(i)*d_time))

# Probes Signal Extraction
# ===========================

files = os.listdir(probes_file_directory)
n_probes = len(files)

print "number of probes analysed = ", n_probes
print "lenght of the pressure signal = ", s

p = [[0 for x in range(s)]for y in range(n_probes)]
p_fluct = [[0 for x in range(s)]for y in range(n_probes)]

# to be sure to read probes in order.....
tag = [0 for x in range(len(files))]
j = 0
for ifile in files:
```

```
  tag[j] = int(ifile.split("probe.")[1])
  j = j + 1
files_sorted = sorted(tag)
root = files[0].split("_probe")[0]

signal = 0
for j in files:

  print "working on ...", str(probes_file_directory+root+"_probe."+str(files_sorted[signal]).↩
       zfill(5))
  infile = open(str(probes_file_directory+root+"_probe."+str(files_sorted[signal]).zfill(5)),"r"↩
       )

  iteration = int(it_start)

  for i in range(s):
    # pressure reading from hmb file
    line_probe_hmb = infile.readline()

    # skip line coordinate
    while (len(line_probe_hmb) < 50):
      line_probe_hmb = infile.readline()

    # skip previous steps
    while (int(line_probe_hmb.split(" ")[0]) < iteration):
      line_probe_hmb = infile.readline()
      # skip line coordinates from restart
      while (len(line_probe_hmb) < 50):
        line_probe_hmb = infile.readline()

    p_hmb = float(line_probe_hmb.split(" ")[6])

    p[signal][i] = p_hmb * conv_p

    iteration = iteration + 1

  signal = signal + 1

  infile.close()

# ------------------------------------------------------------------
for i in range(n_probes):

  p_mean = sum(p[i]) / float(s)

  for j in range(s):
    p_fluct[i][j] = p[i][j] - p_mean

# Output file writing
# ===========================

outfile = open(ofile,"w")

for i in range(s):

    # time vector writing
    outfile.write(str(time[i]))

    # pressure writing of all the probes
    for j in range(n_probes):

      outfile.write(" " + str(p_fluct[j][i]))

    outfile.write("\n")

outfile.close()

# ------------------------------------------------------------------
# OVERALL SPL

ospl = [0 for x in range(n_probes)]
p_ref = 2.0e-05

for i in range(n_probes):

  var_p_fluct2 = 0
  for j in range(s):
    var_p_fluct2 = var_p_fluct2 + math.pow(p_fluct[i][j],2)

  ospl[i] = 10.0 * math.log10(var_p_fluct2 / float(s) / math.pow(p_ref,2) )

infile_loc_prob = open(ifile_location_probes,"r")
```

```
ofile2 = str("OSPL" + ofile)
outfile = open(str(ofile2),"w")

for i in range(n_probes):
  line = infile_loc_prob.readline().split("(")[1].split(")")[0]
  outfile.write(line.split(",")[0] + " " + line.split(",")[1] + " " + line.split(",")[2] + " " +↩
       str(ospl[i]) + "\n")

outfile.close()

# ------------------------------------------------------------------
print "Acoustic pressure signal computed"
print "here with:", ofile, "!!!"

# ======================================================================
# FFT with Tecplot
# ======================================================================

# writing Tecplot macro
# ---------------------------------

def TecFFT(n_probes,var_in,var_out,name_in,name_out):

  # open file
  output = """#!MC 1410

$!VarSet |probe_file| = '"""+name_in+"""'

$!READDATASET  '"|probe_file|"'
  READDATAOPTION = NEW
  RESETSTYLE = YES
  VARLOADMODE = BYNAME
  ASSIGNSTRANDIDS = YES
  VARNAMELIST = '"""+str(var_in)+"""'

$!VarSet |varFFT| = ("""+str(n_probes)+""" + 1)

  $!FOURIERTRANSFORM
  INDEPENDENTVAR = 1
  WINDOWFUNCTION = RECTANGULAR
  DEPENDENTVARS =  [2-|varFFT|]
  SOURCEZONES =  [1]
  INCLUDECONJUGATES = NO
  OBEYSOURCEZONEBLANKING = NO
  REPLACEMATCHINGRESULTZONES = YES
  REPLACEMATCHINGRESULTVARIABLES = YES

$!VarSet |probe_fft_file| = '"""+name_out+"""'

  $!WRITEDATASET  "./|probe_fft_file|"
  INCLUDETEXT = NO
  INCLUDEGEOM = NO
  INCLUDEDATASHARELINKAGE = YES
  ZONELIST =  [2]
  VARPOSITIONLIST =  ["""+str(var_out)+"""]
  BINARY = NO
  USEPOINTFORMAT = YES
  PRECISION = 9
  TECPLOTVERSIONTOWRITE = TECPLOTCURRENT

"""
  return output

# ---------------------------------

var_in = "\"V1\""
for i in range(n_probes):
  var_in = str(var_in + " \"V" + str(i+2) + "\"")

var_out = str(str(n_probes + 2) + "-" + str(n_probes+3))
for i in range(n_probes-1):
  var_out = str(var_out + "," + str((n_probes+3) + 3 * (i + 1)))

name_out = str(root_out+"_FFTprobes_pt.dat")

macrofile2 = open('FFTProbesSteadyBlade_python.mcr','w')
macrofile2.write(TecFFT(n_probes,var_in,var_out,ofile,name_out))

macrofile2.close()

# execution Tecplot macro
```

```
# ------------------------------------
os.system("tec360 -mesa -b FFTProbesSteadyBlade_python.mcr")

# ------------------------------------------------------------------
print "FFT - Acoustic pressure done"

# ==================================================================
# SPL computation
# ==================================================================

sig_length = s
fft_lenght = int((sig_length - 1)/2 + 1)
ofile_spl = str(root_out+"_SPL_probes_pt.dat")

p_fluct = [[0 for x in range(fft_lenght)]for y in range(n_probes+1)]
spl = [[0 for x in range(fft_lenght)]for y in range(n_probes+1)]

header = 7 +  n_probes

infile = open(name_out,"r") # skip line header file
for i in range(header):
   infile.readline()

for i in range(fft_lenght):

  line = infile.readline()

  for j in range(n_probes):
    p_fluct[j][i] = float(line.split()[j])

  p_fluct[n_probes][i] = float(line.split()[n_probes].split("\n")[0])

infile.close()

# ------------------------------------------------------------------

amplitude_factor = 2.0/sig_length
p_ref = 2.0e-05

for i in range(fft_lenght):

  spl[0][i] = p_fluct[0][i] # frequency

  for j in range(n_probes):

    spl[j+1][i] = 20.0 * math.log10((p_fluct[j+1][i] * amplitude_factor)/ p_ref)

# ------------------------------------------------------------------

outfile = open(str(ofile_spl),"w")

for i in range(fft_lenght):

   for j in range(n_probes):

       outfile.write(str(spl[j][i]) + " ")

   outfile.write(str(spl[n_probes][i]) + "\n")

outfile.close()

print "SPL computation done"

print "here with:", ofile_spl, " !!!"

# ------------------------------------------------------------------
# clean up
os.system("rm -f  FFTProbesSteadyBlade_python.mcr")
os.system("rm -f  batch.log")
```

A.3. A-Weighting Filter Application

This program implements the A-weighting noise filter [243, 245]. It takes in input the SPL as function of frequency, and gives in output the ASPL spectrum and the OASPL. The number of harmonics to account for in the computation of the OASPL can be

specified by the user.

Listing A.3: Program “Aweighting.py”

```
# ================================================================================
# ================================================================================

USAGE = """-------------------------------------------------------
~ USAGE: input Parameters:
                          1) SPL function of the frequency file (input format: frequency,SPL1(f↩
                              ),SPL2(f),... SPLN(f)) - ex. "SPL_XXX.dat" output of ↩
                              splBladeSteady.py)
                          2) number of signals
                          3) A-SPL output file name (without location, it will be printed in ↩
                              the current directory)
                          4) number of harmonics (BPF) you want to consider in the computation ↩
                              of the OSPL
                          5) file OSPL ("OSPLprobes_pt.dat" output of splBladeSteady.py) or ↩
                              simply file with location of the probes (x,y,z)
                          6) number of blades of the full propeller (IMPACTA = 8)
                          7) half BPF tones present? 0 = NO, 1 = YES (modified configuration)

        output: 1) A-SPL output with frequency, SPLA value of the signals and A weight value (↩
             last column)
                2) Overall SPLA from the contribution of desired harmonics
-------------------------------------------------------
"""
# ================================================================================
# ================================================================================

import math
import os,sys

if (len(sys.argv) != 8):
  print "~ ERROR    ~ incorrect number of parameters"
  print "-------------------------------------------"
  print USAGE
  sys.exit()

splf_inputfile = sys.argv[1]
nsignals = int(sys.argv[2])
splA_out = sys.argv[3]
harmonics = int(sys.argv[4])
probelocation = sys.argv[5]
nblades = int(sys.argv[6])
halBPF = int(sys.argv[7])

# ================================================================================

n_frequencies = 0
infile = open(str(splf_inputfile),"r")
for line in infile:
  n_frequencies = n_frequencies + 1
infile.close()

print "number of lines SPL input file", n_frequencies

# ------------------------------------------------

print "number of signals analysed", nsignals

splf = [[0 for x in range(n_frequencies)] for y in range (nsignals+1)] # f,spl1,spl2,...,splN

infile = open(str(splf_inputfile),"r")

for i in range(n_frequencies):

  line = infile.readline()

  for j in range(nsignals):
    splf[j][i] = float(line.split()[j])

  splf[nsignals][i] = float(line.split()[nsignals].split("\n")[0])

infile.close()

# ------------------------------------------------

deltaA = [0 for x in range(n_frequencies)] # A weight
```

```
f2 = math.pow(1000,2)

ra1000 = math.pow((12200*f2),2) / ( (f2 + math.pow(20.6,2)) * (f2 + math.pow(12200,2)) * math.↩
     sqrt(f2 + math.pow(107.7,2)) * math.sqrt(f2 + math.pow(737.9,2)) )

offset = - 20.0 * math.log10(ra1000) # (NOTE: offset is usually approximated with 2.00)

for i in range(n_frequencies):

  f2 = math.pow(splf[0][i],2)

  ra = math.pow((12200*f2),2) / ( (f2 + math.pow(20.6,2)) * (f2 + math.pow(12200,2)) * math.sqrt↩
       (f2 + math.pow(107.7,2)) * math.sqrt(f2 + math.pow(737.9,2)) )

  if (ra != 0):
    deltaA[i] = 20.0 * math.log10(ra) + offset

# ------------------------------------------------

splA = [[0 for x in range(n_frequencies)] for y in range (nsignals+2)] # splA

for i in range(n_frequencies):

  splA[0][i] = splf[0][i] # frequency

  for j in range(nsignals):

    splA[j+1][i] = splf[j+1][i] + deltaA[i] # spl A

  splA[nsignals+1][i] = deltaA[i] # A weight

outfile = open(str(splA_out),"w")

for i in range(n_frequencies):

  for j in range(nsignals+1):

    outfile.write(str(splA[j][i]) + " ")

  outfile.write(str(splA[nsignals+1][i]) + "\n")

outfile.close()

# ------------------------------------------------

osplA = [0 for x in range(nsignals)] # Overall splA for the considered harmonics

for i in range(nsignals):

  sumharm = 0.0

  if (halBPF == 0): # standard propeller configuration

    for j in range(harmonics):

      index_freq = (j+1) * nblades

      sumharm = sumharm + math.pow(10,(splA[i+1][index_freq]/20))

  elif (halBPF == 1): # modified hub configuration

    for j in range(2*harmonics):

      index_freq = (j+1) * (nblades/2)
      sumharm = sumharm + math.pow(10,(splA[i+1][index_freq]/20))

  else:
    print ("~ ERROR ~ inconsistent choice parameter n 7")
    print "-----------------------------------------"
    print USAGE
    sys.exit()


  osplA[i] = 20.0 * math.log10(sumharm)


infile = open(str(probelocation),"r")

osplA_out = str("Overall_harm" + str(harmonics) + "_" + splA_out)
outfile = open(str(osplA_out),"w")
```

```
for i in range(nsignals):

  line = infile.readline()

  outfile.write(line.split(" ")[0] + " " + line.split(" ")[1] + " " + line.split(" ")[2] + " " +↩
       str(osplA[i]) + "\n")

infile.close()
outfile.close()

print "here with ", splA_out, " and ", osplA_out
```

A.4. Interior Sound Estimation via Transfer Functions

This script determines the sound signal heard by the considered passenger, via experimental Transfer Functions, and generates the corresponding audio file in *wav* format. The only required inputs are the dimensional acoustic pressure time histories on the exterior fuselage surface at the TF measurement points, and the audio desired parameters (name, lenght, sampling rate). The TF application and the .wav file writing are done by two dedicated external programs called inside the Python script. These are reported in the Subsections below. Knowing the pressure signal, SPL, or ASPL, for the passenger can then be determined in the same way as shown in the previous Sections.

Listing A.4: Program “interiorSound.py”

```
# ================================================================================
# ================================================================================

USAGE = """-------------------------------------------------------------
~ USAGE: input Parameters:
                          1) time history of dimensional acoustic pressure [Pa] (input format: ↩
                               time,p1'(t),p2'(t),...,pN'(t) - ex. "probes_pt.dat" ouput of ↩
                               splBladeSteady.py)
                          2) lenght of input signal (NOTE: maximum allocated in fortran program↩
                                = 1441!)
                          3) angular resolution of the input signal
                          4) RPM propeller
                          5) name audio output file (with location)
                          6) resulting audio signal lenght in seconds
                          7) scale audio signal amplitude to a range from -1 to +1 (0 = NO, 1=↩
                               YES)

                         + IF you want to specify a sample rate different from the natural one
                          8) Sample rate (integer number!!)

  NOTE: the script is done to be applied to the HIGH_WING AIRCRAFT fictitous fuselage of the ↩
       IMPACTA project with 1056 probes!! REMEMBER that the transfer functions are available ↩
       only on a grid of 32x32 points!
-------------------------------------------------------------
"""

# ================================================================================
# ================================================================================

import math
import os,sys

if (len(sys.argv) < 8 or len(sys.argv) > 9):
  print "~ ERROR ~ incorrect number of parameters"
  print "-------------------------------------------------------------"
  print USAGE
  sys.exit()

acousticpressure_file_1 = sys.argv[1]
```

```
lenght_psignal = int(sys.argv[2])
deltadeg = float(sys.argv[3])
rpm = float(sys.argv[4])
nameoutput = sys.argv[5]
audio_lenght = float(sys.argv[6])
scale = int(sys.argv[7])

if (len(sys.argv) == 9):
  sampleRate = int(sys.argv[8])

# ================================================================================

print "preparation input files for transfer functions fortran program"

try:
    os.system('mkdir tmp_acoustic_pressure_signal')
except:
    pass

for j in range(32):

   for i in range(32):

       # transfer function grid point
       ix = i + 1
       iy = j + 1
       kl = (iy-1)*33 + ix

       outfile = open(str("./tmp_acoustic_pressure_signal/probe." + str(kl).zfill(4)),"w")

       infile = open(str(acousticpressure_file_1),"r")

       for i in range(lenght_psignal):
          outfile.write(str(infile.readline().split(" ")[kl]) + "\n")

       outfile.close()
       infile.close()

# ------------------------------------------------------------
print "application of transfer functions ..."

intf = str("./tmp_acoustic_pressure_signal/probe." + " 0 " + str(lenght_psignal) + " " + str(↩
    deltadeg))
cmd = "/home/cfd/gchirico/PROJECT/Resources/CabinNoise/applayTF_giulia_phase.exe " + intf

os.system(cmd)

print "done"

# ------------------------------------------------------------

print "generation sound file for the point inside the cabin"

lenght_psignal = lenght_psignal - 1

psignal = [0 for x in range(lenght_psignal)]

infile = open('pressure_inside_cabin_s1.dat',"r")
for i in range(lenght_psignal):
  psignal[i] = float(infile.readline().split()[0])
infile.close()

if (scale == 1):
   min_p = min(psignal)
   range_p = max(psignal) - min_p

   psignal_scaled = [0 for x in range(lenght_psignal)]
   for i in range(lenght_psignal):
      psignal_scaled[i] = 2 * (psignal[i] - min_p)/range_p - 1

if (len(sys.argv) == 8):
   nsamples1rev = 360.0/deltadeg
   nrev1s = rpm/60.0 # n revolutions in 1 s
   sampleRate = round(nsamples1rev * nrev1s,0)

print "sample rate", sampleRate
numFrames = audio_lenght * sampleRate
print "number of desired frames ", numFrames

replicate = int(numFrames / float(lenght_psignal))
print "number of replication of the original signal", replicate
```

```
signalp_long = "signal_pressure_long.dat"
outfile = open(signalp_long,"w")

realFrames = replicate * lenght_psignal
total_lines = realFrames + 1
outfile.write(str(total_lines) + "\n")

if (scale == 1):
  for i in range(replicate):
    for j in range(lenght_psignal):
       outfile.write(str(psignal_scaled[j]) + "\n")
elif(scale == 0):
  for i in range(replicate):
    for j in range(lenght_psignal):
       outfile.write(str(psignal[j]) + "\n")
else:
  print "~ ERROR ~ incorrect values for the parameter scale"
  print "-------------------------------------------------"
  print USAGE
  sys.exit()

outfile.close()

inwritewav = str(signalp_long + " " + nameoutput + " " + str(int(sampleRate)))
cmd = "/home/cfd/gchirico/PROJECT/Resources/WAVgeneration/writeWav_giulia.exe " + inwritewav
os.system(cmd)

print "here with ", nameoutput

# ============================================================================
# cleanup
os.system("rm -f signal_pressure_long.dat")
os.system("rm -rf tmp_acoustic_pressure_signal")
```

A.4.1 TF Application

The interior sound is determined as the convolution of the exterior pressure field and the Transfer Functions, i.e. as the multiplication of the two in the frequency domain. The TF are given, from the experiments, as a matrix of complex coefficients. The code, which takes in iput the CFD pressure signals at the microphone locations and the TF, was therefore written in Fortran 90 for simplicity. The output of the code is the unsteady pressure time history for the considered passenger.

Listing A.5: Program “applaytransferfunction.F90”

```
program applaytransferfunction

  ! variable declaration
  parameter (np=32, nf=700, nix=33, niy=32, ns=1441)
  integer ns1, forminput, nout
  real pt(ns), pts1(ns), ns2, freq(10), abspf(nix*niy,10), abspftr(nix*niy,10)
  complex*8 tr(nix*niy,nf), pf(nf), ci
  character cdum*8, filnamp*132, rootname*100
  real*4 shaftspeed

  nargs = iargc()
  if( nargs .lt. 3 ) then
    call print_usage
    stop
  endif

  call getarg(1, rootname)
  write(*,*) 'Root name probe input files: ', rootname
  call getarg(2, cdum)
  read(cdum,*) forminput ! input format 0 or 1
  write(*,*) 'input flag: ', forminput
  call getarg(3, cdum)
  read(cdum,*) ns1
```

```
write(*,*) 'signal lenght: ', ns1
call getarg(4, cdum)
read(cdum,*) ns2
ns2 = 360.0/ns2
write(*,*) 'steps in 1 period: ', ns2

! variable initialisation
ci = (0., 1.) ! complex imaginary unit
pi = 4*atan(1.) ! number pi

tr = (0., 0.) ! transfer function coefficients
pts1 = 0. ! acoustic presure signal at position s1 inside the cabin

shaftspeed = 14.27547 ! shaft rotational speed [Hz]
freq = 0. ! frequency = shaft order * shaft rotational speed

! open and read transfer function file
open (21, form='unformatted', file='transfer_functions.out', access='direct', recl=nix*niy*nf↩
    *8)
read(21,rec=1) tr
close(21)

do iy=1,np ! cycle along the fuselage axis
    do ix=1,np ! cycle along the fuselage azimuth

        ! open and read input pressure signal

        kl = (iy-1)*nix + ix ! considered grid point

        pt = 0. ! acoustic pressure signal (time domain) outside the cabin (program input)

        if (forminput==0) then ! read input file containing just pressure signal
          write(filnamp,'(a,i4.4)') trim(rootname), kl ! string reconstruction probe file name
          ! print *, kl, filnamp ! print on screen list probes file to check
          open (11, file=filnamp) ! open probe file
          do j=1,ns1 ! cycle along the signal
            read(11,*) pt(j)
          end do
        end if

        if (forminput==1) then ! read input file in probe format (line 1 = position + step, ↩
            time, pressure for the rest)
          if (kl < 1000) then
            write(filnamp,'(a,i3.3)') trim(rootname), kl ! string reconstruction probe file ↩
                name
          else if (kl >= 1000) then
            write(filnamp,'(a,i4.4)') trim(rootname), kl ! string reconstruction probe file ↩
                name
          end if
          ! print *, kl, filnamp ! print on screen list probes file to check
          open (11, file=filnamp) ! open probe file
          read(11,*) cdum !
          do j=1,ns1 ! cycle along the signal
            read(11,*) idum, rdum, pt(j)
          end do
        end if

        close(11)

        ! passage in the frequency domain and application of transfer functions

        pf = (0., 0.) ! pressure signal in the frequency domain
        nout = 0 ! index output with pressure map in the frequency domain before and after the↩
             applicatio of TF

        do m=1,700 ! cycle over the shaft orders

            ! Fourier transform
            do j=1,ns1 ! cycle along the signal
                pf(m)  = pf(m) + pt(j)*exp(-ci*2*pi*m*(j-1)/ns2)
            end do

            if (m==4 .or. m==8 .or. m==12 .or. m==16 .or. m==20 .or. m==24 .or. m==28 .or. m↩
                ==32 .or. m==36 .or. m==40) then
               nout = nout + 1
               ! write(*,*) kl, m, nout
               freq(nout) = m * shaftspeed ! frequency
               abspf(kl, nout) = cabs(pf(m))
            end if

            ! multiplication by transfer function
            pf(m) = pf(m)*tr(kl, m)
```

```
              if (m==4 .or. m==8 .or. m==12 .or. m==16 .or. m==20 .or. m==24 .or. m==28 .or. m↩
                  ==32 .or. m==36 .or. m==40) then
                 abspftr(kl, nout) = cabs(pf(m))
              end if

          end do

          ! summation over all the probes inverse transform
          do j=1,ns1 ! cycle along the signal
              do m=1,700 ! cycle over the shaft orders
                  pts1(j)  = pts1(j) + (2/float(ns1)) * real(pf(m)*exp(ci*2*pi*m*(j-1)/ns2))
              end do
          end do

      end do
  end do

  ! open and write output files
  open (19, recl=6400, file='pf_map_BPFs.dat')
  write(19,*) 'VARIABLES = "IX" "IY" "PF" "PFTF"'
  do j=1,10  ! cycle over the frequencies
    write(19,*) 'ZONE T = "frequency ', freq(j), '"'
    do iy = 1,np ! cycle along the fuselage axis
      do ix = 1,np ! cycle along the fuselage azimuth
            kl = (iy-1)*nix + ix ! grid point
            write(19,*) ix,iy,abspf(kl,j),abspftr(kl,j)
      end do
    end do
  end do
  close(19)

  open (19, recl=6400, file='pressure_inside_cabin_s1.dat')
  do j=1,ns1
      write(19,*) (pts1(j))
  end do
  close(19)

  stop

end program applaytransferfunction

! ------------------------------------------------------------------

subroutine print_usage
  write(*,*) 'Usage: '
  write(*,*) '1) root file name acoustic pressure [Pa],'
  write(*,*) '2) format flag (0=just acoustic pressure, 1=standard HMB probe output with ↩
      iteration,timestep and pressure),'
  write(*,*) '3) signal lenght (ATTENTION! maximum 1441 allocated as default)'
  write(*,*) '4) azimuthal resolution of samples'
end subroutine
```

A.4.2 Generation of Audio File .wav

This short C program reads a pressure signal and writes the audio file in *wav* format. The sampling rate is selected by the user.

Listing A.6: Program “WAVgeneration.c”

```
#include <stdio.h>
#include <math.h>
#include <malloc.h>
#include <sndfile.h>
#include <string.h>

/* Compile: gcc -o writeWav_giulia.exe writeWav_giulia.c -I ./include -L ./lib -lsndfile */
/* Run: ./writeWav_giulia.exe sampleRate inputfile.dat outputfile.wav  */

int main(int arg_count, char *argv[])
{
  int j,sampleRate;
```

```
  long c;
  double v1, numFrames;
  FILE *input;
  char filename[128];

  printf("Wav Write Test\n");
  if (arg_count != 4) {
    fprintf(stderr, "input files: <file.dat with acoustic pressure signal [Pa]> <outputfile.wav>↩
         <sampleRate [frames per second]>\n");
    return 1;
  }

       sampleRate = atoi(argv[3]);
  printf("Sample rate %d\n",sampleRate);

  // Read in input file
  strcpy(filename,argv[1]);
       input = fopen(filename,"r");
  fscanf(input,"%d\n",&c);
  numFrames = c-1;
  fprintf(stdout, "%d\n",c);

  // Allocate storage for frames
  double *buffer = (double *) malloc(numFrames * sizeof(double));
  if (buffer == NULL) {
    fprintf(stderr, "Could not allocate buffer for output\n");
  }

  for (j=0;j<numFrames;j++){
               fscanf(input,"%lf\n",&v1);
    buffer[j]=v1;
               if (j==(numFrames-1)){
      printf("%d %lf \n",j,v1);
    }
  }

  // Set file settings, 16bit Mono PCM
  SF_INFO info;
  info.format = SF_FORMAT_WAV | SF_FORMAT_PCM_16;
  info.channels = 1;
  info.samplerate = sampleRate;

  // Open sound file for writing
  SNDFILE *sndFile = sf_open(argv[2], SFM_WRITE, &info);
  if (sndFile == NULL) {
    fprintf(stderr, "Error opening sound file '%s': %s\n", argv[2], sf_strerror(sndFile));
    free(buffer);
    return -1;
  }

  // Write frames
  long writtenFrames = sf_writef_double(sndFile, buffer, numFrames);

  // Check correct number of frames saved
  if (writtenFrames != numFrames) {
    fprintf(stderr, "Did not write enough frames for source\n");
    sf_close(sndFile);
    free(buffer);
    return -1;
  }

  // Tidy up
  sf_write_sync(sndFile);
  sf_close(sndFile);
  free(buffer);

  return 0;
}
```

Appendix B

Channel Effect Correction for the IMPACTA Experiments

To validate the HMB solver for propellers in an installed configuration, as shown in Section 4.2, the experiments carried out by ARA during the IMPACTA project [8, 250] were used. Measurements were supplied to the author after standard wind tunnel corrections used by ARA were applied. However, an additional correction was required for the tests conducted with the acoustic liner inside the test chamber.

B.1. The Channel Effect

The presence of the acoustic liner in the working section of the ARA transonic wind tunnel[255] alters the porosity of the walls, resulting in practice in solid walls close to the model. Because of this, a channel effect is produced in the chamber and the upper* wing surface of the model experiences a Mach number slightly higher compared to a non-intrusive scenario. Therefore, the measured pressure data need to be corrected to account for this effect.

B.2. Correction Method

The procedure recommended directly by ARA was followed. The pressure variation caused by the Mach number increase is quantified by the difference of local C_p registered by the pressure taps on the acoustic liner floor between the cases of installed and uninstalled wing, for each configuration:

$$\Delta C_p = C_{p,\text{liner IN-wing ON}} - C_{p,\text{liner IN-wing OFF}}. \tag{B.1}$$

* The IMPACTA rig is mounted inverted in the ARA wind tunnel.

In particular, a 3*rd* order polynomial interpolation of the data in the vicinity of the wing was employed, as shown in Figure B.1 for the two cases reported in this thesis.

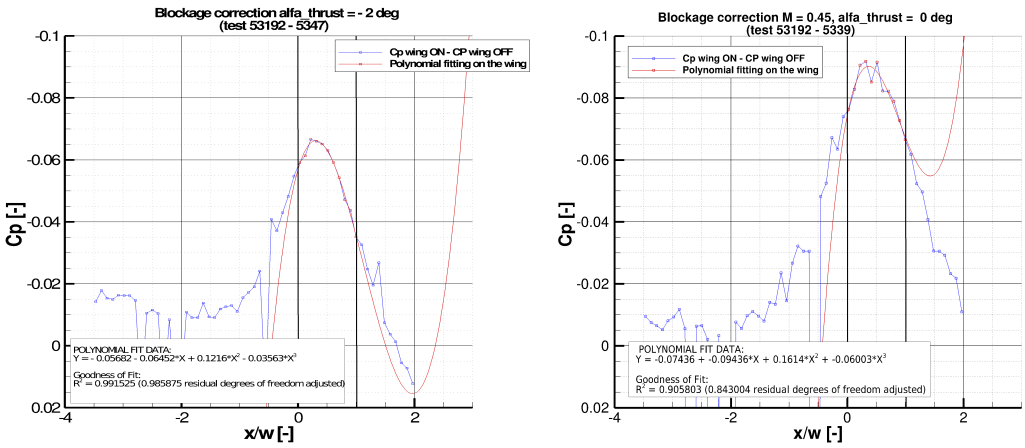

(a) **Cruise** operating conditions: $M = 0.5$, $\alpha_T = -2$ deg.

(b) **Climb** operating conditions: $M = 0.45$, $\alpha_T = 0$ deg.

Figure B.1: Pressure coefficient correction for the channel effect due to the presence of the acoustic liner in the wind tunnel chamber: computation of the ΔC_p as proposed by ARA. x/w a-dimensional wing chord-wise coordinate, with origin at the wing leading edge and positive in the flow direction.

The pressure coefficient of the model upper wing is then computed as:

$$C_{p,\text{corrected}} = C_{p,\text{liner IN}} - \Delta C_p, \tag{B.2}$$

while the measured data on the lower wing surface are left unchanged.
It is noted that the correction term ΔC_p is computed using measurements carried out at the same conditions but without the propeller blades installed on the model. This can therefore affect the effectiveness of the suggested experimental data correction, since it is not included the flow forcing by the propeller rotation.

B.3. Evaluation of the Correction Effectiveness

To assess the adopted procedure, Figures B.2 and B.3 present the comparison between corrected liner-IN measurements and liner-OUT measurements for the test cases simulated in this thesis. As can be seen, the proposed correction approach appears to work very well for the cruise case, where liner-IN corrected data match almost everywhere the liner-OUT data (Figure B.2). By contrast, the correction is not very effective for the climb case (Figure B.3). In particular, it is noted that: *(i)* the suction peak on the port wing is larger in the corrected liner-IN measurements than in the liner-OUT measurements, *(ii)* the corrected liner-IN data on the upper surface of all wing stations, from about 30% of the chord to the trailing edge, exhibit a lower loading than

the liner-OUT data. This can be partly due to the use of all floor pressure taps in the determination of ΔC_p, even if some irregularities are visible and may denote some sensor fault (see Figure B.1(b)). Moreover, a difference can be observed between the liner-IN and the liner-OUT lower pressure curves towards the wing leading edge, especially for the starboard stations inside the propeller slip-stream (refer to Figures B.3(c) and B.3(d)). The liner-IN tests display a larger loading up to about 30% of the wing chord. No correction was applied in this region to the experimental data, and this may influence the comparison with the CFD predictions which do not include the wind tunnel walls.

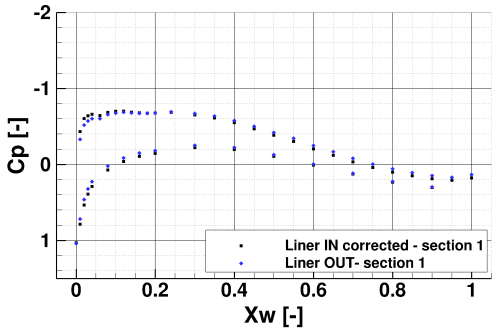

(a) Span-wise station S1: $y = -0.9R$.

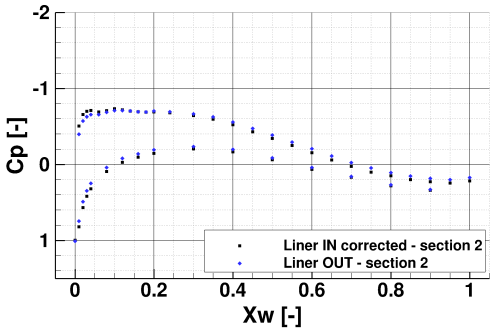

(b) Span-wise station S2: $y = -0.7R$.

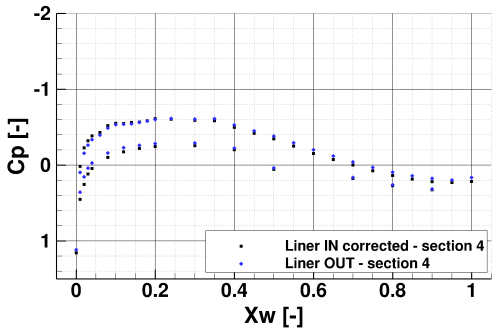

(c) Span-wise station S4: $y = 0.7R$.

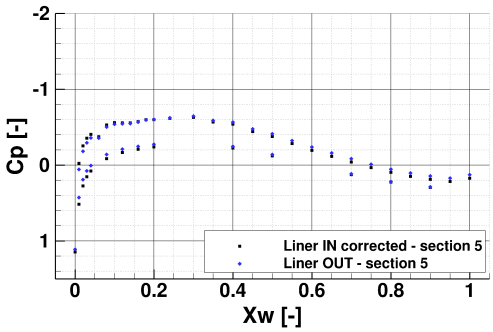

(d) Span-wise station S5: $y = 0.9R$.

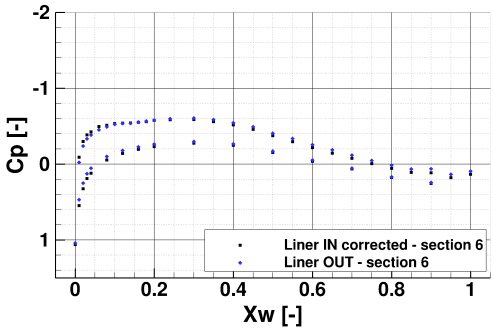

(e) Span-wise station S6: $y \sim 1.3R$.

Figure B.2: Evaluation of the effectiveness of the pressure coefficient correction for the channel effect: **cruise** operating conditions ($M_\infty = 0.5$, $RPM \sim 4050$, $\alpha_T = -2$ deg).

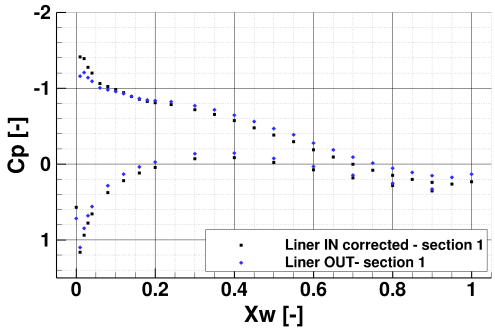

(a) Span-wise station S1: $y = -0.9R$.

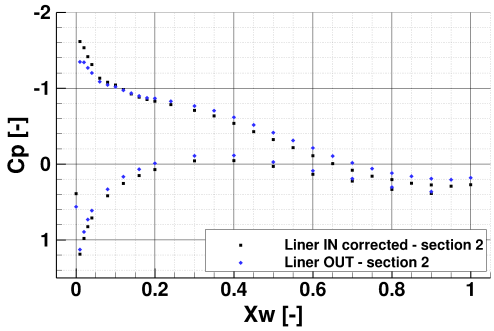

(b) Span-wise station S2: $y = -0.7R$.

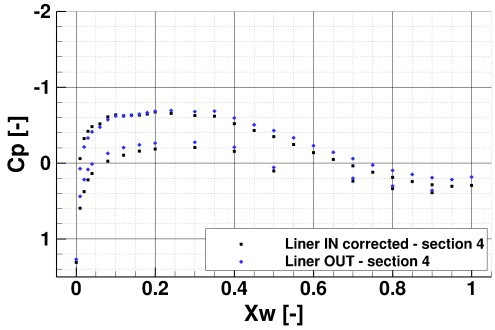

(c) Span-wise station S4: $y = 0.7R$.

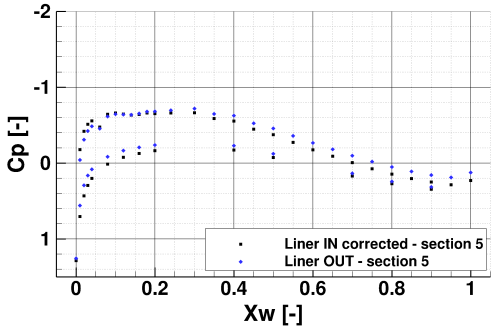

(d) Span-wise station S5: $y = 0.9R$.

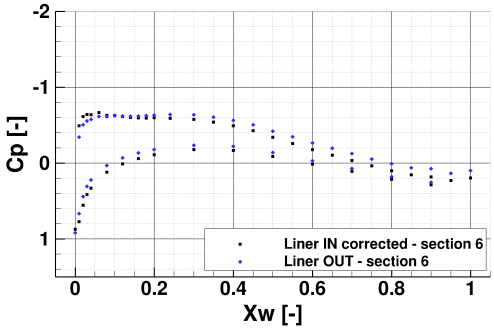

(e) Span-wise station S6: $y \sim 1.3R$.

Figure B.3: Evaluation of the effectiveness of the pressure coefficient correction for the channel effect: **climb** operating conditions ($M_\infty = 0.45$, $RPM \sim 4410$, $\alpha_T = 0$ deg).

Appendix C

HMB3 Preliminary Validation Tests

Before computing the complex flow of the IMPACTA propulsion unit, preliminary tests of the wind tunnel model without the propeller were performed to check the chosen numerical setup, i.e. no wind tunnel walls simulated and sliding planes to include the propeller in the grid.

Computations were carried out on the starboard half of the model, exploiting its symmetry with respect to the xz plane, and run as steady RANS with the $k-\omega$ SST turbulence model [215]. The considered flow conditions are given in Table C.1. The first has the same thrust incidence of the climb state, but a higher Mach number. The second is representative of the cruise state. The grid used is the same employed for the complete IMPACTA model, with the exception of the propeller drum containing only the spinner (see Figure C.1(a)). The mesh counts approximately 8.6M cells, which corresponds to the coarse version of the IMPACTA model grid.

	Test 1	Test 2
Free-stream Mach M_∞	0.5	0.5
Thrust line incidence α_T	0 deg	-2 deg

Table C.1: IMPACTA propulsion unit: flow conditions for preliminary steady tests without blades.

C.1. Wing Pressure Comparison against Experimental Data

Figure C.1(b) shows, as an example, the pressure coefficient distribution on the model for $M_\infty = 0.5$ and $\alpha_T = -2$ deg. The pressure on the starboard stub wing was compared against the experimental data of ARA (see Figure C.1(a) for the pressure taps location). Figures C.2 and C.3 show this comparison for the two simulated test cases respectively. Measurements carried out with the acoustic liner inserted in the

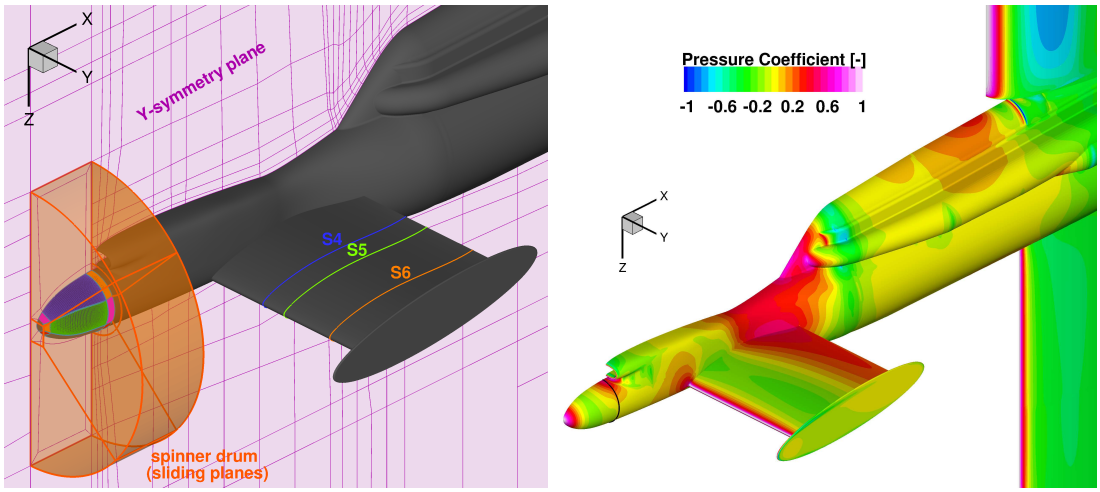

(a) Grid layout visualisation.

(b) Pressure coefficient for $M_\infty = 0.5$ and $\alpha_T = -2$ deg.

Figure C.1: HMB3 validation - preliminary study: IMPACTA wind tunnel model without the propeller.

wind tunnel are reported, corrected for the channel effect as explained in Appendix B. As can be seen, the predictions of HMB3 agree very well with the experimental data, for both flow conditions and at all the three span-wise stations. Suction and pressure sides are both represented satisfactorily. The small differences between the three stations are also captured by the CFD solver. The numerical setup is therefore proved to be adequate to represent the wind tunnel tests, and the mesh density appears sufficient for aerodynamic predictions, at least in absence of the propeller.

C.2. Estimation of Spinner Loads

The simulation at cruise conditions (test 2 of Table C.1) was also used to have an approximation of the effect of the mere spinner on the propeller loads. This was done to be able to estimate the apparent propeller thrust, i.e. the shaft thrust minus the spinner drag, in the same way of the experiments.

During the wind tunnel tests, the spinner drag was measured from the shaft balance with the hub rotating without blades installed. To evaluate the CFD-predicted spinner drag, pressure and viscous stresses were integrated over the spinner surface (region ahead of the black line in Figure C.1(b)). In particular, the integration was performed using Tecplot on cell-vertex surface results. A difference of +29% with respect to the experimental data was observed, which means +37 drag counts for the cruise validation test case (see Table 4.1 for the details on the operating conditions). This difference may be due to:

1. the fact that the spinner is not rotating in the CFD simulation as opposed to the

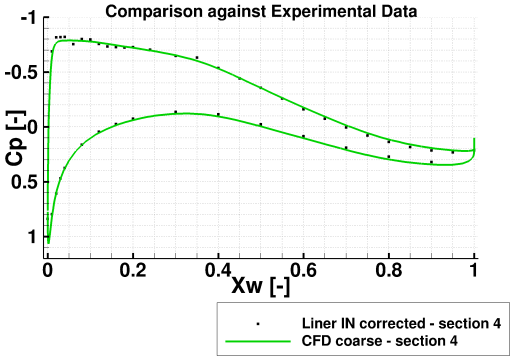

(a) Span-wise station S4: $y = 0.7R$.

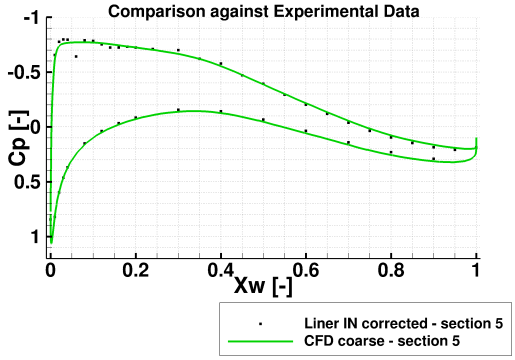

(b) Span-wise station S5: $y = 0.9R$.

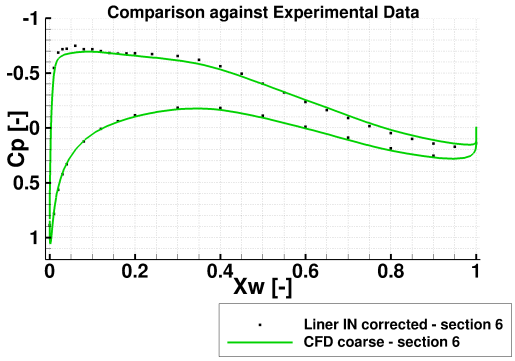

(c) Span-wise station S6: $y \sim 1.3R$.

Figure C.2: HMB3 validation - preliminary study: pressure coefficient on the IMPACTA wind tunnel model without the propeller for $M_\infty = 0.5$ and $\alpha_T = 0$ deg (test 1).

experiments,

2. the effect of the gap between propeller hub and engine in the wind tunnel model not accurately taken into account,

3. HMB3 over-predictions and/or measurement errors.

To quantify the effect of the spinner rotation on its drag estimate, the CFD steady prediction was compared against the CFD unsteady result for the cruise validation test case as an example. The latter was computed integrating directly in the code the loads on the spinner area (thus using cell-center data), and an averaged value over one complete propeller revolution was considered. It is noted that the integration area is slightly smaller because of the presence of the blades installed. The unsteady prediction differ from the steady one by -11 drag counts, yielding closer results to the experimental data. It was therefore decided to use the unsteady estimate of the hub drag to compare the HMB3 results with the ARA performance measurements (refer to Table 4.2 for the comparison). For this reason, a steady simulation without blades at climb conditions was not carried out.

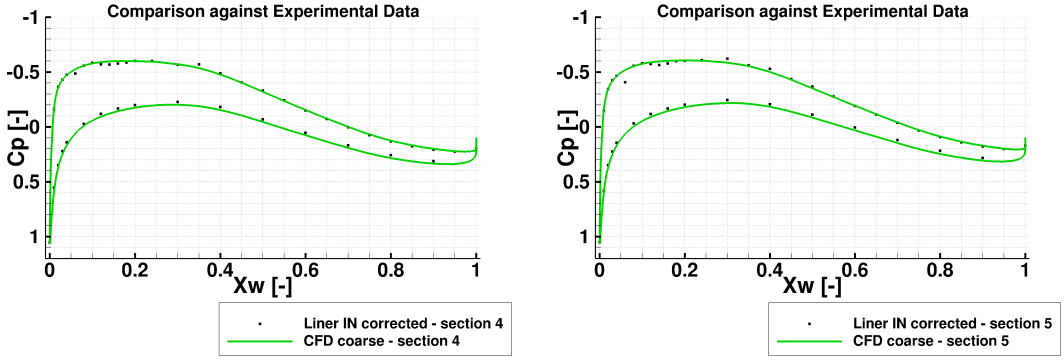

(a) Span-wise station S4: $y = 0.7R$.

(b) Span-wise station S5: $y = 0.9R$.

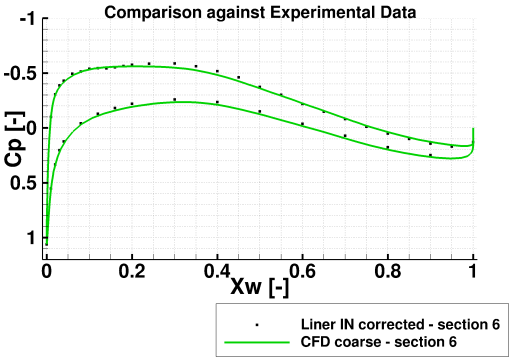

(c) Span-wise station S6: $y \sim 1.3R$.

Figure C.3: HMB3 validation - preliminary study: pressure coefficient on the IMPACTA wind tunnel model without the propeller for $M_\infty = 0.5$ and $\alpha_T = -2$ deg (test 2).

Appendix D

Sound Levels Correction for Thrust Difference

The semi-empirical approaches employed to correct the noise levels to account for a difference in propeller thrust are shortly described below. For the overall A-weighted SPL, the Dobrzynski's method was used. For the harmonic SPL, the ESDU 76020 procedure was followed.

D.1. Dobrzynski's Method

Dobrzynski developed a semi-empirical method[261] from a dataset of noise calculations for a generic general aviation propeller, varying number of blades, diameter, and operating conditions. Calculations were performed using the FW-H equation[42] solved in the time domain (the employed method is described in detail in [273]). Simple equations were derived by the author to approximate the overall A-weighted sound pressure, taking as input only easily accessible design parameters such as number of propellers N_p, number of blades N_b, diameter D, tip rotational and helical Mach numbers M_{TIP} and $M_{h,\text{TIP}}$, RPM, power P and flyover height H. The method assumes subsonic propellers with $0.45 \leq M_{h,\text{TIP}} \leq 0.85$.

D.1.1 Estimation Procedure

The OASPL is determined as:

$$OASPL = 108.6 + \sum_{i}^{7} L_i \text{ dB}_A, \tag{D.1}$$

where the L_i contributing terms represent the effect of different factors on the overall noise. In particular, they are defined as follows:

$L_1\left(\frac{P}{M_{\mathbf{TIP}}^3 D^2 N_b}, M_{h,\mathbf{TIP}}\right)$ accounts for the effect of the blade loading,

$L_2\left(N_b, M_{h,\mathbf{TIP}}\right)$ accounts for the effect of the number of blades,

$L_3\left(RPM, M_{h,\mathbf{TIP}}\right)$ accounts for the effect of the propeller rotational speed,

$L_4\left(\frac{D}{H}\right)$ accounts for the effect of the flyover distance,

$L_5\left(M_{h,\mathbf{TIP}}\right)$ accounts for the effect of the helical tip Mach number,

L_6 corrects for climb out conditions if needed,

$L_7\left(N_p\right)$ accounts for the effect of the number of propellers.

Equations to calculate each L_i term can be found in [15].
The variation of L_1 can be therefore used to estimate the impact of a change in the propeller loading on the OASPL:

$$\Delta OASPL = 10(2.36 - 1.25 M_{h,\mathrm{TIP}}) \log\left(\frac{P(T_T)}{P(T_S)}\right) \text{ dB}_A, \tag{D.2}$$

where $P(T_T)$ and $P(T_S)$ are the propeller power at the target and at the simulated thrust, respectively. The first is unknown but, assuming that T_T is close enough to T_S, it can be approximated using the momentum theory and keeping constant the ratio between actual and ideal power (P and P_i, respectively), i.e. $P(T_T) = \frac{P(T_S)}{P_i(T_S)} P_i(T_T)$.

D.2. ESDU Method 76020

The Engineering Sciences Data Unit (ESDU) service[274] provides validated analysis tools, data, principles, and related software, for a wide range of engineering fields. This extensive database includes published and unpublished data and methods that allow fast and low-cost predictions with engineering accuracy, resulting very useful in the design process.
The *Aircraft Noise* ESDU series comprises items on noise estimation from the different aircraft sound sources, noise propagation and transmission in the cabin, and noise reductions. The ESDU method 76020[262], "Estimation of the maximum discrete frequency noise from isolated rotors and propellers", allows to quickly estimate the sound pressure level of propeller tones. Graphical procedures are given to estimate the SPL of the first harmonic, and corrective terms for the higher harmonics, starting from propeller's number of blades N_b, diameter D, tip Mach number M_{TIP}, thrust T, power P and distance from the source d. A computer program is also available. The method is based on Gutin's theory[36], and uses experimental measurements from static tests. A subsonic axial flight is assumed (non-axial conditions are dealt in ESDU 11005[275]).

D.2.1 Estimation Procedure

The SPL at the propeller fundamental frequency is determined from the summation of five components I_i as follows:

$$SPL(BPF) = I_1\left(\frac{T}{D^2}\right) + I_2\left(\frac{D}{d}, M_{\text{TIP}}\right) + I_3\left(\frac{P}{T}, M_{\text{TIP}}\right) + I_4\left(M_{\text{TIP}}, N_b\right) + \\ + I_5\left(\frac{T}{D^2 M_{\text{TIP}}^2}\right) \text{ dB}. \tag{D.3}$$

The noise at higher tones is then evaluated via the addition of two corrective terms:

$$SPL(mBPF) = SPL(BPF) + I_6\left(M_{\text{TIP}}, m\right) + I_7\left(\frac{T}{D^2 M_{\text{TIP}}^2}, m\right) \text{ dB}, \tag{D.4}$$

where $m = 2, 3, ..$ is the harmonic order.
Graphics for each contributing term I_i are given in the document. Some can be easily expressed via lines equations, others show a non-linear trend.
As can be seen from the formula D.3 and D.4, the propeller thrust appears in only four components: I_1, I_3, I_5 and I_7. The difference between their value for the target thrust T_T, and that for the actual thrust at the simulated conditions T_S, can be used to estimate the noise level correction for the different thrust:

$$\begin{cases} \Delta SPL(BPF) = \sum_j [I_j(T_T) - I_j(T_S)], & j = 1,3,5 \\ \Delta SPL(mBPF) = \Delta SPL(BPF) + [I_7(T_T) - I_7(T_S)]. \end{cases} \tag{D.5}$$

Since a change in the thrust is connected to a change in the power, to determine $I_3(T_T)$, an estimate of the power at the target thrust $P(T_T)$ is required. This was computed assuming a ratio between actual and ideal propeller power (P and P_i, respectively) as that of the simulated conditions, i.e. $P(T_T) = \frac{P(T_S)}{P_i(T_S)} P_i(T_T)$, where P_i is calculated from the momentum theory.
For the sake of completeness, here below are reported the equations used to evaluate ΔSPL of the first three tones for the IMPACTA propellers analysed in Chapter 5:

$$\begin{cases} I_1 = 111 + \frac{19}{\log(9)} \log\left(\frac{T}{p_{ref} D^2} 10^{-6}\right) \text{ dB}, \\ I_3 = 10 M_{\text{TIP}}^2 - 8 M_{\text{TIP}} - 5.6 + \frac{-2.5 M_{\text{TIP}}^2 + 2.25 M_{\text{TIP}} + 1.15}{log(1.25)} log\left(2.5 \frac{P}{T a_\infty}\right) \text{ dB}, \\ I_5 = 0.25 - \frac{0.25}{0.03}\left(\frac{2T}{N_b \rho_\infty Dc (M_{\text{TIP}} a_\infty)^2} - 0.09\right) \text{ dB}, \\ I_7 = \begin{cases} -2.5 + \frac{-6+2.5}{0.154-0.064}\left(\frac{2T}{N_b \rho_\infty Dc (M_{\text{TIP}} a_\infty)^2} - 0.064\right) \text{ dB} & m = 2, \\ -3.5 + \frac{-8+3.5}{0.118-0.052}\left(\frac{2T}{N_b \rho_\infty Dc (M_{\text{TIP}} a_\infty)^2} - 0.052\right) \text{ dB} & m = 3. \end{cases} \end{cases} \tag{D.6}$$

It is noted that these formula derive from the interpolation of the ESDU curves only in the needed parameters range. In particular, it was assumed that:

$$0.5 \leq M_{\mathrm{TIP}} \leq 0.7, \quad 0.5 \leq \frac{P}{Ta_\infty} \leq 0.6, \text{ and } \quad 0.09 \leq \frac{2T}{N_b \rho_\infty Dc(M_{\mathrm{TIP}} a_\infty)^2} \leq 0.12. \tag{D.7}$$